Javier Contreras Aparicio

Mestrado em Robótica e Automação

AMORPHOUS SILICON 3D SENSORS APPLIED TO OBJECT DETECTION

Dissertação para obtenção do Grau de Doutor em
Engenharia dos Materiais, especialidade Microelectrónica e Optoelectrónica

Orientador: Doutora Isabel Maria Mercês Ferreira, Professora Associada, Faculdade de Ciências e Tecnologia da Universidade Nova de Lisboa

Co-orientador: Doutor Rodrigo Ferrão de Paiva Martins, Professor Catedrático, Faculdade de Ciências e Tecnologia da Universidade Nova de Lisboa

Doutor Luis Filipe dos Santos Gomes, Professor Associado, Faculdade de Ciências e Tecnologia da Universidade Nova de Lisboa

Júri:

Presidente: Prof. Doutor Paulo da Costa Luís da Fonseca Pinto

Arguentes: Prof. Doutor João Lemos Pinto
Prof. Doutor Armando Jorge Miranda de Sousa

Vogais: Prof. Doutora Elvira Maria Correia Fortunato
Prof. Doutor Henrique Leonel Gomes
Prof. Doutora Maria Teresa Varanda Cidade
Prof. Doutor Luís Miguel Tavares Fernandes

FACULDADE DE CIÊNCIAS E TECNOLOGIA
UNIVERSIDADE NOVA DE LISBOA

Outubro de 2014

Javier Contreras Aparicio

Mestrado em Robótica e Automação

AMORPHOUS SILICON 3D SENSORS APPLIED TO OBJECT DETECTION

Dissertação para obtenção do Grau de Doutor em
Engenharia dos Materiais, especialidade Microelectrónica e Optoelectrónica

Orientador: Doutora Isabel Maria Mercês Ferreira, Professora Associada, Faculdade de Ciências e Tecnologia da Universidade Nova de Lisboa

Co-orientador: Doutor Rodrigo Ferrão de Paiva Martins, Professor Catedrático, Faculdade de Ciências e Tecnologia da Universidade Nova de Lisboa

Doutor Luis Filipe dos Santos Gomes, Professor Associado, Faculdade de Ciências e Tecnologia da Universidade Nova de Lisboa

Júri:

Presidente: Prof. Doutor Paulo da Costa Luís da Fonseca Pinto

Arguentes: Prof. Doutor João Lemos Pinto
Prof. Doutor Armando Jorge Miranda de Sousa

Vogais: Prof. Doutora Elvira Maria Correia Fortunato
Prof. Doutor Henrique Leonel Gomes
Prof. Doutora Maria Teresa Varanda Cidade
Prof. Doutor Luís Miguel Tavares Fernandes

FACULDADE DE CIÊNCIAS E TECNOLOGIA
UNIVERSIDADE NOVA DE LISBOA

Outubro de 2014

AMORPHOUS SILICON 3D SENSORS APPLIED TO OBJECT DETECTION

In memory of my godfather, Ramon Cañas Represa for setting an example on perfection and of my uncle Pepe Contreras for his successful career and of my friend Ricardo Mengibar for his friendship, during their lifetime.

Acknowledgements

I would like to take this opportunity to thank everyone who supported me and who contributed in some way during my PHD studies.

To my co-supervisor Professor Doctor Rodrigo Martins, my supervisor Professor Doctor Isabel Ferreira and my co-supervisor Professor Luis Gomes for giving me the chance to be able to perform my PHD studies in Portugal, giving me all the necessary support, and funding, so as to complete this project in a satisfactory manner. Most importantly, I would like to thank them for believing in me and my ideas as well as for the fact of giving me the freedom to operate and risk on the scientific initiatives taken. This has given me the necessary knowledge to grow in my career and acquire huge expertise in this area of application.

I would also like to greatly express my gratitude towards Professor Doctor Rodrigo Martins, Professor Doctor Isabel Ferreira and Professor Doctor Elvira Fortunato for their overall help and support during my stay in Portugal and especially for the fact of having to put up with me!

I would like also to thank Professor Luis Gomes and Duarte Guerreiro for providing me with great assistance in order to develop, test, fix, mount, and assemble all electronics systems I have constructed during my stay at CENIMAT-CEMOP, and again, thanks to Professor Luis Gomes for guiding me on the development of electronics and software aspects.

I also specially thank the ASSEMIC European project network and the coordinator in charge Professor Werner Brenner for their cooperation and collaboration for my PhD studies in Portugal.

I would also like to thank Engineer Stephen Thomas from RAL in UK, for helping me enormously during my stay in Portugal with every aspect of his expertise on microelectronics as well as for providing me with some electronic items at no cost whatsoever in order to support my PhD research work. I extend this gratitude towards Mike Homer from SENSTECH in UK, for his help provided on every aspect regarding XDAS system integration as well as for providing me and CENIMAT-CEMOP with faulty X2CHIP components for testing and integration at no cost whatsoever. This appreciation also applies to everyone at RAL and SENSTECH in UK, who has helped me at one point or another.

This expression of gratitude is of course extended to all the partner institutions, staff and fellows from the ASSEMIC European project who collaborated with me and CENIMAT-CEMOP in secondments, meetings and conferences. This allowed the proposed objectives to be reached successfully. I thank specially, Marek Idzikoski from the University of Oldenburg, for providing me that extra help that an expert programmer like him is able to deliver. And I also thank Rafal Wierzibicki for providing me with micro objects for my experiments and Samuel Serra from RAL in UK for providing assistance with CENIMAT-CEMOP's developments. Of course this thankfulness also applies to the staff and fellows inside my own institution, namely being CENIMAT-CEMOP. Therefore I thank David Alves (now at INETI), Daniel Costa, Miguel Moreira, Ricardo Ferreira and Carlos Alcobia for helping me with the electronics testing and development and for the discussions held.

I thank Leonardo Silva for his help and discussions held during my stay at CENIMAT-CEMOP as well as for the efforts made.

I specially thank Sonia Pereira, Lucia Gomes, Diana Gaspar, Antonio Vicente, Tiago Mateus, Sergej Filonovich and Professor Doctor Hugo Águas, from CENIMAT-CEMOP for their valuable help regarding the fabrication of 3D sensors.

I specially thank Sergej Filonovich and Professor Doctor Hugo Águas for their extra help, advices and discussions regarding the 1D-3D sensors during my stay at CENIMAT-CEMOP.

I specially thank Pawel Wojcik and Antonio Vicente for their help and discussions on experiments and manuscript image preparation. I thank Ricardo Ferreira for his general help on various technical aspects.

Of course, also I can’t forget the help given by the rest of my colleagues at CENIMAT-CEMOP, such as Luis Pereira, Alexandra Gonçalves, Gonzalo Gonçalves, Pedro Barquinha, Iwona Bernacka, Manuel Quintela, Carla Saldanha, Filomena Calixto, Sara Oliveira, Joana Vaz Pinto, Raquel Barros, Vitor Figueiredo, Paulo Manteigas, Rita Branquinho, Sonia Seixas and Salomão Lopes, amongst others. I also thank anyone who helped me along these years and whom I have forgotten to mention here.

I would also like to thank FCT-MCTES for providing me with the PhD fellowship SFRH/BD/62217/2009.

Finally, I would like to thank my family for supporting me during my PhD studies and stay in Portugal.

Resumo

Hoje em dia, as câmaras 3D e microscópios disponíveis no mercado usam sensores digitais ou discretos, como por exemplo CCDs ou CMOS para aplicações de deteção de objetos. No entanto, estes sistemas não são suficientemente rápidos para algumas aplicações porque precisam de grandes recursos no processamento da informação e podem ser lentos. Portanto, existe um claro interesse na exploração das possibilidades de aplicação de sensores analógicos tal como os *arrays* de sensores de posição, com o objetivo final de integrá-los em câmaras de varrimento 3D ou na deteção de micro objetos.

O trabalho realizado nesta tese pretendeu contribuir com um estudo detalhado para a implementação de protótipos de sistemas de deteção de objetos utilizando sensores de posição (PSD) de 32 e 128 linhas que foram fabricados na câmara limpa do CENIMAT-CEMOP. Durante a primeira fase do trabalho, o ponto de partida consistiu na fabricação e no estudo das especificações estáticas e dinâmicas dos sensores e seu condicionamento em relação ao conhecimento científico e tecnológico existente. Consequentemente, foi implementada a eletrónica adequada e relevante para a aquisição de dados e processamento de sinais. Vários protótipos foram construídos com *arrays* de sensores PSD de 32 e 128 linhas. Soluções óticas apropriadas foram integradas para funcionar com os protótipos construídos, permitindo realizar os testes necessários à obtenção dos resultados apresentados nesta tese. O *software* de controlo, aquisição de dados e plataforma de varrimento 3D foram implementados e combinados para formar vários sistemas integrados com os sensores 3D (*arrays* de PSDs) de 32 e 128 linhas. O rendimento do *array* de sensores PSD de 32 linhas e respetivo sistema de aquisição foi testado em aplicações de visão de máquina, como por exemplo o varrimento de objetos em 3D, e também para aplicações de microscopia, com por exemplo a deteção de movimento de micro objetos. Também foram realizados testes em *arrays* de sensores PSD de 128 linhas tendo-se obtido não linearidades de aproximadamente 4 a 7% nos sensores 1D. Os resultados obtidos mostram a possibilidade de usar um *array* linear de 32/128 sensores 1D baseados na tecnologia do silício amorfo para o varrimento de objetos 3D e replicação do seu perfil. O sistema e a configuração da plataforma 3D apresentada permite o varrimento 3D a elevadas velocidades e taxas de aquisição. O detalhe ou defeito mínimo que pode ser detetado pelo sistema e sensor é de aproximadamente 350μm usando a configuração estudada. Também é possível identificar as dimensões reais de um objeto 3D em função do ângulo de varrimento, na gama de 15º a 85º, da distância objeto-sensor e da ótica utilizada. Usando estes sensores e respetivo sistema de deteção, objetos simples e complexos podem ser reproduzidos em 3D com elevada precisão e resolução. O sistema de sensores de estrutura nip pode detetar objetos com cores primárias e mesmo com cores derivadas, pelo ajuste correto do tempo de integração do sistema e pela combinação de fontes de luz branca e vermelha, verde e azul (RGB), tendo-se obtido um erro colorimétrico médio de 25,7. Para além disso, o sistema produzido também permite detetar o movimento de micro objetos com recurso a um microscópio. Este oferece a possibilidade de detetar se um micro objeto está em movimento, as suas dimensões (2D) e a sua posição, mesmo para elevadas velocidades de varrimento. Os resultados mostram uma não-linearidade de cerca de 3% e uma resolução < 2µm.

Palavras-chave: Silício amorfo, sensores de posição, deteção de objetos 3D, triangulação laser, deteção de movimento de micro objetos

Abstract

Nowadays, existing 3D scanning cameras and microscopes in the market use digital or discrete sensors, such as CCDs or CMOS for object detection applications. However, these combined systems are not fast enough for some application scenarios since they require large data processing resources and can be cumbersome. Thereby, there is a clear interest in exploring the possibilities and performances of analogue sensors such as arrays of position sensitive detectors with the final goal of integrating them in 3D scanning cameras or microscopes for object detection purposes.

The work performed in this thesis deals with the implementation of prototype systems in order to explore the application of object detection using amorphous silicon position sensors of 32 and 128 lines which were produced in the clean room at CENIMAT-CEMOP. During the first phase of this work, the fabrication and the study of the static and dynamic specifications of the sensors as well as their conditioning in relation to the existing scientific and technological knowledge became a starting point. Subsequently, relevant data acquisition and suitable signal processing electronics were assembled. Various prototypes were developed for the 32 and 128 array PSD sensors. Appropriate optical solutions were integrated to work together with the constructed prototypes, allowing the required experiments to be carried out and allowing the achievement of the results presented in this thesis. All control, data acquisition and 3D rendering platform software was implemented for the existing systems. All these components were combined together to form several integrated systems for the 32 and 128 line PSD 3D sensors. The performance of the 32 PSD array sensor and system was evaluated for machine vision applications such as for example 3D object rendering as well as for microscopy applications such as for example micro object movement detection. Trials were also performed involving the 128 array PSD sensor systems. Sensor channel non-linearities of approximately 4 to 7% were obtained. Overall results obtained show the possibility of using a linear array of 32/128 1D line sensors based on the amorphous silicon technology to render 3D profiles of objects. The system and setup presented allows 3D rendering at high speeds and at high frame rates. The minimum detail or gap that can be detected by the sensor system is approximately 350 μm when using this current setup. It is also possible to render an object in 3D within a scanning angle range of 15º to 85º and identify its real height as a function of the scanning angle and the image displacement distance on the sensor. Simple and not so simple objects, such as a rubber and a plastic fork, can be rendered in 3D properly and accurately also at high resolution, using this sensor and system platform. The nip structure sensor system can detect primary and even derived colors of objects by a proper adjustment of the integration time of the system and by combining white, red, green and blue (RGB) light sources. A mean colorimetric error of 25.7 was obtained. It is also possible to detect the movement of micrometer objects using the 32 PSD sensor system. This kind of setup offers the possibility to detect if a micro object is moving, what are its dimensions and what is its position in two dimensions, even at high speeds. Results show a non-linearity of about 3% and a spatial resolution of < 2µm.

Keywords: Amorphous silicon, position sensitive detectors, sheet-of-light range imaging, micro object detection, triangulation systems, 3D object detection

Table of contents

List of Figures

List of Tables

List of symbols, acronyms and abbreviations

ASIC	Application Specific Integrated Circuit
a-Si:H	Hydrogenated Amorphous Silicon
CCD	Charge Coupled Device
CIE	Commission Internationale d'Eclairage (International Commission on Illumination)
CMM	Coordinate measuring machine
CMOS	Complementary Metal Oxide Semiconductor
CMYK	Cyan, Magenta, Yellow and Black
FPGA	Field programmable gate array
j.n.d	Just noticeable difference
LED	Light emitting diode
NEP	Noise equivalent power
NIP	n-i-p semiconductor structure
PCB	Printed circuit board
PECVD	Plasma enhanced chemical vapor deposition
P-N	P-type and N-type silicon
PIN	p-i-n semiconductor structure
PSD	Position Sensitive Detector
Q.E.	Quantum efficiency
RF	Radio frequency
RGB	Red, Green and Blue
SW	Staebler-Wronski
TCO	Transparent Conductive Oxide
TDI	Time delay and integration technology
UV	Ultra-violet
VHF	Very high frequency
1D, 2D, 3D	One, two and three dimensional

μ	Micro
R_λ	Responsivity
I_p	Photocurrent
P	Incident light power
λ	Wavelength
h	Planck’s constant
c	Speed of light in vacuum
q	Electron charge
C_j	Junction capacitance
R_{sh}	Shunt resistance
R_s	Series resistance
I_{ph}	Incident light generated photocurrent
I_d	Forward current through diode
I_o	Output current
V_o	Output voltage
R_L	Load resistance
σ_e	Linearity error
S_m	Standard deviation
ΔE	Colourimetric error

Chapter 1

Machine Vision

Chapter 1. Machine Vision

Summary

This chapter provides an introduction to machine vision starting by a brief history and market analysis, and subsequently reviewing more in depth, each of the components of a typical machine vision system, with a special emphasis on the characteristics of the existing types of sensors such as discrete or analogue in accordance to the state of the art. Colour concepts are also addressed in this chapter.

1.1. Introduction

Quality is nowadays a critical factor in industry since it allows companies to be competitive in the market while being able to deliver optimum products to its clients. Companies in Japan became pioneers in manufacturing quality products by the 1970s. By the 1990s, companies in Europe and America were obliged to introduce quality control procedures into their goods and manufacturing processes for competing with Japanese ones. Machine vision has become an essential quality control tool for increasing manufacturing quality.

We could define machine vision as the process of designing, developing and integrating automatic imaging systems to improve manufacturing processes in industry. Automation, mechanical engineering, optics and computer science make up machine vision.

However, another suitable definition for machine vision can be quoted:

"The use of devices for optical, non-contact sensing to automatically receive and interpret an image of a real scene in order to obtain information and/or control machines or processes" [1].

The initial concept of using machine vision for industrial inspection dates back to the 1930s, although it was only after the 1970s that the idea developed further into a system. Then in the 1990s, the concept received special interest due to the advances and progress made in vision systems image and processing technology. This resulted in huge growth of the machine vision industry. Finally, in the 2000s, considerable technology improvements have taken place and the market is still growing and expanding at a fast pace.

However, it must be stated that, the successful design and integration of these systems is still a bottleneck and remains a challenge in several areas, partly due to the lack of skilled labour [2].

The components of a machine vision system do not suffer from fatigue as humans do, and neither do they do mistakes or take decisions which could affect the procedure. In machine vision systems it is necessary to collect and process each individual pixel and construct a relevant image from these. Even though human vision has been regarded as impractical for industrial inspection, up to date no machine vision system is capable of matching human optics on some aspects such as, tolerance to changes in lighting and degradation of the image, interpretation and comprehension of the image, flexibility or variability of parts inspected, etc. On the other hand, some industrial applications do not need the high precision offered by human vision [3, 4]. Tasks typically allocated to these systems include the detection of surface defects, serial number identification, counting parts on a conveyor belt, etc. Amongst the vast majority of sectors, automobile and semiconductor manufacturing, pharmaceutical packing and film container printing are some related examples. So, today, machine vision systems are a vital component of quality control processes present in all areas of industry.

Figure 1.1 illustrates the European vision technology market, total turnover of vision products, in the year 2006. The automotive sector amounts to a great percentage of the manufacturing industry, 29% of the market share, and this is followed by the glass, printing, electronics and other sectors.

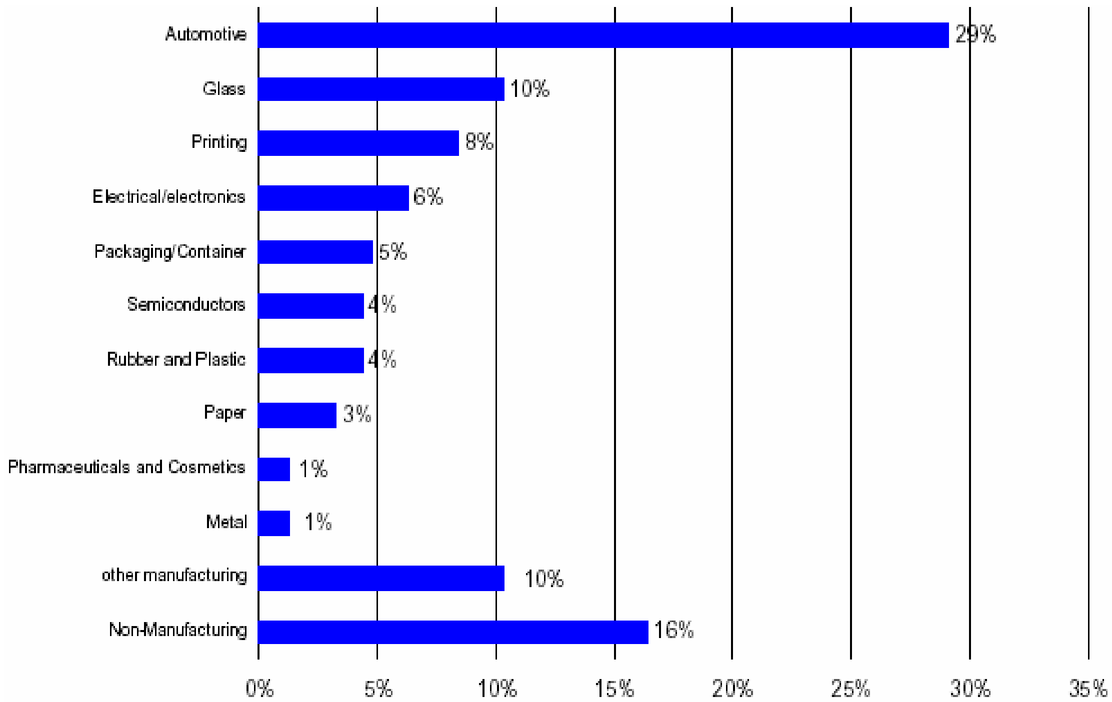

Figure 1.1 – European market total turnover of vision products 2006.
Percentage turnover shares by industries (%) [5].

Figure 1.2 shows the total revenue derived from vision products worldwide in the year 2006. Europe accounts for 68% of the market share and it is particularly interesting that the highest percentage of sales achieved worldwide by European Companies were in Portugal and Spain [5].

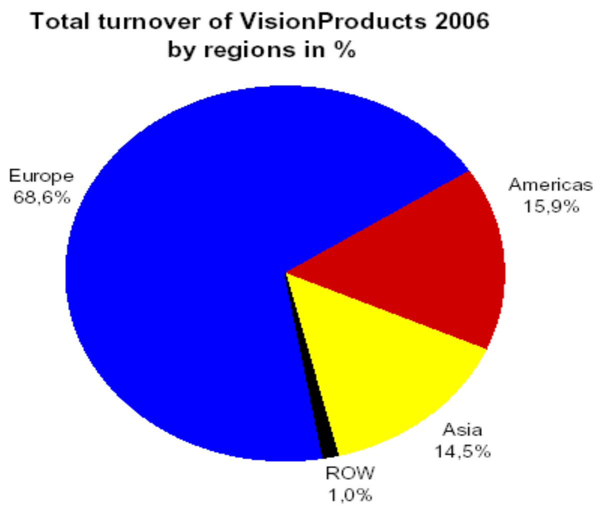

Figure 1.2 – Worldwide total turnover of Vision Products 2006 by regions (%) [5].

Traditional machine vision systems usually employ a Charged Coupled Device (CCD) as the vision sensor component. A CCD is normally comprised of a matrix of pixels and so therefore each pixel has to be analysed and processed when an image is projected on it.

In the following work the CCD's detection principle and components are revised in order to be compared to position sensitive detectors (PSD).

1.2. Components of a machine vision system

A typical machine vision system is usually composed of several or all of the following components:

- One or more image sensor structures. Usually one or more digital or analogue cameras are used.
- Suitable optics for image focusing and projection. Lenses are normally used to focus the desired field of view onto the image sensor.
- Suitable light sources (Lasers, LEDs, Fluorescent or Halogen lamps, etc).
- An interface device (analogue to digital converter) to digitize and transfer images to the processor/PC.
- Input/Output hardware. Usually being a processor/PC or embedded processor.
- Software platforms for image processing and representation. These platforms are also currently used to detect and recognise relevant image features.
- A synchronized system configuration involving sensors (magnetic, optical, etc) to detect movement of parts, for example, on a production line which would trigger image acquisition and processing. Actuators are also welcome to sort, route or reject defective parts if necessary.

1.3. Photodiodes

The most used sensor structures in CCDs are silicon PIN photodiodes since they have a fast response speed, an excellent photo to dark current ratio and a wide spectral response. Other existing types of structures are PN, Schottky and Avalanche junctions however they have lower sensitivity performances [6].

1.3.1. Operating characteristics of a photodiode

1.3.1.1. Spectral response

The spectral response or responsivity (R_λ) is the ratio of the photocurrent I_p to the incident light power P at a given wavelength of a silicon photodiode [7].

$$R_\lambda = \frac{I_p}{P} \qquad \textbf{[1.1]}$$

where, R_λ units are A/W.

1.3.1.2. Quantum Efficiency

Quantum efficiency, Q.E., is the ratio of the number of charge carriers (or electron-hole pairs) generated to the number of photons striking the detector and it is related to responsivity R_λ by [7]:

$$Q.E. = R_\lambda \frac{hc}{\lambda q} \approx 1240 \frac{R_\lambda}{\lambda} \qquad \textbf{[1.2]}$$

where, λ is the wavelength of the light in nanometers (nm), h is Planck's constant (6.63×10^{-34} Js), c is the speed of light in vacuum (3×10^8 m/s), and q is the electron charge (1.6×10^{-19} C).

1.3.1.3. Linearity

As far as sensor detection is concerned, linearity is an important characteristic, as a linear increase of the generated photocurrent in accordance with an increase of the incident light power must be verified. Noises current as well as the series and load resistances determine linearity. Photodiode nonlinearities are typically less than 1%. Figure 1.3, shows a photodiode's equivalent circuit where an ideal diode is in parallel with a current source, a junction capacitance C_j and a shunt resistance R_{sh} and in series with resistance R_s:

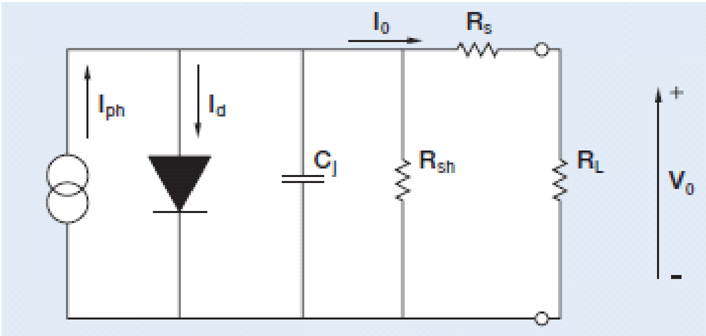

Figure 1.3 – Equivalent circuit of a silicon photodiode [7].

where, I_{ph} is the incident light generated photocurrent, I_d is the forward current through the diode, I_o is the output current and V_o is the output voltage.

The p-n junction is represented by the diode and the photocurrent generated by the incident light is represented by the current source. An ideal photodiode should have no series resistance and an infinite shunt resistance [7-9]. Dark current is the existing leakage current flowing when the photodiode is in dark conditions. Extremely low light levels, when the photocurrent equals the level of the noise generated, compromise the usefulness of the device.

1.3.1.4. Response time

The product of the junction capacitance C_j and the external load resistance R_L shown in figure 1.3 determines the response time of a photodiode. In turn, the existing p-n junction depletion region within the photodiode defines the junction capacitance C_j. However, the response time is always influenced by the load resistance, the wavelength of the light and the applied voltage on the diode. The response time can be analyzed by measuring the rise time t_r or the fall time t_f. The rise time is the time taken for the output response to rise from 10% to 90% of its final value and the fall time is the time taken for the output response to fall from 90% to 10% of this same final value. The rise time t_r is defined by the following expression [7]:

$$t_r = 2.2\tau_1 = 2.2C_t \times R_L \qquad \textbf{[1.3]}$$

where, τ_1 is the time constant, determined by the product of the load resistance R_L and the terminal capacitance of the photodiode C_t. C_t is the sum of the photodiode junction capacitance Cj and the package capacitance.

The rise time t_r is also influenced by τ_2, which is the diffusion time of carriers generated outside the depletion layer and when the product of C_t and R_L shown in equation 1.3 is small, it is exclusively τ_2 which defines the response time of a photodiode.

The response waveform of a photodiode is illustrated in the following figure, figure 1.4:

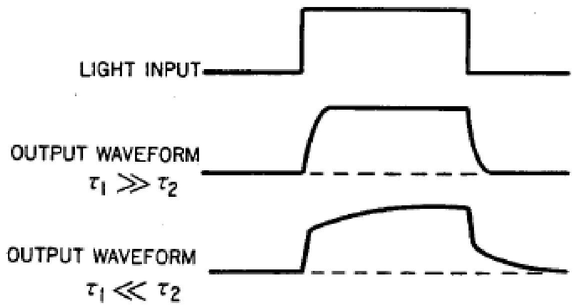

Figure 1.4 – Photodiode response waveform [7].

1.3.1.5. Operating modes

A photodiode allows the photovoltaic or unbiased mode and the photoconductive or biased operating mode. The specifications of the application determine which operating mode is most appropriate. Photovoltaic mode is suitable for low light level and low frequency applications and it allows simplicity in system design and development. When considering the photoconductive mode of operation, response speed and linearity could certainly improve via the application of a reverse bias, however, dark and noise currents as well as response variations due to temperature are likely to increase.

Despite these drawbacks and as previously stated, for high speed applications such as optical communications and remote control, PIN photodiodes offer not only a good response speed but excellent dark current and voltage resistance characteristics when a reverse voltage is applied.

It is also relevant to know that the measurements of signals from a photodiode can be performed either as a current or voltage. Clearly, a much better performance in terms of linearity, offset and bandwidth is obtained when reading a current, since it is proportional to the incident light power. A trans-impedance configuration should be used in order to convert from current to voltage and in fact the read out circuitry of a photodiode is generally a trans-impedance amplifier as shown below in figure 1.5:

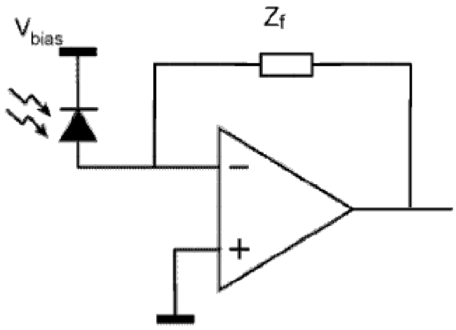

Figure 1.5 – Trans-impedance amplifier read out circuitry of photodiode [9].

In order to keep the trans-impedance amplifier stable the impedance Z_f is used and this is usually a resistance R_f in parallel to a capacitance C_f.

1.3.1.6. Current –Voltage characteristics

The current-voltage curve of an ideal diode shows a small reverse saturation current generated when a reverse bias is applied (V_R) and an exponential increase in current occurs for forward bias (V_F) (see figure 1.6). The relationship between the dark and the saturation current of the ideal diode is established by the following equation [7]:

$$I_D = I_{SAT}\left(e^{\frac{qV_A}{k_BT}} - 1\right) \qquad \textbf{[1.4]}$$

where, I_D is the dark current, I_{SAT} is the reverse saturation current, q is the electron charge, V_A is the applied voltage, k_B is Boltzmann's constant (1.38×10^{-23} J/K) and T is the temperature.

Under illumination and in photovoltaic mode (V = 0) the current given by the diode is the reverse saturation current. Therefore the IV curve in the reverse bias shifted by an amount equal to I_p, proportional to the level of light power, therefore separate curves are obtained for different light levels which are represented by P_0, P_1, P_2 in figure 1.6. At P_1, the photodiode has already been illuminated and the photocurrent can be obtained by equation 1.5 [7]:

$$I_{TOTAL} = I_{SAT}\left(e^{\frac{qV_A}{k_BT}} - 1\right) - I_P \qquad \textbf{[1.5]}$$

where, I_{TOTAL} is the total current and I_p is the measured photocurrent for a certain light power.

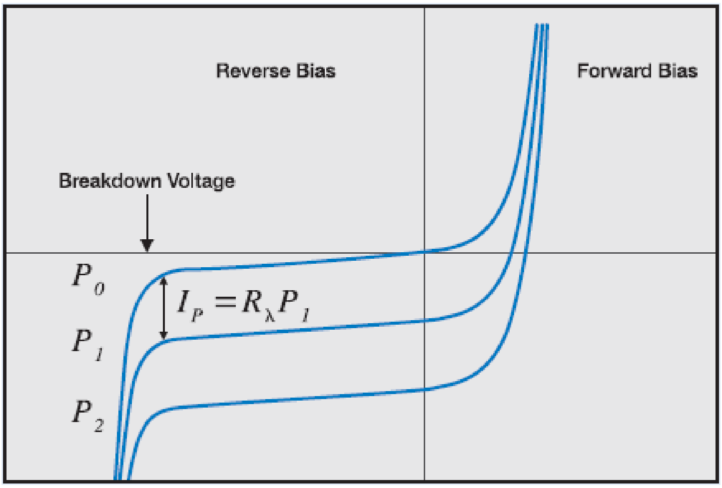

Figure 1.6 – Photo-current/Voltage curves under different level of illumination [7].

The maximum applied reverse bias voltage can never reach the breakdown voltage, since severe damage can occur on the device, as shown in figure 1.6.

1.3.1.7. Noise characteristics

In a photodiode the total noise takes into account the Johnson noise and the shot noise. The Johnson noise is related mainly to the shunt resistance, with substantial contribution from all other resistors (including the load resistor) and it is the dominant noise when working in unbiased (photovoltaic) mode. Its magnitude is calculated using the following expression [7]:

$$I_{jn} = \sqrt{\frac{4k_B T\Delta f}{R_{sh}}} \qquad \textbf{[1.6]}$$

where, I_{jn} is the Johnson noise current, Δf is the noise measurement bandwidth and T is the temperature.

The shot noise is related to photocurrent and dark current oscillations and it is the dominant noise when working in biased (photoconductive) mode. Its magnitude is calculated using the following expression [7]:

$$I_{sn} = \sqrt{2q(I_P + I_D)\Delta f} \qquad \textbf{[1.7]}$$

where, I_{sn} is the shot noise current, I_P is the photocurrent and Δf is the noise measurement bandwidth.

The total photodetector noise current is related to the Johnson and the shot noise currents by the following expression [7]:

$$I_{tn} = \sqrt{I_{sn}^2 + I_{jn}^2} \qquad \textbf{[1.8]}$$

where, I_{tn} is the total photodetector noise current, I_{sn} is the shot noise current and I_{jn} is the Johnson noise current.

1.3.1.8. Noise Equivalent Power (NEP)

The quantity of incident light power on a photodiode required to produce a photocurrent equivalent to the existing noise level is regarded as the noise equivalent power and it is given by [7]:

$$NEP = \frac{I_{tn}}{R_{\lambda}} \qquad \textbf{[1.9]}$$

where, NEP is the noise equivalent power ($W/(Hz)^{1/2}$), I_{tn} is the total photodetector noise current and R_{λ} is the responsivity (A/W).

1.4. Discrete image sensors

1.4.1. Charged Coupled Devices (CCDs)

The use of Charged Coupled Devices or CCDs as image sensors has spread hugely over a broad range of applications ranging from astronomy, medicine or microtechnology to all kinds of recognition and mapping procedures. CCDs are used virtually everywhere, such as for example photographic cameras, standard video cameras, security cameras, fax machines, bar-code readers, photocopiers, and others [10, 11].

The main purpose of a CCD is to generate object images but it is also able to transfer electrical charge or store information. The incident light coming from an object is the optical input to a CCD and the output is an electronic signal which needs to be processed using hardware. Subsequently, suitable software should be used to present the data or to represent it as an image to the user [12, 13].

CCD imagers are made using silicon manufacturing processes. The fabrication process and device architecture has been optimized to achieve the best possible optical properties, which is ideal for applications where image quality is the primary concern.

As shown in figure 1.7, a CCD is an X-Y matrix of rows and columns composed of photodiodes and adjacent charge holding regions. Light is incident on the photodiodes and the charge generated is subsequently transferred to the adjacent cells within the columns. This charge is then converted to voltage after serial readout and finally amplified. Several clock signals and bias voltages are required to operate the device. The architecture permits high performance imaging plus offering low noise and it would not be suitable to integrate further electronics onto the silicon [14].

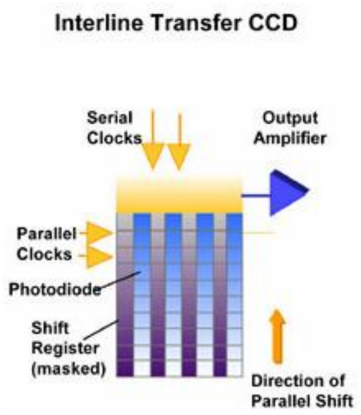

Figure 1.7 – Schematic of the architecture of a CCD (Interline type) [14].

CCD technology is most suitable for applications requiring the highest standards of image quality such as the majority of medical and scientific tasks, digital photography, specific industry imaging and broadcast TV. Therefore, even though image quality and flexibility are advantages of CCD based systems, overall system size is a disadvantage now that some applications require the integration of small sized solutions [15].

Advances are constantly being made and some companies are already offering ultra-high resolution CCDs with ultra-high frame rates. The resolution is already as large as 33 megapixels and can reach up to more than 100 megapixels on custom devices! Of course, due to their capabilities these imagers are excellent in the highest performance applications. Figure 1.8(a) shows a photograph of an “Area Scan” or large pixel area device manufactured by DALSA Corporation. It is regarded as “Area Scan”, because the application scans the whole area provided by the CCD and so the imaging process benefits from all the existing pixels.

Another type of CCD is the linear array of pixels, also regarded as a “Line Scan” CCD. This is effectively the same as using just one row or column from a large pixel area CCD. A photograph of the device is shown in figure 1.8(b).

The “Line Scan” device is composed of just a single array of pixels and it is integrated in linear array cameras. The vision systems formed by these cameras generate just one line of image per frame (instant of time). Therefore, all frames acquired over time are combined to illustrate the two dimensional image resulting from this continuous process. The resolution range available for the “Line Scan” device is usually from 512 to 17000 pixels and some examples of relevant applications include electronics, postal or parcel inspection as well as pick and place operations.

Figure 1.8 – (a) Photograph of an “Area Scan” or large pixel area CCD (b) Photograph of a “Line Scan” or linear array of pixels CCD, (c) Photograph of a TDI (Time Delay and Integration) “Line Scan” CCD manufactured by DALSA Corporation [16].

A specific “Line Scan” CCD is also available for high speed and low light level applications. This line scan technology is called TDI or time delay and integration technology and it is ideal for situations where high illumination levels might cause damage to products or where objects are moving at high speeds in a conveyor belt. The device is far more sensitive than the standard “Line Scan” CCD and the resolution can go up to 12000 pixels or beyond. Semiconductor wafer inspection and food inspection are perfect applications for such a device [16]. Figure 1.8(c) shows a photograph of the TDI “Line Scan” CCD.

1.4.2. Complementary Metal Oxide Semiconductor (CMOS) Imagers

CMOS imagers can be regarded as systems on a chip. They are used in applications where image quality is not important or where the size of the system is particularly relevant. Low quality videoconferencing, simple scanners, toys, as well as the majority of high volume applications are examples of where these devices are integrated.

Just as CCD imagers, which were described in section 1.4.1, CMOS imagers are also manufactured using silicon technology. However, both devices are substantially different in various aspects. For example, CMOS imagers offer lower image quality and flexibility than CCD imagers but, on the other hand they consume less power and are easier to integrate resulting in an overall smaller system size. Another advantage or added bonus is that they are able to profit from continuous semiconductor technology advances and this allows any extra needed electronic components to be further integrated on the chip itself deriving in an overall lower system cost than CCD imager based systems.

Figure 1.9(a) shows the architecture of the CMOS imager. As can be seen, a photodiode, a charge to voltage conversion unit, a transistor and an amplifier can be found in each pixel or photo site. Timing and readout signals are applied through a grid of metal interconnects which overlay the entire sensor area. A set of decoding, multiplexing and readout electronics is connected to an array of column output signal lines or interconnects which also overlay the sensor area. This type of arrangement allows signal readout to be performed by applying a simple X-Y addressing method and thus, data can be acquired either from the whole array of pixels or from chosen sub-sections or from even just a single pixel. This is another advantage over CCD imagers since the signal readout in the latter has to be performed sequentially and there is no possibility of selecting only a region of interest or just a single pixel [15].

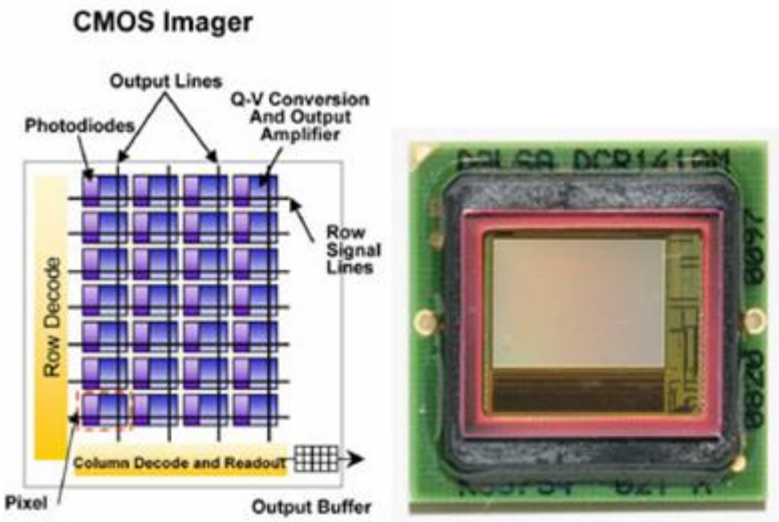

Figure 1.9 – (a) Schematic of the architecture of a CMOS Imager [14];
(b) Photograph of a CMOS imager manufactured by DALSA Corporation [16].

Unlike CCD imager architecture, most needed functions are embedded into CMOS imagers and that makes them very suitable for harsh or rugged environment applications. On top of that, a higher speed or frame rate is achieved thanks to this arrangement.

Figure 1.9(b) shows a photograph of a CMOS imager. In this particular design, it is a high speed device able to deliver up to 1000 frames per second. It has a resolution of 14 megapixels [16] and just as described in section 1.4.1 regarding CCDs, CMOS imagers can also be produced in “Line Scan” format apart from the default standard “Area Scan” structure shown in figure 1.8(a).

1.4.3. Comparison table CCD versus CMOS

Table 1.1 presents a comparison between CCD and CMOS devices:

Table 1.1 – Comparison table CCD vs CMOS

Technology (imagers)	**CCD**	**CMOS**
Resolution	High (33-100 Megapixels)	Moderate (10-20 Megapixels)
Integrated electronics	No	Yes
System flexibility	High	Low
System size	Large	Small
Image quality	High	Low
Speed/Frame rate	Moderate	High
Dynamic range	High	Moderate
Sensitivity	High	High
Uniformity	High	Low/Medium
Power consumption	High	Low
Overall system cost	High/Moderate	Low
Overall system integration	Difficult/Moderate	Easy
Windowing (pixel/area selection	Not possible	Possible
Application sector examples	Astronomy, medicine, microtechnology. Recognition, mapping, digital photography.	High volume applications. Harsh or rugged environment applications.
Application examples	Cameras (standard, video, security). Fax machines bar-code readers photocopiers.	Low quality videoconferencing. Simple scanners, toys.

A possible alternative to CCD and CMOS devices could be the 3D sensor, whose structure and technology is substantially different ant it may offer several advantages. However, it still needs to be properly evaluated before it is approved as a successful tool for machine vision. In this thesis, a so called “3D sensor”, which is an array of 32/128 amorphous silicon position sensitive detectors, is integrated inside a self-constructed machine vision system as the vision sensor component and the response is analysed for the required application.

1.5. Analogue sensors

Analogue detectors perform continuous measurements as opposed to discrete or digital, and this is why in turn they produce continuous output signals which are proportional to the amount measured (e.g. voltage, temperature). The most common are position sensitive detectors (PSDs), which can be in one-dimensional (1D PSD), two-dimensional (2D PSD) or three-dimensional (3D PSD) format and can be fabricated using crystalline, amorphous or nanocrystalline silicon low temperature processing technology being therefore less expensive.

1.5.1. Position Sensitive Detectors (PSDs)

Unlike detectors which are formed of discrete elements such as for example, CCDs, PSDs provide continuous position information offering a high speed response and position resolution. A wide spectral response range and high reliability are also offered by this device, plus it is also able to detect simultaneously the intensity and the position of the centre of gravity of a light spot.

PSDs are used in the following applications: position, angle and laser displacement sensing, distortion, vibration as well as lens refraction and reflection measurements, optical remote control, switches, range finders and camera auto focusing [6]. However, it should be emphasized that the main areas of application where PSDs are needed, are those where precision is crucial, such as, machine tool and remote optical alignment, medical instrumentation or robotic vision [17]. Any application which requires low bulks of signal processing power or high speeds in comparison to existing standard video frame rates is an ideal candidate for PSDs.

PSDs are photodiodes which are able to measure the position of a light spot projected on their surface by measuring the photocurrent variation between two equidistant electrodes. Photocurrent is generated in a semiconductor pin junction due to the photovoltaic effect as described by Wallmark in 1957 [18].

1.5.2. One dimensional PSD

Photoelectric conversion takes place in the active i-layer of a 1D PSD (see figure 1.10). The n-layer shown in the structure of figure 1.10 acts as a common electrode. An electric charge is generated at the incident position of the beam and it is proportional to the light intensity. Electrodes Iy1 and Iy2 collect the p-type carriers but due to the high resistivity of the transparent and conductive oxide layer placed on top of the p-layer the photocurrent signal is inversely proportional to the distance between each of the electrodes and from that difference it is possible to calculate the position of the light spot.

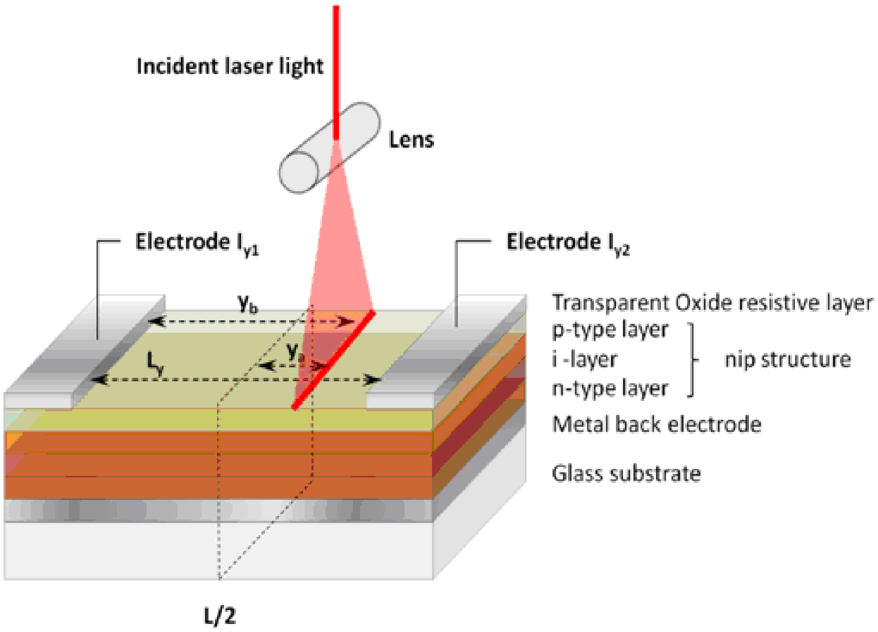

Figure 1.10 – Principle of operation of a 1D PSD.

In order to calculate the incident position of the light spot, Ya, in relation to the middle point of the active area, Ly/2, the following formula is used:

$$\left(\frac{Iy2 - Iy1}{Iy2 + Iy1}\right)\frac{Ly}{2} = Ya \qquad \textbf{[1.10]}$$

where, Iy1 and Iy2 are the output currents from electrodes Iy1 and Iy2 respectively, Ly is the length of the active area or resistance length and Ya is the distance from the centre of the PSD to the incident light input position.

The position worked out from equation 1.10 is effectively the centre of gravity of the projected beam of light. Figure 1.11 shows a sketch of a 1D PSD.

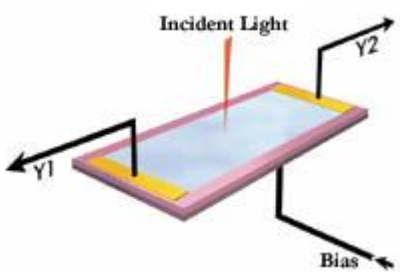

Figure 1.11 – Sketch of a 1-Dimensional PSD [21].

1.5.3. Two dimensional PSD

There are a few types of 2 dimensional PSDs such as, duo-lateral, tetra-lateral and quadrant detector. The quadrant detector structure varies from the others because it is divided into four separate photosensitive elements symmetrically located about its centre and which are equally spaced by a tiny distance. Usually, a light spot is projected onto the four quadrants and the position information is calculated from the relative amplitudes of the four photocurrents generated, since they are proportional to the light spot position on the surface in relation to the centre of the device. These particular type of detectors are ideal for centring applications [19] and they are mainly used in CD-ROMs or audio players [20].

The duo-lateral PSD is not segmented, thereby, it can detect continuously the position of a light spot moving over its surface in two dimensions. The two terminals (figure 1.12) allow the collection of 4 signals from which it is possible to determine the position of the incident light on the surface of the PSD. The four photocurrent signals collected on electrodes x1, x2, y1 and y2 allow the position of the centroid of the incident light to be calculated.

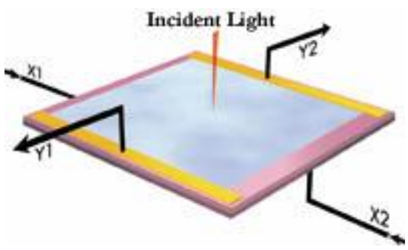

Figure 1.12 – Sketch of a duo-lateral 2-Dimensional PSD [21].

The following formulae show this correlation:

$$\left(\frac{Y1-Y2}{Y1+Y2}\right)\frac{Ly}{2} = YPos \qquad \textbf{[1.11]}$$

$$\left(\frac{X1-X2}{X1+X2}\right)\frac{Lx}{2} = XPos \qquad \textbf{[1.12]}$$

where, Ly and Lx are the length of the PSD in the Y and X dimensions respectively, Y1, Y2, X1 and X2 are the photocurrents from electrodes y1, y2, x1 and x2 respectively, YPos and XPos are the calculated positions in the Y-axis and X-axis respectively.

The duo-lateral PSD offers an outstanding linearity in the two dimensions. It is used in applications such as, position and motion monitoring in car crash analysis, robot check, anatomical studies, measurement of straightness, flatness, parallelism, etc [21].

1.5.4. Three dimensional PSD

A 3D PSD is composed of an array of 1 dimensional PSDs mounted together in parallel to each other. The principle of operation of a 3D PSD is based on the one from the 1D PSD described in section 1.5.2. The number of 1D PSD elements arrayed in parallel defines the performance of a 3D PSD.

A 3D PSD is used for shape measurement triangulation applications as in the example shown in figure 1.13. There, a laser line is scanned over the target object from one side to another and the reflected laser line image is projected on the active area of the 3D PSD array. Subsequent real-time measurements of the laser line frame are taken as the ray of light moves from one side of the target object to the other. The final image generated corresponds to the 3D profile of the scanned object and it is constructed from the values of each 1D sensor of the 3D PSD.

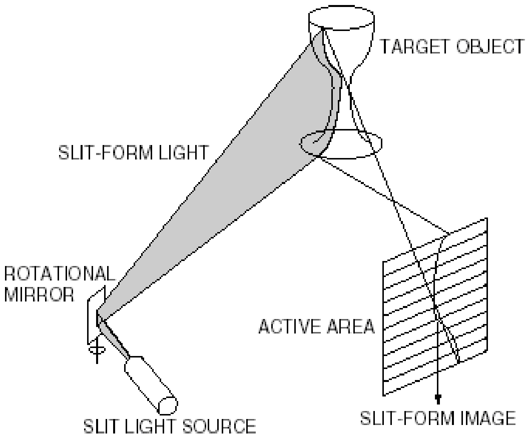

Figure 1.13 – Sketch of the typical shape measurement triangulation application example [adapted from 6].

A 128 element PSD linear array was available in the market, however, it was apparently withdrawn by the manufacturer [6], due to failures associated with temperature. Figure 1.14 shows a photograph of the three dimensional PSD manufactured by Hamamatsu photonics.

Most commercially available PSDs are made out of crystalline silicon [22]. However, the next section covers the work related to PSDs made out of amorphous silicon. Amorphous silicon is a low cost material and so it is a possible alternative to crystalline silicon.

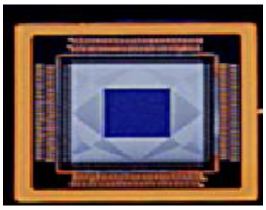

Figure 1.14 – Photograph of the 128 element PSD
linear array manufactured by Hamamatsu [6].

Research on amorphous silicon 1D, 2D and 3D sensors started in CENIMAT/I3N and CEMOP/UNINOVA in the 90s and figure 1.15 shows a photograph of an amorphous silicon 128 element PSD linear array developed in these premises [23]. This 3D PSD and the one presented in figure 1.14 are equivalent, except for the fact that the material structure used to fabricate them is different and therefore each has its own advantages and disadvantages.

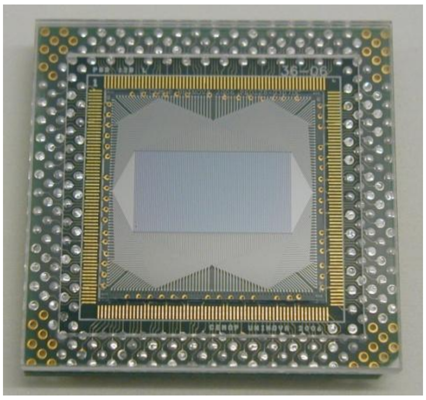

Figure 1.15 – Photograph of the 128 element PSD
linear array developed at CEMOP/UNINOVA.

1.5.5. Amorphous silicon PSDs

Several researchers have used amorphous silicon material to fabricate 1D, 2D and 3D thin film position sensitive detectors [23-26], performing material studies and presenting devices comprising active areas of less than 1 cm^2. Issues such as linearity, spatial resolution and response time were analysed and the discussed characteristics make amorphous silicon structures suitable for optical inspection and image processing applications especially where continuous detection is required.

Most of the work reported on amorphous silicon thin-film PSDs has been performed using the plasma enhanced chemical vapor deposition technique [27-32]. The very high frequency (VHF)

PECVD technique has also proved to be the most suitable for high rate deposition and high quality amorphous and nanocrystalline silicon films [33].

An alternative method, Radio Frequency (RF) Sputtering technique [34] has been applied [17] to deposit amorphous silicon material on a few PSD structures achieving high linearity and sensitivity. Moreover, a good working performance was claimed under unbiased conditions making them ideal for integration into practical applications such as optical sensing, distance measurement or alignment processes. Also, it is claimed that the outputs of the device do not need amplification and thus this offers an extra advantage.

Among all the deposition techniques which can be used to obtain amorphous silicon, the great advantage common to all are the optical and electrical properties of amorphous silicon which can be tuned by controlling the hydrogen content as well as the fact that it is also possible to tune the structure of the material from amorphous to nanocrystalline silicon [35].

1.5.6. Amorphous silicon versus Crystalline silicon

One of the major disadvantages of crystalline silicon PSDs is their high cost due to a costly production process. On top of that, complex and expensive optical systems are necessary in order to be able to utilize their small limited area [32]. These drawbacks are not present when producing and using amorphous silicon PSDs since the fabrication process, running at low temperatures, is relatively cheap as well as simple, and the devices are able to offer large detection areas if needed, thereby allowing the integration of simple optics. They also offer high photo sensitivities, especially at the visible wavelength range and high response speeds of the order of micro seconds. On the downside, these devices suffer from light degradation. It is not known of any amorphous silicon structure which is not affected by the Staebler-Wronski (SW) degradation [36]. It is widely acknowledged that SW degradation is correlated with the materials structure and is “intrinsic” to a-Si:H and related alloys [37]. Such instability does not appear to depend on the amount of hydrogen or on how tightly bonded the hydrogen is since the most stable devices have been obtained mainly using loosely bonded hydrogen [38].

One of the major advantages of amorphous silicon in relation to crystalline silicon is the higher uniformity of the material over the large areas in which it can be deposited. It can also be deposited at very low temperatures and this permits deposition in plastic as well as in glass.

On the other hand, the electrical properties of amorphous silicon are worst than crystalline silicon but researchers are recently closing the gap somehow with nanocrystalline silicon [39].

1.6. Optics

One of the most important aspects of a PSD based application is the optics needed to focus the incident light beam and gather the reflections coming from the surroundings, now that the main 3D object profiling principle deals with the detection of the reflected line beam from the object. This means that some limitations need to be overcome such as low reflecting objects or even the ability to distinguish colours in the object.

The main PSD related optical principle is summarized in the following section.

1.6.1. Reflection

The reflection on an object with a high planarity surface occurs at the same angle of incidence of the light, Snell's law [40]. Therefore, the quantity of light reflected is actually a percentage of the incident light minus the absorption component (in the simplest approximation). However not all surfaces have a high planarity and also the frequency of the reflected light or the composition and colour of the surface strongly influence the reflectance. Thus, specular, diffuse and spread reflections can be obtained, as shown in figure 1.16.

A specular reflection occurs when the angle of incidence equals the angle of reflection, meaning that light usually strikes the surface reflecting away at just one angle. Examples of specular surfaces are shiny surfaces such as mirrors, glass, liquid or metals.

Diffuse reflectance usually occurs when light striking a surface is mainly reflected in all directions (scattering). Examples of good diffuse materials are plain white paper, flat wall paint or rough surfaces, and their reflectance percentage can usually vary from 3% to 95%.

A spread reflection combines both specular and diffuse characteristics. The main specular component present in a spread reflection is also partially diffused by uneven surfaces. Examples of such surfaces or materials include glossy paint or paper [40].

Figure 1.16 – Examples of the different types of reflectance [40].

The maximum range of any sensor depends entirely on the reflectance of the target which is being used and the type of reflectance determines whether a target is cooperative or uncooperative.

The variation of the target's surface angle greatly influences the sensitivity or in other words the quantity of light reflected on a particular sensor. The performance of a device is improved when the reflection from a diffuse target is strong and this also allows precise measurement at fast sampling rates.

1.7. Light sources

Generally, in machine vision applications, light emitting diodes (LEDs) as well as fluorescent and tungsten or quartz halogen light sources are a preferred choice. However, when higher light intensities are required, other types of light sources, such as mercury or xenon are used.

The selection of a suitable light source for the application at hand should be made taking into account a variety of factors, such as its spectral radiance, its area homogeneity and its stability.

Nowadays LEDs offer superb durability as well as great luminous stability and most importantly, they provide flexibility for the application [41].

However, it is necessary that the spectral radiation of the emitting light source matches the spectral response of the detector used in the application. Table 1.2 gives an overview of the most common light sources and presents some of their characteristics or parameters, as well as their main applications in the field.

Since the 3D PSD is mostly suitable for object recognition and it is optimized for red light detection, a red laser beam, or LED are the most adequate. Considering the possibility of using the 3D PSD for coloured object recognition, a combination of white and red, green, blue (RBG) light sources is needed. In the following section we refer to the colour concepts needed for that interpretation.

Table 1.2 – Light source comparison

Light sources	**LEDs**	**Fluorescent**	**Tungsten/ Quartz halogen**	**Mercury**	**Xenon**
Suitable for machine vision	Yes	Yes	Yes	Occasionally	Occasionally
Spectral response range	Fair(470-700nm)	Fair (450-650nm)	Fair (425-700nm)	Specific (at 330, 405, 540, 590nm,	Broad (340 -700nm)
Intensity	Low/ Moderate	Low/ Moderate	Moderate	High	High
Durability	High	High	Low	High	High
Luminous stability	High	Low/ Moderate	High	High	High
Flexibility for application	High	Low	High	High	Low
Cost	Low	Low	Low	Moderate	High
Degradation	Yes	No	No	No	No
Heat generation	Low	Moderate	High	Moderate	Low
Applications	Lighting, digital displays, optical switching, barcode reading, optical rangefinders	All kind of applications	Machine vision inspection, microscopy, industrial engineering, digital imaging, particle detection	Microscopy, graphics exposure, countless outdoor & indoor locations	Machine vision line scan cameras, microscopy, photometric apparatus, semiconductor inspection, scanners

1.8. Colour

The existing colour schemes can differentiate between colours produced by light and colours seen on the surface of an object obtained due to colour pigments within the object itself: additive colour scheme Red, Green, Blue (RGB) or subtractive colour scheme cyan, magenta, yellow and black (CMYK).

1.8.1. RGB or additive colour

Red, green and blue are the primary colours of light with which all the other colours are formed. White light is formed by combining red, green and blue lights together in the same proportion and the rest of the light colours are created by merging one pair of those primary colours. Thereby, magenta is generated by mixing together red and blue light, yellow is created by merging together red and green light and finally cyan is produced by combining blue and green light.

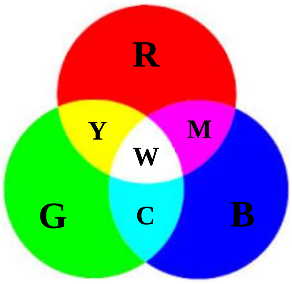

Figure 1.17 – Red, green and blue (RGB) or additive colour scheme.

This particular colour scheme is present in apparatus which make use of light such as cinema projectors, televisions and computer monitors. The images created by these devices are generated by projecting red, green and blue light rays on the screen at a very fast pace and by mixing each of these to obtain the specific colours needed. For example, in order to show the image of a green object on a television screen only green photons of light would be projected [42].

A vast number of colours can be represented on the screen by using the correct mixtures of red, green and blue light intensities. Existing standard displays are able to produce up to 16 million different RGB colour combinations. This is because within the device, 8 bits of information are allocated for each red, green and blue pixel, thereby allowing for 256 possibilities per pixel. The total number of blends is therefore 256 values for red, 256 values for green and 256 values for blue summing a total of 16,777,216 possible colour mixtures.

The standard format colour code string used to indicate the quantity of each RGB primary colour is: (r, g, b) which stands for (red, green, blue) and an example of a common colour code would be (255, 0, 255), which corresponds to magenta.

The darkest colour being black is obtained when no light is projected and this corresponds numerically to an intensity value of 0 for all red, green and blue light components. On the contrary, a maximum intensity value of 256 for all red, green and blue light constituents produces white.

The image quality obtained with 8 bits of information or 256 colour values per pixel is satisfactory, however, for even better quality imaging more sophisticated device technology and more bits per colour pixel are needed.

1.8.2. CMYK subtractive colour

A subtractive colour scheme, developed in 1934, is the four ink CMYK or cyan, magenta, yellow and black colour process which is used in the printing industry. Here, the primary colours are cyan, magenta and yellow and when they are all equally combined and saturated completely, black colour should be obtained as opposed to white. However, in reality this is not the case since such a mixture produces darkish brown. Due to this fact, the printing industry brought into play a fourth primary colour which is black [42].

1.8.3. Colour models

Among several colour models, the Munsell system is the most employed and it can be regarded as the universal lingo of colour since its three dimensional colour space accommodates all colours perceptible to the human eye. A three dimensional representation of a colour can be defined by: the hue or tone; the darkness or lightness, generally regarded as the value of a colour; and the chroma, which is roughly similar and usually treated as the level of saturation of a colour [43]. Such combinations allow the system to classify up to at least 300 colours.

The CIELUV colour space and the internal geometry of the Munsell system are shown in figure 1.18 and in the latter the value or lightness scale is divided into 10 steps which are each subdivided into 10 decimal increments resulting in a total of 100 decimal sub steps. Black corresponds to the lowest value being 0 and white corresponds to the highest value being 10. The chroma scale starts at the lowest value being 0 or grey and ends at the highest value of intensity of that particular colour hue. The highest value or limit is defined by the point where a further increase of the chroma value or colour hue saturation no longer appears to have any effect, without reaching an unwanted glowy or shiny appearance. Moreover, at this point the scale value of grey will be 0.

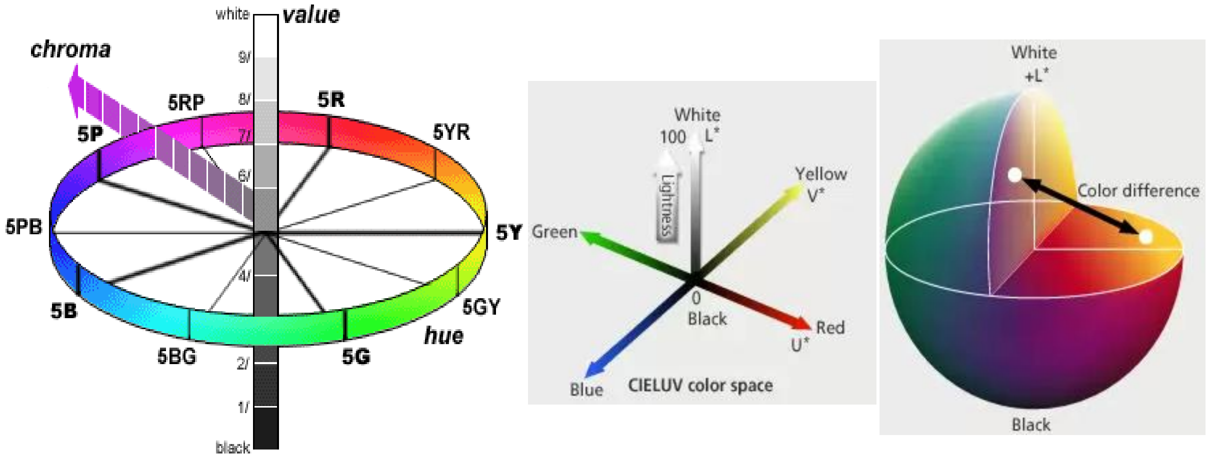

Figure 1.18 – Internal geometry of the Munsell colour system and CIELUV colour space [43].

As indicated in the Munsell system structure of figure 1.18, the hue region is divided into 10 equal parts or sub regions. Each of those 10 parts is subdivided into 10 steps. Thereby, this results in a circle composed of a total of 100 steps or units. The annotation 5R stands for 5 units of red colour where the scale for red starts at 0R and ends at 10R or 0YR, which stands for 0 units of yellow-red and of course, yellow-red is the mixture of red and yellow colours. Obviously, the 0R point which stands for 0 units of red, lies midway between the 5R point and the 5RP point, which stands for 5 units of red-purple and of course red-purple is the mixture of red and purple colours. To clarify, the list of the colour hue abbreviations in clockwise order shown in figure 1.18 are 5R (5 units of red), 5YR (5 units of yellow-red), 5Y (5 units of yellow), 5GY (5 units of green-yellow), 5G (5 units of green), 5BG (5 units of blue-green), 5B (5 units of blue), 5PB (5 units of purple-blue), 5P (5 units of purple) and 5RP (5 units of red-purple).

In order to classify a specific colour within the model, a colour code with the format "hue value/chroma" is used. It includes decimal numbers and defines in this order, the hue, value and chroma. For example, the code 4.5Y6.5/10 identifies a colour hue of 4.5 in the Y or yellow sub region with a lightness or darkness of 6.5 in the scale and a chroma equal to 10.

Present tools allow correct colour conversions between the Munsell and other colour systems. Examples of these tools include the Trumatch, Pantone or Toyo which are employed in the graphics design or colour printing industry and the well known CIE system implanted by the International Commission on Illumination in order to introduce a standard for colour worldwide or internationally [43].

1.8.4. Human colour vision

Humans perceive colour via three photosensitive colour cells or cones which are inside the eye and this is why humans are called "trichromats", now that the number of cones inside the eye is three. Other animals, such as the majority of existing birds have more than three cones while others such as dogs or cats have only two cones inside the eye. The number of cones determines the amount of colours that can be distinguished, so, birds are able to recognise more colours or have better colour vision than humans or dogs [42].

Apart from these cones, other photosensitive cells called rods are found inside a human eye. These rods work when low levels of light are present which is when cones are hardly able to sense anything, hence, they are especially suitable for night vision. Both cones and rods are located in the retina of the eye.

The three cones inside the human eye are sensitive to colour wavelengths around the red, green and blue of the visible spectrum of light. Due to the fact that these cones sense the primary colours red, green and blue, then this means that they are also able to distinguish any colour tone derived from the mixture of those primary colours as described in the RGB or additive colour theory. Figure 1.19(a) shows the spectral response of these three cones, "blue", "green" and "red" [44], while figure 1.19(b) illustrates the overall spectral response sensitivity of the human eye [45].

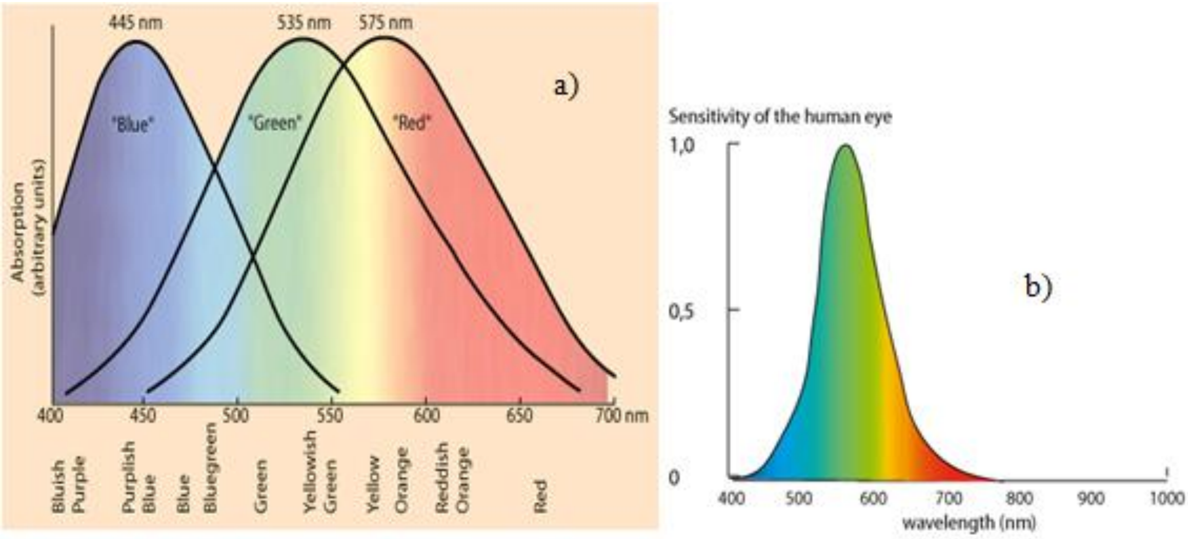

Figure 1.19 – (a) Spectral response of the three colour detection cones inside the human eye [44] (b) Overall sensitivity of the human eye [45].

The combination of all three spectral responses corresponding to the three cones allows a human to distinguish all the indicated wavelength range (visible spectra), although the eye is mostly sensitive to blue-greenish colours [44].

A relationship can be established regarding the percentage contribution of each of the three primary colours to any specific colour tone which is being perceived by the human eye. Such a relationship can be expressed by the following formula:

$$C = xB + yG + zR \qquad \textbf{[1.13]}$$

where, C stands for colour or type of colour, x is a variable, B stands for blue colour, y is a variable, G stands for green colour, z is a variable and R stands for red colour. So for a white colour we obtain: $W = 1B + 1G + 1R$, where variables x, y and z all have a value of 1. The values of all variables x, y and z can be treated as percentage intensity contributions of each primary RGB colour within the listed expressions so the 0 to 1 range would then be from a minimum value of 0% to a maximum value of 100%. Thereby, for the case of magenta for example, the intensity would be 100% for blue, 0% for green and 100% for red.

1.8.5. Colour sensors

The use of discrete silicon sensor arrays is frequent in colour detection applications and they are usually employed in conjunction with optical filters. D. Knipp et al. [46] developed vertically integrated amorphous silicon thin-film colour sensors which do not need to operate in conjunction with optical filters since the colour information is detected at the same exact position as the sensor array. Such structures are able to detect colour information at various depths within the arrangement itself since every layer is sensitive to a different wavelength of light. The spectral response of some of these devices can be modified by varying the applied bias voltage across the device. Other researchers [47-51] also describe amorphous silicon structures as colour sensors.

Colour sensors in the market [52-55] generally work by analyzing the level of light intensity reflected back from objects when white light is projected onto their surfaces. These sensors read a light intensity value for each of the RGB components of white light. If the combination of these values matches a previously stored combination of values in the system, then there is a colour match. Among the broad range of existing colour applications, these kind of sensors are used for example in production lines to discriminate goods according to their specific colour [56]. Chung et al. [57] present a 3D scanning system which is able to detect the colour of objects. The system scans the object of interest in 3D by using a laser scanner and the colour information is obtained by employing a digital camera. A digital 3D colour replica of the real object is then rendered.

1.9. 3D PSD for micro objects

The detection of micro objects needs an optical system such as a microscope. Nowadays cameras are used to capture images of specimens in microscopes and these images are then processed, analyzed and displayed on a computer. For the majority of applications the sensor employed inside the camera is a standard CCD matrix and the image of the sample being studied under the microscope is formed by the combined optical pieces. The image obtained is a two dimensional representation of the scene containing information on the amount of light intensity at each sampled point. Thereby, the real three dimensional object is not totally represented by such a two dimensional portrait. Unwanted effects also appear while the two dimensional image is being formed plus the fact that it generally lacks on resolution [58]. The end result can be regarded as a two dimensional picture of light intensities consequently having brighter areas corresponding to higher object reflections and darker areas corresponding to lower object reflections.

Now that the obtained image is in two dimensions, for processing such an image it is possible to access the light intensity information at every acquired pixel by moving in the X or Y axis within the object. So, every pixel as well as any area of the two dimensional representation can be located by a specific X and Y position. In theory, the intensity of the light can also be regarded as the third dimension or Z axis and in this way a three dimensional picture can be formed. The microscope image capturing and digital processing sequence is shown in figure 1.20.

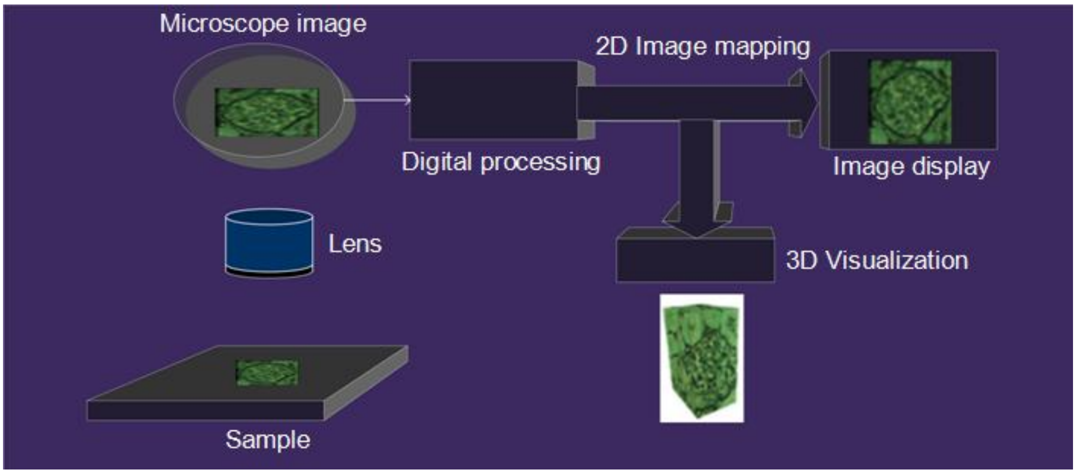

Figure 1.20 – Optical path followed by light inside a microscope.

The image of a specimen placed on the microscope stage can be projected on the surface of a sensor or camera via the optical components and the objective lens. The image is then digitized or transformed into a digital format and it can also be displayed to the user. By a process called interpolation the image is subsequently transformed into a 3D portrait which is a more realistic representation of the real specimen.

Besides the observation of micro objects another important part in microscopy is the processing of acquiring images [58]. Generally, a computer coupled to a CCD camera is used to analyze, interpret and present the images obtained.

There are some microscope systems which are able to construct 3D images by sampling the object along the Z-axis and subsequently an appropriate software module constructs the corresponding image. Measurement rulers are frequently coupled to the microscopes so as to provide the correct size/dimensions of visualized objects.

The optical enlargement or magnification of a sample observed on a microscope is defined by the type of objective lens employed. These play a crucial role in determining the resolution or smallest perceptible detail of the sample.

The numerical aperture of the lens is defined by:

$$NA = n\sin(\theta) \qquad \textbf{[1.14]}$$

where, NA is the numerical aperture, n is the refractive index of the medium and θ is the angular aperture (degrees).

The minimum distance that can be detected under the microscope on the object of analysis between two specific points is regarded as the resolution and it is defined by:

$$R = \lambda / 2NA \qquad \textbf{[1.15]}$$

where, R is the resolution (distance between two specific points), λ is the wavelength of the light and NA is the numerical aperture.

The resolution is proportional to the wavelength of the light and when the imaging medium between the objective and the specimen is air, a significantly higher resolution is obtained than when other more dense mediums are present, such as for example, oil [58]. Equation 1.15 also shows that the higher the numerical aperture, the higher the achieved resolution.

In this work we have used a 3D PSD system to inspect micro objects, via the lens of a microscope. Similar works have never been published.

1.10. References

[1] “AVA Machine Vision Glossary”, Automated Vision Association, 1985.

[2] B. G. Batchelor and P. F. Whelan, “Intelligent Vision Systems for Industry”, Springer Verlag, 1997, ISBN 3-540-19969 1.

[3] J. Hochberg, “Machines should not see as people do, but must know how people see”, Computer Vision, Graphics and Image Processing 37, 221-237, 1987.

[4] M.H. Lee, “Intelligent Robotics”, Open University Press, 1989.

[5] “European Vision Technology Market Statistics 2007”, European Machine Vision Association (EMVA), www.emva.org, (accessed 22-01-2013).

[6] Product Catalogue, Hamamatsu Photonics, Hamamatsu City, Japan, www.hamamatsu.com, (accessed 23-01-2013).

[7] Product Catalogue, Photodiode characteristics and applications (Application notes), OSI Optoelectronics, Hawthorne, CA, USA, www.osioptoelectronics.com, (accessed 25-01-2013).

[8] M A. Rogalski, K. Adamiec and J. Rutkowski, “Narrow-Gap Semiconductor Photodiodes”, SPIE Press, 2000.

[9] S. Xia, F. Sarubi, R. Naulaerts, S. Nihtianov and L. Nanver, "Response Time of Silicon Photodiodes for DUV/EUV Radiation," Instrumentation and Measurement Technology Conference Proceedings, IMTC. IEEE , 1956, 1959, 12-15, May 2008.

[10] C. Slaughter, "Cooled Cameras Help Discover Drugs", Laser Focus World, 103-107, November 2000.

[11] D. E. Weisner, "Charged-Coupled Devices", McGraw-Hill Encyclopedia of Science and Technology. 7th ed. McGraw Hill Inc.: New York, 1992.

[12] D. J. Burt, "Basic Operation of the Charge Coupled Device". International Conference on Technology and Applications of Charge Coupled Devices, Edinburgh, University of Edinburgh, Centre for Industrial Consultancy and Liaison, Sept. 1974.

[13] J. Fink, "Television". The New Book of Popular Science: Deluxe Library Edition, ed. Grolier Inc.: Chicago, 6, 1996.

[14] Product catalogue, Silicon Imaging, Inc., 25 Covington Court, Niskayuna, NY 12309, USA, www.siliconimaging.com/ARTICLES/sensors.htm, (accessed 25-01-2013).

[15] D. Litwiller, “CCD vs. CMOS: Facts and Fiction”, Photonics Spectra, 154-158, Jan. 2001, Dalsa Corporation, Waterloo, Ontario, Canada, www.dalsa.com, (accessed 26-01-2013).

[16] Product Catalogue, DALSA Corporation, Waterloo, Ontario, Canada, www.dalsa.com, (accessed 26-01-2013).

[17] J. Henry and J. Livingstone, “Sputtered a-Si:H thin-film position sensitive detectors”, Journal of Physics D: Applied Physics, 34, 1939-1942, 2001.

[18] Wallmark J 1957 Proc. IRE 45 474

[19] A. Mäkynen, “Position-sensitive devices and sensor systems for optical tracking and displacement sensing applications”, Dissertation, Department of Electrical Engineering, University of Oulu, Finland, 2000 (ISBN 951-42-5780-4)

[20] K. C. Pohlmann, “The compact disk handbook”, The Computer Music and Digital Audio Series, A-R Editions, Middleton, Wisconsin, 5, 1992 (ISBN 0-89579-300-8).

[21] SiTek Electro Optics · Ögärdesvägen, Partille, Sweden, www.sitek.se, (accessed 27-01-2013).

[22] J. Geist, “Sensor Technology and Devices” ed L Ristik, (Boston, MA: Artech House Publishers), 1994.

[23] R. Martins, J. Figueiredo, V. Silva, H. Aguas, F. Soares, A. Marques, I. Ferreira and E. Fortunato, “32 linear array position sensitive detector based on NIP and hetero a-Si:H microdevices”, Journal of Non-Crystalline Solids 299–302, 1283–1288, 2002.

[24] E. Fortunato, F. Soares, P. Teodoro, N. Guimaraes, M. Mendes, H. Aguas, V. Silva and R. Martins, “Characteristics of a linear array of a-Si:H thin film position sensitive detector”, Thin Solid Films, 337, 1-2, 222-225, 1999.

[25] A. Cabrita, J. Figueiredo, L. Pereira, H. Aguas, V. Silva, D. Brida, I.Ferreira, E. Fortunato and R. Martins, “Thin film position sensitive detectors based on pin amorphous silicon carbide structures”, Applied Surface Science, 184, 1-4, 443-447, 2001.

[26] L. Pereira, D. Brida, E. Fortunato, I. Ferreira, H. Aguas, V. Silva, M. F. M. Costa, V. Teixeira and R. Martins, “a-Si:H interface optimisation for thin film position sensitive detectors produced on polymeric substrates”, Journal of Non-Crystalline Solids, 299-302, 2, 1289-1294, 2002.

[27] A Toneva, Tzv. Mihailova, D. Sueva and S. Georgiev, “Homogeneous CVD a-Si:H thin film based position sensitive photodetector”, Vacuum, 47, 10, 1207-1209, 1996.

[28] S. Arimoto, H. Yamamoto, H. Ohno and H. Hasegawa, J. Appl. Phys. 57, 4778, 1985.

[29] E. Fortunato and R. Martins, Solid State Phen. 44–6, 883, 1995.

[30] E. Fortunato, G. Lavareda, R. Martins, F. Soares, and L. Fernandes, “Large-area 1D thin-film position-sensitive detector with high detection resolution,” Sensor Actuators, A, 51, 135–142, 1996.

[31] S. Arimoto, H. Yamamoto, H. Ohno, and H. Hasegawa, Electron. Lett. 19, 628, 1983.

[32] T. Takeda, “Amorphous and Microcrystalline Semiconductor Devices: Optoelectronic Devices” ed J Kanicki (Boston, MA: Artech House Publishers), 1991.

[33] S.J. Jones, T. Liu, X. Deng, and M. Izu, “a-Si:H-Based Triple-Junction Cells Prepared at i-Layer Deposition Rates of 10 Å/Sec using a 70 MHz PECVD Technique,” Proc. of the 28th IEEE Photovoltaic Specialists Conf. 845, 2000.

[34] K. Wasa and S. Hayakawa, “Handbook of Sputter Deposition Technology. Principles, Technology and Applications” (Park Ridge, NJ: Noyes Publications) ch 3, 1992.

[35] A. Dutta, K. Murakami, Y. Hatanaka and T. Yamamoto, Proc. of the Technical Digest of the 7th Sensor Symposium (Tokyo), 233, 1988.

[36] B. von Roedern and J.A. del Cueto, “Model for Staebler-Wronski Degradation Deduced from Long-Term, Controlled Light-Soaking Experiments,” Materials Research Society Symposia Proceedings, 609, A10.4, 2000.

[37] J.D. Cohen, J. Heath, K.C. Palinginis, J.C. Yang, and S. Guha, “Light-Induced Annealing of Deep Defects in Low Ge Fraction a-SiGe:H Alloys: Further Insights into the Fundamentals of Light-induced Degradation,” Materials Research Society Symposia Proceedings, 664, A12.5, 2001.

[38] J. Yang and S. Guha, “Amorphous Silicon Alloy Materials and Solar Cells Near the Threshold of Microcrystallinity,” Materials Research Society Symposia Proceedings, 557, 239, 1999.

[39] B. Yan, G. Yue, J.M. Owens, J. Yang, and S. Guha, “Over 15% Efficient Hydrogenated Amorphous Silicon Based Triple-Junction Solar Cells Incorporating Nanocrystalline Silicon”, Conf. Record of the 2006 IEEE 4th World Conf. on Photovoltaic Energy Conversion, 1477, (Hawaii, USA, May 7-12, 2006).

[40] A. Ryer, “Light Measurement Handbook” Technical Publications Dept International Light, Inc. Newburyport. ISBN 0-9658356-9-3. (personal communication), www.intl-lighttech.com, (accessed 29-01-2013).

[41] D. Martin, “A Practical Guide to Machine Vision Lighting”. October 2007, Daryl Martin. Midwest Sales and Support Manager. Advanced illumination, Inc. Rochester, USA, 2007 (personal communication), www.advill.com. (accessed 29-01-2013).

[42] J. L. Morton, “Color matters”, Colorcom publishing and Color Matters, 3905-C Maunahilu Place, Honolulu, Hawaii 96816, United States (personal communication), www.colormatters.com, (accessed 31-01-2013).

[43] B. MacEVoy, “Color vision”, Handprint, Sebastopol, CA, United States, (personal communication, 2008), www.handprint.com, (acessed 02-02-2013).

[44] C. R. Nave, “Hyperphysics”, Department of Physics and Astronomy, Georgia State Univ., Atlanta, Georgia 30303, USA, (personal communication, 2000-2003), http://hyperphysics.phy-astr.gsu.edu/hbase/hph.html, (accessed 06-02-2013).

[45] C. H. Hilgers, “Red Fluorescence”, Technisches Buero, Hauptstrasse 82, D-53639 Koenigswinter, Germany (personal communication), http://www.hilgers.com/FAQ/IR_Filter_engl.htm, (accessed 26-10-2013).

[46] D. Knipp, R.A. Street, H. Stiebig, M. Krause, J.-P. Lu, S. Ready and J. Ho, “Color Aliasing free Thin-Film sensor Array”, Sensors and Actuators A: Physical, 128, 2, 333, 2006.

[47] K. Eberhardt, T. Neidlinger and M.B. Schubert, "Three-color sensor based on amorphous nipin layer sequence," IEEE Trans. Electron Devices 42, 1763-1768, 1995.

[48] J. Zimmer, D. Knipp, H. Stiebig and H. Wagner, "Amorphous silicon based unipolar detector for color recognition," IEEE Trans. Electron Devices 46, 884-891, 1999.

[49] P. Rieve, M. Sommer, M. Wagner, K. Seibel and M. Böhm, "A-Si:H Color Imagers and Colorimetry," J. Non Cryst. Solids 266, 1168-1172, 2000.

[50] H. Stiebig, J. Giehl, D. Knipp, P. Rieve and M. Böhm, "Amorphous silicon three color detector," Mat. Res. Soc. Symp. Proc. 377, 517-522, 1995.

[51] D. Knipp, H. Stiebig, J. Fölsch, F. Finger and H. Wagner, "Amorphous silicon based nipin structure for color detection," J. Appl. Phys. 83, 1463-1468, 1998.

[52] B. E. Bayer, “Color imaging array,” U.S. Patent 3 971 065 (1976).

[53] R. B. Mirell, “Color separation in an active pixel cell imaging array using a triple-well-structure,” U.S. Patent 5 965 865 (1999).

[54] F. Palma, "Multilayer Color Detectors," Springer Series in Material Science, R.A. Street (Ed.), Springer, Berlin, 37, 306-338, 2000.

[55] P. G. Herzog, D. Knipp, H. Stiebig, and F. König, “Colorimetrical Characterization of novel multiple-channel sensors for imaging and metrology,” J. Electron. Imaging, 8, 4, 342–353, 1999.

[56] Product Catalogue, Balluff Inc., Florence, Kentucky, USA, www.balluff.com, (accessed 28-10-2013).

[57] T.-T. Chung, C.-Y. Liao, "An integrated scanning system for reconstructing 3D color models of general objects," Mechatronics, 2005. ICM '05. IEEE International Conference on, 477-482, July 2005.

[58] Q. Wu, F. A. Merchant and K. R. Castleman, “Microscope image processing”, Elsevier/Academic Press, 2008.

Chapter 2

Applications of machine vision

Chapter 2. Applications of machine vision

Summary

This chapter provides an overview of machine vision techniques and applications. Several methods and systems are reviewed, with a special emphasis on the sheet-of-light triangulation method which is directly relevant to this thesis. Applications based on discrete and analogue sensors are also examined, including microscopy vision scenarios.

2.1. Machine vision techniques

The application of machine vision systems in industry represents an alternative to traditional surface contact measuring techniques. Such techniques require relevant system probes to be in contact with the surface being measured. As the system probe moves along, the shape of the surface is sensed and acquired. However, even though these techniques are extremely accurate, they are exceedingly slow and cannot sense elastic material since the probe removes or deforms the material. Simple surfaces are properly inspected using these processes but when it comes to complex structures more advanced contact measurement machines need to be used and even when using these, some specific positions cannot be reached and sensed due to physical limitations such as, articulated or deformable time-varying shapes, which are caused by the motion of these complex or non-rigid structures [1].

A vast range of existing machine vision approaches permits the gathering of information from a surface without having to make any contact with it. Such non-contact techniques employ all kinds of discrete or analogue sensors, as well as many different types of light sources and optical arrangements. The precise acquisition of the geometry of a real captured scene, in three dimensions, is the main goal. As such a cloud of points in 3D are put together and used for subsequent scene reconstruction. The precise image reconstruction depends on the acquired number of features. Present systems are able to scan large amounts of data at relatively fast rates. However, they do not have the accuracy that contact measurement systems have and they often suffer from occlusion problems when trying to capture the data of areas where the impinging light does not reflect back to the system sensor head. In turn, if the surface is too shiny the high light reflection will cause wrong readings to be recorded. Coatings such as for example Teflon are generally used to cover shiny surfaces before scanning and other methods are also used to reduce any excessive stray or ambient light that might be present.

The scanning capabilities of non contact systems are suitable for applications where speed is important. In terms of precision, a reasonable level of accuracy is offered by these systems and even though it is continuously improving over time, sometimes it is not enough for some applications where high precision is crucial, such as, machine tool and remote optical alignment, medical instrumentation, robotic vision, detection of surface defects in the micrometer range, astronomy, medicine, microtechnology or microelectronics inspection. In fact, in terms of accuracy, machine vision systems cannot compete with any traditional or even modern contact system since the accuracy of the latter ranges from a few microns to a few tenths of microns and this is much higher than any existing non contact machine vision system.

The procedure for acquiring data from the surrounding environment starts by focusing on a specific area or objects and subsequently real time three dimensional space measurements are performed as we move along the area. Each measurement represents a three dimensional point in space and it is defined by X, Y and Z coordinates. With current technology, nowadays it is possible to acquire millions of points. However, depending on the application requirements sometimes a few thousand points might be enough for object representation. Such a large matrix of points defining a three dimensional image is usually regarded as a cloud of points. The overall aim of these scanning procedures is to be able to process such 3D images and develop digital replicas of the objects [2].

2.1.1. Stereovision

Stereovision is a very popular method of obtaining three dimensional data from the surrounding environment and it is often used in obstacle detection and routing applications. However, it does not reach the level of precision demanded by industrial applications. In stereovision, two cameras are placed mimicking two human eyes and in order to achieve a proper representation of the obtained information all points captured by one camera need to be associated to all of the same points obtained by the other camera. In this arrangement there is no physical or artificial light source present and the only source of illumination is ambient light. Such an arrangement of having two cameras and no physical light source (ambient light only) is regarded as a passive stereo setup. The accuracy of this passive stereo or stereovision technique is lower than other existing methods in which a physical or artificial light source is present [3].

2.1.2. Continuous wave modulation

In this technique, continuous wave modulation is applied and the chosen light source is generally a laser which emits light in a coherent manner towards the object of interest. When the light waves hit a body or surface they get reflected and their phase usually changes. These out of phase reflections arrive at a specific detector and the correspondent object distance is subsequently calculated based on the phase difference between the projected and the reflected light. The precision of the method depends exclusively on the wavelength of the light source employed as well as on the ability of the sensor to detect these phase variations.

2.1.3. Time-of-flight

In the time-of-light method, the light source, generally a laser, emits pulses which are directed towards the surface or object of study. These pulses strike the object and reflect back to the sensor head within the system enclosure. The time taken for those pulses to reach the object of interest and return is measured by the detecting system and depends solely on the velocity of the traveling light pulses. This concept is similar to radar systems where the interaction of light with surfaces, objects or the environment as a whole produces slight variations of speed on the light pulses [4]. Specialized electronic circuits are designed in order to capture these small speed differences with high precision.

2.1.4. Light triangulation

Light triangulation measurements are performed using the triangulation principle where, a light source (usually a laser), an object and a sensor are arranged in a triangular geometry. Such a triangular approach used for three dimensional imaging is employed in order to work out the distance from the sensor to the object being analyzed. The parameters needed to determine that distance are the angle projection of the light source, the viewing angle of the sensor and the distance between the sensor and the light source. When analysing an object, variations on its surface will change the distance from the sensor to the object. By tracking in real time these changes it is possible to work out the shape of the object and build up its 3D image.

Figure 2.1 shows a sketch of the triangulation scheme where the light source (or laser), the sensor and the object form a triangle. Here, the distance between the sensor and the light source is **p**, the distance between the laser and the surface of the object is **d**, the angle of illumination or light projection is **θ** and the viewing angle is **α**. In figure 2.1 we have indicated the sensor as a discrete one, such as a charge coupled device. Thereby, the sensor active area is a two dimensional matrix of pixels which can be referenced by specific values on the x and y axis. The pixel location (x, y) where the light reflection from the object is projected is indicated in figure 2.1 but as all geometric parameters change so does the pixel projection point on the CCD sensor.

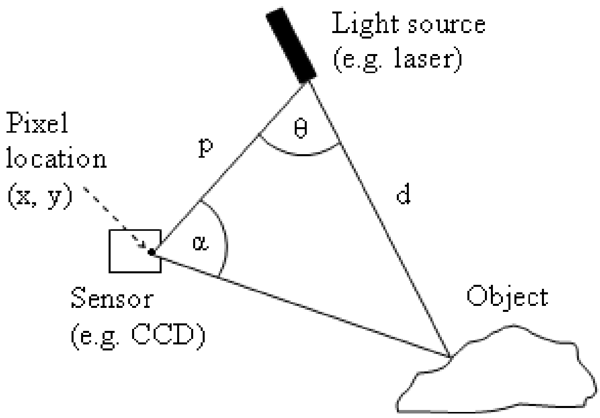

Figure 2.1 – Structured light triangulation configuration

There are similarities between this method and the stereovision technique described in section 2.1.1, however, the main differences are that here only one camera or sensor is used as opposed to the two being employed in stereovision and also a light source is introduced in the setup as a replacement for the second camera [3]. Same as in stereovision, ambient light is still present but the setup is generally isolated from intense ambient light levels which might affect the measurements by placing dark panels or covers. Light triangulation techniques are more accurate than stereovision and the limit of accuracy is mainly defined by the resolution of the detector used. The dimensions of the triangulation geometry and the precision of the light source (e.g. width of laser line/spot) also contribute to some extent towards achieving a high accuracy but clearly the most important parameter is the resolution of the sensor which determines the smallest feature that can be detected.

Light triangulation systems use mainly three types of illumination. These are patterned light projections, spot lasers and sheet-of-light lasers. A laser spot illumination is illustrated in figure 2.1 where just one laser point is projected onto the object and the associated reflection is mapped onto a specific location of the CCD detector. When using a laser spot it takes longer than the other two methods to acquire shapes of objects or surfaces because only one point of data is obtained on each sample acquisition as opposed to many points. The patterned light source approach is faster than the laser spot method but the preparation and use of the required patterns for projection causes a significant drawback. In relevant applications, the sheet-of-light approach is the preferred and fastest choice out of all the three types of illumination. The parallel combination of individual laser spots lead to the concept of generating the continuous laser line created by the sheet-of-light method.

Correctly configured optical triangulation systems are typically able to acquire data faster and more precisely than other conventional existing methods, plus the fact that normally they do not require significant data post processing during real time acquisitions.

Since sheet-of-light is one of the most precise methods of structured light triangulation, such technique is described in detail in the following section.

2.1.4.1. Sheet-of-light

This method uses a laser sheet-of-light which is shined onto the object and the intersection of this light plane with the object creates a line which in turn is reflected and projected onto the image area of the camera. Some commercial sheet-of-light scanners are able to generate 10000 data points (not frames) per second and the technology advances are leading to the fastest 3D data collecting method when compared to other laser scanners [4]. Figure 2.2 illustrates the sheet of light concept when 3D scanning a rounded object, such as a jug.

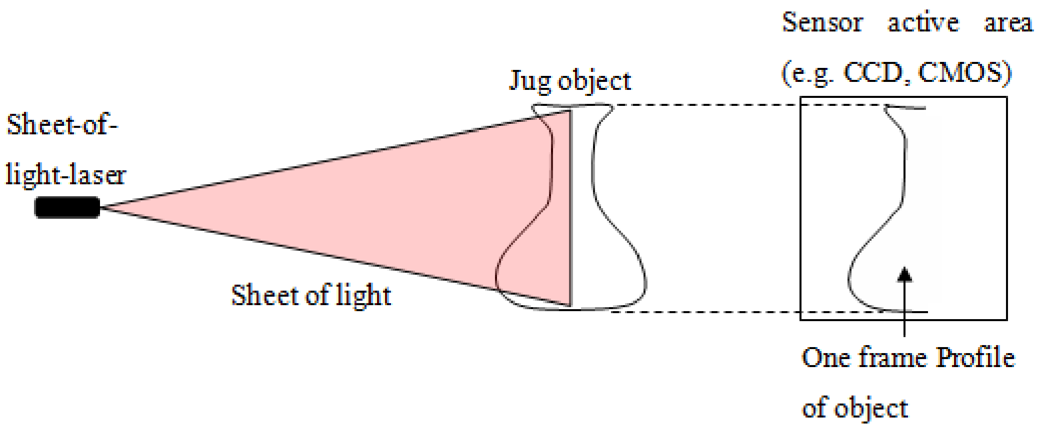

Figure 2.2 – Schematic of the sheet-of-light 3D scanning of a jug and one frame projected on sensor

As indicated in the schematic of figure 2.2, a sheet of light laser projects a plane of light onto the surface of a jug and the corresponding reflection is mapped on the active area of the sensor. As the object rotates or as the laser sweeps the complete area of the object, frames are recorded as fast as possible in order to gather the maximum amount of information from the object. At each instant of time one frame is acquired and stored and at the end of the process all these frames are combined to form a digital 3D image of the scanned object.

A photograph of a commercial sheet-of-light range scanner is shown in figure 2.3 [4]. Here the object of interest lies on a translation table and the 3D scanning of the object is performed when the laser line hits the object, while the translation table moves. Each measurement is one frame or slice profile data from the object at that specific instant of time and all these profiles combined together make up the computer 3D model of the object.

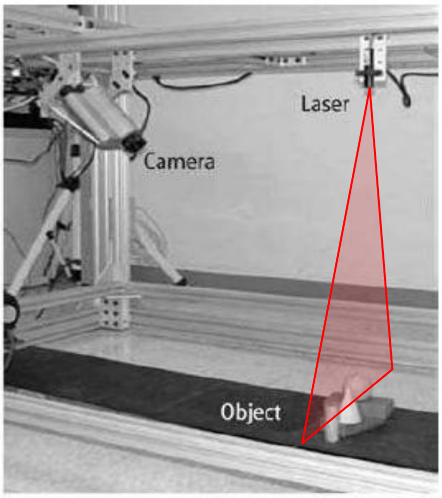

Figure 2.3 – Sheet-of-light commercial range scanner
manufactured by Integrated Vision Products [adapted from 4].

The accuracy of the sheet-of-light method depends mainly on the sensor resolution as well as on the precision of the light source and the geometric dimensions of the set-up used. In a standard camera, the number of pixels of its discrete CCD sensor determines the resolution, which is at least of nine bits. The rate of acquisition and the translation table speed determine the gap between frames of the object. The higher the number of frames the higher the expected profile resolution.

The angle between the laser and the camera is called the viewing angle and it is generally set between 30 and 60 degrees in order to acquire reasonable depth range measurements [4]. Angles above 60º are not suggested since an angle close to 90º would result in depth differences which are too large for the available sensor depth range. Angles below 30º are neither advisable since an angle close to 0º would result in insignificant depth differences which are too small for the available sensor depth range and in fact it would not be possible to sense any information from a surface or object.

One of the major drawbacks of machine vision systems as a whole is occlusion and of course sheet-of-light scanners also suffer from this problem. Occlusion happens when the camera is not able to view a particular portion of an object or surface because other parts of the same object or surface are preventing that section from being seen. Even if the laser is illuminating that occluded section the angle between the laser and the camera is such that it is not possible for the camera to view the occluded region of interest. However, as already stated, other parts of the object or surface of study are generally the cause of this occlusion problem. Figure 2.4 illustrates the issue of occlusion in sheet of light systems.

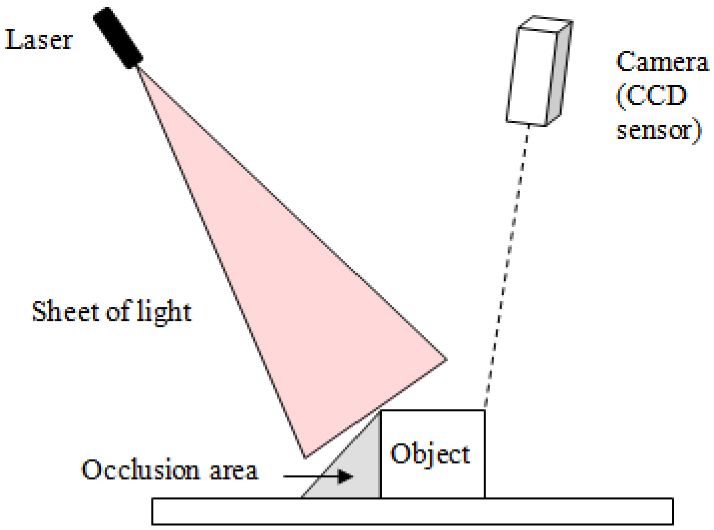

Figure 2.4 – Example of occlusions in sheet-of-light systems.

There is no solution to the occlusion problem and the only workaround is to move the camera or place various cameras (and lasers if needed) at different locations in order to acquire information from different perspectives so as to obtain several diverse views of the object or surface of interest.

2.2. Machine vision state of the art

The state of the art review of commercially available systems as well as their overall capabilities and limitations is important, so as to understand the major advances performed so far in this field. Machine vision systems were introduced in industry as an alternative to traditional contact systems which require being in contact with the scanned surfaces.

2.2.1. Traditional contact commercial systems

Table 2.1 shows the characteristics of traditional commercially available contact systems. As already discussed and as shown in table 2.1 these systems offer high accuracy in comparison to machine vision or non-contact systems, plus the fact that they are cheaper, are able to measure profound areas and are not sensitive to transparent or colour surfaces. On the downside and as already mentioned in section 2.1, these systems are considerably slow and cannot scan data reliably from flexible objects [1].

All systems presented in table 2.1 offer great accuracies in the micron range outperforming any non-contact machine vision system in the market. However it is worth noting the remarkable performance of touch-trigger probe point-to-point sensing coordinate measuring machines (CMM) manufactured by Mitutoyo since their accuracy is as low as 1µm, thereby, beating any other existing system solution.

Table 2.1 – Traditional commercially available contact systems [adapted from 4].

Technology	Company	Model	Accuracy, resolution and speed
Point-to-point sensing with a touch-trigger probe, mechanical arms	Faro Technologies	FaroArm Advantage	Accuracy: ± 0.090 to ± 0.431 mm
		FaroArm Platinum	Accuracy: ± 0.018 to ± 0.086 mm
	Immersion Corp.	MicroScribe MX	Accuracy: 0.1016 mm
		MicroScribe MLX	Accuracy: 0.1270 mm
Analogue sensing with a scanning probe, computerized numerically controlled machines (CNC)	Roland DGA Corp.	Picza PIX-30	Scan pitch in X,Y,Z axis: X, Y: 0.05 - 5.0 mm in steps of 0.05 mm Z: 0.025 mm
		MDX-15	
		MDX-20	
Point-to-point sensing with a touch-trigger probe, coordinate measuring machines (CMM)	Mitutoyo	Euro-C-121210	Accuracy: 0.001 mm
Analogue sensing with a scanning probe, coordinate measuring machines (CMM) and computerized numerically controlled machines (CNC)	Renishaw Inc.	Renscan 200	Speed: 508–1016 mm/min Max data rate: 70 points/s

2.2.2. Machine vision non contact commercial systems

As already discussed in section 2.1 the shape of surfaces and objects in general can be captured by these kinds of systems without needing to make any physical contact with them. Although many of these systems use light as a source for measurement, there are also other systems which employ magnetic fields or sound waves.

Overall, these systems are able to overcome the difficulty that contact system probes may have in accessing some features of the object of study because of the limitations imposed by the dimensions of the probe itself, thereby retrieving information from complex objects which might not be possible when using such contact approaches, thereby and specially in these cases the fact of not making any contact with the subject of interest is clearly an advantage. Nevertheless, the main benefit offered by such non-contact systems is clearly the high speed of operation and in terms of resolution it is good enough for many applications. The detection of colours is also possible, and this is an added value, however, when reflective, transparent or even peculiar colour surfaces comes into play, these systems have significant limitations. Table 2.2 shows the characteristics of non-contact commercially available systems.

The number of applications covered by these non-contact methods is endless as shown in table 2.2. Out of all listed systems a few can be pointed out due to their outstanding capabilities.

Within laser triangulation approaches, the VIVID 910 system manufactured by Konica Minolta is used mainly in quality inspection as well as in 3D graphics applications offering colour detection, a reasonable resolution ranging from 100 to 220μm and a large number of scan points per second ranging from 122,800 to 256,000. However, the laser triangulation system with the highest accuracy is the LC15 manufactured by Metris which is used in the inspection of highly detailed or small objects. On the downside this system does not allow colour to be detected and only provides 19200 scan points per second.

Other commercial triangulation systems which are worth mentioning are for example the CT900 manufactured by Callidus Precision Systems GmbH which offers a resolution ranging from 10 to 70μm and provides 4000 scan points per second or the XC50 cross scanner fabricated by Metris which offers an accuracy of 15μm and at least 64000 scan points per second. Neither of the latter offer colour detection and this can be a significant drawback depending on the application at hand.

The lowest accuracy from all approaches listed in table 2.2 is the one provided by the interferometry system Mini Conoscan 3000 fabricated by Optimet which ranges from 0.5 to 25μm. On the other hand, this system only allows 850 points per second to be recorded but it offers colour detection. Out of all commercial systems presented in table 2.2, the highest number of points per second is provided also by another interferometry quality inspection system, which is the 3-D Mega Capturor II manufactured by Inspeck, capable of scanning up to an outstanding 1.3 million points in just 0.7 seconds while allowing colour detection and providing a minimum resolution of 300μm. Another system which allows a large number of points to be acquired per second is the Rainbow 25 fabricated by Genex. This is a structured light triangulation system which uses a white light pattern as the light source, allowing for 442,368 points per second to be recorded while providing colour detection and an accuracy of 25μm.

Table 2.2 – Machine vision non contact commercially available systems [adapted from 4].

Tech.	Company	Model	Volume, field of view, envelope (mm)	Accuracy, resolution, pitch (mm)	Colour	Speed (points/s)	Applications
Laser triang.	Cyberware	3030RGB ScanHead	FOV: 260×340× 300 FOV = *Y* (at minimum *Z*) × *Y* (at maximum *Z*) × *Z*.	Sampling pitch *X*: 0.250–1.000 *Y*: 0.700 *Z*: 0.100 (minimum)	Yes	14,580	Head and face 3-D colour scanning. medical, anthropometry, human interface, and portrait sculpture.
Laser triang.	Cyberware	3030RGB MS Model Shop 3-D Scanner	FOV:1000×260×300 FOV = Y (at Minimum Z) × Y (at Maximum Z) × Z.	Sampling Pitch: *X*: 0.250–1.000 *Y*: 0.700 *Z*: 0.100 (minimum)	Yes	14,580	Scanning large sculptures,maquettes, and industrial models.
Laser triang.	Cyberware	WB4 hole Body colour 3D Scanner	Cylindrical FOV: Depth: 120 Height: 200	Sampling pitch: Horizontal (*X*): 5.0 Vertical (*Y*): 2.0 Depth (*Z*): 0.5	Yes	60,000	Animation, fashion design; anthropology, animation
Laser triang.	Konica Minolta	VIVID 910	Scanning Volume: Tele: 111 × 84 × 40 Mid: 196 × 153 × 70 Wide: 355 × 266 × 92 (lens at 0.6 m)	*X*: ± 0.220, *Y*: ± 0.160, *Z*: ± 0.100 to the *Z* reference plane. (Condition: Tele or fine mode)	Yes	122,800 and 256,000 (fine and fast mode)	Common RE and quality inspection: 3D graphics and animation, sculpturing, product development and design, tool and die modification, medical modeling, *etc*.
Laser triang.	Konica Minolta	VIVID 700	Scanned area (*X* × *Y*): 70 × 70 to 1100 × 1100	Resolution (X,Y,Z): 200 × 200 × 256 points	Yes	66,666	Common RE and inspection
Interferometry	Optimet	Mini-Conoscan 3000	Scanning volume: 120 × 120 × 0.2 to 120 × 120 × 70	Accuracy: 0.5 to 25 µm	Yes	850	Common RE and quality inspection
Laser triang.	Perceptron	ScanWorks Lite	Stand-off: 107 Volume: based on CMM	Accuracy: ± 0.050 at 3 σ.	No	23,040	Common RE and quality inspection.
Transmission: X-ray computed tomography	Aracor	ICT 2500	Max. object diameter: 2500	Pixel size: 1.220 Resolution: 3.000 Accuracy: 0.250	No	1024 × 1024 ×1024 scan/16 h	Internal viewing, common RE, and quality inspection
Coherent laser radar	Metris	MV224 and MV260	Range: MV224: 1–24 m and MV260: 1– 60 m.	Accuracy (2σ): 16 µm at 1 m. 100 µm at 10 m.	No	Max: 1000	Static and dynamic inspections of aircraft, automotive, and heavy equipment tooling assemblies.

Tech.	Company	Model	Volume, field of view, envelope (mm)	Accuracy, resolution, pitch (mm)	Colour	Speed (points/s)	Applications
			FOV: ± 45 × 360°	240 µm at 24 m			
Laser triang.	Steinbichler Optotechnik	COMET T-Scan	Measuring depth: 75 Scan width: 90 Mean distance: 83	Accuracy: ± 0.03. Length error: ± 0.1 at 3 m distance to a tracking system.	No	Max: 6,666	Common RE and inspection
Struct. light: triang.; white light fringe Projection	Steinbichler Optotechnik	COMET C100 VZ	Measuring area in high resolution and standard mode: 100 × 80	Accuracy: ± 0.020	No	Max: 6,666	Common RE and inspection
Struct. light: triang.; white light fringe Projection	Steinbichler Optotechnik	C400 VZ	Measuring area in high resolution and standard mode: 420 × 340	Accuracy: ± 0.070	No	Max: 6,666	Common RE and inspection
Time of flight: long range 3-D laser scanner	Riegl	LMS Z210i	Range: 4–400 m. FOV: 80° × 360° (vertical × horizontal angle)	Accuracy: ± 25.000 (single shot) ± 15.000 (averaged)	Yes	8,000–12,000	Process automation and robotics, topography, city modeling and urban planning.
Time of flight: long range 3D laser scanner	Riegl	LMS Z420i	Range: 2–1000 m. FOV: 80° × 360° (vertical × horizontal angle)	Accuracy: ± 10.000 (single shot) ± 5.000 (averaged)	Yes	8,000–12,000	Topography, architectural measurement, as-built surveying, archaeology and cultural heritage documentation, city modeling.
Time of flight: long range 3D laser Scanner	Callidus Precision Systems GmbH	CP 3200	Max range: 40 or 80 m FOV = 40° × 360° to 180° × 360° (vertical × horizontal angle)	Accuracy: 5.000	Yes	1,750	Process automation and robotics, architectural and facade measurement, civil engineering, city modeling, mining, geology.
Struct. light: triang.; white light pattern Projection	Genex	Rainbow 250	FOV: 250 × 200 × 200	Accuracy: 0.250	Yes	442,368	Common RE and inspection, face recognition, medicine and dentistry.
Struct. light: triang.;white light pattern Projection	Genex	Rainbow 25	FOV: 32 × 25 × 20	Accuracy: 0.025	Yes	442,368	Common RE and inspection, face recognition, medicine and dentistry.
Laser triang.	Metris	LC15	Width of view: 15 Depth of view: 15 Standoff: 70	Accuracy: 8 µm (1σ sphere fit)	No	19200	Inspection of small and detailed objects; RE with specific needs for highest accuracy.
Time of flight phase Shift: Short range 3D laser scanner	Surphaser	Surphaser Model 25	Max Range: 400–5.000 FOV: 150–3.000 View angle: 22°, 30°, 40°	Range accuracy: 0.025 Angular accuracy: 0.0030	Yes	200.000	Common RE and inspection, scanning the inside of holes, cavities and concave surfaces

Tech.	Company	Model	Volume, field of view, envelope (mm)	Accuracy, resolution, pitch (mm)	Colour	Speed (points/s)	Applications
Transmission: X-ray computed tomography	Aracor	Konoscope 200	Max object diameter: 200	Pixel size: 0.200 Resolution: 0.400 Accuracy: 0.040	No	1024 × 1024 × 1024 scan/16h	Internal viewing, common RE, and quality inspection
Transmission: X-ray computed tomography	Aracor	Konoscope 160	Max object diameter: 160	Pixel size: 0.100 Resolution: 0.250 Accuracy: 0.020	No	1024 × 1024 × 1024 scan/16h	Internal viewing, common RE, and quality inspection
Interferometry	Inspeck	3-D Mega Capturor II	FOV: 435 × 350, Standoff distance: 900 Reference distance ($z = 0$): 1,100	Resolution: $X = 0.300$ $Y = 0.300$ $Z = 0.400$	Yes	1.3 million points in 0.7 s.	Common RE and quality inspection
Interferometry	Inspeck	3-D Capturor II	FOV: 360 × 270, Standoff distance: 900 Reference distance ($z = 0$): 1,100	Resolution: $X = 0.600$ $Y = 0.600$ $Z = 0.400$	Yes	0.3 million points in 0.4 s.	Common RE and quality inspection
Laser triang.	Callidus Precision Systems GmbH	CT 900	- Max. object size: 1600 × 1400 Measuring range: + Horizontal: 180 + Depth: 700	Accuracy: 0.100 Resolution: + Near: 0.010 + Far: 0.070	No	4,000	Common RE and quality inspection
Laser triang.	Callidus Precision Systems GmbH	CT180	Max. object size: 350 × 375. Measuring range: + Horizontal: 180 + Depth: 700	Accuracy: 0.1 Resolution: + Near: 0.025 + Far: 0.070	No	4,000	Common RE and quality inspection
Transmission: X-ray computed tomography	Micro Photonics Inc.	Skyscan 1172	Max. object diameter: 68	Pixel size: 0.9–1.6 µm Resolution:5–8 µm Smallest detail detectability: 1 µm	No	6.8 s per cross section 1024 ×1024 pixels	Biomedical, biological specimens, medical imaging, bone analysis, nondestructive inspection, diamonds, electronic components and packaging.
Laser triang.	Metris	XC50 cross scanner	Width of view: 3 × 15 Depth of view: 3 × 15 Standoff: 70	Accuracy: 15 µm (1 σ sphere fit)	No	3 × 64000	A multi-strip laser sensor is used: efficient scanning of features: holes, slots and gaps are typically inspected: automotive applications.

2.3. Discrete sensor based machine vision applications

The majority of existing machine vision applications use discrete detectors to acquire data from the object of interest and these discrete sensors are generally either CCD or CMOS.

Christoph Steiger et al. [5] describe Plasmo™, which is a system used frequently in the automotive industry to control automatically the quality of laser welding processes. Here the most important aspect is to reliably detect failures or flaws in the process in order to maintain the high quality control requirements imposed by industry. The approach used in this machine vision system is high speed laser triangulation. Such an approach allows fast data acquisition and subsequent three dimensional model representation of the welds. The system can detect defects as small as 100µm while scanning at speeds of approximately 16.6cm per second and can acquire images at about 10000 frames per second. A camera is used to acquire the required information and the sensor employed inside this camera is a CMOS chip composed of a matrix of 512 x 512 pixels.

M. Baba et al. [6] developed a rangefinder system based on the triangulation principle which is able to measure the 360º shape of an object at different surface reflectance. The system allows Lambertian and specular light reflections from objects to be measured. Moreover, it is able to detect hybrid reflections, which are a mixture of both Lambertian and specular ones. The sensing part is composed of multiple linear CCDs arranged so as to be able to be moved freely in the vertical direction, essentially for optical alignment purposes. Each linear CCD contains 2048 pixels and the size of each pixel is about 14µm. A rotation stage is used in order to measure the complete 360º shape of an object.

The triangulation platform geometry scheme is similar for most of the optical triangulation systems reported. Frequently and as described in the work of T. A. Clarke et al. [7], S. Klancnik et al. [8] and A. Peiravi et al. [9], CCD cameras in combination with laser spots or stripes are used for the study of the triangulation system parameters or related distance and angle calculations as well as for the detection of objects in 3D.

Within the triangulation approach, M. Johanesson et al. [10-12] report research work on the sheet-of-light method described in section 2.1.4.1 using discrete sensors. Here, the main application is real time sorting of fish cans. The profile images of fish tins or cans are acquired as they travel on a conveyor belt. These obtained image frames are combined to create and represent 3D models of the tins. The system is able to obtain up to a maximum of 800,000 frames per second. Its camera sensor is composed of a matrix of 256 x 256 photodiodes. Such a real time sheet-of-light range imaging application is also able to scan and determine the orientation of up to ten fish tins per second.

Another powerful technique used in machine vision systems which should be taken into account is interferometry. Section 2.2.2 lists a few commercial machine vision systems based on this interesting technique. A. Devillez et al. [13] suggest detecting metal cutting tool wear through the use of white light interferometry. Such an approach is a non-contact optical method suitable for measuring shapes and heights of surfaces at great speeds and accuracies. The system works by splitting white light rays and re-directing them to both the surface of interest and a mirror. Once these light rays recombine an interference pattern is created. The maximum image contrast for a particular point within a sample happens to be at the best focused location of that imaged interference pattern. Frames of the interference data coming from that specific location are acquired by a CCD camera. This particular system allows surfaces with a reflectivity of 1 to 100% to be scanned. A surface height range from nanometers to millimeters can also be detected. The system is capable of scanning keeping up with the typical metal cutting application speeds ranging from 60 meters per minute to about 960 meters per minute. The Wyko®NT1100 optical profiler was used to create 3D images of the wear surfaces and to examine the parameters involved in the metal cutting procedures. Even though for this specific application this interferometry technique proves to be more accurate than other machine vision approaches such as three dimensional computer vision [14] or stereovision [15], the disadvantage here lies in the fact that the wear examination is only possible after the metal cutting process has finished. In addition, this method does not allow on site metal cutting tool measurement.

2.4. Analogue sensor based machine vision applications

Some applications employ analogue sensors, such as position sensitive detectors, as opposed to discrete ones. F. Martinez et al. [16] present a system which scans objects in 3D with a precision of about 50µm and a speed of about 5000 points per second. The experimental setup includes two standard CCD cameras, one PSD camera and one linear CCD camera as well as a light projector and a laser. All this equipment allows 3D object data acquisition to be performed using the triangulation principle via the PSD or linear CCD camera as well as using the stereovision technique between the two standard CCD cameras. The linear CCD camera contains 5000 pixels. The PSD camera sensor is a two dimensional PSD and it is able to detect currents from nanoampers to milliampers.

The use of light patterns in combination with the stereovision technique allows the detection of sudden depth changes on the surface being analyzed as well as the recognition of precise surface contours. The integration of several machine vision approaches within a single setup eliminates occlusion to a great extent, improves accuracy and reduces noise.

The work performed by K. Araki et al. [17] is another example of the integration of analogue sensors within a machine vision system. In this case an array of 128 position sensitive detectors is used as the sensor component. The system developed is able to perform continuous 3D measurements at high speeds and this is primarily because it is based on the sheet-of-light triangulation technique as well as on the fact that the information coming from the analogue sensor array used does not require much processing power.

All analogue data coming from the position sensitive detector array is fed to an analog signal processor and is subsequently multiplexed via multiplexers. It is then converted to digital data by analogue to digital converters and is subsequently stored in relevant memory locations. The system is capable of continuously acquiring 3D range data from scanned objects at standard video rates while claiming an accuracy of about 0.3%. A series of human face 3D scans were realized at speeds of about 30 frames per second. These scans were repeated while the lips of the human face were moving during speech. Realistic results were obtained showing that the system is capable of detecting and representing properly in 3D, object surfaces formed by edges or smooth curves. According to K. Araki et al. [17], an enhancement of the system architecture multiplexer module could improve the acquisition time (frames per second) by at least 125 times. The active area of the developed 128 position sensitive detector array is 30 x 25.4 mm and the response time is claimed to be of 1μs. The light source is a 200mW laser diode with a wavelength of about 810nm. An optical lens with a 50mm focal length is also employed.

2.5. Conclusions on machine vision

From previous sections it can be concluded that a vast range of systems and solutions exist in the market which allow information or data from an object to be obtained, even in real time. However, the theme of this thesis is directly linked to non-contact sheet-of-light triangulation systems and all related work was performed with the goal of developing examples of such systems, using as sensors the 32 and 128 amorphous silicon PSD arrays (3D sensors). With the exception of some minor work performed using similar crystalline silicon sensors [17], to our knowledge, a-Si:H sensors for high speed 3D object profile detection (laser triangulation) have not been reported yet. Laser triangulation systems exist using mainly CCD and CMOS sensors. Recently, up-to-date information was found on the latest systems available in the market in this field. The following company in Germany [18] manufactures the most advanced CMOS sensor based sheet-of-light laser triangulation 3D cameras. They use digital sensors such as CMOS sensors (E.g. 1280 x 1024 pixels). The principle of application of these 3D sheet-of-light cameras is exactly the same as the one used for the 32 and 128 amorphous silicon 3D PSD sensor systems and thereby they are the most advanced direct competitors in terms of speed, resolution and overall system performance, since they claim their cameras are the fastest in the world. As can be seen in their product catalogue [18], one of their cameras (C4-1280) reaches 40000 profiles/frames per second, when using 128 pixels and 128 rows of the sensor so only just a small part of the whole sensor (1280 x 1024 pixels).

Amorphous silicon 32/128 PSD array 3D sensors would be an alternative to these CMOS cameras in similar application scenarios. The overall performance between both technologies is expected to be similar or better when using the 128 PSD sensor system.

The resolution of these 3D CMOS cameras is quite good depending on the application and in some applications they claim to reach resolutions of about 35µm or even 10 or 5µm. Thereby it seems 3D cameras with digital sensors are already quite advanced and relatively cheap since their unit price ranges from 3000 to 9000 euros. This price includes the camera, laser and lens but not the software, nevertheless, third party software is readily available.

Anyhow, in relation to machine vision applications, one of the main objectives of this thesis is the application of amorphous silicon 3D PSD sensors to 3D object profiling, and this has involved studies relating the incident angle of 3D scanning plus other aspects of the 3D triangulation scanning scheme such as the geometry.

2.6. Microscopy applications

Interest in optical microscopy applications for micron and submicron research has grown enormously in a wide range of disciplines during the last ten years [19-23]. Moreover, as the size of devices is getting smaller and the production of nanocomponents is increasing, the development of systems able to process and detect small device movements and dimensions is of great importance. Thereby, the need to perform tracking and record movements or dimensions of objects under the microscope is clear in many scientific applications. Various software applications have been developed to track the movement of microstructures under the microscope.

2.6.1. Discrete sensor based microscopy applications

In most cases the imaging system associated to these applications is composed of a video camera, a frame grabber card and a personal computer [24]. Nowadays, the position/movement of micro objects can be filmed by a high quality camera with more than 50 images per second. Every single image of the CCD camera is then analyzed in real-time by image processing algorithms in order to extract and obtain the desired information. However, this whole process is too slow for some applications.

P. Gualtieri et al. [25] present a digital microscope which can detect the movement of microorganisms in real time. Such an analysis is performed by studying time sequences which are saved by the system. Typical common devices, such as a digital frame grabber or a television camera are embedded in the microscope enabling it to work in real time.

Real time analysis is particularly important nowadays since it allows researchers to monitor events as they are taking place. Traditional methods fail to capture circumstances which occur in a rapid manner, however, digitized video microscopy is a prevailing strategy used to detect those fast events [26]. Such a technique employs CCD cameras which have a typical resolution of 8 bits per pixel and generally obtain images at video frame rates via the usual digital frame grabber board operating inside a PC. These approaches are able to acquire low signal levels and usually perform averaging on the acquired image information.

2.6.2. Analogue sensor based microscopy applications

Regarding the use of analogue sensors within microscopy applications, to date, the advantage clearly lies on the high speed and low processing power allowed by analogue sensor detecting principles. For example, fast feedback techniques have relied on quadrant photodiode position detectors [27], which measure the position of the image of an optically trapped object at rates up to 10 kHz. Position sensitive detectors are ideal for any application requiring low levels of signal processing power or high speeds in comparison to existing standard video frame rates. Similarly to what happens with charge coupled device detectors (CCD) [28] the data recorded is also processed by a computer, but with a major advantage being that the detection is not limited to 50 or 100 frames per second.

Another example of the integration of analogue sensors in microscopy applications is the use of an amorphous silicon 32 position sensitive detector array [29] for the detection of micro objects, based on reflecting light coming from those objects [30, 31]. Such work proposes the use of the presented sensor array and relevant system for detecting micro object movement and dimensions even at high speeds and the details are also explained in chapter 4 of this thesis.

2.6.3. Fluorescence approaches

A large number of biotechnology applications use fluorescence microscopy to study living specimens. Standard fluorescence methods traditionally examine every frame of the acquired sequence of images in order to identify fluorescence spots and those which are equal are associated between frames and thereby can be tracked. Typically, in order to excite the fluorescence specimens being studied, a mercury arc or xenon lamp is used and its wavelength as well as its intensity is usually controlled.

I. Bechar et al. [32] use video microscopy methods to analyze the motion of fluorescence spots. In such methods the obtained 3D video microscopy images are separated into small sections and the presence of fluorescence is examined in all existing image pixels at the same time. The variation of fluorescence in pixels from section to section allows the analysis of the relevant fluorescence spot movement. Apart from the fact that fluorescence digitized video microscopy provides a sequential analysis of data, such a technique also allows researchers to pinpoint essential information on spatial resolutions or distances. X. F. Wang et al. [26] evaluate a few video fluorescence microscopy techniques used to examine the molecular structure of living cells in terms of their limitations, as well as their ease of use and improvement possibilities. Thanks to these techniques, cell hypoxic injury behavior is better understood and tackled. Latest developments are now even allowing specific fluorescence microscopes to represent cell behavior and arrangement in three dimensions. For example, Los Alamos National Laboratory have developed a microscope for three dimensional imaging and tracking specifically targeted for fluorescence microscopy applications [33].

2.6.4. Tracking

As microscopic imaging state of the art techniques are continuously being improved over time, the number of applications requiring object tracking possibilities under the microscope is constantly increasing. Detection of the movement behavior of specimens is of most importance, especially in biotechnology applications where for example, the tracking of cells is crucial for disease studies and related. A manual study of the images obtained under the microscope does not offer sufficient accuracy or repeatability and it generally takes too long. In addition, present state of the art does not allow an automatic proper image analysis and understanding, thereby not fulfilling the demands of the application at hand. Current techniques usually detect the subjects of study within the acquired images during a first analysis and then try and associate these between different image frames. However, when noise or fluctuations are present on the images it becomes difficult for these techniques to perform their tasks correctly [34]. On top of that, various incorrect assumptions are made by these methods, such as the fact that the specimens being studied hardly ever modify their velocity or their moving direction unexpectedly [35], or the fact that the intensity of the image stays constant as time progresses [36]. Due to these overall constraints researchers are developing solid and reliable methods to track specimens precisely under the microscope. A commercial solution already referred to in section 2.6.3 is a three dimensional tracking microscope produced at Los Alamos National Laboratory [33]. Such equipment is able to track the movement of fluorophores in three dimensions sufficiently fast, meeting for example, the speed requirements for the majority of cell motion tracking applications. It is suitable for molecular spectroscopy, biomedical research and cellular biology. A typical application scenario could be the study of viral or bacterial incursions of living cells. A spatial accuracy in all X, Y and Z axis of about 100nm is claimed by the system. The tracking speed is higher than standard video frame rates and the system is able to track movement at μm/sec rates. Thereby, the three dimensional analysis of the motion of biospecimens and their behavior can be studied since the system is continuously acquiring and recording the position of the subjects at hand in three dimensional space as time passes. On top of that, the 3D tracking microscope is also able to determine the lifetime of fluorophores or fluorescent specimens.

2.6.5. Conclusions on microscopy

As referred to in the reviewed state of the art a large range of options are available to detect the presence, track the movement and represent the images of specimens under the microscope. A wide portfolio of systems and solutions mainly based on discrete sensors such as CCDs or CMOS exist in the market and the most recent and advanced ones permit real time acquisition and representation in 2D and even in 3D. The operating speeds of the latter are higher than standard video frame rates, however, they are still not fast enough for some applications. Analog devices such as position sensors or position sensitive detectors are used in those applications requiring higher speeds and lower signal processing resources, due to their particular characteristics which are ideal for those tasks. On the other hand, most of these analog sensors cannot provide high quality imaging of the specimens being analyzed and thereby they are mainly used for fast tracking and detection purposes.

In this thesis, an analog sensor such as the proposed amorphous silicon 32 PSD array and its relevant hardware/software system are mounted on the microscope in order to detect the presence, movement and dimensions of micro objects.

When comparing the performance of this sensor to the state of the art, it is clear that a good image quality is not provided, just as with other analog sensors. However, it is possible to reach extremely high speeds of detection in real time. The sensor system is capable of determining, if a micro object is under the ocular of the microscope, how fast is moving and in which direction, in 2D (X and Y), as well as what are its dimensions, also in 2D (width and length).

Amorphous silicon 32/128 PSD array 3D sensors could be an alternative or a complement to discrete CMOS or CCD based systems in some microscopy application scenarios where high speed of detection or low signal processing resources are needed.

Nevertheless, in relation to microscopic vision applications, one of the main objectives of this thesis is the application of amorphous silicon 3D PSD sensors to micro object detection, and this has involved the study of the light intensity reflected by the micro objects so as to determine the resolution of movement detection in 2D (X and Y) plus other aspects, such as the measurement of micro object dimensions in 2D (width and length).

2.7. References

[1] R. J. Campbell and P. J. Flynn, “A survey of free-form object representation and recognition techniques”, Comput. Vision Image Understanding 81(2):166–210, 2001.

[2] O.D. Faugeras, “Three-Dimensional Computer Vision: A Geometric Viewpoint”, MIT Press, Cambridge (MA) (1993).

[3] D. Page, A. Koschan, Y. Sun, and M. Abidi, "Laser-based Imaging for Reverse Engineering", Sensor Review, Special Issue on Machine Vision and Laser Scanners, 23, 3, 223-229, 2003.

[4] V. Raja and K. J. Fernandes, “Reverse Engineering - An Industrial Perspective”, Springer, 17-27, 2008.

[5] Ch. Steiger, W. Ptacek, G. Kronreif and C. Wögerer, “Online Control Sensors for Various Welding Processes Based on Optical Recognition” – PLASMO™”, 6th IFAC Symposium on Fault Detection, Supervision and Safety of Technical Processes, 6, 1, Tsinghua University, Beijing, China, 2006.

[6] M. Baba, D. Narita and K. Ohtani, “360° shape measurement system for objects having from Lambertian to specular reflection properties utilizing a novel rangefinder”, J. Opt. A: Pure Appl. Opt. 4, 295-303, 2002.

[7] T. A. Clarke, K. T. V. Grattan and N. E. Lindsey, "Laser-based triangulation techniques in optical inspection of industrial structures," Proc. SPIE 1332, 474, 1991.

[8] S. Klancnik, J. Balic, and P. Planincic, “Obstacle detection with active laser triangulation,” Adv. Prod. Eng. Manage.2, 79–90, 2007.

[9] A. Peiravi and B. Taabbodi, “A reliable 3D laser triangulation-based scanner with a new simple but accurate procedure for finding scanner parameters,” Am. J. Sci.6, 80–85, 2010.

[10] M. Johanesson and A. Astrom, “Sheet-of-light range imaging with MAPP2200,” Technical Report LiTHISY-1–140 1, Dept. EE, Linköping University, Linköping, Sweden, SE-581 83 (personal communication, 1992).

[11] M. Johannesson, “Sheet-of-light range imaging in: linköping studies in science and technology,” Dept. EE, Linköping University, Linköping, Sweden, SE-581 83 (personal communication, 1993).

[12] M. Johannesson, “Can sorting using sheet-of-light range imaging and MAPP2200,” in Conference Proceedings., International Conference on Systems, Man and Cybernetics, 'Systems Engineering in the Service of Humans', 3, 17–20, 325–330, 1993.

[13] A. Devillez, S. Lesko and W. Mozer, “Cutting tool crater wear measurement with white light interferometry”, Wear, 256, 1–2, 56-65, 2004.

[14] Y. Shirai, “The Three Dimensional Computer Vision”, Springer, Berlin, 1987.

[15] K. N. Prassad and B. Ramamoorthy, “Tool wear evaluation by stereo vision and prediction by artificial neural network”, J. Mater. Process. Technol. 112, 43–52, 2001.

[16] F. Martínez, J. Mitxelena, G. Obieta and J. Ruano, “Sistema sensorial dinamico para modelizacion de solidos camara PSD”, Ikerlan, Dpto. de Sensores y Visión Artificial, Apdo. 146. 20500, Mondragón, Spain (personal communication).

[17] K. Araki, M. Shimizu, T. Noda, Y. Chiba, Y. Tsuda, K. Ikegaya, K. Sannomiya and M. Gomi, “High speed and continuous 3-D measurement system,” in Proceedings., 11th IAPR International Conference on Pattern Recognition, Vol. IV. Conference D: Architectures for Vision and Pattern Recognition, 30, 62-65, 1992.

[18] Product Catalogue, AT-Automation Technology GmbH, Bad Oldesloe, Germany, www.automationtechnology.de. 10/09/2013.

[19] B. Herman and J.J. Lemasters, “Optical Microscopy: Emerging Methods and Applications”; Academic Press: New York, NY, USA, 1993.

[20] S. Inoué and K.R. Spring, “Video Microscopy: The Fundamentals”, 2nd ed; Plenum Press: New York, NY, USA, 1997.

[21] S. Bradbury and B. Bracegirdle, “Introduction to Light Microscopy”; BIOS Scientific Publishers Ltd.: Oxford, UK, 1998.

[22] E.M. Slayter and H.S. Slayter, “Light and Electron Microscopy”; Cambridge University Press: Cambridge, UK, 1992.

[23] M. Pluta, “Advanced Light Microscopy” (3 volumes); Elsevier: New York, NY, USA, 1989.

[24] P.J. Wit, J. Noordmans and H.J. Busscher, “Tracking of colloidal particles using microscopic image sequence analysis. Application to particulate microelectrophoresis and particle deposition”, Colloid. Surf. A, 125, 85-92, 1997.

[25] P. Gualtieri and P. Coltelli, “A digital microscope for real time detection of moving microorganisms”, Micron and Microscopica Acta, 20, 2, 99-105, 1989.

[26] X. F. Wang, K. Florine-Casteel, J. J. Lemasters, and B. Herman, “Video fluorescence microscopic techniques to monitor local lipid and phospholipid molecular order and organization in cell membranes during hypoxic injury”, J. Fluoresc. 5, 1, 71-84, 1995.

[27] K. Visscher and S.M. Block, “Versatile optical traps with feedback control, methods in enzymology”, Method. Enzymol. 298, 460-489, 1998.

[28] H. Kahmen and M. Roic, “A new generation of measurement robots for object reconstruction without targeting”, In Optical 3d Measurements III; A. Grün, H. Kahemen, Eds.; Herbert Wichmann Verlag: Heidelberg, Germany, 251-262, 1995.

[29] R. Martins, J. Figueiredo, V. Silva, H. Aguas, F. Soares, A. Marques, I. Ferreira and E. Fortunato, “32 linear array position sensitive detector based on NIP and hetero a-Si:H microdevices”, Journal of Non-Crystalline Solids 299–302, 1283–1288, 2002.

[30] J. Contreras, C. Baptista, I. Ferreira, D. Costa, S. Pereira, H. Águas, E. Fortunato, R. Martins, R. Wierzbicki, and H. Heerlein, “Amorphous silicon position sensitive detectors applied to micropositioning,” J. Non-Cryst. Solids 352, 9-20, 1792–1796, 2006.

[31] J. Contreras, D. Costa, S. Pereira, E. Fortunato, R. Martins, R. Wierzbicki, H. Heerlein, and I. Ferreira, “Micro cantilever movement detection with an amorphous silicon array of position sensitive detectors,” Sensors (Basel, Switzerland) 10, 9, 8173–8184, 2010.

[32] I. Bechar and A. Trubuil, "Reliable Motion Detection and Analysis in Live-cell Imaging", Biomedical Imaging: From Nano to Macro, 2007. ISBI 2007. 4th IEEE International Symposium on, 12-15, 280-283, April 2007.

[33] Licensable technologies, Los Alamos National Laboratory, Los Alamos, New Mexico, USA. www.lanl.gov/partnerships/license/technologies. 12/09/2013.

[34] M.K. Cheezum, W.F.Walker, and W.H. Guilford, “Quantitative comparison of algorithms for tracking single fluorescent particles,” Biophys. J., 81, 4, 2378–88, Oct. 2001.

[35] D. Chetverikov and J. Verestóy, “Feature point tracking for incomplete trajectories,” Computing, 62, 4, 321–38, 1999.

[36] C.B. Bergsma, G.J. Streekstra, A.W. Smeulders, and E.M. Manders, “Velocity estimation of spots in three-dimensional confocal image sequences of living cells,” Cytometry, 43, 4, 261–72, Apr. 2001.

Chapter 3

Experimental procedures

Chapter 3. Experimental procedures

Summary

The experimental details in relation to the fabrication of the sensors and their detecting electronic systems as well as their application to the detection of 3D object profiles and micro objects are described in this chapter. Sensor fabrication steps are listed and explained. Hardware and software module developments are also presented. Moreover, all relevant and required 3D object scanning and micro object detection experimental procedures are reviewed and illustrated in this chapter.

3.1. Fabrication of a-Si:H 32/128 position sensitive detector arrays

The fabrication of the amorphous silicon position sensitive detector array sensor (PSD) was not the main goal of this thesis, since it was the subject of previous works [1-3]. Anyhow, we present here the main steps for the fabrication of the 32 or 128 amorphous silicon position sensitive detector arrays in accordance to the standard procedures used to produce amorphous silicon PSDs. The required steps are listed below and described in more detail in APPENDIX A:

1. Proper cleaning of the substrate.
2. First photolithography step.
3. First substrate curing in the oven.
4. First mask aligning process for metal mask pattern transfer onto the substrate.
5. First developing process to remove existing photoresist from all areas where the metal mask pattern is present.
6. Metallization - Chromium is deposited via thermal evaporation assisted by electron-gun.
7. Lift-off - Performed to remove metal from all areas not corresponding to metal mask pattern.
8. PECVD - Amorphous silicon material is deposited onto the substrate.
9. Second photolithography step. Same as step 2.
10. Second substrate curing in the oven. Same as step 3.
11. Second mask aligning process for silicon mask pattern transfer onto the substrate.

12. Second developing process to remove existing photoresist from all areas where the silicon mask pattern is present.

13. Dry etching - Performed to remove silicon from all areas not corresponding to silicon mask pattern.

14. TCO deposition - Transparent conductive oxide material is deposited onto the substrate.

15. Third photolithography step. Same as step 2.

16. Third substrate curing in the oven. Same as step 3.

17. Third mask aligning process for TCO mask pattern transfer onto the substrate.

18. Third developing process to remove existing photoresist from all areas where the TCO mask pattern is present.

19. Wet etching - Performed to remove TCO from all areas not corresponding to TCO mask pattern.

3.1.1. Cleaning of the substrate

The substrate must be properly cleaned before any thin film deposition. This is important as dirt particles accumulated on the surface of the substrate can easily modify the electric, optical and adhesion properties of the material being deposited [4]. The preparation of the substrates and their cleaning procedure is described in detail in section A1 of APPENDIX A.

3.1.2. Photolitography

Photolitography is performed in order to pattern the material deposited onto the entire substrate using the design of each layer of the sensor. For that, a pattern is transferred to a light sensitive material, photoresist, which will protect the deposited material in areas where it should stay while the other regions will be removed by an etching process. As listed in section 3.1, photolitography is performed three times at different stages of the sensor fabrication process and is described in detail in section A2 of APPENDIX A.

3.1.2.1. Mask aligning and developing process

The pattern transfer is performed by placing a mask on top of the photoresist layer and shining it with a UV light (as the photoresist is sensitive to it). The regions exposed to light will be removed after a developing process. In order to properly align the mask containing the pattern, a mask aligner with a resolution better than 10μm is used. As mentioned in section 3.1.2, all related sub-tasks described in section A2 of APPENDIX A are carried out three times. That is, three different stages of the sensor fabrication need different geometries corresponding to different masks: metal, silicon or TCO.

Each of the masks is composed of transparent regions, which correspond to areas where the photoresist should be removed, now that light passes and reaches the photoresist.

Figure 3.1 shows photographs of masks for the metal (a), silicon (b) and TCO (c) layers used for the production of the 32 PSD sensors:

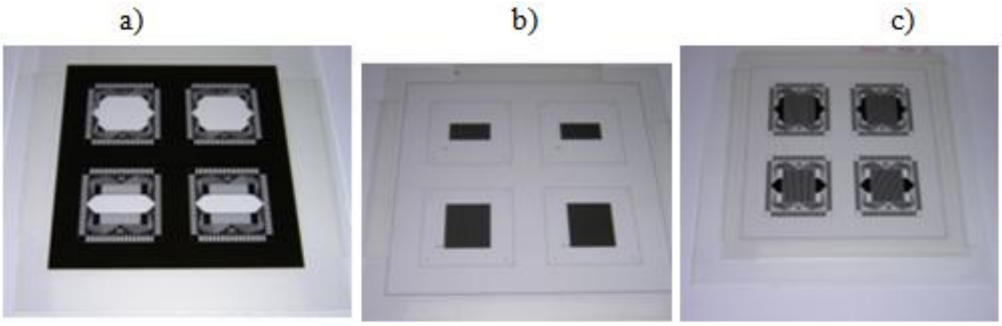

Figure 3.1 – Photographs of the masks for: a) metal; b) silicon; c) TCO layers

The mask aligning and developing process is described in detail in section A3 of APPENDIX A.

3.1.3. Metallization

The first layer of the sensor is the metal one. This layer is obtained by thermal evaporation assisted by an e-beam process. The material to be deposited onto the substrate, is placed in a crucible. Electron bombardment of the material inside the crucible occurs via an electron beam which is created by a tungsten filament heated until it becomes incandescent resulting in the emission of electrons. The beam of electrons is focused by the existing electric and magnetic fields onto the crucible causing a localized melt of the material which is evaporated and subsequently reaches the substrate where it is deposited. Of course, the evaporation of the material occurs when atoms acquire enough kinetic energy to overcome and release themselves from the material surface tensions to which they are subjected. Thereby, deposition occurs when metal vapor atoms break free from those tensions and adhere onto the substrate surface.

The metallization process is described in detail in section A4 of appendix A.

3.1.4. Lift-off

The lift-off process is performed after metallization. The substrate needs to be immersed in acetone in order to remove the photoresist located underneath the metal, dragging the metal along with it. Thereby only the existing metal mask pattern covered with metal is left on the substrate. The lift-off process is described in section A5 of appendix A.

3.1.5. PECVD – Plasma Enhanced Chemical Vapour Deposition

For the PSD sensors the amorphous silicon films are deposited onto the substrate by Plasma Enhanced Chemical Vapour Deposition (PECVD). This technique allows the deposition of thin films onto a substrate from a vapour phase to a solid state due to the chemical reactions taking place. The gases involved in the process are decomposed by plasma which is created via radio frequency between two electrodes and the space in between is where the gases react together at a molecular level. The resulting particles are deposited on the surface of the growing thin film. The rate of growth of the film obviously depends on the number of particles reaching the substrate.

The optical and electrical properties and overall quality of all sensor structure layers and in particular the N, I and P layers are meticulously controlled via the deposition parameters which are involved in the process. These parameters are: radiofrequency (RF) power density; temperature of substrate; composition and flux of gases; deposition pressure; distance between electrodes; geometry of chamber and electrodes.

Thereby, prior to sensor fabrication the deposition parameters of the individual Si layers must be optimized. The PECVD process is further described in section A6 of APPENDIX A.

3.1.6. Dry etching

After the photolithography process which defines the lines (strips) of the sensor, the unwanted material is removed by dry etching. The material of the lines (strips) is protected by photoresist while the other material is etched way by a plasma of SF6 gas. This is a precise and selective process that is described in more detail in section A7 of APPENDIX A.

3.1.7. Sputtering

The sputtering technique consists on the bombardment of a target by argon ions formed in a plasma and created when a voltage is applied between a cathode and an anode. The cathode is the target support containing the material to be deposited which in this case is ZnO:Al, and the anode is the substrate holder. The source of the material (the target) is subjected to strong ion bombardment. Due to this bombardment, material particles break free from the target and are projected in the direction of the substrate where they are deposited, being formed a thin film. In this deposition technique the parameters to be controlled are: gas flux, applied power; substrate temperature; distance to target; pressure; time. For the production of the PSD sensors the Argon gas flux used is 15 sccm, the temperature is set to ambient temperature, the deposition pressure is 2 mTor, the deposition time varies from 15 to 11 minutes depending on the target used and the applied RF power is 150 W. Concerning the production of the 32 PSD sensors, a suitable value for the resistivity of the TCO layer is determined between 14-20 KΩ on all areas of the surface of the sensor. Figure 3.2 shows a photograph of the sputtering system used in the production of the PSD sensors.

Figure 3.2 – Photograph of the sputtering system.

3.1.8. Wet etching

Once again, after the deposition of TCO on the substrate area, and after photolitography is performed to define the areas of TCO, the unwanted regions should be removed. These are removed by wet etching. For that, the substrate with photoresist, protecting the desired areas, is immersed in a chemical solution to etch ZnO, containing acetic, phosphoric acid and water. Acetone is then used to remove the photoresist protecting the TCO areas needed to make the signal contacts of the sensor. The wet etching process is thoroughly described in section A8 of APPENDIX A.

The fabrication of the PSD sensors ends at this stage and the unwanted glass areas are then cut on the edges of the substrates. Figure 3.3 shows the sensor produced. The active area located in the middle of the sensor is composed of 32 detector strips each connected to a metal contact at each side of the strip. There are 64 metal contacts.

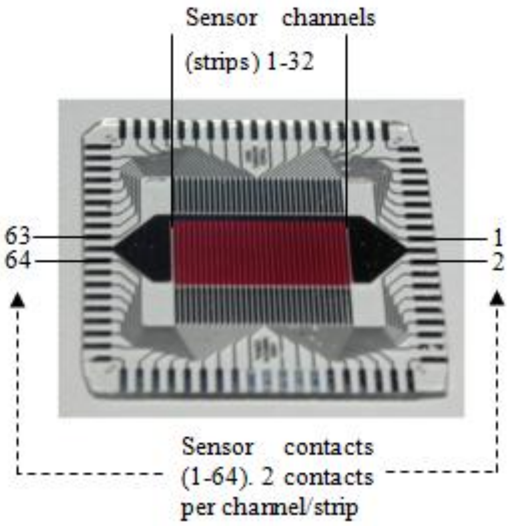

Figure 3.3 – Photograph of the 32 position sensitive detector (PSD) array sensor.

3.2. Hardware development for PSD sensor array systems

Hardware prototype systems were developed for data acquisition from the 32 and 128 PSD sensor arrays. These allow the measurement of current delivered by the sensors. Characterization of the sensors and their application in different scenarios is possible due to the development and assembly of these specific prototype systems.

3.2.1. 32 PSD sensor array hardware system

A data acquisition prototype system integrating the 32 linear array of position sensitive detectors was developed as shown in figure 3.4.

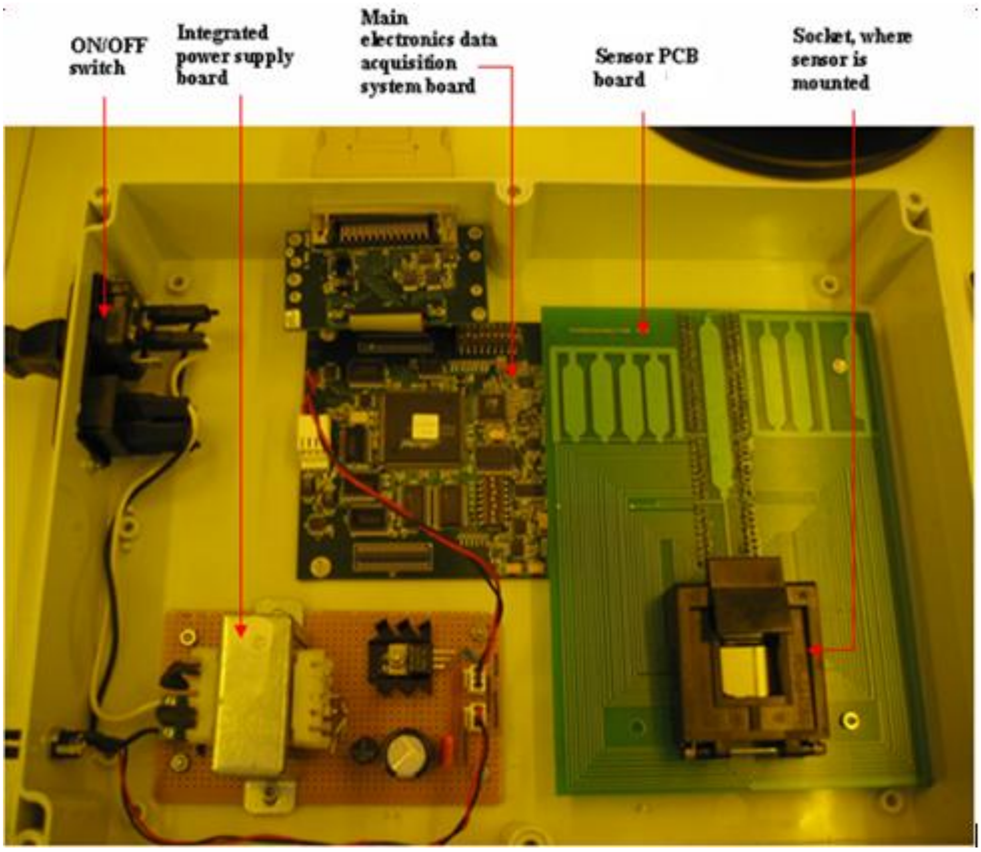

Figure 3.4 – Photograph of the data acquisition prototype system.

The system is comprised of two printed circuit boards connected together. The main electronics data acquisition system board contains electronics used in X-Ray detection systems, mainly due to its processing capabilities and it is a commercially available electronics module provided by Sens-Tech Ltd [5], also suitable for photodiode data acquisition operations. The sensor printed circuit board or adapter module was self developed and is comprised of 64 routed channels as well as a socket to accommodate the PSD (position sensitive detector) sensor. The socket shown in figure 3.4 allows for removal and replacement of the PSD sensor whenever needed. Pin connectors were used to attach both boards together within the prototype system.

A schematic of the main electronics system module responsible for the data acquisition and control is shown in figure 3.5.

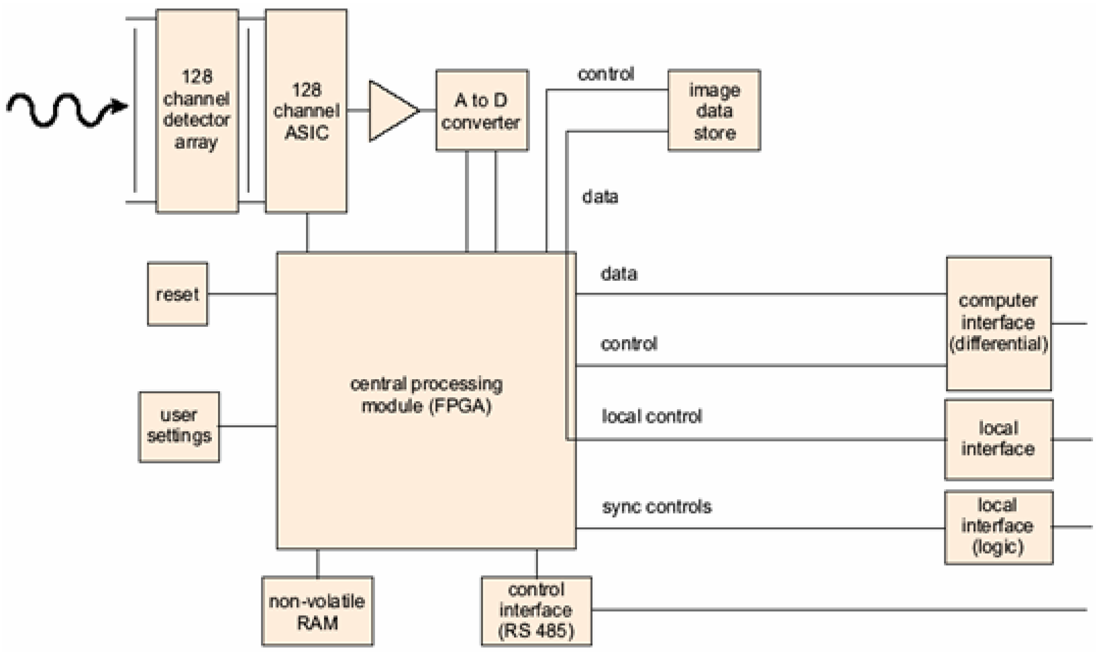

Figure 3.5 – Schematic of the main electronics system module
responsible for the data acquisition and control [5].

As illustrated in figure 3.5, either a 32 or a 128 channel detector array [6] is connected via a printed circuit board adaptor to a specially manufactured integrated circuit (ASIC), which amplifies and subsequently multiplexes the input signals. An A/D converter then converts the signals from analogue to digital and passes the data to a field programmable gate array (central processing module––FPGA). This module controls the operation of the system, sends the processed data to the PC and communicates with the other modules and devices via the control lines shown in figure 3.5 sending the data through the data lines. Other modules are used, for example, to save user settings or image information. The system can acquire a single line of data in a minimum time of 10μs, performing simultaneous data acquisition and read-out, offering a wide dynamic range able to deliver 16 bit output, plus having a high speed SCSI-USB link to the PC.

As noticeable in figure 3.4, three external cables are connected to the prototype system. These are, a mains supply cable providing the system with AC voltage supply, another thin black cable supplying enough current for the RS232/Parallel (from PC) to SCSI connection, and a SCSI cable. The SCSI cable carries mainly the data acquired.

Two cables (red & black colour in figure 3.4) provide DC supply voltage for the system. A power supply board was self constructed and integrated onto the prototype system box. It provides 5 volts output to drive the electronics of the main data acquisition system board.

The sensor system prototype was tested proving to be very sensitive to light, however, this is a good advantage towards the detection of low light levels such as for example reflections that are coming from small objects. The sampling frequency is usually set at 1 KHz, however the main electronics system board allows a sampling frequency of at least 100 KHz. Anyhow, the default sampling frequency is appropriate for the intended application.

The developed prototype sensor system also functions with 0 bias voltage applied to the sensor. This means that the sensor works in photovoltaic mode [7]. This mode is suitable for low light level and low frequency applications and it allows simplicity in system design and development. Response speed and linearity could be improved via the application of a reverse bias, however, dark and noise currents as well as response variations due to temperature are likely to increase. The tests performed have proved a good reliability of the system and its speed of operation is as required.

3.2.2. 128 PSD sensor array hardware system

Two other data acquisition prototype systems for controlling and acquiring the signals from the 128 linear array of position sensitive detectors were also developed. These two different 128 PSD sensor systems were called “XDAS 128 system” and “NIDAQ 128 system” respectively. Each of them is described in the following sections.

3.2.2.1. XDAS 128 system

This system was developed based on the experience of the 32 PSD sensor system described in section 3.2.1. The concept was extended further and thereby two more commercially available electronics modules, called “XDAS”, also provided by Sens-Tech Ltd [5] were combined together with a self constructed adaptor board for the 128 PSD sensor as a single 128 sensor prototype system. The new system build up (XDAS 128 system) was assembled integrating the 128 linear array of position sensitive detectors illustrated in figure 1.15 of chapter 1. Figure 3.6 shows a photograph of the XDAS 128 system and figure 3.7 illustrates a detailed view of the boards placed on the right position for detecting an object, where a lens is already accommodated in order to focus the image frame onto the active area of the sensor.

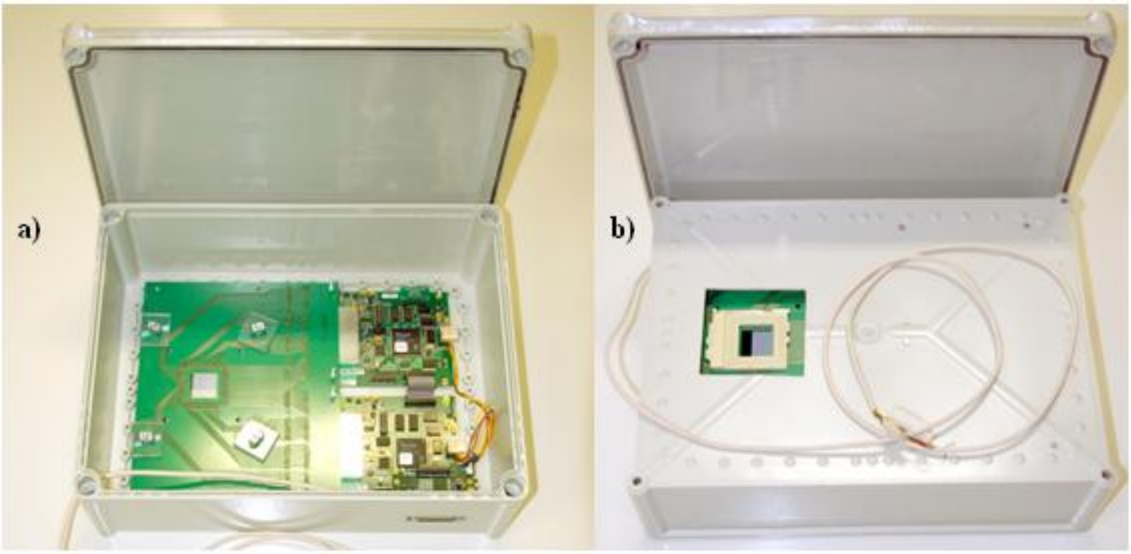

Figure 3.6 – a) View of the XDAS 128 sensor system. b) View of the 128 sensor socket exposed outside the box for light detection purposes.

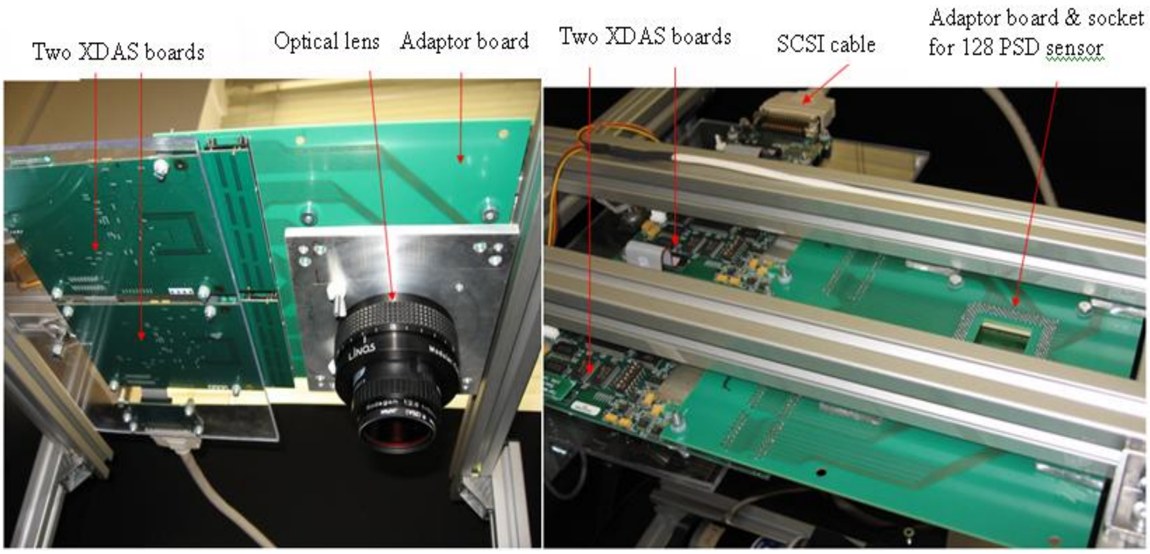

Figure 3.7 – XDAS System for 128 PSD data acquisition.

The prototype system is comprised of three printed circuit boards connected together. The two equal sized boards (XDAS boards) on the left side of figure 3.7 are exactly the same as the main electronics data acquisition board mounted inside the 32 PSD sensor system presented in figure 3.4 of section 3.2.1. The remaining printed circuit board (adaptor board, on the right side of figure 3.7) is comprised of 256 routed channels as well as a socket to accommodate the 128 PSD (position sensitive detector) based sensor. A lens (left side in figure 3.7) is being used to focus object profile images onto the 128 sensor.

The explanation given in section 3.2.1 for the operation of the main electronics data acquisition module (also XDAS) shown in figure 3.5 also applies to the two XDAS modules used in this 128 PSD XDAS system.

3.2.2.2. NIDAQ 128 system

This system was specially designed to work with the 128 PSD array of detectors. ORCAD, a software package for hardware design and routing was used to produce the PCB hardware designs. The latest version of the hardware board (PCB) is comprised of 5 LAYERS as shown in section B1 of APPENDIX B. The finished fabricated and assembled PCB is shown in figure 3.8.

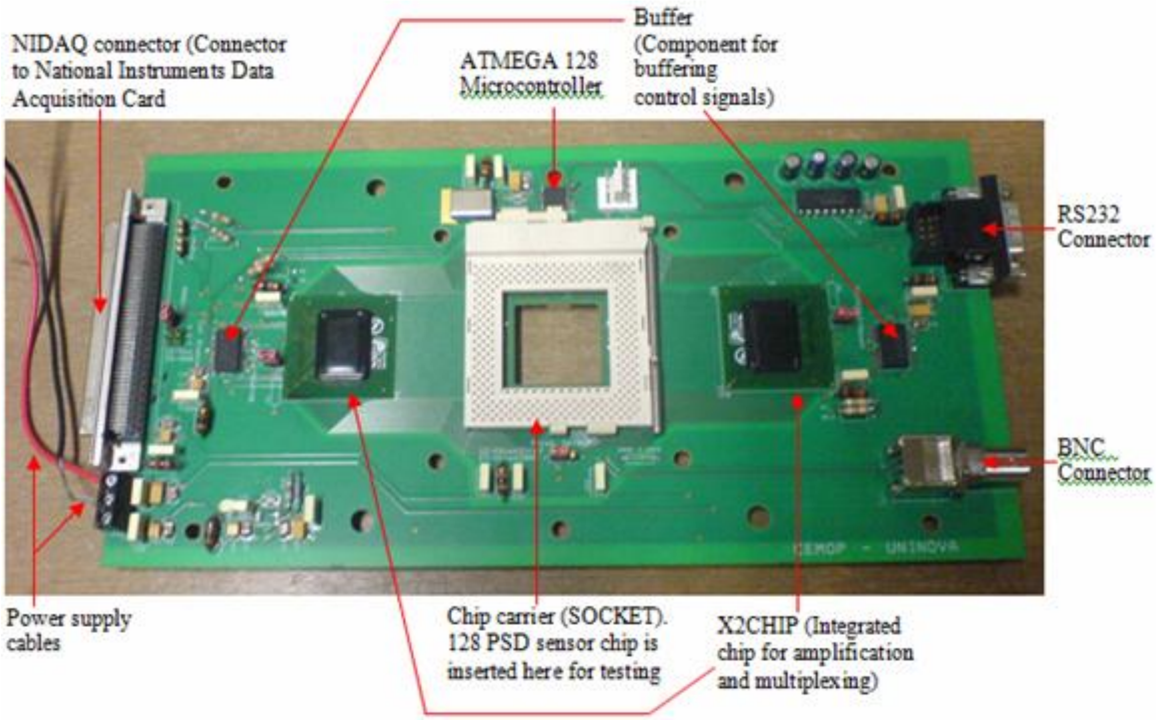

Figure 3.8 – NIDAQ 128 system. Circuit board ready for testing in conjunction with 128 PSD sensor.

An important element of the circuit is the X2CHIP, which performs the amplification and multiplexing of the signals coming from the sensor. Two of these chips are needed and as it is a ball grid array component, special equipment is needed in order to solder it onto the board.

However, a problem believed to be related to noise is affecting the main Application Specific Integrated Circuit (ASIC) or X2CHIP. The X2CHIP is a 128 channel amplifier and multiplexer circuit and it needs very low noise (1mV RMS on its VDD pin and 100μV RMS on its VREF pin) to operate properly.

The latest version of the printed circuit board shown in figure 3.8 uses a microcontroller to control the X2CHIP which means that effectively, the required digital waveform is being generated by the microcontroller and is being sent to the X2CHIP. The correct waveform notifies the X2CHIP to start acquiring data at each of its 128 channels, in this case coming from the 128 PSD array. This data is transferred from the X2CHIP to a NI6031E PCI National Instruments card which has an embedded 16-bit Analog to Digital (A/D) converter. Synchronization between these events is achieved due to the communication channel established between the microcontroller and the PC through the RS232 connector shown in figure 3.8. The buffer components are obviously there to achieve buffering or a required delay on the control signals. The chip carrier socket allows the 128 PSD sensor chip carrier to be inserted or removed whenever necessary. The BNC connector is connected to the sensor bias point and thereby allows any voltage bias to be applied through the sensor. The NIDAQ connector connects to the data acquisition NI6031E PCI National Instruments card inside the PC via a 100 pin cable. As already mentioned, a microcontroller (ATMEGA 128) generates the control waveform needed for the X2CHIP.

3.3. Software development for PSD sensor array systems

Software platforms and user interfaces were developed to acquire the data of the developed 32 and 128 PSD sensor array hardware systems. These allowed the calculation, representation and storage of the measurements coming from the sensors. Such software platforms were constructed so as to be used in 3D rendering or object movement detection applications and they adjust to different scanning speeds and other related parameters. The software acquires in real time the intensity signal coming from the 64 (32 PSD sensor) or the 256 (128 PSD sensor) contacts and computes the centroid position of the incident light (e.g. laser line) for each of the 32/128 sensor strips of the array. It also displays in real time a 3D virtual model of the 32/128 array sensor in which the channel intensities and calculated positions are simultaneously shown. This virtual model can also be rotated and translated in all dimensions (X, Y, Z), thereby viewed as wanted by using the keyboard.

A secondary part of the software is an OpenGL based 3D map in which the calculated sensor positions represent height information. Positions are displayed forming a 3D height map in real time. This virtual model can also be rotated and translated in all dimensions (X, Y, Z), thereby also viewed as wanted by using the keyboard.

The data acquisition is controlled by the software and the minimum time for data acquisition is currently set by using a timer. However, the timer and the minimum time for real time 3D profile construction and display are limited by the 10 μs minimum allowable time provided by the electronics module in combination with the speed of the computer processor and the graphics card being used. The software allows the acquired data to be saved to disk for later retrieval, treatment and interpretation. Detailed explanations and screenshots regarding the software developed as well as relevant testing results are shown in section B2 of APPENDIX B.

Prior to scanning any object a calibration procedure is performed as described in section B2 of APPENDIX B. An example of a 3D scanning procedure is shown in figure 3.9(a), where the 3D profile of a white plastic fork is represented. Figure 3.9(b) shows the white plastic fork itself.

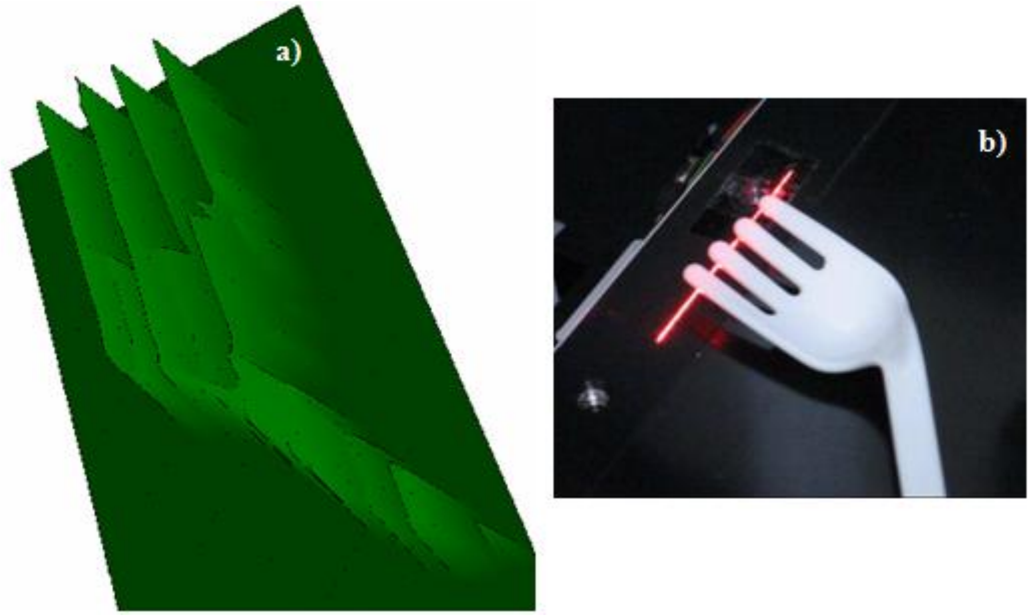

Figure 3.9 – (a) 3D representation of the white plastic fork on the 3D map. (b) Plastic white fork scanned using a RED laser line.

3.3.1. 128 PSD sensor array software platform

The underlying complete software platform architecture designed for the data acquisition prototype systems integrating the 128 linear array of position sensitive detectors is very similar to the one developed for the 32 PSD sensor array system described in section B2 of APPENDIX B. Anyhow, more detailed explanations and screenshots as well as relevant software testing results are shown in section B3 of APPENDIX B.

For testing purposes another existing commercial 3D rendering software platform based on DELPHI programming code was used. The chosen object in this case was a blank sheet of paper shaped to form a small bump and figure 3.10(a) shows its 3D representation. Figure 3.10(b) shows the real object itself.

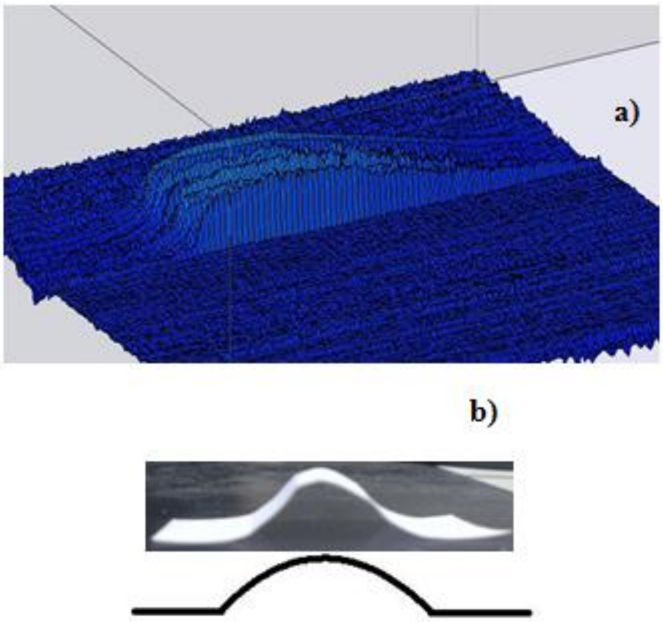

Figure 3.10 – (a) 3D object profile of the blank sheet of paper shaped to form a small bump. (b) Blank sheet of paper shaped to form a small bump.

3.4. Machine vision

The objects represented in figures 3.9(a) and 3.10(a) were obtained using the set-up sketched in figure 3.11.

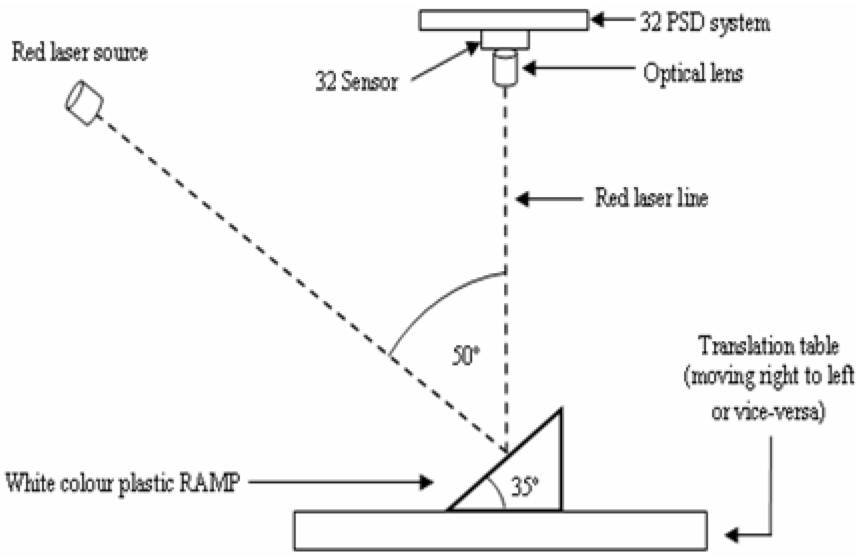

Figure 3.11 – Sketch of the generic experimental setup composed of a laser line source, an optical lens, a white plastic ramp, a translation table, and the system integrating a 32 PSD array sensor.

3.4.1. Dynamic experimental procedure

As sketched in figure 3.11, a laser light line incident on the object (placed on a controllable translation table) is reflected onto the 3D sensor using a lens with a reduction factor of about 5.3. The dynamic experimental procedure was the following: the translation table was moved from right to left and vice-versa so that the object, white colour plastic ramp in this case, was scanned by the system. As the translation table moved with the object, the ramp object structure caused the laser line (632nm, 30mW) to be projected (after lens reduction) from the right side to the left side of the sensor (and also vice-versa, when performed from left to right). In this case the distance traveled from right to left (or vice versa) on the translation table was about 37mm. This corresponded to a measured distance on the sensor of about 7mm, which matches the width of the active area and the position detection range of the sensor. The range of positions on the sensor is 7mm wide and expands from -3.5mm to +3.5mm. The light intensity range varied from 1.79µW/cm² on the right side of the sensor to about 0.447µW/cm² on the left side of the sensor.

This setup enabled us to analyse the dynamic behaviour of the system/sensor combination in terms of linearity and other parameters of the system such as for example the limit of saturation and the integration time or dynamic range. The ramp object structure allowed us to sweep the reflected laser line from the right to the left of the sensor covering the whole width of the sensor active area. The linearity of the sensor was thereby evaluated. A measurement was recorded every time the translation table moved 339µm.

The integration time of the system controls the current amplification acquired for every channel and the default value of this parameter was 1ms. An experimental study of the influence of the integration time on the sensor response was also performed by lowering the default integration time from 1ms to 0.8ms, 0.7ms, 0.6ms and 0.5ms respectively. These trials were repeated using sub-sampling or sample averaging in order to improve signal response flickering or instability. Sub-sampling is the calculation of the average of a predefined number of acquired samples and although it is applied to reduce signal noise, unfortunately it slows the rate of acquisition.

3.4.2. Static experimental procedure

In this experimental procedure the object (white colour plastic ramp) was placed on top of the translation table and in this case there was no movement at all. A laser line (632nm, 30mW) was shined in triangulation mode as already shown in figure 3.11, but however this time instead of being projected on the middle point of the ramp (see figure 3.11), the line was projected on the right hand side of the white plastic ramp, which is the highest point or top of the ramp.

Therefore, the top of the ramp object caused the reflected laser line to be projected (after lens reduction) on the right hand side of the sensor. The recorded light intensity (right side of ramp) was 2.20µW/cm².

As previously stated, the integration time of the system controls the charge amplification acquired for every channel and the default value of this parameter was 1ms, however, the system also allows lower values to be set. This is specially required when the sensor signal saturates. A set of experiments were performed to see how the intensity (in arbitrary units) of the 32 (right side) sensor contacts (see figure 3.3) varied, as the integration time (or system amplification) was reduced from 1ms to 0.1ms. Similarly, a test was performed to investigate how light intensity influences the signal intensity. This was done by using optical filters as indicated in table 3.1.

Table 3.1 – Correspondence of filters with light intensity.

Filter transmission (%)	Laser power intensity ($\mu W/cm^2$)
100.0	2.20
91.4	2.01
79.4	1.75
50.0	1.10
31.7	0.70
10.0	0.22
1.0	0.022
0.1	0.0022

These measurements were repeated as the integration time (signal amplification) was reduced from 1ms to 0.5ms in steps of 0.1ms.

As shown in figure 3.3 and as already stated, the 32 PSD sensor array has 32 detector strips each with a metal contact at each side of the strip. Out of these 64 individual sensor contacts, the 32 contacts on the right hand side were analyzed because the laser line is actually projected on that side of the sensor. This applies for all of these static experiments. Another aspect to consider here is the fact that only signal intensities were recorded and no sensor positions were calculated for this analysis. Thereby, these tests were performed using the sensor as a photodetector and not as a position detector, since the analyzed values were those measured at the contacts nearest to the illuminated region of the sensor.

3.4.3. 3D object profiling experimental procedure

The 3D object profiling experimental procedure was the same as the one described in section 3.4.1 for the dynamic experimental procedure (see figure 3.11). However, in these tests, no white colour plastic ramp was present and instead, a white rubber or plastic fork were used as the scanning objects.

3.5. Detection of micro objects

The 3D PSD, consisting of 32 1D detectors forming an array sensor was applied in micro positioning or micro movement detection applications. A few micro objects, in particular a micro cantilever and a micro gripper supplied by NASCATEC GmbH, were used. The positions of the micro cantilever and the micro gripper were tracked while they moved in the X and Y directions and the opening and closing of the micro gripper was also detected and recorded. Concerning the use of this sensor towards the detection of very small objects, based on reflecting light, no work has been reported before.

3.5.1. Sensor/System micropositioning experimental procedure

The use of the 32 PSD sensor array together with a microscope is a relevant system for detecting micro object movement and dimensions even at high speeds. A photograph of the experimental set-up used is shown in figure 3.12. Preliminary tests were performed in order to evaluate the feasibility of the procedure. For that, the procedure used for the measurements was the following: the sensor was fixed on the top of the focusing lenses and the object was placed on the X–Y moving table and was then focused by using the microscope 10x embedded magnification lens. The photovoltage of the 32 1D sensors was initially measured at background reflected light level (without the object appearing within the image scope). Subsequently, measurements were recorded when the cantilever was appearing on the ocular of the microscope and when it was moving in X and Y direction, respectively, in controlled steps. Figure 3.12 shows photographs of the experimental set-up and the sensor holder. A common microscope (Leitz Laborlux 12 ME ST) working in the reflective mode was used.

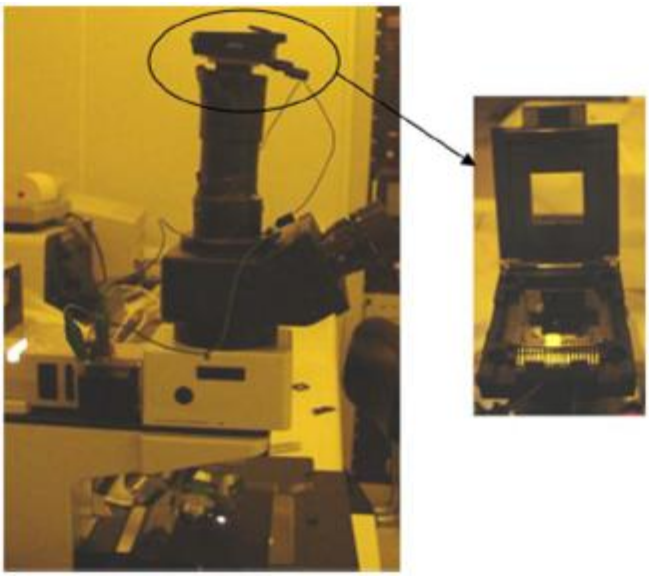

Figure 3.12 – Photograph of the microscope system used with the sensor holder in detail.

A 30µm wide by 400µm long micro cantilever from NASCATEC was detected on a microscope by the 32 lines array of 1D amorphous silicon position sensitive detectors (PSD). The sensor was placed in the ocular used for the CCD camera of a microscope and the alignment, focusing and positioning of the cantilever was achieved using the X–Y–Z translation table of the microscope that has a micrometer resolution controller. The light reflected by the micro cantilever was detected by the 1D/3D PSD and converted to an analog signal proportional to the movement concerning the micro positioning of the cantilever and its holding structure. The signal coming from the 32 PSD sensor array was analyzed directly using a multimeter, thereby not employing any electronic readout system or data algorithm.

Figure 3.13(a) shows a sketch of the 32 linear array of 1D detectors with appropriate line numbering on which the image of the micro cantilever is represented at its corresponding starting movement position. Figure 3.13(b) shows a photograph of the 32 PSD sensor array. The detector, formed by an array of 32 sensors each with 270 µm width and 1.4 cm length, was placed on the top of the vertical objective of the microscope where the digital camera is usually connected. This way the light arriving onto the sensor was the reflected light from the micro object traveling through the microscope which was then focused onto the 3D sensor active area. The active area of the sensor is 0.7 cm x 1.7 cm but, after focusing, the illuminated area of the sensor was around 1 cm in diameter. Thus, all measurements are related to that area. The intensity of the light (lamp of the microscope) focused on the sensor varied from the background light (using a black surface) of 9µW/cm^2 to the maximum light reflect by the object of 700 µW/cm^2. The object consists of a cantilever and its holding structure as shown in the photograph of figure 3.13(c).

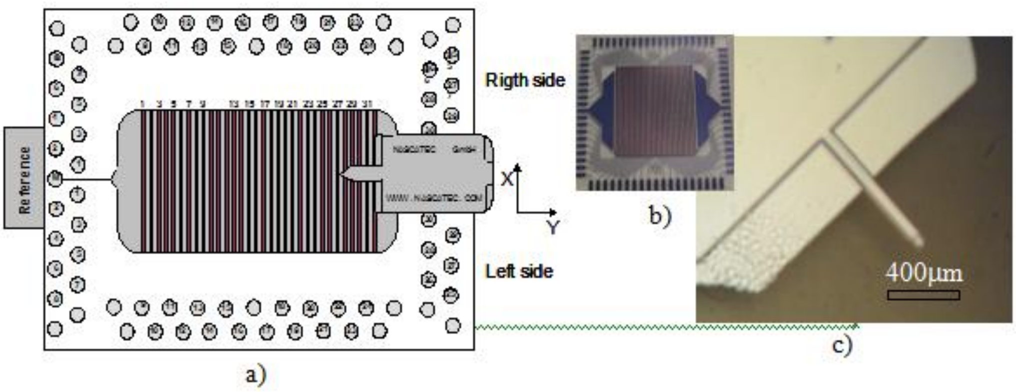

Figure 3.13 – (a) Sketch of the 32 linear array of 1D detectors including the image of the cantilever and its corresponding starting movement position. (b) Photograph of the PSD. (c) Photographs of the object (cantilever and its holding structure supplied by NASCATEC GmbH.

The dimensions of the micro cantilever are 400µm in length by 30µm in width, and the sensor should be able to detect the position not only of the structure but also of the cantilever (see figure 3.13(c)).

After testing the procedure, the constructed portable data acquisition prototype system integrating a linear array of 32 1D amorphous silicon position sensitive detectors (PSD) was mounted on the ocular of the microscope, normally used for the CCD camera, as shown in figure 3.14.

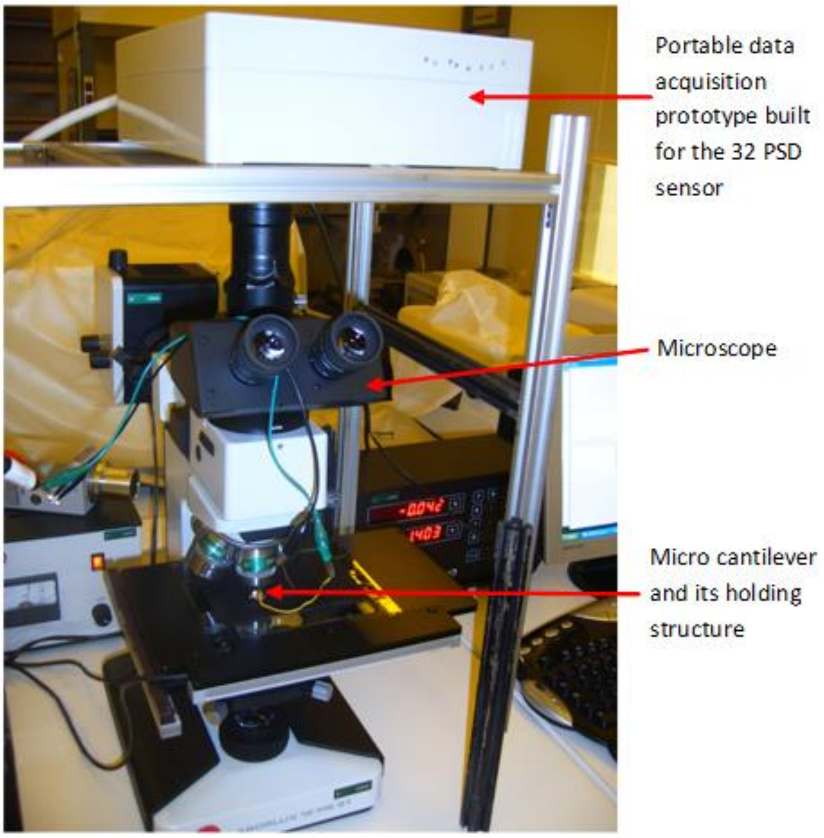

Figure 3.14 – Photograph of the experimental setup including the built data acquisition prototype, the microscope and the micro cantilever or microgripper together with its holding structure.

The measurements were performed as referred previously, however in this case, instead of photovoltages, photocurrents were measured from the 32 PSD detectors. All values were also recorded within an area of approximately 0.5cm² and the photocurrent was initially measured at background reflected light level (without the object appearing within the image scope), giving an offset noise signal level response. Again, all readings were obtained when the microcantilever or microgripper was appearing on the ocular of the microscope while moving in two dimensions (X or Y), however, this time the movement occurred in controlled 5µm steps.

Figure 3.15 shows a sketch of the image of a microgripper and its holding structure being reflected on the sensor. The field of view of the microscope objective is also indicated as a red circle, thereby only the part of the micro object located inside that circle is the one being detected. The microscope light path, the microgripper with its holding structure and the translation table are illustrated too. Of course the image of the micro object is always enlarged by microscope optics since the real micro object lying on top of the support can hardly be seen with the naked eye. The translation table moves automatically in controlled 5µm steps and so does the micro object.

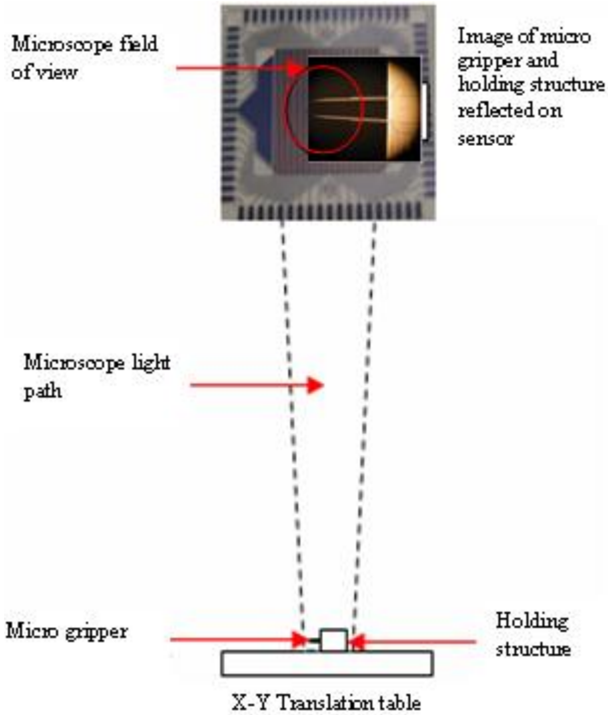

Figure 3.15 – Sketch of the light path, sensor, microgripper and reflected image setup

The whole set of results were taken with and without using a focusing lens placed before the sensor on the microscope.

The micro cantilever was also immersed inside a liquid and for this particular experiment a focusing lens was always present and the liquid used was propanol. Nowadays, there are many scenarios in which micro objects are residing inside a liquid. Due to this, it was interesting and useful to check if a movement signal was being detected when the medium was changed from air to liquid (propanol). The refractive index changes from air to liquid and so it was expected that the signal might not be detected as well as when the medium was air.

3.6. Sensor spectral response experimental procedure

In order to measure the spectral response of the 32 sensor (shown in figure 3.3), a 1D PSD or detector strip from the sensor was placed and fixed on top of a support holder. Two cables were connected from a Keithley measurement unit to two metal pins, one being in contact with the GND of the sensor and the other being in contact with one of the contacts of one position sensitive detector.

A monochromatic light (one specific wavelength at a time, range 400-800nm) was incident on the detector and the diameter of the circle of illumination was measured as 3mm.

The spectral response in the 400-800nm wavelength range was obtained from equation 3.1 considering the sensor area 0.009 cm²:

$$S(\lambda) = \frac{J}{\phi(\lambda)} \qquad \textbf{[3.1]}$$

where, $S(\lambda)$ is the Spectral response (A/W) for a particular wavelength, λ; J is the Photocurrent density (A/cm²); and $\phi(\lambda)$ is the Photonic irradiance (W/cm²).

3.7. References

[1] E. Fortunato, G. Lavareda, M. Vieira and R. Martins, "Thin film position sensitive detector based on amorphous silicon p-i-n diode", Rev. Sci. Instrum. 65, 3784-3786, 1994.

[2] R. Martins and E. Fortunato, "Lateral photoeffect in large area one-dimensional thin-film position-sensitive detectors based in a-Si:H P-I-N devices". Rev. Sci. Instrum. 66, 2927-2934, 1995.

[3] E. Fortunato, F. Soares, P. Teodoro, N. Guimarães, M. Mendes, H. Águas, V. Silva and R. Martins, "Characterisitcs of a linear array of a-Si:H thin film position sensitive detectors", Thin Solid Films, 337, 222, 1999.

[4] W. Kern, "Handbook of Semiconductor Wafer Cleaning Technology – Science Technology and Application", Noyes Publications, USA 2000.

[5] Product Catalogue. Langley, Berkshire, U.K., Sens-Tech Ltd. www.sens-tech.com (accessed 27-06-2013).

[6] R. Martins, L. Raniero, L. Pereira, H. Águas, S. Pereira, L. Silva, A. Gonçalves, I. Ferreira, and E. Fortunato, "Nanostructured silicon and its application to solar cells, position sensors and thin film transistors," Phil. Mag., 89, 2699–2721, 2009.

[7] E. Fortunato, L. Pereira, H. Aguas, I. Ferreira, R. Martins, "Flexible a-Si:H position sensitive detectors", Proc. IEEE, 93, 1281-1286, 2005.

Chapter 4

Results and discussions

Chapter 4. Results and discussions

Summary

The following chapter describes overall results gathered during this thesis work. That is, relevant results obtained for the majority of machine vision experiments carried out are presented as well as the most significant results regarding micropositioning and movement detection tests. The chapter starts by showing the dynamic and static responses of the developed sensor systems and subsequently moves on to describe results for various application scenarios including 3D scanning, color sensing and microobject movement detection trials.

4.1. Dynamic response

The sensors were tested to determine their linearity. The results obtained for the position linearity of two of the channels or detector strips of the 32 array PSD sensor (figure 3.3, chapter 3), are shown in figure 4.1.

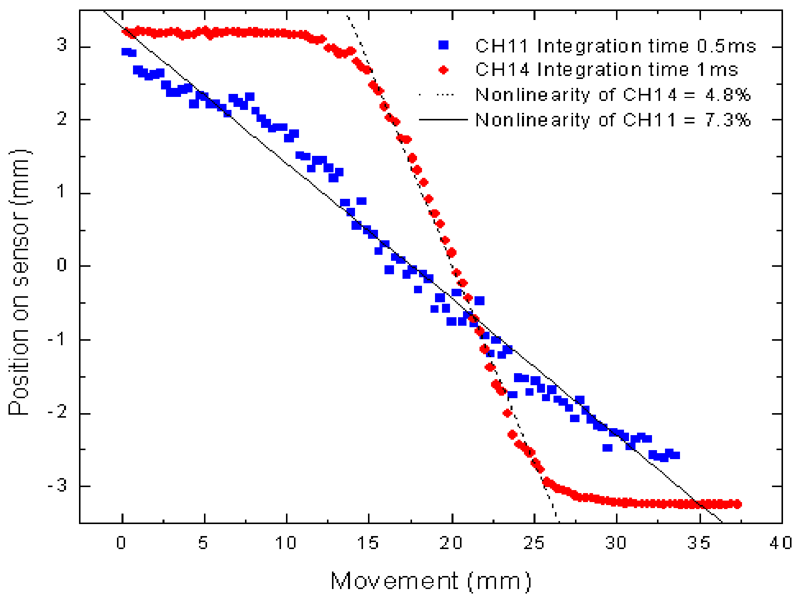

Figure 4.1 – Dynamic response and linearity of sensor channel 14 and 11 at integration times of 1ms and 0.5 respectively. Distance scanned vs. position on the sensor.

The non-linearity of sensor channel 14 at a default value of 1ms integration time is 4.8%. The majority of the channels tested (not shown here for clarity) show a similar response in terms of linearity at this or similar integration times. At an integration time of 1ms, linearity is obtained for about 10 mm of table movement, which does not correspond to the total object dimension (37 mm). A range of integration times (1ms, 0.8ms, 0.7ms, 0.6ms and 0.5ms) was experimented and the position detection behaviour of the sensor channels at each of those times was analysed. When using integration times of 1ms and 0.8ms it seems that the acquired signal intensities (deriving calculated position data) are saturated near both edges of the sensor strip (see figure 1.10, chapter 1 and figure 3.3, chapter 3). Therefore, the sensor position range of +3.5mm to -3.5mm or useful active area width is reduced to the region where linearity exists. This concludes that saturation reduces the active position detecting area of the sensor. Of course, this effect depends on the sensor intensities recorded and so in our case, it will vary from detector to detector and to a lesser extent, even from sensor strip to sensor strip, if they do not have similar characteristics.

This effect is not shown for sensor channel 11 in figure.4.1, at an integration time of 0.5ms. When setting integration times down to 0.7ms, 0.6ms and 0.5ms, the saturation effect at the ends of the detector strip reduces gradually and substantially as illustrated by the response of channel 11 where the saturation effect is not observed.

It is interesting to see that at low signal levels a reasonable non-linearity (7.3%) is still obtained.

The non-linearity of every channel is worked out using the relationship below [1]:

$$\sigma_e = \frac{2S_m}{F} \qquad \textbf{[4.1]}$$

where, σ_e is the linearity error or error in the position detection; S_m is the standard deviation; and F is the total scale of the measurement.

In order to clearly identify the influence of the integration time on the dynamic response, a good approach is to combine the response of a single channel for several integration times. The integration time controls the amplification of the signal acquired for every channel. The response of channel 13 is illustrated in figure 4.2. The results reveal that when using integration times of 1ms, 0.8ms and 0.7ms, the acquired signal intensities (deriving calculated position data) saturate near the ends of the sensor. Therefore the sensor position range of 3.5mm to -3.5mm or useful active area width is reduced to the region where linearity exists.

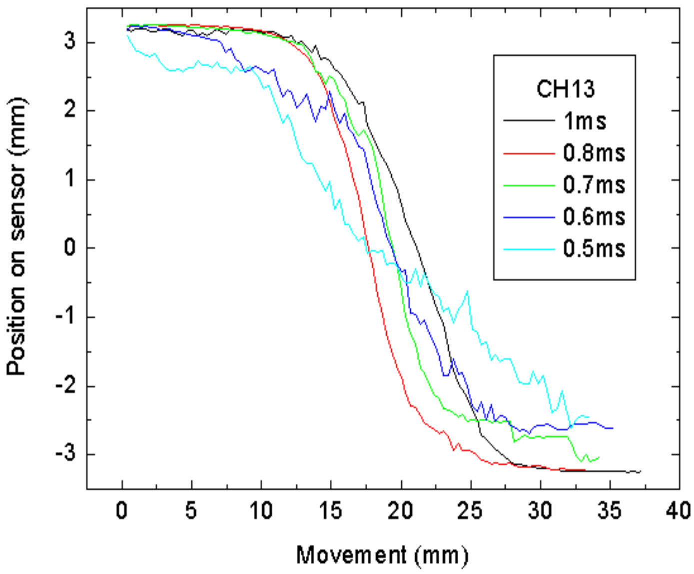

Figure 4.2 – Dynamic response at integration times of 1ms, 0.8ms, 0,7ms, 0.6ms and 0.5ms respectively. Distance scanned versus position on the sensor.

The signal ripple due to instability or sensor noise is less at integration times of 1ms, 0.8ms and 0.7ms in comparison to integration times 0.5ms and 0.6ms. The saturation effect at the ends of the sensor reduces gradually and substantially as the integration time changes from 1ms to 0.5ms.

Repeated measurements were performed using system sub-sampling (multiple sample averaging) to determine its influence on the signal response flickering or instability. So, the average of a predefined number of acquired samples was performed and figure 4.3 shows the 0.6ms integration time response for channel 26 together with the same response acquired under sub-sampling conditions, in this case being 128 subsamples.

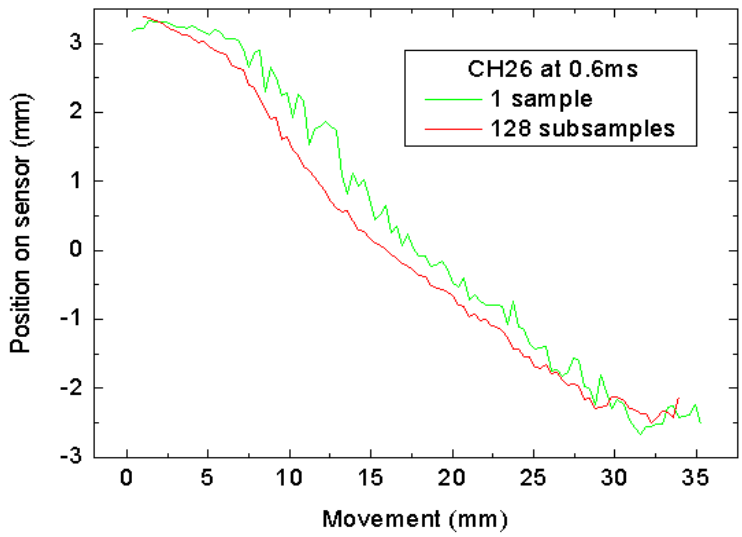

Figure 4.3 – Dynamic response and linearity of sensor channel 26
at an integration time of 0.6ms together with the same response acquired
under sub-sampling conditions. Distance scanned versus position on the sensor.

The results obtained verify that using averaging or sub-sampling greatly improves the overall signal response. This excellent improvement on signal quality is confirmed by looking at the difference between the signal responses shown in figure 4.3. This behaviour was further verified for all studied cases.

Overall, the studies performed in this section conclude that less active area of the sensor is available when saturated signal intensities are present on each side of the sensor.

Moreover, these studies also confirm that signal response flickering or instability can be improved by averaging a significant number of acquired sub-samples.

4.2. Static response

The variation of the signal intensity (in arbitrary units) of the sensor (contacts 4 and 6) in relation to the integration time is shown in figure 4.4. The intensity signal of the sensor decreases as the integration time (or system amplification) is reduced from 1ms to 0.1ms.

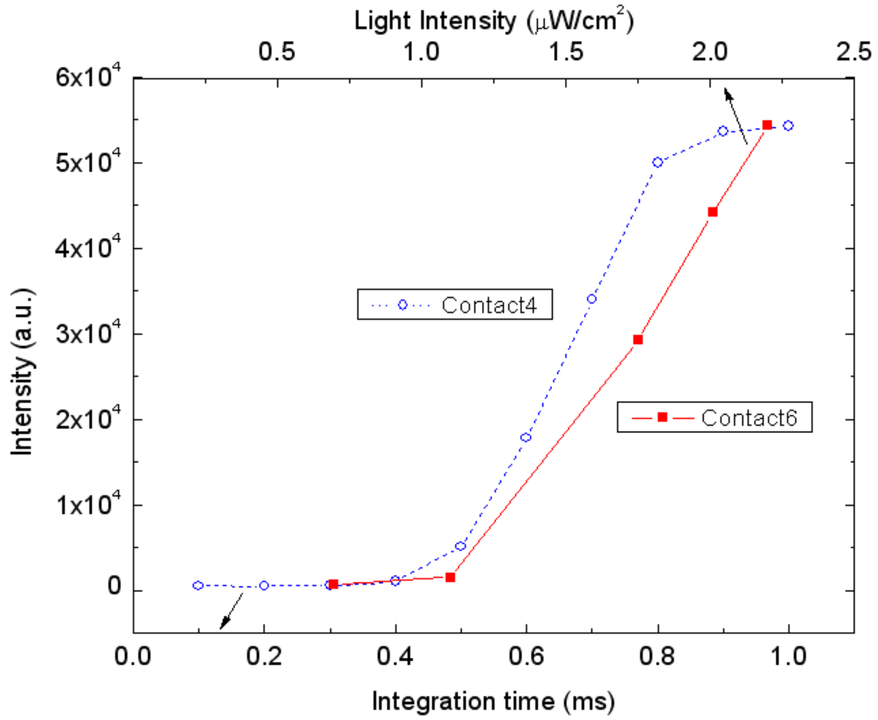

Figure 4.4 – Static responses of sensor contacts 4 and 6. Intensity (in arbitrary units) of the sensor as a function of the integration time (or system amplification), and corresponding light intensity.

From the results shown in figure 4.4, related to sensor contact 4, it can be concluded that the linear region lies at integration times of 0.7ms, 0.6ms and 0.5ms. For the case of sensor contact 6 the signal intensity varied as the light intensity impinging on the right hand side of the sensor was reduced gradually from 100% of its value to 0.1% by using 7 optical neutral density filters as already explained in section 3.4.2, table 3.1. However, no measurable values could be obtained when using filters with 10, 1.0 or 0.1% transmission since the light intensity is too low and it is equivalent to the noise signal of the sensor. A linear behavior is observed whenever the saturation effects described in section 4.1 are not affecting the response.

The variation of the signal intensity in accordance to the light intensity and integration time is shown in figure 4.5. As expected, a different response is obtained for each value of integration time tested being 0.4ms, 0.5ms, 0.6ms, 0.7ms, 0.8ms and 1ms.

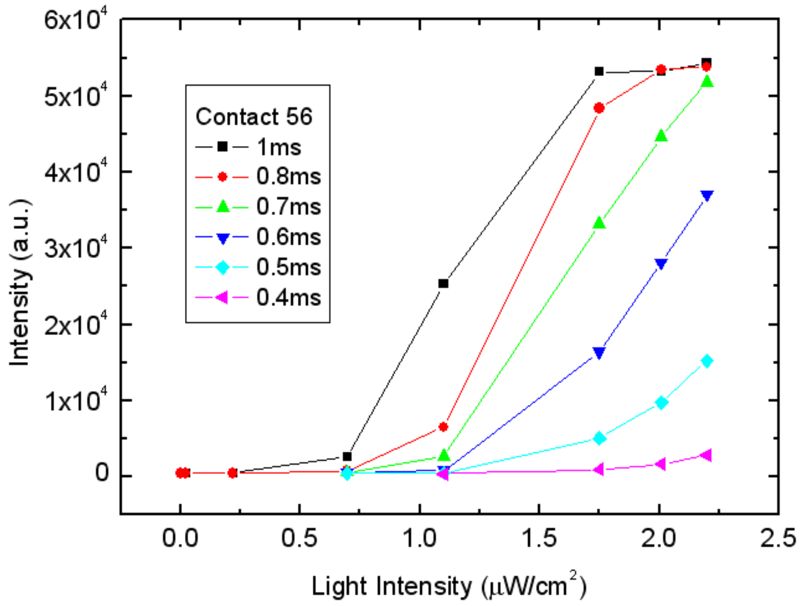

Figure 4.5 – Static responses of sensor contact 56. Signal intensity
(in arbitrary units) as a function of light intensity and integration time.

The results show that for instance, when setting integration times of 1ms and 0.8ms, the linear region is found between 0.7μW/cm² (about 32% light transmission) and 1.75μW/cm² (about 79% light transmission). This allows light intensities within that range to be registered without saturation. Performing measurements at lower integration times of 0.7ms and 0.6ms allows recording signal intensities (without saturation) between 1.1μW/cm² (about 50% light transmission) and 2.24μW/Cm² (about 100% light transmission). At lower integration times such as 0.5ms and 0.4ms, light intensities higher than 2.24μW/Cm² (about 100% light transmission) are easily detected. This correlation between light intensity and integration time is clearly visible in figure 4.6 for different sensor contacts being 6, 18, 30, 54 and 56.

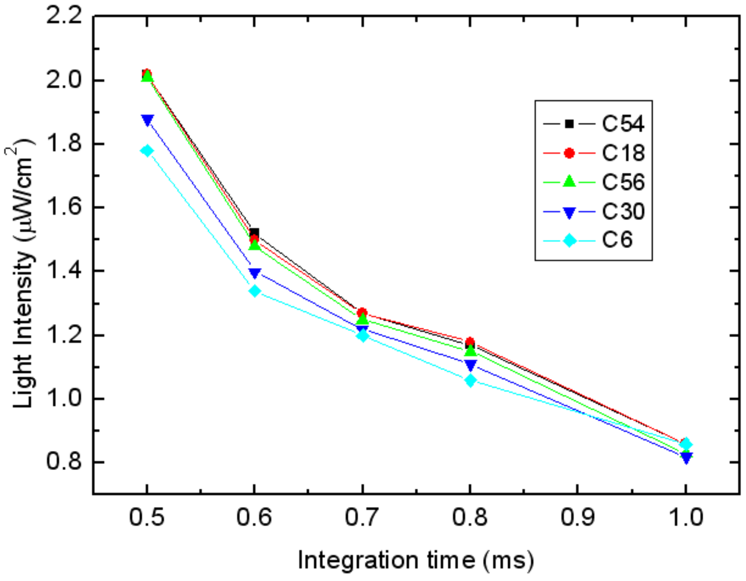

Figure 4.6 – Relationship between filtered light intensity and system integration time for sensor contacts 6, 18, 30, 54 and 56.

All sensors show a similar linear behavior. For example for the case of contact 6 (C6), and assuming that the measurement at an integration time of 0.5ms falls out from the linear pattern and is not taken into account, the equation of the line is given by:

$$y = -1.194x + 2.041 \qquad \textbf{[4.2]}$$

Where, the linearity of the curve is 99.6%.

From these results we conclude that the adjustment of the integration time is possible according to the level of intensity coming from the object so as to optimize the sensor signal. This is very important since it does not limit the system to the detection of high reflective surfaces. Thus, the system offers a wide dynamic range allowing it to adjust to the maximum intensity levels of each sensor. In turn, this also means that a wide range of laser light source power levels is accepted by the system (even low ones). A sensor non-linearity of approximately 4 to 7% has been achieved.

In order to obtain better 3D profile image quality an improvement on sensor channel position response is desirable. Overall, the results obtained show the possibility of using a linear array of 32 1D line sensors based on the amorphous silicon technology to render 3D profiles of objects. The system and setup presented allows 3D rendering at high speeds and at high frame rates.

4.3. Simple object detection

In order to understand the effect of an object's feature on the response obtained and to what extent it could be clearly noticed and detected we have introduced a small bump on the ramp object. The small white plastic bump used is illustrated inside figure 4.7 and its dimensions are the following: the longer side measures about 3.85mm and the middle top measures about 2.29mm; the shorter side measures about 2.32mm; and the height of the bump is 2.93mm. The width of the whole structure is 7.96mm and the angle of the longer side ramp is about 35º.

Figure 4.7 shows the response obtained for channel 22 after scanning the ramp with the white bump glued on it. As in all experiments, subsampling or an average of 128 samples was acquired for each measurement.

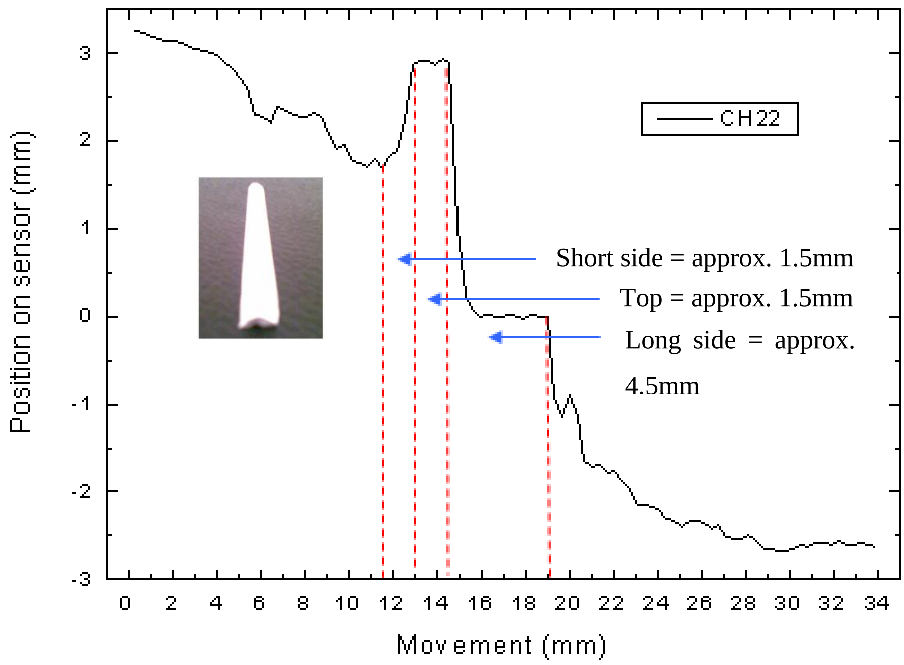

Figure 4.7 – Dynamic response of channel 22 at an integration time of 0.6ms and 128 subsampling for a small bump glued on the ramp. The photograph of the bump is displayed inside the figure.

The bump is detected and clearly noticeable in figure 4.7. The shape of the detection is similar to a step response for a 0.6ms integration time setting. Figure 4.7 also shows the approximate dimensions detected for the bump. There is no laser line projected in the region of the longer side of the small bump because it is occluded, not reflecting the laser light and thereby there is no detection in that region.

The small white bump from figure 4.7 was also cut into four parts and these were glued back again onto the ramp creating 3 different gaps in between. The experiments in this section were repeated together with an analysis of the influence of the speed of the translation table on these scanning responses. The widths of the gaps are shown in figure 4.8.

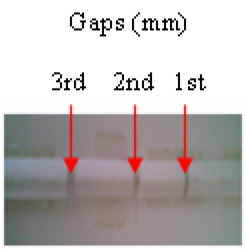

Figure 4.8 – Photograph of the small white plastic bump cut into 4 parts. These parts were separated by the gaps shown.

The translation table speeds experimented were: 1, 2, 5, 10, 15, 20, 25, 30 revs/sec which correspond to 0.32, 0.64, 1.6, 3.2, 4.8, 6.4, 8, 9.6 mm/sec respectively.

The experiments started with the lowest speed being 0.32 mm/sec and finished with the highest speed being 9.6mm/sec. For clarity, only results regarding the slowest and fastest speeds are shown. Figure 4.9 shows the scan response of 3 channels for a 0.6ms integration time at a speed of 0.32mm/sec and figure 4.10 shows the scan response of 5 channels for an integration time of 0.6ms at a speed of 9.6mm/sec.

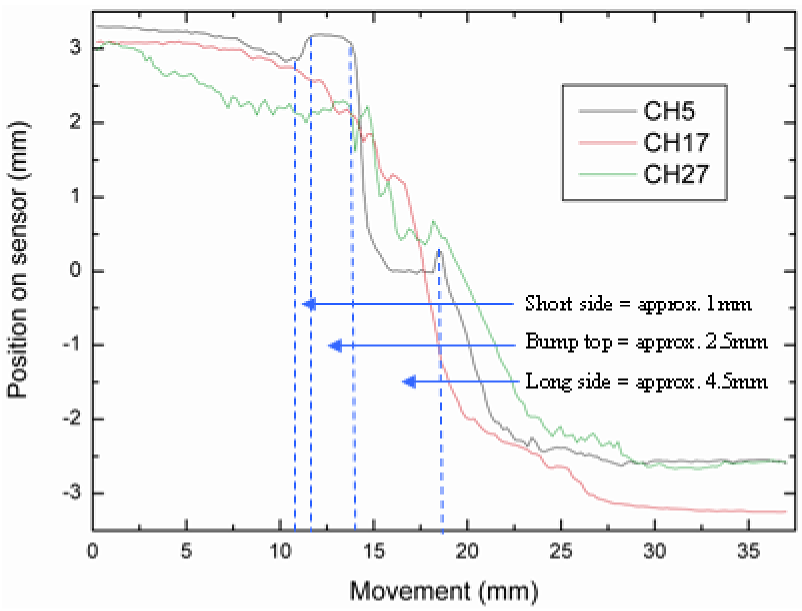

Figure 4.9 – Dynamic response of 3 channels at 0.32mm/sec, 0.6ms integration time for a small bump cut in 4 parts and glued on the ramp.

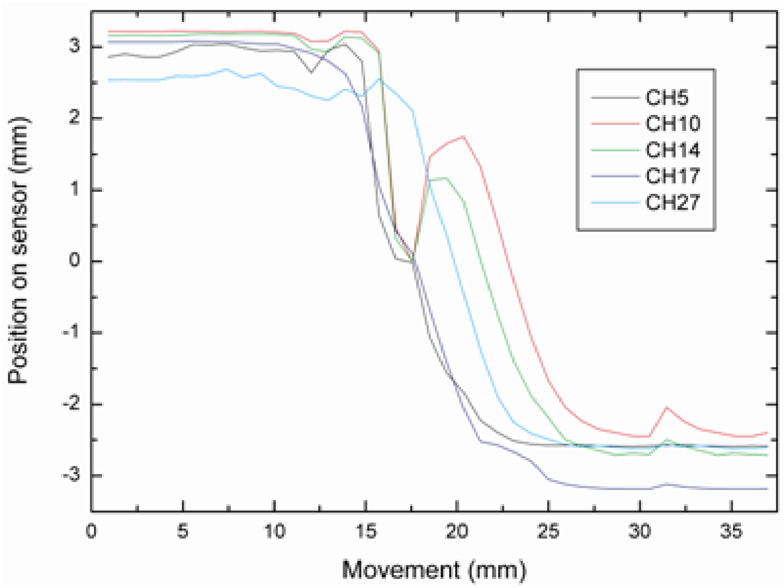

Figure 4.10 – Dynamic response of 5 channels at 9.6mm/sec, 0.6ms integration time for a small bump cut in 4 parts and glued on the ramp.

The bump is detected in figure 4.9 by channel 5 and in figure 4.10 by channels 5, 10 and 14. The detection responses coming from channels 17 and 27 are an exception because they are not detecting any bump and this is because they are detecting the gaps (in between) present in the bump and so effectively each of these is the same or similar response to a ramp without any bump, as shown for example in figure 4.3. Figure 4.9 also shows the approximate dimensions detected for the bump in this case. A comparison between the detected (figure 4.9 at 0.32mm/sec) and the real dimensions of the white plastic bump is listed below in table 4.1.

Table 4.1 – Comparison of detected (0.32mm/sec) versus real dimensions of white plastic bump

	Detected dimensions (mm)	Real dimensions (mm)	Error (mm)
Short side	1	2.32	1.32
Middle top of bump	2.5	2.29	0.21
Long side	4.5	3.89	0.61
Width of bump	8	7.96	0.04

As previously stated, channels 17 and 27 indicate the presence of gaps since their overall response is just a like the ramp on its own, without any bumps (see figure 4.3).

The speed of the translation table does not seem to influence to a large extent the obtained results. All speeds and responses analyzed do not differ very much between them. However, at higher speeds such as 8 or 9.6 mm/sec the detected responses show a rounded shaped bump as opposed to a step shaped bump and this is because the scanned 3D profile is acquired with a significantly lower number of points in total at these speeds and therefore the profile has a lower image resolution and is reconstructed also with lower definition (lower number of 3D points). At the highest speed (9.6 mm/sec) the number of scanned points was only 40 for the whole scan, as opposed to the 169 points scanned for the lowest speed (0.32mm/sec) response. The sensor therefore is able to respond and detect all these features at different speeds.

4.4. Sensor degradation

The degradation of the 32 PSD sensor was performed by illuminating continuously the sensor and measuring the intensity response over time. In these tests, a few detectors from two different 32 PSD sensors were analyzed.

The responses of various channels from sensor 2-11 are analyzed. Each of the experiments was running for 1 week or about 168 hours non-stop.

Similar to the generic experimental setup illustrated in figure 3.11, a red laser line was projected on a white colour plastic rubber object and this laser line was then reflected on one side of the sensor array. The light intensity recorded on the sensor was approx. 3.17μW/cm². Figure 4.11 shows a sketch of the experimental setup used.

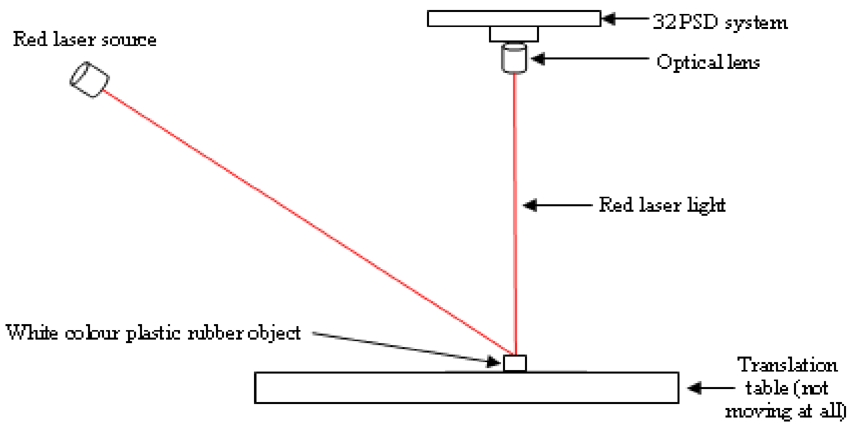

Figure 4.11 – Experimental setup for studying the degradation of the 32 PSD sensor

Figure 4.12 shows the variation of the intensity signal for each sensor channel over time (170 hours), while being exposed to light.

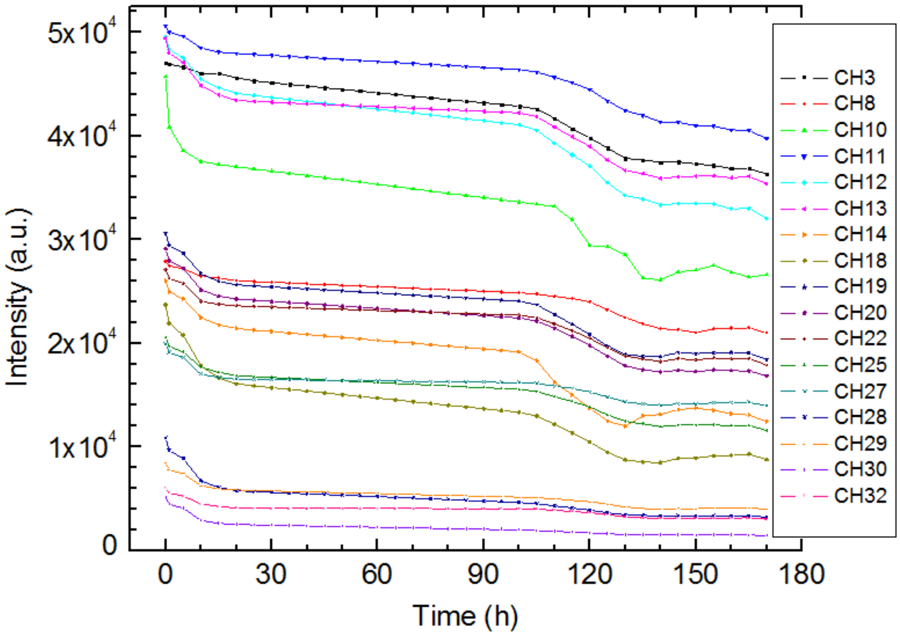

Figure 4.12 – Variation of the sensor channel signal intensity over time (170 hours), while being exposed to light.

Figure 4.12 shows that all sensors, independent of having lower or higher initial intensity signals, have a strong degradation in the first 10 hours. After that, the degradation tends to stabilize, and in the next 80-100 hours just a small and gradual reduction is observed. After this period most of the sensors again have a strong degradation. We may correlate such behavior with the initial SW effect for the first 10 hours and for after 100 hours with the oxidation of silicon or sensor contacts.

In order to understand if the degradation is related to the SW effect or to the oxidation of the sensor/contacts over time, a sensor covered with SiO_2 was tested. However, the results were inconclusive since the degradation of some channels improved while others were even worse than without SiO_2. The degradation of every channel was between 20% and 71% without SiO_2. Figure 4.13 shows the number of channels degrading for each percentage region and for each of the sensors used without (2-11) and with SiO_2 (3-11).

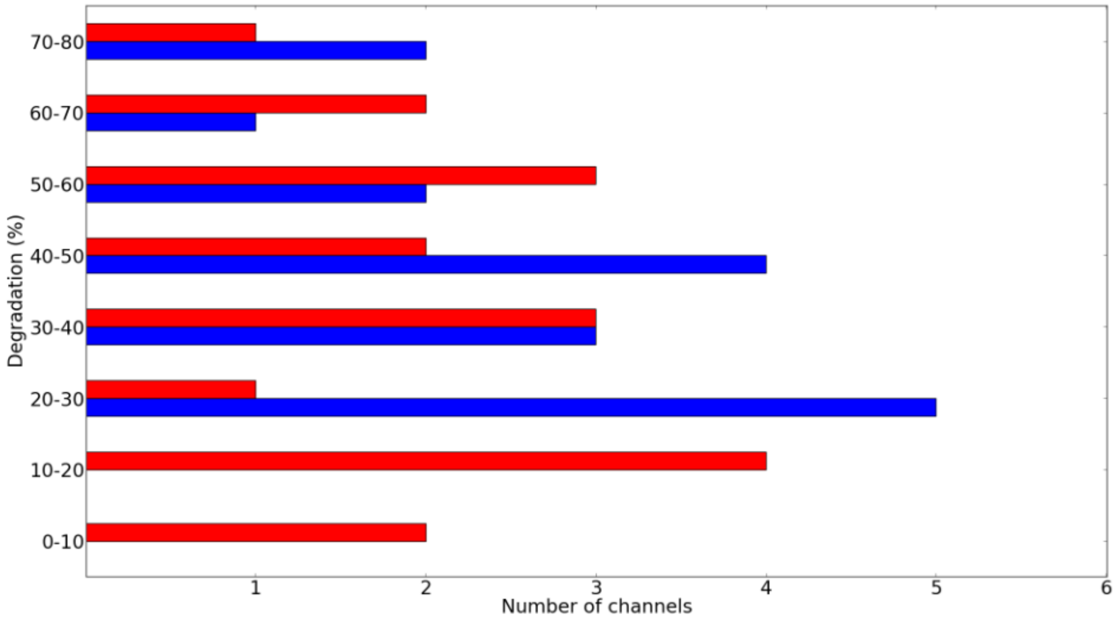

Figure 4.13 – Comparison of the degradation percentage range
for sensors without SiO_2, 2-11 (blue), and with SiO_2, 3-11 (red).

Overall, the degradation experiments demonstrate a strong degradation of the sensors over time, nevertheless, they also show quite different levels of degradation amongst them. Typical degradation caused by the SW effect on amorphous silicon is in the range of about 20%. Thus, higher degradations of about 30% or more may be related to other experimental factors such as metal contact deterioration due to a frequent repetitive physical contact of the measurement tips, among others.

4.5. Dynamic response to different colour illumination

The 32 array PSD sensors were optimized to detect red light as shown in the spectral response of figure 4.14. There, the measured spectral response of a single amorphous silicon PSD element from the 32 PSD sensor array is illustrated.

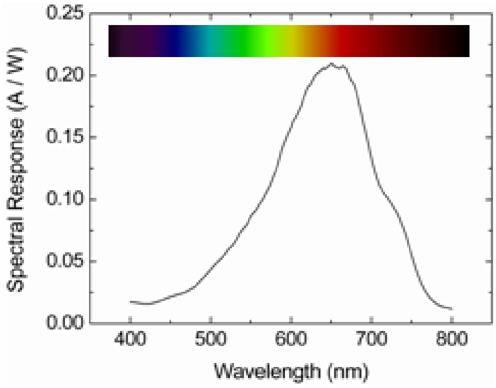

Figure 4.14 – Measured spectral response of a single amorphous silicon PSD element from the sensor array.

The spectral response of the nip device that constitutes each line of the PSD array is a measure of its sensitivity to light, being defined as the ratio of the current generated by the device to the amount of light falling on it. The spectral response peak is located at around 650 nm and the highest recorded values are obtained between 600 and 700 nm, corresponding to the maximum quantum efficiency of the i layer [2]. The overall response of the device extends from approximately 500 to 750 nm.

Overall, the data shows that the spectral response decreases as the wavelength increases beyond 650 nm, due to an enhancement of the optical losses in the red region of the spectrum. The spectral response also decreases as the wavelength decreases below 650nm, due to losses related to phonons [3].

Although the sensors are optimized for red light we have also tried to determine the PSD sensitivity to green light.

4.5.1. Dynamic response with red and green laser

Aiming to compare measurements taken using a red laser line with measurements obtained using a green laser line a white plastic ramp was scanned. The same 32 PSD sensor and sensor channels were used to perform both red and green laser scan measurements.

A higher dynamic range of 10pF was used to obtain results associated to red laser line scanning because the currents recorded are higher and so they need to be accommodated in a higher dynamic range of signals which allows higher currents to be acquired. A lower dynamic range of 2pF was needed to obtain results regarding green laser line scanning because in this case a lower current signal is detected by the sensor due to its spectral response, which is higher for red wavelengths than for green ones. Figure 4.15 shows the dynamic response of channel 14 for a red and green laser line scan at integration times of 0.8ms and 0.5ms respectively.

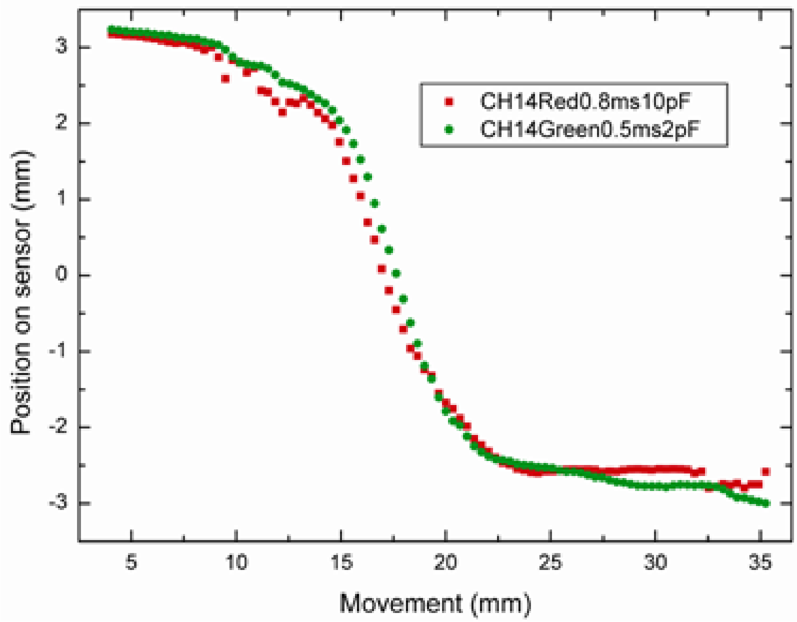

Figure 4.15 – Dynamic response of sensor channel 14
for Red (0.8ms/10pF) and Green (0.5ms/2pF) lasers.

Results show that there is no significant difference in the values obtained between the red and green light sources. All responses are similar when comparing similar counterpart integration times for both dynamic ranges.

4.6. Dynamic response to colour objects

Following the different colour laser light detection experiments, a wood ramp was used as opposed to a white plastic ramp. Thereby, in this case the colour of the ramp was no longer white, but brown. The light intensity range during the scan varied from 0.0563μW/cm² on the right side of the sensor to 0.036μW/cm² on the left side of the sensor.

Similar to the non-linearity obtained for a white plastic surface, the non-linearity calculated on channel 13 when scanning a wood surface is 5% as shown in figure 4.16.

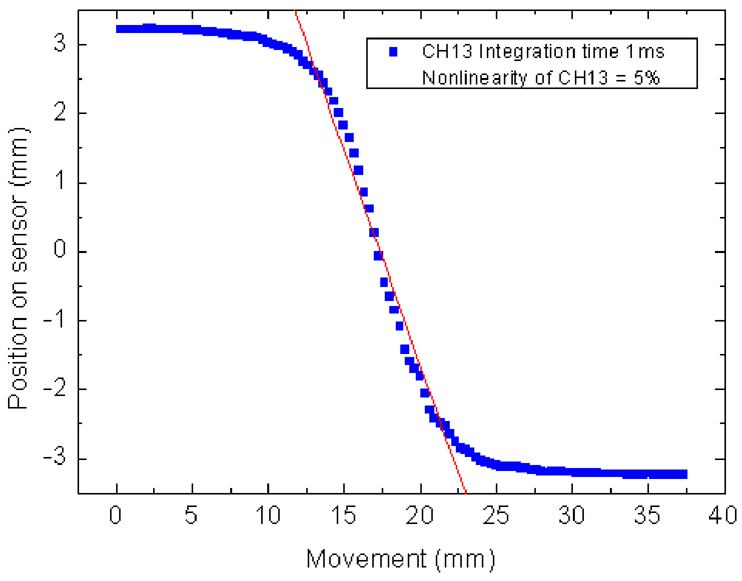

Figure 4.16 – Dynamic response and linearity of sensor channel 13 at an integration time of 1ms. Distance scanned versus position on the sensor.

Therefore these results reveal and conclude that it is possible to use the sensor and system to detect surfaces other than plastic and colours other than white. In this case a wood surface with light brown colour was detected.

4.7. 3D Scanning characteristics of the sensor/system

The detection of the features of an object is also an important aspect of the detectability of the constructed 3D scanning sensor/system. Besides that, the determination of the size of these features is also of extreme importance for 3D representation. These measurements depend of triangulation angles, and so it is important to study the influence of angles of reflection on the mapping of objects. Therefore, the relationship between the scanning angle of the incident light onto the object and the image displacement distance on the sensor was determined in this system setup. Here, rendering of 3D object profiles was also performed at a significantly higher number of frames than in previous trials.

For these experiments the amorphous silicon 32 element PSD linear array was mounted on the experimental setup shown in figure 4.17(a) and (b). The red laser line width reflected on the active area of the sensor after lens reduction was approximately 1mm and its length was about 18 mm making sure that all sensor channels were covered by the laser projection. The angle of projection was fixed to about 45 º as in the set of experiments performed in previous sections and here it was varied from 15 º to 85 º.

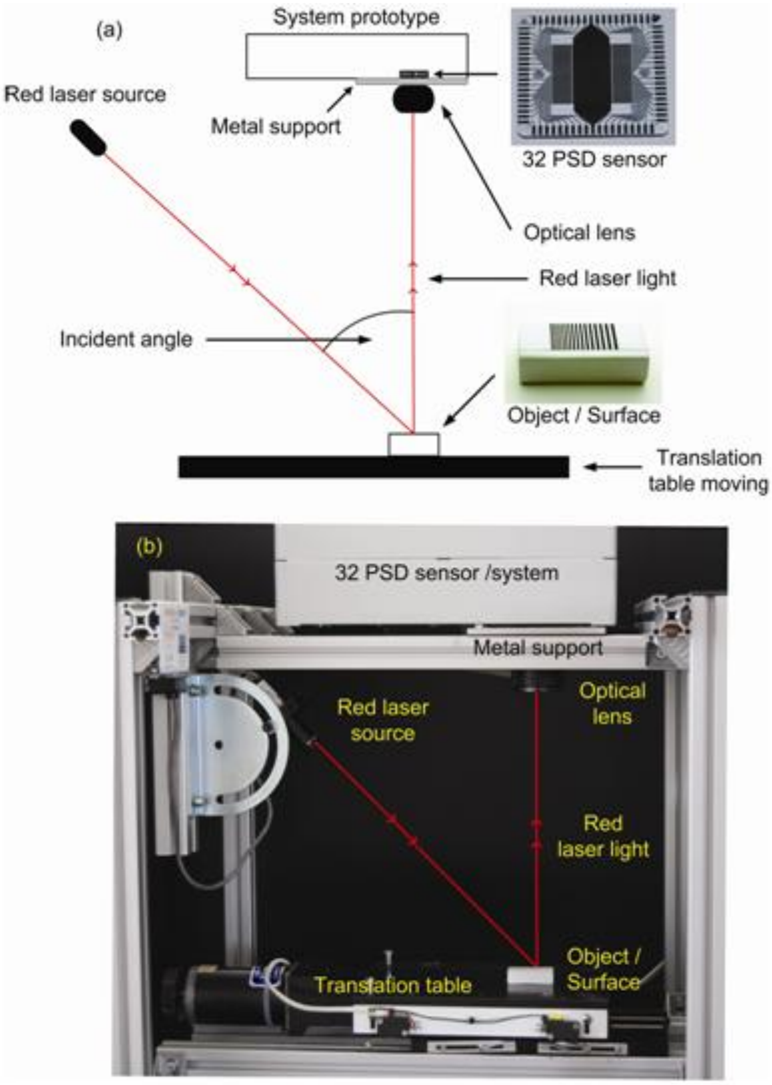

Figure 4.17 – (a) Sketch of the experimental setup for 3D profile scanning. (b) Photograph of the experimental setup.

4.7.1. 3D profile detection setup

The spatial resolution is the minimum distance that can be clearly measured when the light spot/line is moved from one position to another. For the array under analysis, the resolution along the x direction depends on the 1D sensor performances and its resolution along the y direction is limited by the tolerance of the patterned lines that constitute the array as well as by the spacing between them. On the other hand, the resolution along the z axis (perpendicular to the xy plane) depends on the incident angle (see figure 4.17(a) and (b)).

The following experimental procedure was performed to infer the smallest gap (resolution) that can be detected by the sensor system while scanning a predefined prepared pattern which was glued on top of a white rubber (object). This predefined black and white stripe pattern aims to emulate the presence of small gaps or defects on the surface of an object, thereby mimicking surface defect detection procedures in industrial processes.

The width of the related frame image projection of the white rubber on the sensor is only covered by a few sensor channels. The velocity of the scanning system was also reduced to the smallest possible in order to analyze its influence on the obtained resolution of detection. In turn, the rate of acquisition was also varied to observe the effect on the pattern detection.

A laser line was projected on a white rubber with a black and white pattern glued on it and the scanning process occurred while using the minimum rate of acquisition being 8 ms. The translation table moved from right to left so that the object (white rubber with black and white pattern) was scanned by the system. The object with the pattern and the pattern itself are shown in figures 4.18(a) and (b) respectively.

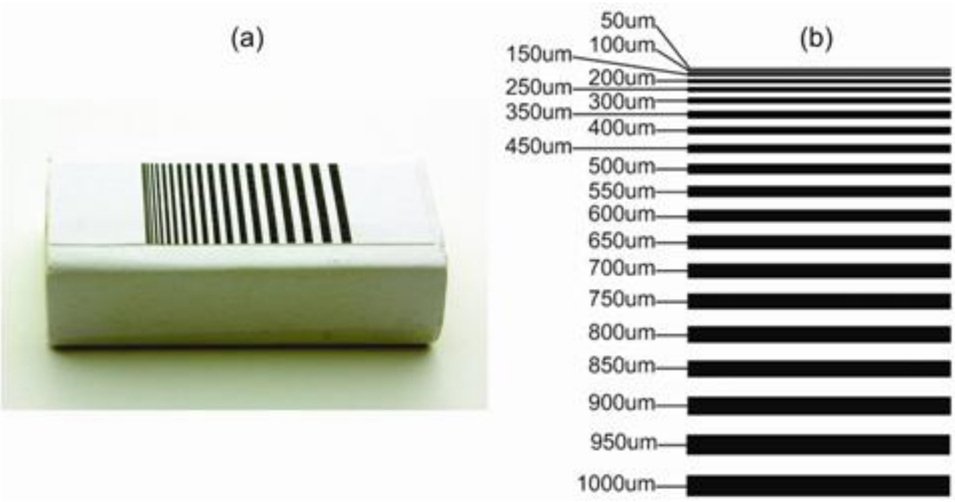

Figure 4.18 – (a) Horizontal photograph of the white rubber (object) with black and white pattern glued on top. (b) Black and white pattern (50 µm – 1000 µm).

The object was placed on top of a translation table structure as it is shown in figure 4.17(a) and (b). This triangulation configuration is the standard one to render objects in 3D using a sheet of light laser [4]. The object reflection was projected onto an area of the sensor covered only by just a few detectors. The dimensions of the white rubber object are the following: Length = 40.86 mm; Width = 18.49 mm; Height = 11.32 mm.

When the translation table moved and the laser hit the rubber rectangular object, the laser line was projected (after a lens reduction) on the sensor. The height of the object creates a difference in the reflection profile frame as shown in figure 4.19(b), (d) and (f).

In these experiments, the rubber was placed directly on top of the translation table (black background). This means that initially the laser line was not projected on the sensor because of the black background. When the object was shined, the reflection from the object did project itself onto the sensor. In this case the light intensity recorded was 2.76 µW/cm² for all these experiments.

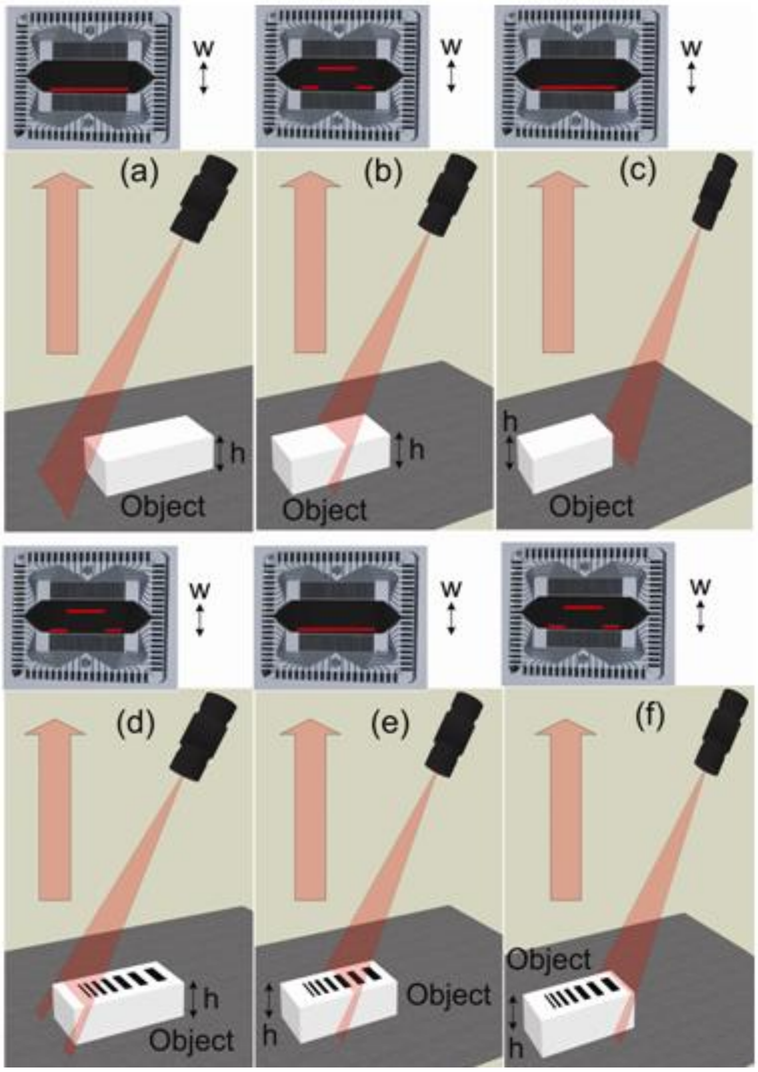

Figure 4.19 – Sketch of how the reflection of the height of the object looks like on the sensor active area. This is one frame of the object. (a) Laser line not incident on the object. (b) Laser line strikes the object. (c) Laser line does not strike the object. (d) Laser line strikes the object. (e) Laser line strikes a black stripe on the object (same as no object). (f) Laser line strikes the object.

The distance travelled from right to left on the translation table was about 69 mm and the incident angle shown in figure 4.17(a) and (b) was 45 º and remained constant for all experiments. The rate of acquisition was set at 8 ms, for a translation table (object scanning) speed of 1.97 mm per second, in order to view the relevant influence on the response and to determine the minimum or smallest gap detection. Other results were taken at the following acquisition times when the translation table speed was kept at 1.97 mm per second: 1000 ms, 800 ms, 600 ms, 400 ms, 200 ms, 80 ms, 60 ms and 40 ms. The integration time of the system was set to 0.085 ms for all cases and each measurement acquired was the average of 128 samples.

4.7.2. 3D profile detection resolution

The pattern tested (figure 4.18(b)) contains 19 noticeable white and black strips each with sizes varying from 1000 µm to 100 µm.

The position versus displacement illustration of figure 4.20(a) displays the response of channel 11 although channels 13 and 15 have a similar response (not shown for clarity). The peaks detected correspond to the white colour gaps in figure 4.18(b) and the gaps (or absence of peaks) correspond to the black colour stripes. Therefore, 14 white colour gaps and 14 black colour stripes are detected in figure 4.20(a). The last white colour gap or black colour stripe detected is 350 µm. Thereby, it can be stated that the minimum detail detected by the system in these conditions is 350 µm. Figure 4.20(b) shows a magnification of the response of channel 15 for the smallest peak detected. Here the detected peak is analysed closer and the width of the peak can be measured to see if it approximately matches the smallest detection value of about 350 µm. As shown in figure 4.20(b) the peak extends from 12.7 to 13.1 mm and therefore its estimated width is considered to be 375 µm ±25 µm. This data is in conformity with what was expected, where deviations are assigned to factors involved in the scanning process such as possible translation table vibrations or light optics alignment issues. Figure 4.20(c) presents the scanning response of sensor channel 17 when rendering the side region indicated, corresponding to the white rubber itself without the black and white pattern. In these experiments the laser line and the frame of the object are also projected in perpendicular to the length of each detector. Therefore each individual detector sees a change in height, which comes from a change in the position on each detector. The real measured height of the white rubber object without the black and white pattern glued on top is 11.32 mm. In this particular case (see figure 4.20(c)), this is equivalent to a height of 3 mm (from -3.5 mm to -0.5 mm on the Y axis) as detected by channel 17. Moreover, for full device reliability the sensors’ response to the optical stimulus must be the same, within one allowable marginal error of ±1%.

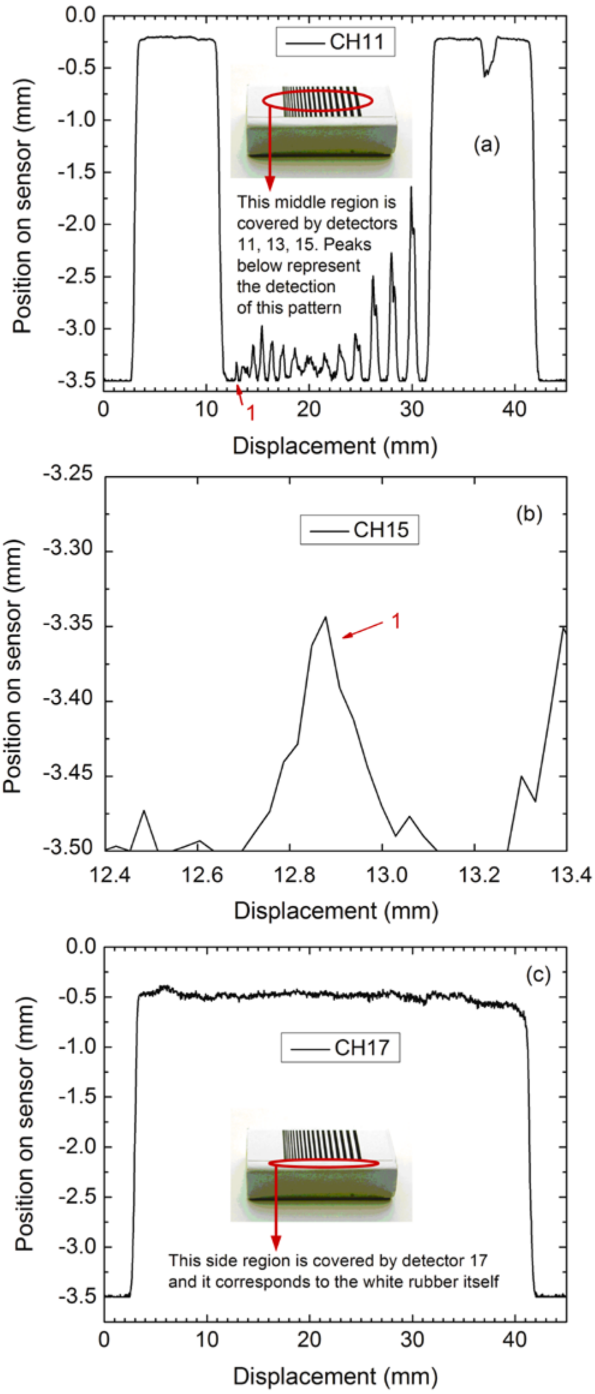

Figure 4.20 – (a) Sketch of the 3D scanning response of sensor channel 11 when rendering the white rubber object glued with the black and white pattern. (b) Sketch of the magnification of the smallest peak detected from the 3D scanning response of sensor channel 15 when rendering the white rubber object glued with the black and white pattern. (c) Sketch of the 3D scanning response of sensor channel 17 when rendering the side region indicated, corresponding to the white rubber itself without the black and white pattern.

Another interesting observation is that the length of all channel responses analysed corresponds to the measured length of the rubber object being approximately 40.86 mm. This length of 40.86 mm was measured using an electronic ruler, and all responses are detecting for approximately 40 mm so the correspondence is quite good.

As already mentioned, results were taken at the following acquisition times: 1000 ms, 800 ms, 600 ms, 400 ms, 200 ms, 80 ms, 60 ms and 40 ms.

Table 4.2 provides an approximate guideline for the theoretical minimum possible detectable gaps at each of the acquisition times experimented.

Table 4.2 – Resolution of detection at a speed of 1.97 mms-1

Data acquisition rate (ms)	Minimum detectable gap (µm)
1000	1970
800	1580
600	1180
400	788
200	394
80	158
60	118
40	79
20	39
8	16

The data show that the peak or gap detection is not lower than 350 µm due to experimental setup limitations, such as the image frame optics reduction factor. Regarding detector 11, the laser line is reflected and the detection is performed along the analogue length of the detector. The image frame is reduced in size after the lens, conditioning the spatial limit of detection to 350 µm. These restrictions lead to the fact that below the 350 µm limit of detection or 350 µm black line the white gaps between black lines are so small that the relevant sensor channel does not notice them and thereby only detects black colour or absence of light.

Results show that the pattern starts to be detected effectively once the acquisition time is decreased down to 80 ms. Above 80 ms, the results are not regarded as completely reliable. When using an acquisition time of 80 ms or lower, 14 black colour peaks or 14 white colour gaps are detected, and this corresponds to a minimum detail detection of 350 μm. Under these conditions, in theory and according to table 4.2, a minimum gap of 158 μm or lower should be detected, however as already mentioned, this is not the case due to optical arrangement and laser line thickness limitations. Anyhow, a minimum gap detection of 350 μm still follows the theoretical guideline provided in table 4.2.

Reducing the speed of the translation table by half, from 1.97 mms^{-1} to the minimum value of the translation table movement which is 0.985 mms^{-1} did not result in a smaller detail detection than 350 μm.

4.7.3. Influence of the incident angle on the detection resolution

The influence of the incident angle on the detection of the rubber object is shown in figure 4.21 corresponding to the response of channel 4. As can be noticed, the higher the angle, such as for example 75 º, the higher the difference between the top laser line and the bottom laser lines seen in figure 4.19(b), (d) and (f). Inversely, the lower the angle, such as 15 º, the lower the difference.

Another interesting observation in figure 4.21 is that the length of all angle responses analysed corresponds closely enough to the measured length of the rubber object being 40.86 mm. In relation to the measured width of the object being 18.49 mm, a rough estimate can be obtained by counting the number of channels detecting and measuring that specific area covered by those detectors on the sensor. This area will be the closest match to the width of the object. According to the 65 º angle response in figure 4.21, the real measured height of the rubber being 11.32 mm, is equivalent in this case to a height of approximately 1.5 mm (from -3.5 mm to -2 mm on Y axis) measured on the active area of the sensor. However, this value differs for each angle.

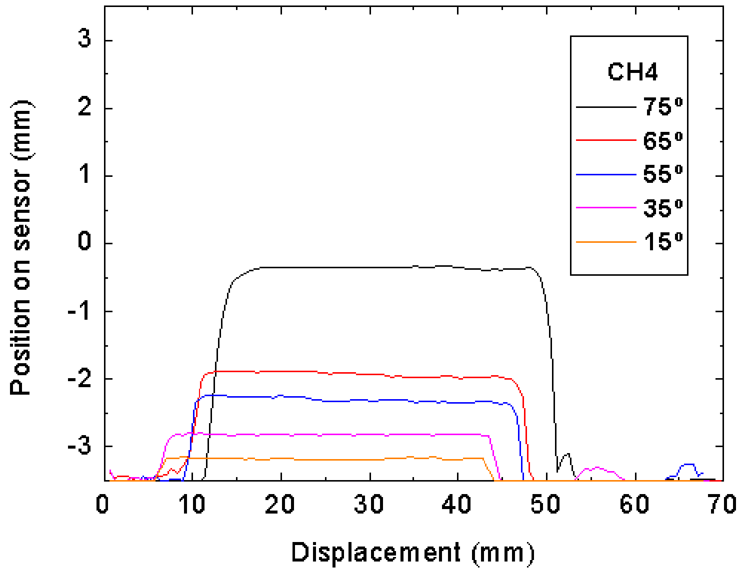

Figure 4.21 – Sketch of the 3D scanning response of sensor channel 4 at several angles when rendering the white rubber itself.

Figure 4.22 shows the response of channel 17 from the sensor when scanning and rendering a white ramp object at different incident light angles. The distance travelled during the scanning process by the translation table was about 37 mm. With a default angle of about 50 º, this corresponds to a measured distance from one side to the other on the sensor of about 7 mm. With a different angle the scenario changes accordingly as shown in figure 4.22.

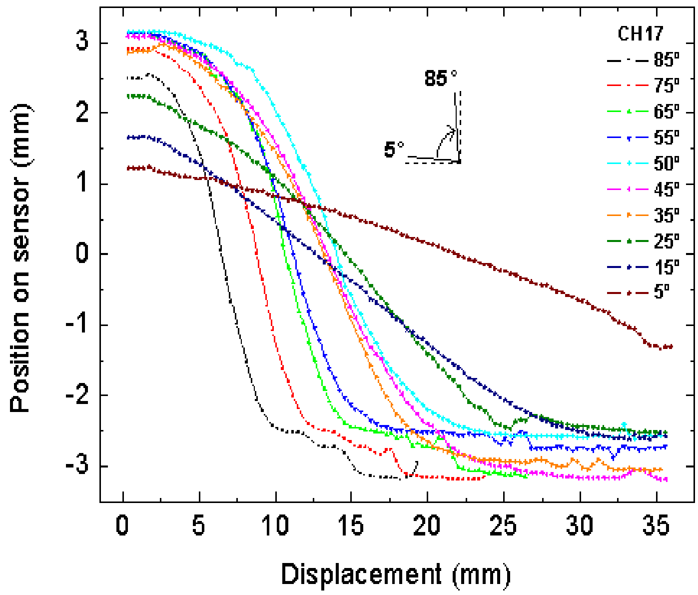

Figure 4.22 – Sketch of the 3D scanning response of sensor channel 17 at several angles when rendering the white ramp.

The angle of incidence clearly influences the projected image on the sensor. It is observed that for angles above 45º the laser line sweeps the ramp distance in shorter displacements (7.5mm for the case of 85ºC): from 2.5 mm to 10 mm as shown in the X-axis of figure 4.22). For small angles such as 5 º or 15 º, the laser line moves along only a relatively short distance on the active area of the sensor and in the case of a 5 º angle it does not sweep the whole of the ramp distance (see figure 4.22). Regarding the 15 º angle response, it spreads from 2 mm to about 30 mm (according to X axis in figure 4.22) so therefore it takes 28 mm for the laser line to sweep the ramp distance as well as to travel from approximately 1.75 mm to -2.5 mm on the sensor active area.

A 15 º angle is probably suitable for analysis of fine details when scanning a ramp or a range of heights although in this case only a range from 1.75 mm to -2.5 mm on the sensor was detecting the signal as opposed to the possible existing sensor range (3.5 mm to -3.5 mm).

The above results demonstrate that the angle of incidence of the light on the object behaves as another parameter that should be controlled to maximize the information we may obtain from the object. Thus, the relationship between the angle and height of the object was studied.

4.7.4. Geometry analysis of the triangulation platform

As mentioned elsewhere [4], within this active stereo approach and structured light technique, the height or depth of the object is computed using triangulation since the laser line source, the sensor and the object are arranged together forming the geometry of a triangle. The size of the increments within the same height range (for all angles), is proportional to the distance between the laser line source and the sensor.

A geometrical analysis of a very similar optical triangulation platform is already presented elsewhere [5] and the main difference in terms of geometry between the latter and the triangulation platform presented here is that, here, the laser light source is inclined at an angle as opposed to being perpendicular to the plane of the object and the sensor is perpendicular to the plane of the object as opposed to being inclined at an angle. A schematic of the triangulation scheme is presented in figure 4.23, in which all distances and angles of interest are shown as well as the liaison between **w**, being the image displacement distance associated to object height difference projection (after lens reduction) on the sensor active area, **h**, being the real height of the object and **z** being the diagonal distance between the two object height points.

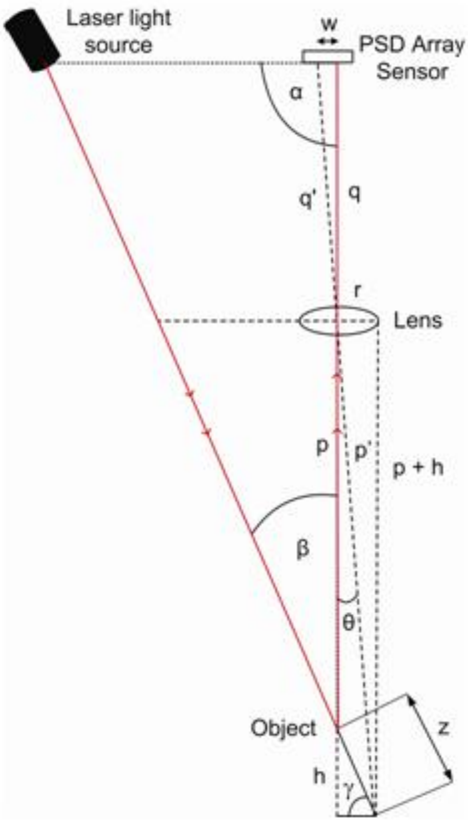

Figure 4.23 – Schematic of the geometry of the triangulation platform scheme.

As in reference [5], all appropriate derivations have been worked out in order to be able to obtain the required distance or angle relationships. The relevant explanations, formulae and calculations are presented below:

In order to find out the distance from the object to the lens or **p** and the distance from the lens to the sensor or **q**, it is necessary to use the well known lens equation presented below:

$$\frac{1}{\mathrm{f}} = \frac{1}{p} + \frac{1}{q} \qquad \textbf{[4.3]}$$

where **f** is the focal length of the lens used.

Similarly, in order to work out an expression for **p'**, or the distance from the lowest new object height point related to the associated height difference distance **w** (see figure 4.23), and **q'** being the new distance from the lens to the sensor in relation to the associated height difference distance **w** (see figure 4.23), the same lens equation can be used by simply replacing **p** and **q** by **p'** and **q'**. By resolving equation 4.3, an expression for **q** in terms of **p** is obtained (or **p** in terms of **q**) as shown:

$$q = \frac{pf}{p - f} \quad \text{or} \quad q' = \frac{p' f}{p' - f} \qquad \textbf{[4.4]}$$

similarly, an expression for **q'** in terms of **p'** can be obtained (or **p'** in terms of **q'**).

In order to work out an expression relating the distance **w** to the angle **θ**, trigonometry can be used for the triangle formed by **w**, **q'** and **q**:

$$\mathrm{w}^2 = q^2 + q'^2 - 2qq'\cos\theta \qquad \textbf{[4.5]}$$

by resolving equation 4.5, an expression of the cosine of the angle **θ** is obtained as shown below:

$$\cos\theta = \frac{q^2 + q'^2 - w^2}{2qq'} \qquad \textbf{[4.6]}$$

similarly, in order to work out an expression relating the distance **z** to the angle **θ,** trigonometry is applied to the triangle formed by **z**, **p'** and **p**:

$$\mathrm{z}^2 = p^2 + p'^2 - 2pp'\cos\theta \qquad \textbf{[4.7]}$$

by resolving equation 4.7, an expression of the cosine of the angle **θ** is also obtained:

$$\cos\theta = \frac{p^2 + p'^2 - z^2}{2pp'} \qquad \textbf{[4.8]}$$

if we combine equations 4.6 and 4.8 an expression combining **z** and **w** is worked out:

$$\mathrm{w} = \left[q^2 + q'^2 - \frac{(p^2 + p'^2 - z^2)qq'}{pp'} \right]^{1/2} \qquad \textbf{[4.9]}$$

this relationship is in effect also linked to the real object height, or **h**, since:

$$\cos\beta = \frac{h}{z} \qquad \textbf{[4.10]}$$

where **β** is the viewing angle or the angle between the laser light source and the axis perpendicular to the sensor.

Finally, it is possible to work out the distance **p'** in relation to the viewing angle **β**. The following expressions are obtained for the two triangles formed by **r**, **p'**, **p** + **h** and **h**, **r**, **z**:

$$\mathrm{p}'^2 = (p + z\cos\beta)^2 + r^2 \qquad \textbf{[4.11]}$$

$$\mathrm{z}^2 = z\cos\beta^2 + r^2 \qquad \textbf{[4.12]}$$

by resolving equations (4.11) and (4.12) an expression of **p'** in terms of **z** and **β** is obtained:

$$\mathrm{p}' = \left(p^2 + 2pz\cos\beta + z^2\right)^{1/2} \qquad \textbf{[4.13]}$$

since **p'** is known, **q'** can be obtained by substituting equation 4.13 back into equation 4.4.

All these expressions allow the calculation of all required parameters for the analysis of the triangulation system platform presented.

Thus we obtain a relationship between the image displacement distance on the sensor, or **w** and the real height of the object **h**, at a specific angle **β**. It is important to note that the focal length **f** is always a fixed value of 50mm for the particular lens used in our experiments. However, the modular focus present in our optical system allows us to change the magnification, which in turn alters distances **p** and **q**. The expression below defines magnification in terms of **p** and **q**:

$$m = -\frac{q}{p} \quad \textbf{[4.14]}$$

For the case of the 45 º result obtained in figure 4.20(c), the magnification used was approximately -0.26 obtained from table 4.3 below, where **q** = 63.16 mm and **p** = 240 mm. This corresponds to a frame or image reduction factor of about 3.8 for this particular case.

Table 4.3 shows the theoretical calculated values for image displacement distance on the sensor, **w**, for a white rubber object height **h** of 11.32 mm, when the viewing or scanning angle varies from 5 º to 85 º at intervals of 5 º. Associated distances **z**, **p**, **q**, p' and q' as well as the fixed focal length **f** are also presented or calculated.

As noticeable in table 4.3 for the 45º, an image displacement distance (on sensor) **w** of 2.92 mm is obtained and this approximately matches the height of the scanned 3D white rubber object profile shown in figure 4.20(c) which is about 3 mm (from -3.5 mm to -0.5 mm on Y axis). Similarly, concerning the results obtained in figure 4.21, the magnification used was approximately -0.08 obtained from table 4.4 below, where q = 54 mm and p = 675 mm. This corresponds to a frame or image reduction factor of about 12.5. As in table 4.3, table 4.4 presents all specific values for this particular case plus the error between theoretical and experimental values of **w** for the angles of interest.

Table 4.3 – Theoretical calculated values of w, for a fixed h and varying angle β,

Viewing angle (**β**)	Distance in mm (**z**)	Distance in mm (**p**')	Distance in mm (**q'**)	Image displacement distance in mm (**w**)
5	11.36	251.32	62.42	0.78
15	11.72	251.34	62.42	1.06
20	12.05	251.35	62.42	1.27
25	12.49	251.38	62.41	1.51
35	13.82	251.44	62.41	2.12
45	16.01	251.57	62.40	2.92
55	19.74	251.84	62.39	4.10
65	26.79	252.49	62.35	6.09
75	43.74	254.85	62.20	10.47
85	129.89	282.67	60.74	29.27

As noticeable in table 4.4, the image displacement distance (on sensor) **w** obtained for all cases of interest, approximately matches the height of the scanned 3D white rubber object profile for all those cases of interest or all angles shown in figure 4.21. For example, for the 55 º case, figure 4.21 shows a height of about 1.25 mm (from -3.5 mm to -2.25 mm on Y axis) and its theoretical calculated value (see table 4.4) is 1.27 mm, thereby a good match exists.

Table 4.4 – Theoretical calculated values of **w**, for a fixed **h** and varying angle **β**, where f=50mm; **p**=675mm; **q**=54mm and **h**=11.32mm.

Viewing angle (**β**)	Distance in mm (**z**)	Distance in mm (**p'**)	Distance in mm (**q'**)	Theoretical distance in mm (**w**)	Exp. distance in mm (**w**)	Error in mm (E**w**)
5	11.36	686.32	53.93	0.11	-	-
15	11.72	686.33	53.93	0.25	0.32	0.07
20	12.05	686.33	53.93	0.33	-	-
25	12.49	686.34	53.93	0.42	-	-
35	13.82	686.37	53.93	0.63	0.68	0.05
45	16.01	686.41	53.93	0.89	-	-
55	19.74	686.51	53.93	1.27	1.24	0.03
65	26.79	686.75	53.93	1.91	1.61	0.3
75	43.74	687.62	53.92	3.32	3.15	0.17
85	129.89	698.41	53.86	10.04	-	-

Figure 4.24 illustrates the match between theoretical and experimental values of **w** for the angles of interest.

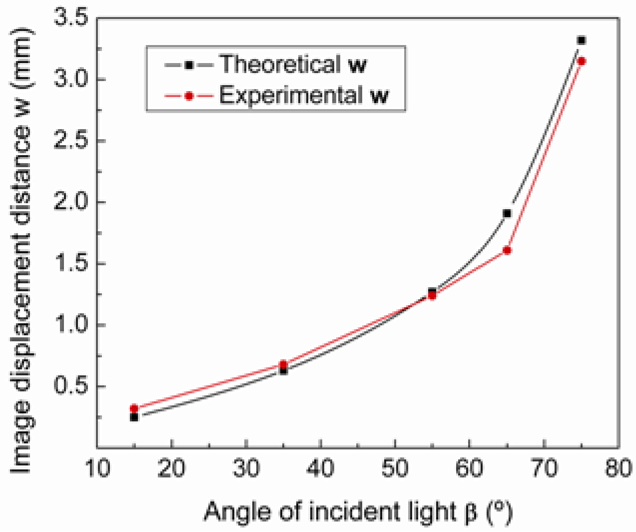

Figure 4.24 – Sketch of the theoretical versus the experimental values of **w** for the angles of interest.

Overall, the set of results presented indicate that an angle of 85º or higher becomes impractical since such a large angle derives in a height difference which is too large and extends beyond the available height range. Similarly, an angle of 5 º or lower is also impractical since such a small angle causes no noticeable significant height difference between the object being present or not. Therefore, a 5 º angle or lower cannot be used in this system setup since no height difference detection will occur. These observations agree with the work performed elsewhere [4].

From the above results we conclude that the angle variation is another parameter that can be used to obtain particular features of objects and that by knowing the light incidence angle and all geometric parameters of the system we are able to obtain the height of the object as demonstrated in tables 4.3 and 4.4. The results are in good agreement with the ones published by other authors [4].

4.7.5. Resolution and accuracy

To analyze the resolution and accuracy of the system, the influence of the rate of data acquisition by software while scanning the object was studied. This study was performed on the rubber object (without black and white pattern) of figure 4.18(a). As in other experiments the translation table moved and the laser hit the rubber rectangular object. The distance traveled by the translation table was about 69mm and it took about 35 seconds to travel this distance, thereby, the speed of the translation table was about 1.97 mms^{-1}. The incident angle was 45º and remained constant for all experiments performed. The rate of acquisition was varied in order to obtain the relevant influence on the response and determine the resolution. Results were taken at the following acquisition times: 1000ms, 800ms, 600ms, 400ms, 200ms, 80ms, 60ms, 40ms, 20ms, 8ms. The light intensity recorded was 2.14μW/cm² and the integration time was set at 0.085ms for all experiments and as in previous results a 128 sample averaging (or 128 sub-sampling) of the acquired measurements was performed in order to achieve a low noise performance. Only results recorded at an acquisition time of 8ms are presented because it is the lowest acquisition time (8ms), which leads to the highest resolution. In addition, the acquisition time limit in Windows is 8ms and cannot be lower than this. Figure 4.25 shows the profile obtained by one of the sensor channels (channel 12 - CH12). The total number of frames of such a profile was 2323 and this is equivalent to approximately 66 frames per second.

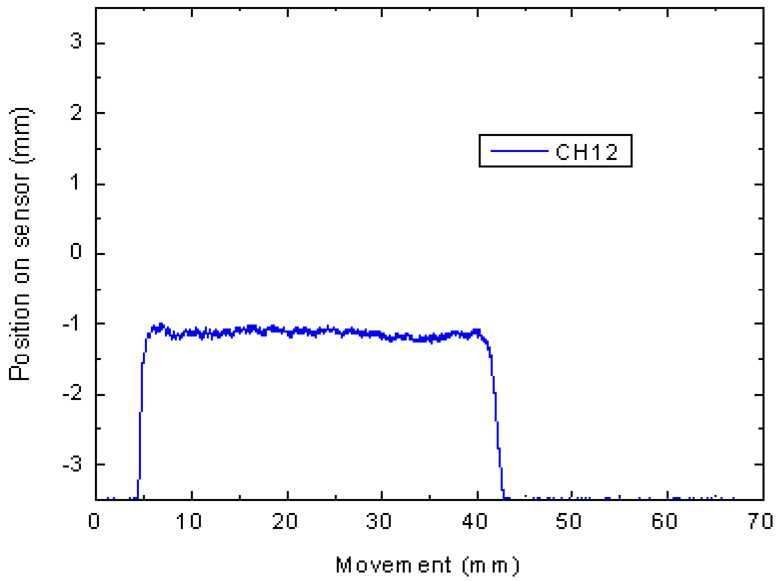

Figure 4.25 – Scan of the white rubber object by channel 12 of the sensor. Acquisition time of 8ms.

For each of the acquisition times experimented the following respective 3D profile resolutions were worked out: 1.92mm (for 1000ms), 1.57mm (for 800ms), 1.13mm (for 600ms), 784µm (for 400ms), 388µm (for 200ms), 179µm (for 80ms), 120µm (for 60ms), 89µm (for 40ms), 59µm (for 20ms) and 30µm (for 8ms).

All mentioned resolutions take into account a speed of 1.97mm per second and they were worked out by dividing the total scan distance (69mm) by the total number of acquired frames for each scan. For example, the lowest possible resolution being 30µm was obtained by dividing 69mm by 2323 frames.

Results in figure 4.25 indicate that the 3D detection of the rubber object starts at position 4.1283 mm and finishes at position 42.9165 mm. This means that according to the sensor system the rubber object measures 38.7882 mm. If we assume that the correct length of the rubber is 40.86mm as measured by hand using an electronic ruler then a sensor system accuracy of about 94.93% is calculated.

The measured height of the rubber being 11.32mm is equivalent to the height of 2.5mm (from -3.5mm to -1mm on the Y axis in figure 4.25) detected on the sensor active area after a lens reduction.

The number of acquired points or frames grew as we decreased the acquisition time from 1000ms to 8ms, thereby, the higher the number of frames or points the higher the 3D profile resolution obtained.

4.7.6. Repeatability of measurements

Repeatability and the ability to reproduce the same sensor/system measurements in each repetitive trial is also a very important aspect for 3D object profiling. Using the same acquisition time as previously described (8ms the lowest possible) the rubber was again scanned several times (20) to determine if there were any differences between all of the scans performed. To guarantee the stability of the reflection or provide equal reflection conditions for the whole rubber object, a white piece of paper was glued on top of the rubber object covering the whole top area. This ensured a stable response without differences from reflections coming from any possible defects on top of the rubber object. All experimental parameters (scan distance, angle, scanning speed, number of sub-sampling measurements) were kept at the same values as used previously. Figure 4.26 shows the 20 profiles (equivalent to the 20 scans) obtained by one of the sensor channels (channel 13 - CH13).

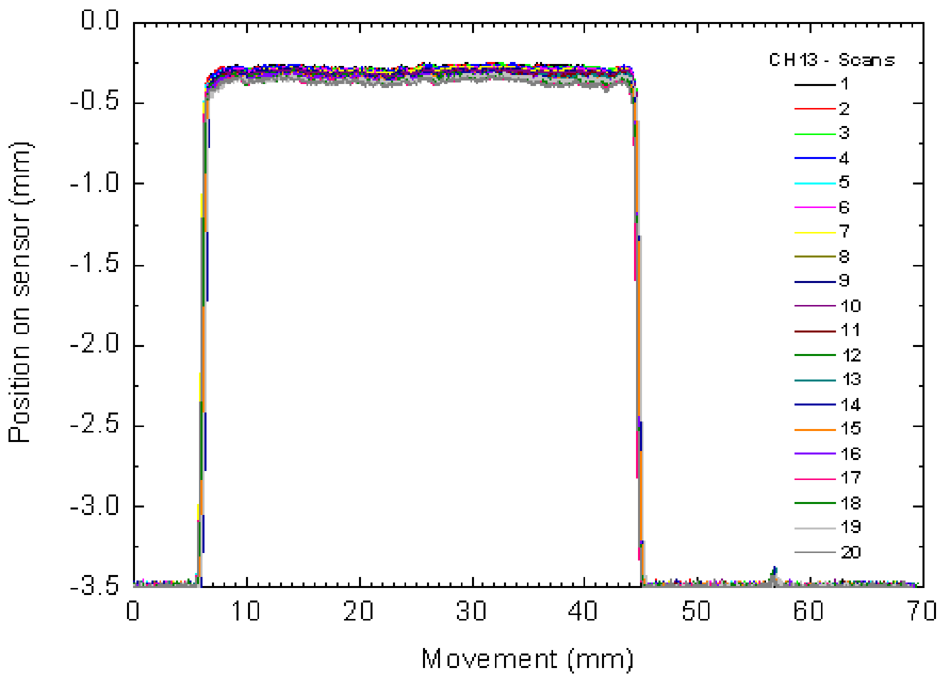

Figure 4.26 – White rubber object 3D profile scans.
20 repeated scans obtained with channel 13 of the sensor.

The repeatability of the results obtained for the system/sensor combination is excellent since all responses in figure 4.26 show almost exactly the same outcome in terms of length, height and stability. In order to quantify a measure of the repeatability of the sensor/system, the values recorded for the 20 scan responses at a particular point in the scan (approx. at 30mm) were chosen. The maximum value of all those 20 scan points was treated as the 100% reference and the values of the 19 remaining scan points were expressed as a percentage of that maximum reference point (100%), thereby establishing the percentage repeatability for each of the 19 scan measurement points. The mean percentage repeatability for all 19 scan points (at approx. 30mm) was then worked out as 98.6%, thereby confirming the remarkable performance of the sensor/system for scanning 3D profiles of objects.

4.7.7. 128 PSD array system 3D object profile scanning

The experimental setup and procedure for obtaining 3D object profiles with the 32 PSD sensor system have already been addressed in section 3.4.3 (chapter 3), and these also apply for the 128 PSD sensor system. Also in this case another white rubber object was used as the trial object and was scanned at the maximum acquisition rate of 8ms (WINDOWS limitation). Here, only a few working channels (detectors) from a few 128 PSD array sensors were employed. The width of the rubber is small and it is only covered or detected by a few sensor channels. The translation table (and object) moved from one side to the other so that the object (white colour rubber as shown in figure 4.27(a)), was scanned by the 128 PSD sensor laser sheet-of-light system. The dimensions of this white rubber object as measured by an electronic ruler were the following: length = 41.90mm, width = 16.70mm and height = 11.74mm.

Again, all experimental parameters (scan distance, angle, scanning speed, number of sub-sampling measurements) were kept the same as in the previous section. The light intensity recorded on the active area of the 128 PSD sensor array was about 2.53μW/cm² for all cases.

The results obtained when channel 54 and 75 of 128 PSD sensor array A and B respectively detect the white rubber object 3D profile are combined and illustrated in figure 4.27(b).

The response regarding channel 54 (sensor A) was acquired at almost 67 frames per second adding to a total of 2332 frames and the response regarding channel 75 (sensor B) was recorded at about 65 frames per second leading to 2289 frames in total.

Using an acquisition time of 8ms and bearing in mind a speed of 1.97mm per second a calculated scanning resolution of around 30μm is expected. However, as already discussed in previous sections the maximum resolution which can be obtained with an acquisition time of 8ms derives from the number of maximum possible frames in one second taking into account the lowest possible scanning speed. Thereby, 1/0.008s = 125 frames per second is the maximum possible acquisition frame rate at present (WINDOWS limitation).

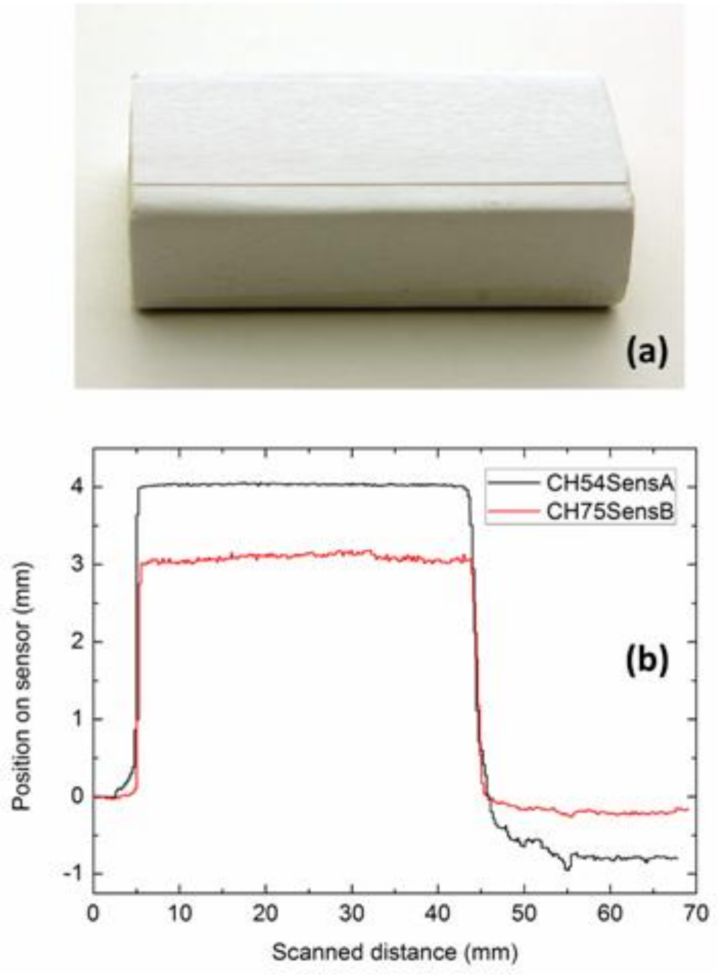

Figure 4.27 – (a) Photograph of a white rubber object. (b) 3D object profile representations for the individual detections of channels 54 (128 PSD array sensor A) and 75 (128 PSD array sensor B).

An interesting observation from both of the responses shown in figure 4.27(b) is that they correspond fairly well to the measured length of the rubber object being 41.90mm as measured by an electronic ruler. Channels are detecting for about 41mm.

When looking for example at channel 75 (sensor B), in figure 4.27(b), the real measured height of the rubber being 11.74mm is equivalent to a height of about 3mm (from 0mm to 3mm on the Y axis) measured of course on the sensor active area after a lens reduction. The other response coming from channel 54 (sensor A) in figure 4.27(b), differs slightly as it is extremely stable (smooth) and it is equivalent to a height of about 4mm measured on the sensor active area after a lens reduction. This is because each sensor and even each detector within that same sensor can behave in its own way now that, at present, the material fabrication processes cannot guarantee an equal response signal level for all detectors or sensors.

Anyhow, the stability of both of the profiles detected is quite acceptable since not much flickering is seen.

4.8. 3D object profiling results

4.8.1. Low resolution 3D object scanning

In the previous section the 3D detection was analysed for individual detectors of a 32 PSD sensor. Although not all detectors of the 32 PSD have the same sensitive performances the 3D profile of an object was evaluated.

In line with the experimental trials described in section 3.4.3 (chapter 3), figure 4.28 shows the results of scanning a fork (shown in figure 3.9(b)). The fork is used as the sample to be evaluated in 3D, using in this case, only 110 frames in total.

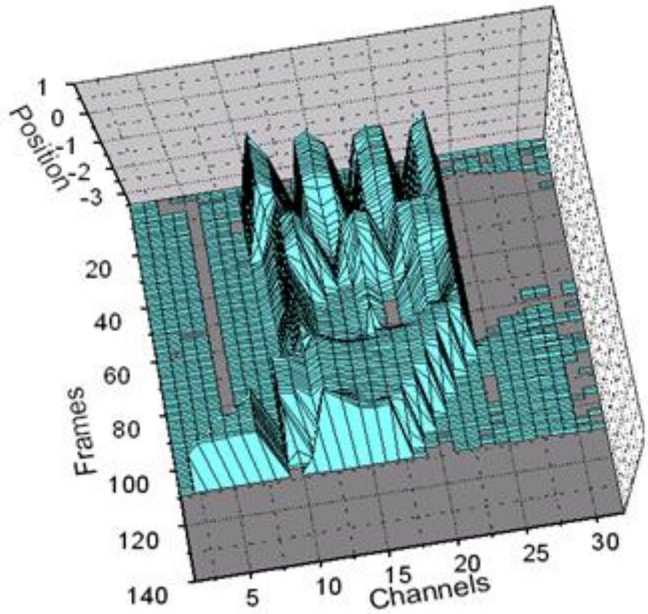

Figure 4.28 – 3D Image of rendered fork using only 110 frames for the whole scan.
The height of the fork is represented by respective sensor position values in the Z-axis.

Position values are shown on the Z-axis representing object height. Frames lie on the Y-axis and sensor channels lie on the X-axis. The quality of the 3D profile obtained is not optimum and can be improved. Indeed a sensor channel position response identical for all channels will ensure the best 3D object profile image quality. An even higher image quality could be achieved by integrating a higher number of strips (higher than 32 or 128) on the sensor area. Finally, another approach to improve the 3D object profile image quality is to pick up the continuous (along each sensor strip) profile information (per second) from the object as fast as possible. This means that the faster the data acquisition the higher the number of frames obtained for a complete 3D object profile and so for example, the 3D object profile shown in figure 4.28 would have a much higher number of frames (e.g. 2300 frames instead of 110) within the same scanning distance. In turn, the faster the acquisition, the higher the 3D profile image resolution, and the limitation here is not on the software but rather on the hardware or sensor as explained next.

Since a line of data or a frame was acquired every 339μm, the system/sensor resolution for the results obtained in this section is of 339μm. The software timer has a limit of approximately 8ms set by Windows. The translation table velocity was set at approximately over 1 millimetre per second for the experiments performed in this section and the scan distance was approximately 37mm. At this velocity, it took approximately 35 seconds to travel that scanned distance. Thereby, when setting a rate of acquisition of 8ms, a minimum resolution of 8.5μm should be obtained. This condition allows 125 frames to be acquired per second. Correspondingly, if one frame is acquired every 8.5μm, then a total of 4375 frames should be acquired for a distance of 37mm.

The software can be updated by removing the 8ms limitation of Windows, simply acquiring at the speed allowable by the PC processor. If the sensor response time is fast enough (<10μs) and assuming a capable minimum acquisition time per frame of 10μs provided by the electronics module, a rate of 100K frames (data lines) or 12.8 million data points per second could be possible.

All of the results reported in this work can be reproduced when using the 128 position sensitive detector (PSD) array sensor system. The reason is that the underlying hardware and functioning of the 32 and 128 PSD systems is exactly the same.

4.8.2. High resolution 3D object scanning

The high resolution 3D profile of the white colour rubber object (already described) shown in figure 4.29(a), was obtained using the same 32 sensor channels (0-31), but at approximately 2273 frames or 72736 points. Therefore the size of the rendered 3D image is 72736 points. The gap seen on the rubber 3D object representation in figure 4.29(a) is there because one or two relevant sensor channels covering that specific scanning area are not responding properly and so therefore they are not detecting the height difference properly as they should be. The 3D rubber object representation looks very similar to the real rubber object shown in figure 4.18(a) (without the black and white pattern). The length of the profile also matches correctly the one from the real object as was discussed in previous sections.

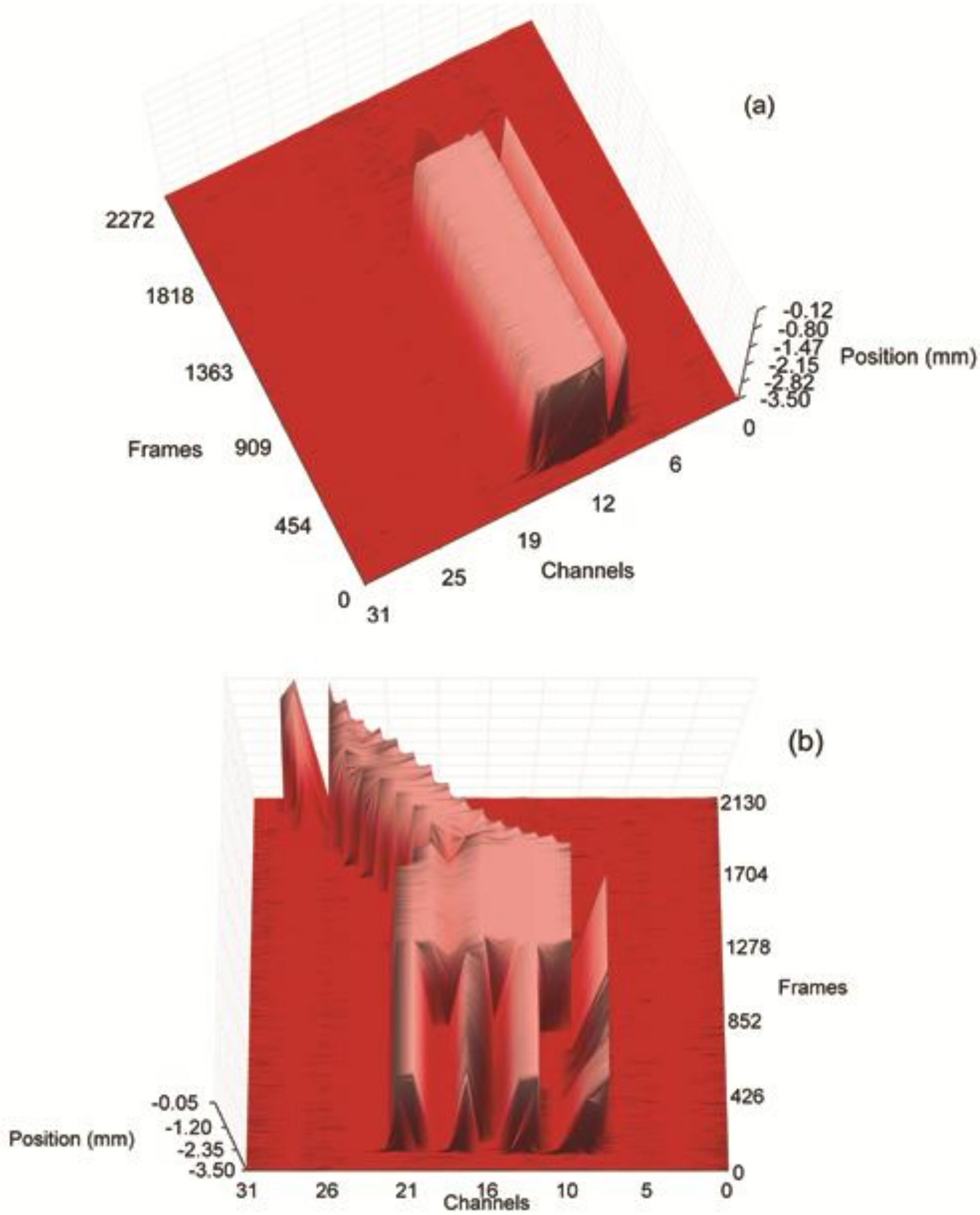

Figure 4.29 – (a) High resolution 3D rendered profile of the white colour rubber.
(b) High resolution 3D rendered profile of the white colour fork.

The high resolution 3D rendering result for the white colour plastic fork is also shown in figure 4.29(b). As in the rubber object 3D representation, sensor channels not responding properly lead to a gap in the 3D profile. The resolution of the fork is approximately 2130 frames or 68160 points.

Further improvements were made and new employed sensors responded better than in the past. This means that the sensor provided a more accurate and correct measure of the real position on its active area while 3D object scanning was being performed. Furthermore, since the sensor was responding fairly well, although still not at its 100% correct performance, no baseline software correction functions were needed. Due to these facts, a more realistic and improved 3D object profile was obtained for the white plastic fork shown in figure 4.30(a) or figure 4.18(a), as can be seen in figure 4.30(b). The 3D object scan and representation of the white fork shown in figure 4.30(b), is a substantial improvement in terms of image quality and realism when compared to the other 3D white plastic fork scans performed in the past. This specific 3D profile was scanned at about 63 frames per second deriving in a total of 2209 frames and 70688 3D scan points.

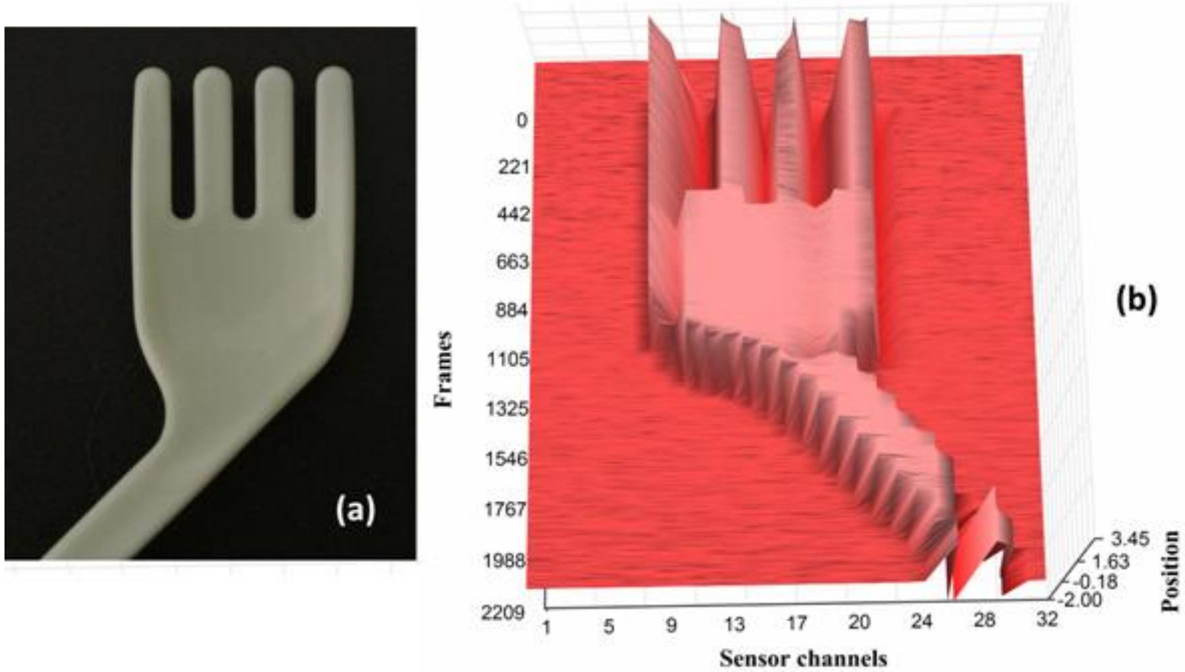

Figure 4.30 – (a) Photograph of the white plastic fork.
(b) 3D Object representation of the scanned white plastic fork.

A highly detailed (high number of frames) 3D object profile can be also obtained when using small angles although it can take a large amount of time to perform the 3D scan. Similarly, a low detailed (low number of frames) 3D object profile will be obtained when using large angles taking a small amount of time to perform the 3D scan.

We have confirmed that it is possible to render an object in 3D within a scanning angle range of 15 º to 85 º and identify its real height as a function of the scanning angle and the image displacement distance on the sensor. Overall, and based on these results, it can be concluded that small angles allow for a high detailed but slow 3D analysis of the object and inversely, large angles allow for a low detailed but rapid 3D analysis of the object. The accuracy of the method depends mainly on the sensor resolution as well as on the precision of the light source and the optical geometric dimensions used. The rate of acquisition and the translation table speed determine the gap between frames of the object. The higher the number of frames the higher the expected profile resolution. Accuracy of the system is mainly dependent on the acquisition time but it is above 95% and resolution can be as low as 30μm. The ability to reproduce measurement values is above 98%.

It has been demonstrated that both amorphous silicon 32 and 128 PSD sensor arrays and their corresponding systems are working correctly and can be used as high speed and high resolution sheet-of-light 3D object scanning systems. Improvements are needed in order to achieve 100% correct sensor position response, especially for the 128 PSD array sensor and such a goal could be attained by fabricating the sensor using other materials such as nanocrystalline silicon which hardly degrades the overall position response of the structure over time.

Anyhow, the successful integration of amorphous silicon PSD array sensors into suitable sheet-of-light 3D object rendering systems is now possible and feasible. The quality and realism of the 3D object profiles depends on the correct and accurate position response of each detector from the sensor as well as on the size of the PSD array, meaning that theoretically the higher the number of PSDs integrated in the array, the higher the 3D object profile resolution in the discrete sensor axis. Subsequently, the higher the number of detectors (sensor channels) in the X-axis (see figure 4.30(b)), the higher the number of total image 3D scan points.

4.9. Colour sensing ability of the sensor/system

The results shown previously concern the rendering of 3D objects. The measurements were performed using a red laser line although a green laser line was also tested. However these measurements were not able to detect or at least identify the colour of the object. Moreover as it was demonstrated it is preferable to have high reflective surfaces, although some degree of freedom is obtained by changing the integration time. Since colour detection can be an important complement asset to 3D rendering, the colour sensing ability of the data acquisition prototype system integrating the 32 linear array of 1D amorphous silicon position sensitive detectors (PSD) was analyzed. Here, the static and dynamic colour detection responses obtained are shown. The system was used to differentiate primary red, green and blue (RGB) colours and even derived colours. It is also able to match a light intensity value or range of values to a particular RGB hue. Results show that the colour of the surfaces can be detected using a combination of light colours and integration times. The RGB light colours are reflected the most when the incident light has the corresponding colour and there is more absorption when complementary colours exist thereby agreeing well with the theory. A mean colourimetric error of 25.7 was obtained. Finally, it can be concluded that colour separation is possible via the use of this sensor array system, composed by a simple amorphous silicon nip junction.

Colour detection using a “3D sensor” with a simple nip amorphous silicon structure was never tried before according to our knowledge, since the most common arrangement is to produce tandem pin/pin structures in which the first i layer is made out of silicon carbon [6].

In comparison to the work of other researchers [7-11] who also present amorphous silicon structures as colour sensors our approach is simpler in terms of production steps, and the sensitivity to colour is achieved by adjusting the system integration time for every light intensity as opposed to varying the bias voltage across the device [12]. The integration time can be varied using software instructions while colour detection takes place. Due to this simplicity it should be possible to perform colour detection and 3D object rendering at the same time using such a system. P. Rieve et al. [9] use a 3 colour discrete (pixels) pi^3n type a-Si:H sensor and achieve colour separation by applying a voltage across the device thereby modifying the spectral response while measuring with a large dynamic range. J. Zimmer et al. [8] also employ a 3 colour pi^3n type a-Si:H sensor leading to voltage controlled spectral response measurements under different monochromatic bias illumination. K. Eberhardt et al. [7] present a 3 colour n-i-p-i-n a-Si:H sensor with a suitable dynamic range and here too small bias voltages of the range of ±2V are applied across the device to modify the spectral response and perform colour detection. Most of these approaches are similar and differ from our approach since we do not need to apply a voltage and we can perform colour detection by simple software integration time modifications. On the other hand in our method the use of RGB light sources is also required in order to obtain clear colour discrimination.

Separation or discrimination is simply the ratio between the light intensity related output values (arbitrary units/integration times) coming from the sensor system for the different reflected colour lights. Each recorded value or range of values is associated to a specific colour and so the colour discrimination will be achieved simply by reading the recorded light intensity related value and by verifying which colour corresponds to that value or range of values.

Our sensor system detects a different value of light intensity for each colour when multiple light colour source illumination is used. Thereby every colour tone is associated to a particular light intensity value which could then be compared to known colour pattern. Our sensor system also provides a good dynamic range and a low noise level for measurements [13]. In our system, software averaging (128 sub-sample average) is performed on each measurement in order to obtain a low noise response and all subsequent experiments were performed under these conditions ensuring the highest signal-to-noise ratio on every acquired reading.

A colour object was placed on top of a translation table as shown in figure 4.31. Since our previous studies were performed using a white object, this was used also in this study as the reference. A white polyethylene glossy plastic ramp (45 º) served as support to glue a mirror (concave, diameter of 2.8cm and 50mm focal length), a white paper surface or a colour surface (white paper with different printed colours: red, green or blue). The colours were printed on white paper using a multifunctional laser colour printer (Xerox ColorQube 9201) with a resolution of 2400dpi in a 7.5 cm width × 4.8cm length piece of paper.

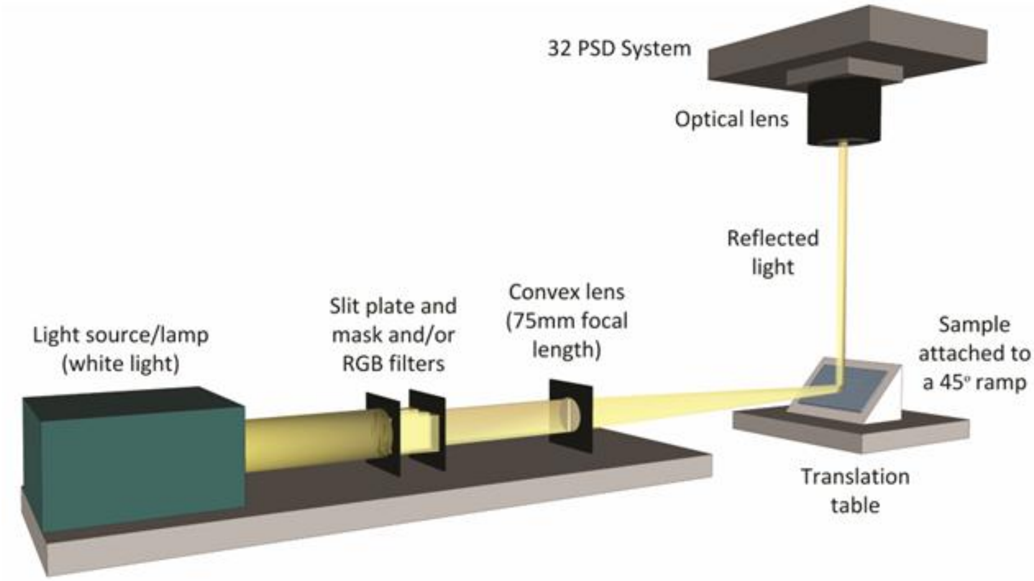

Figure 4.31 – Experimental setup for the scanning of the attached sample.

A Tungsten-Halogen (250W) white light source was shined at right angles to the 32 PSD prototype system as shown in figure 4.31. A stripe of white, red, green, green/blue or blue light was projected on the required surface at the middle point of the ramp. Thereby, the ramp object structure caused the reflected light stripe to be projected (after lens reduction) on the active area of the sensor.

The light colours red, green, green/blue and blue were obtained by using filters whose transmittances are shown in figure 4.32. Figure 4.32(a) shows a schematic view of the reflectivity of the colour surface in accordance to the correspondent light colour being used. Figure 4.32(b) shows the transmittance of RGB colour filters and figure 4.32(c) the one obtained by combining two different filters (blue).

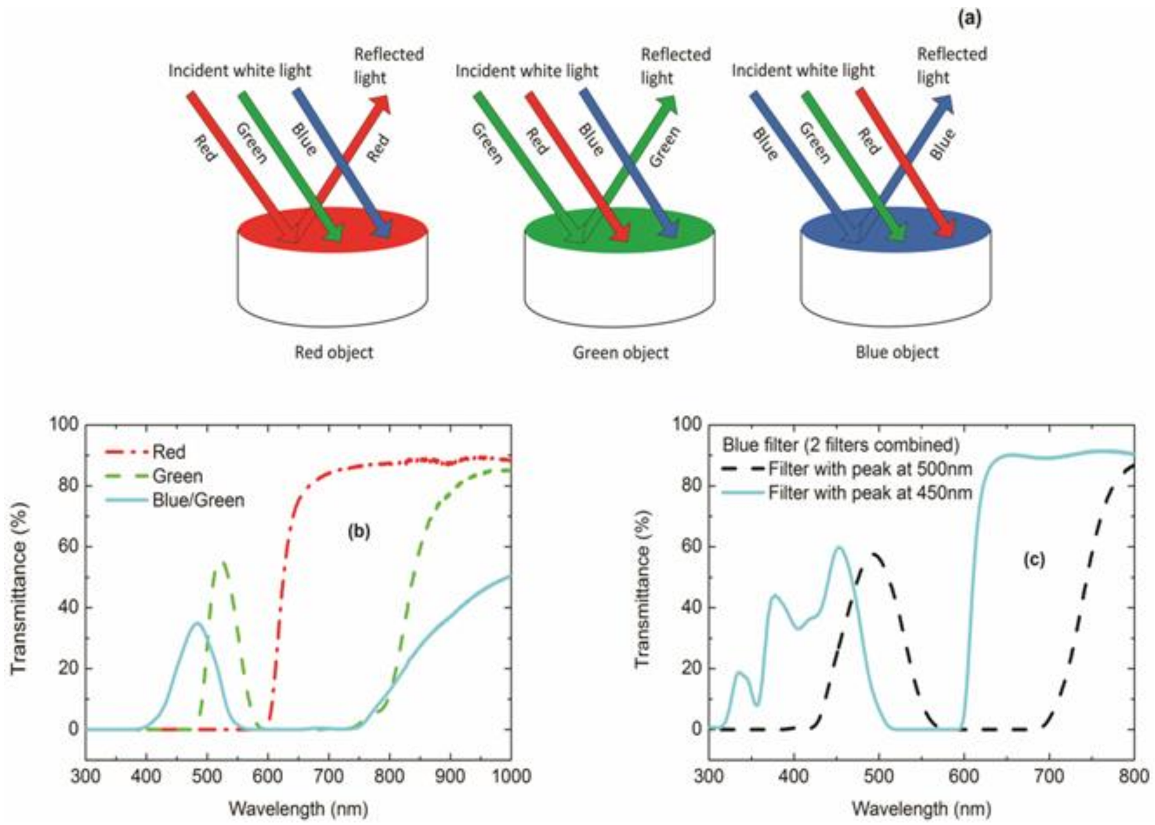

Figure 4.32 – (a) Schematic view of the reflectivity of the colour surface in accordance to the correspondent light colour being used. RGB incident light was obtained using filters whose transmittance is shown. (b) Red filter, Green filter, Green/Blue filter. (c) Blue filter by combining two different filters.

A line of light obtained by placing a slit mask after the filter was focused onto the object using a 75mm focal length convex lens (figure 4.31). The light intensity reaching the sensor system was measured by a radiometer (International light IL1700). According to our previous studies shown in section 4.2, the power light intensity has a linear relationship with integration time. Thereby the value of the light intensity recorded by the sensor system can either be expressed as a power light intensity (μW/cm²) or as a value of integration. In fact the range of values of the integration time defines the large dynamic range of the sensor system.

In order to evaluate the ability of the sensor system to detect colour light, and since it measures reflected light, the intensity of the light impinging on it was measured prior to each experiment. Therefore the mirror was placed in the sample holder (45º ramp) and the reflected light (white or RGB colour light) arriving on the sensor was recorded. The variation of the light intensity was recorded on the sensor system (as arbitrary units/integration times) as the integration time changed in relation to the specific light colour used and such task was repeated in exactly the same conditions with the radiometer. The same procedure was followed to determine the light intensity reflected by the colour surfaces used.

Knowing the light intensity of the light source, the ability of the system to detect colour objects, was then analyzed by gluing a piece of office paper with four 1cm width × 4.8cm length colour stripes (white, red, green or blue) to the support ramp (see figure 4.33(a)). These were illuminated by white, red, green or green/blue light. Since the white colour surface is the most reflective it serves as reference.

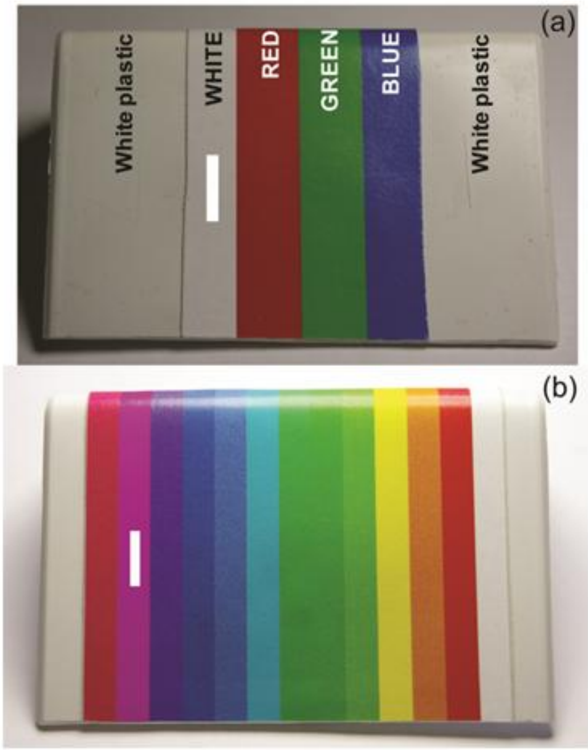

Figure 4.33 – Photograph of the combined colour surface attached to the white plastic ramp with the simulated projection of a white light stripe (white mark). (a) Primary RGB colours. (b) Derived/intermediate colours.

Similarly, the same experiment was performed using as the sample another piece of office paper (see figure 4.33(b)) with thirteen 0.5cm width × 4.8cm length colour stripes (red/magenta, magenta, violet, dark blue, light blue, cyan, green/blue, dark green, light green, yellow, orange, red and white) and just for this particular case it was illuminated by white, red, green or blue light.

Figure 4.33(a) shows a photograph of the combined white and primary RGB colour surface attached to the white plastic ramp while figure 4.33(b) shows a photograph of the combined white and primary/derived/intermediate colour surface. The white mark shown in figure 4.33(a) and (b) simulates a white ray of light being projected on the colour surface when experiments are performed. The stripe of white light (white mark) was obtained as sketched in figure 4.31: a white light beam passes through a slit mask, and a 75mm focal length convex lens focuses the light onto the object.

However as already mentioned, using filters, a red, green, green/blue or blue stripe colour of light is projected on the surface.

In order to evaluate the ability of colour detection it was important to obtain the exact colours reflected by the surface to be analysed. Thus, the colour reflectivity of the surface was obtained by reflectance measurements (in a Shimadzu UV-3101PC Spectrophotometer) in the spectral wavelength range from 300nm to 800nm. Figure 4.34(a) shows the reflectance for the white paper, white plastic and primary red, green, blue colour surfaces. The reflectance of the derived magenta, cyan and yellow colour surfaces are shown in figure 4.34(b) while figure 4.34(c) illustrates the reflectance for the intermediate colour surfaces such as red-magenta, violet, light blue, green-blue, light green and orange.

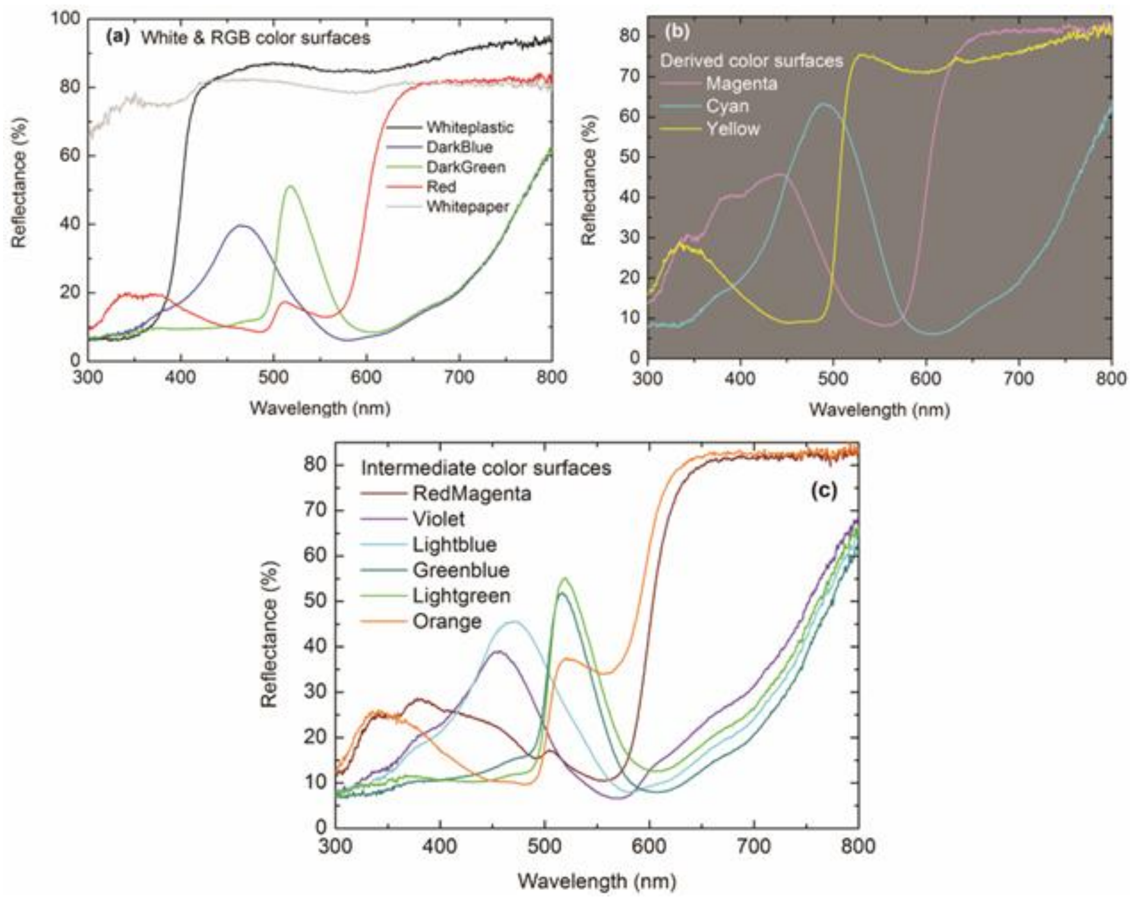

Figure 4.34 – Reflectance over the spectral wavelength range from 300nm to 800nm for the 14 individual target colour surfaces of the combined colour surface (a) Reflectance for the white paper, white plastic and primary colour surfaces. (b) Reflectance for the derived colour surfaces. (c) Reflectance for the intermediate colour surfaces.

Subsequently, and taking into account the previously mentioned background information, the ability of the PSD system to detect also colour from objects was tested using two approaches: the first one was based on the reflected intensity variation of white light as a function of the colour surface; the second approach was based on the total reflectivity of the colour surface in accordance to the correspondent light colour being used as sketched in figure 4.32(a). For both approaches it was necessary to adapt the integration time as referred previously.

Besides static measurements, dynamic measurements were also performed. For the latter, the object (plastic ramp) was placed on top of the translation table, moved continuously from right to left (diagonally away from the viewer in figure 4.31 and vice-versa at a speed of 1.97mm/sec. Such movement and speed was controlled by software instructions sent to the translation table controller. The width of the surface stripes is constant and the integration time was different for each light source and scan performed. When a specific light colour (white, red, green or blue light) or light power is incident on the target surface, the dynamic range of the system allows various light intensities coming from different colour surfaces to be recorded (as arbitrary units) for each scan performed. Thereby a different dynamic range (or integration time) setting was used to perform each scan (for each light colour) and this allows a range of arbitrary units to be recorded within that dynamic range.

4.9.1. Static colour detection response

The measurements of power light intensity recorded by the radiometer versus the sensor system integration time setting for all light colour detection responses for the 19th detector of the sensor (sensor channel 19 - CH19), are shown in figure 4.35. As expected, the sensor/system and radiometer detect the highest intensity values for white light.

The light intensity recorded by the radiometer for the white light being projected on the mirror was 31.3µW/cm² and due to the high light intensity the sensor system integration time had to be reduced to 0.07ms to avoid saturation. For RGB colour light the intensity recorded by the radiometer was 19.4µW/cm² for red light, 11.7µW/cm² for green light and 2.62µW/cm² for green/blue light. The integration time of the sensor system had to be altered to 0.25ms for red light, 0.6ms for green light and 1.4ms for green/blue light in order to accommodate the acquired signal to a detectable range.

The results presented in figure 4.35 are in agreement with those of figure 4.14 and 4.34, since they show the highest reflectance of light at wavelengths corresponding to the maximum spectral response of the sensor. Using this information we are able to detect the different RGB colours and match a light intensity value or range of values to a particular RGB colour, by adjusting the integration time of the system.

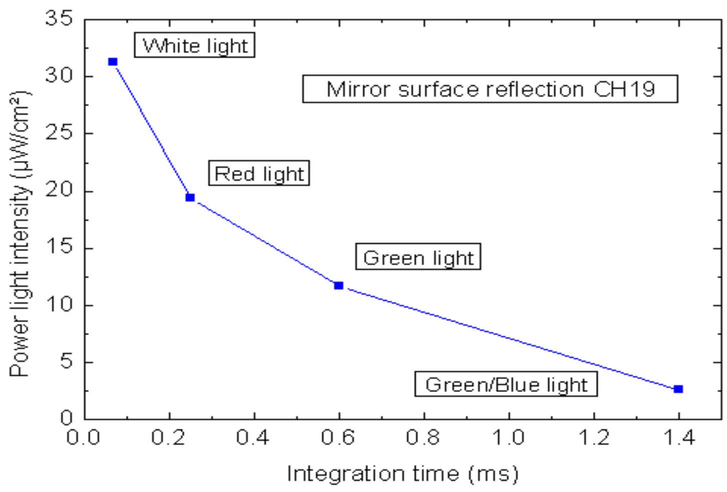

Figure 4.35 – Mirror surface reflection. Power light intensity versus integration time.

Figure 4.36 shows the correspondence, for the 25th detector of the sensor (sensor channel 25 – CH25), between the measured power light intensity and the integration time of the system when either a white, red, green or green/blue colour light was incident on either a white, red, green or blue surface. Results show a similar behavior to that one observed in figure 4.35 for a mirror surface. The maximum power light intensity and the lowest integration time were obtained when white light was projected on all surfaces. The second most intense signal was obtained for the light colour corresponding to the colour surface. On the other hand, we observed also a significant difference between the signal reflected by white light on red and green or blue surfaces.

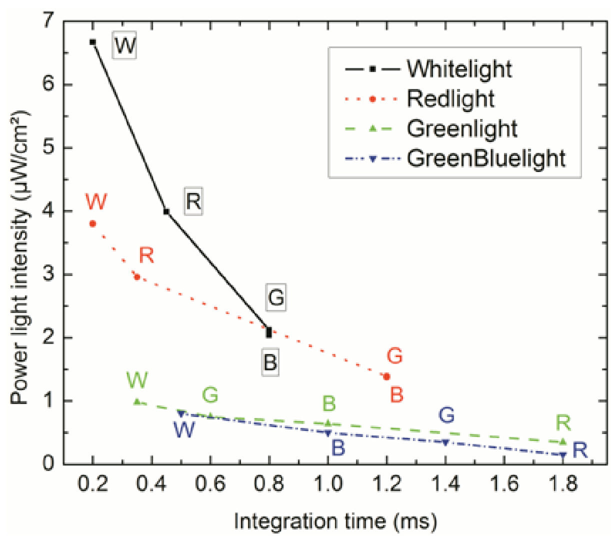

Figure 4.36 – Static surface colour analysis using white, red, green and green/blue light. Power light intensity versus integration time, CH25.

This is related to the spectral response of the sensor which is optimized for red light detection as well as to the low intensity of the blue and green light sources. Figure 4.36 also shows possible colour delectability by illuminating the colour surface with RGB light colours.

4.9.2. Dynamic colour detection response

Results concerning dynamic colour detection were obtained as the object was moving (from right to left). Here, the objects were the combined colour surface ramps shown in figure 4.33(a) and figure 4.33(b). The integration time of the system varied for the different colour scans performed according to figure 4.36 and can be set by software functions, thus, it can be thoroughly controlled even while acquiring data in real time. This means that the integration time is changed in real time as the light intensity varies, in order to accommodate those signal changes during the scanning process. The distance scanned from right to left was approximately 69mm for each combined colour surface scan and covered most of the width of the ramp structure (see figure 4.33(a) and 4.33(b)).

The detection responses related to the scanning of the colour surface illustrated in figure 4.33(a) are shown in figure 4.37(a), (b), (c) and (d) respectively for white, red, green and green/blue light.

When white light was shined on the surface of the object, different reflected light intensities were recorded. Overall, as shown in figure 4.37 and independent of the light source colour and intensity, white paper surface reflects the most followed by the white surface of the ramp (white plastic). Regarding coloured surfaces, it can be seen that the highest signal recorded by the sensor was obtained when the sample was shined with the respective light colour. This was expected, as sketched in figure 4.32(a).

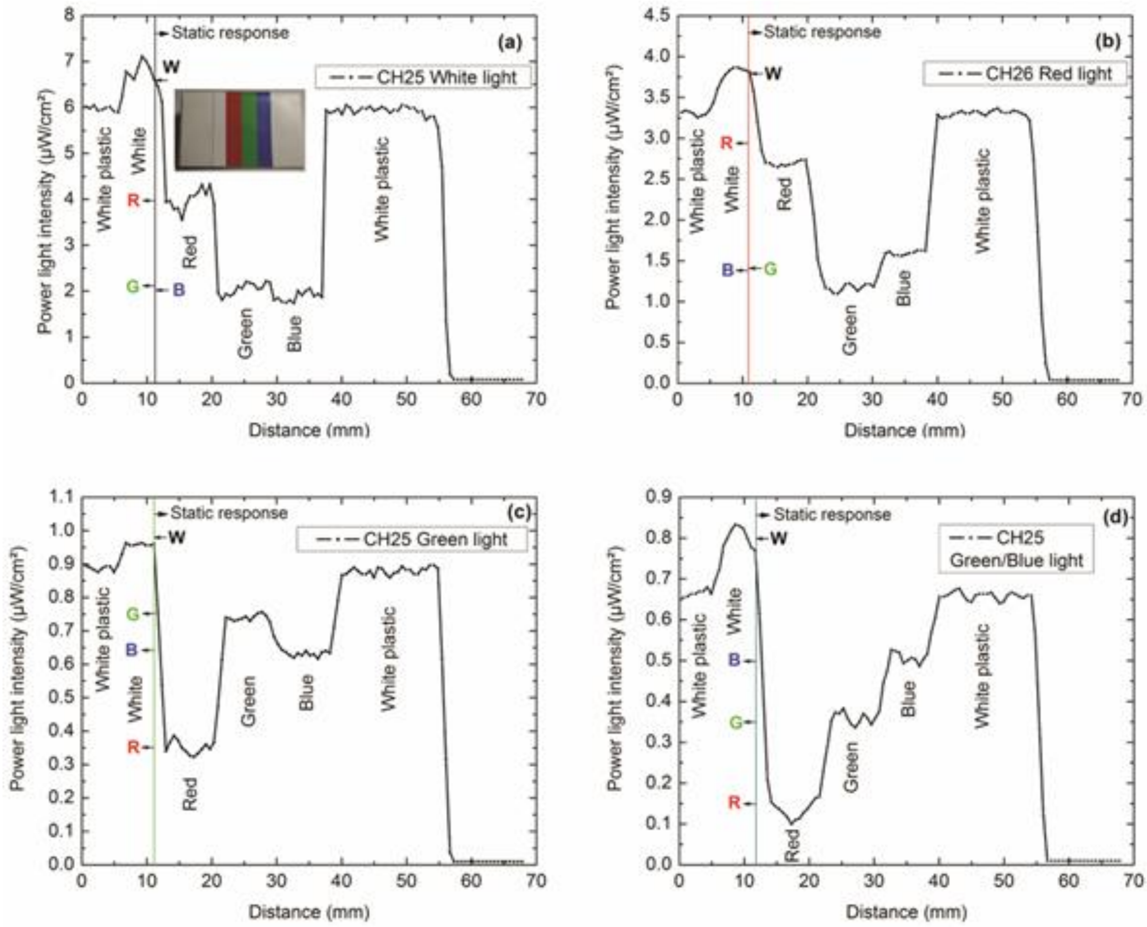

Figure 4.37 – Dynamic surface colour analysis using white, red, green and green/blue light. Power light intensity versus distance. Comparison to static surface colour analysis. (a) White light, CH25. (b) Red light, CH26 (c) Green light, CH25 (d) Green/Blue light CH25.

Under white light illumination (figure 4.37(a)), signal discrimination is noticeable between the white and red surfaces but not between the green and blue ones. For red light illumination signal discrimination was obtained between the white and red, and red and green surfaces, as well as between the green and blue ones, even though the latter is less significant. Under green light projection, discrimination between the signals related to the red and green or blue surfaces was also obtained even with much lower signal intensity. Interestingly, when the sample was shined with green/blue light clear signal discrimination between the green, blue and red surfaces was observed even though low light intensity levels were recorded plus taking into account the feeble spectral response of the sensor for blue. Table 4.5 presents the ratio between signal intensities obtained from different colour surfaces (figure 4.37) as a function of the light colour shined at each surface.

Table 4.5 – Ratio between signal intensities obtained from different colour surfaces for each light colour source.

Light colour	Ratio between signals from different surfaces					
	W/R	W/G	W/B	R/G	R/B	G/B
White	1.6	3.3	3.3	2.0	2.0	1.0
Red	1.3	3.5	2.3	2.8	1.8	0.7
Green	2.7	1.3	1.5	0.5	0.5	1.2
Green/Blue	5.3	2.3	1.6	0.4	0.3	0.7

Thus from the results we conclude that via the use of white and RGB light colour sources we are able to discriminate between different RGB colour surfaces with our simple nip structure 1D sensors.

As depicted in figure 4.37, the static responses shown in figure 4.36 have also been plotted overlapping the dynamic responses. This allows comparing the values between the static and dynamic results. Results show a good correlation between the static and dynamic condition since no significant variations were observed.

There was also a desire to observe a possible discrimination between derived colours and even between intermediate colours. The combined surface illustrated in figure 4.33(b) was used for this purpose and it is also shown for clarity in figure 4.38.

Figure 4.38 shows the normalized (relative to the signal of white colour) light signal intensity response (recorded by the sensor system) coming from the reflection of the combined colour surface (14 different colour target surfaces) in figure 4.33(b), when white, red, green or blue light illumination was used, as these surfaces moved from right to left (full travel distance of about 69 mm). The results were normalized in order to express the detected signal in accordance to its relative strength.

The results in figure 4.38 show good signal discrimination between primary colours and also between derived colours obtained by using different light sources. However, intermediate colour surface discrimination is more difficult, especially in the wavelengths corresponding to the lower spectral response of the sensor, such as blue and green. The sensor was designed to have an optimized response to red, in order to perform 3D profile detection using a red laser light. It can be redesigned in order to have a broader spectral response similar to a pin solar cell. Nevertheless, the results present a remarkable difference in the selectivity of the sensor for yellow, reddish derived and intermediate colours (red/magenta, magenta, yellow, orange and red). As already referred, the greenish and bluish colours are more difficult to discriminate due to the weak spectral response of the sensor to these wavelengths. Overall, results show that there are clear differences on the detection between derived colours, and also to a lesser extent, between intermediate colours.

When comparing the responses between primary, derived and intermediate colour surfaces, the relative differences are high between red-magenta, yellow, orange and red, and small between violet, dark blue and light blue as well as between green-blue, dark green and light green. The outcome is much the same when red light is employed although in this case the variations between yellow, orange and red are fairly small. Under green light illumination variations between the greenish colour surfaces are minor and so are the ones between red-magenta, magenta and the bluish colour surfaces. However, the differences between yellow, orange and red are considerable and there is a clear distinction between the greenish colour surfaces including cyan and the others.

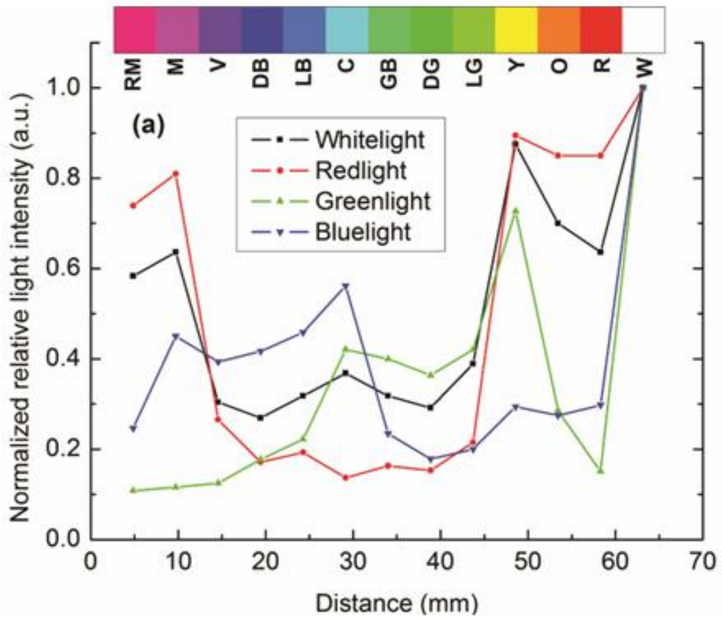

Figure 4.38 – Normalized relative light intensity as a function of the distance from right to left for the combined colour surface scanned (white, red, green and blue light).

As shown in figure 4.38, when blue light is employed small intensity variations are observed between the bluish colour surfaces as well as between the greenish colour surfaces and also between yellow, orange and red. A clear distinction between the bluish and greenish or reddish colour surfaces is noticeable. Overall, results show that using this sensor system in combination with various light sources it is possible to detect a specific colour by associating it to a particular value of integration time or to a precise power light intensity value.

Nevertheless, regarding the colour target surfaces shown in figure 4.33(b), a standard quantitative analysis based on the commonly known CIELUV colour model [14] was performed using the results obtained in figure 4.38 together with the measured spectral reflectance responses in figure 4.34. The CIELUV (CIE 1976 (L*, u*, v*) colour space) is a colour space adopted by the International Commission on Illumination (CIE) in 1976 and it is used to represent colourimetry colours as linear combinations of so-called primaries in a three-dimensional vector space [14]. In this colour space, the distance between two points approximately identifies how different the colours are in terms of luminance, chroma and hue. A uniform chromacity chart in this case related to CIELUV, illustrates the 2D positions of the reference and detected colours in order to be able to view the differences between them. In our case the detected colours refer to the values detected by the sensor system (figure 4.38) and the reference colours refer to the values measured by the spectrophotometer (figure 4.34). All existing monochromatic colours of the spectrum can be represented as fully saturated on the graph boundaries and as 0 saturated on the white (colour) point, located near the centre. Using this approach the colour detection performance of the sensor system is analyzed via the representation of colourimetric coordinates and subsequent colourimetric error calculation [14].

The RGB coordinates for each colour target surface were obtained using the detected values in figure 4.38 for the sensor system and using the measured (reference) values in figure 4.34 for the spectrophotometer. For example, for the case of a Magenta (M) colour target surface, the normalized values in figure 4.38 for each of the red (0.81), green (0.12) and blue (0.45) light reflections were converted respectively to each of the R (206.43), G (29.57), B (114.86) units or coordinates corresponding to the magenta colour surface. The RGB coordinates for every target colour surface shown in figure 4.34 were obtained at 700nm for Red (R), 546nm for Green (G) and 436nm for Blue (B), in accordance to the CIE Standard Primaries (1931).

The problem of negative weights in the RGB colour model was tackled in 1931 (CIE) replacing R, G, B by three new primaries **X**, **Y**, **Z**, when performing colour matching. The quantity of each of these **X**, **Y**, **Z** primaries required to match a specific colour **C** was characterized to be (*X*, *Y*, *Z*), leading thereby to the following expression [14]:

$$\mathbf{C} = X\mathbf{X} + Y\mathbf{Y} + Z\mathbf{Z} \qquad \textbf{[4.15]}$$

The CIELUV coordinates (L*, u*, v*) can be worked out from the tristimulus values XYZ or the chromaticity coordinates (x, y) using the relevant formulae, where the subscript w denotes the values for the white (colour) point [15]:

$$u^* = 13L^* \, [u' - u_w] \qquad \textbf{[4.16]}$$

$$v^* = 13L^* \, [v' - v_w] \qquad \textbf{[4.17]}$$

$$u' = \frac{4X}{X + 15Y + 3Z} \qquad \textbf{[4.18]}$$

$$v' = \frac{9Y}{X + 15Y + 3Z} \quad \textbf{[4.19]}$$

$$L^* = 116(Y / Y_w)^{\frac{1}{3}} - 16 \;,\; Y / Y_w > 0.01 \quad \textbf{[4.20]}$$

and in order to quantify the colour accuracy of the sensor system the colourimetric error, ΔE, is calculated using the following colour difference formula:

$$\Delta E = \sqrt{(L^*_2 - L^*_1)^2 + (u^*_2 - u^*_1)^2 + (v^*_2 - v^*_1)^2} \quad \textbf{[4.21]}$$

Once the RGB coordinates were known, the tristimulus values XYZ were calculated [14] and substituted into equations 4.18 and 4.19 in order to work out the CIELUV coordinates (L*, u*, v*). Figure 4.39 shows the resulting CIELUV plot comparing detected colours from the sensor system with reference colours measured by the spectrophotometer. Also the 3 standard well known genuine colours whose RGB values correspond to red (255, 0, 0), green (0, 255, 0) and blue (0, 0, 255) are plotted in order to define the CIELUV model boundaries of the diagram. The point where white colour lies, near the centre, is also clearly noted on the diagram.

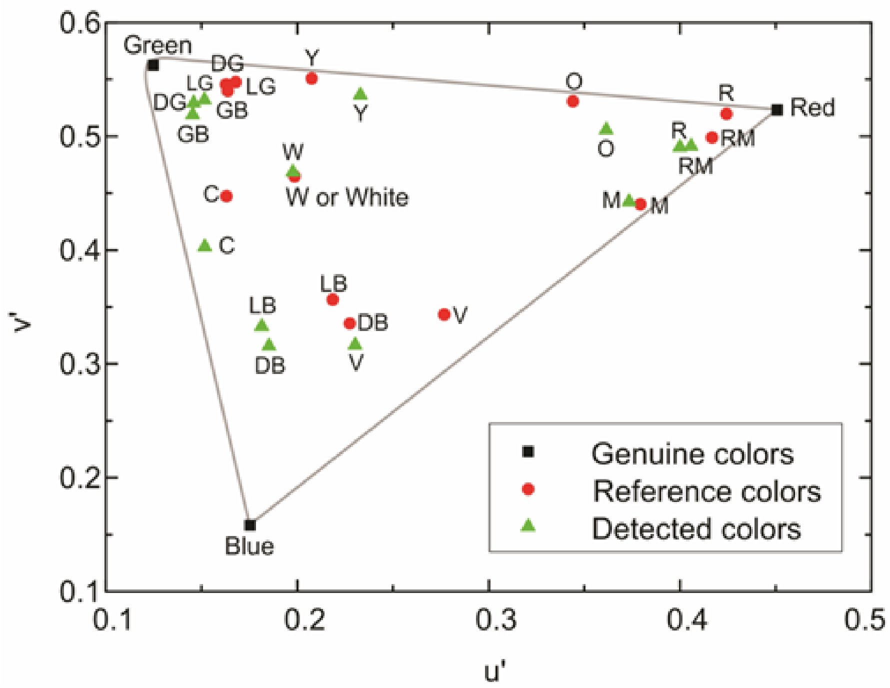

Figure 4.39 – CIELUV plot. Comparison between detected colours from the sensor system and reference colours measured by the spectrophotometer.

Table 4.6 lists the calculated CIELUV L*, u', v' and ΔE values for the sensor system and spectrophotometer for all target colour surface reflections. The units for the colourimetric error ΔE are just noticeable differences (j.n.d) for the human eye [14].

Table 4.6 – CIELUV L*, u', v' and ΔE values for the sensor system and spectrophotometer for all target colour surface reflections.

	Sensor system CIE-LUV			Spectrophotometer CIE-LUV			
Colour Surf.	*L**	*u'*	*v'*	*L**	*u'*	*v'*	ΔE (j.n.d.)
R/M	41.09	0.41	0.49	55.93	0.42	0.50	51.25
M	46.07	0.37	0.44	57.00	0.38	0.44	30.79
V	20.71	0.23	0.32	25.47	0.28	0.34	17.82
DB	21.87	0.19	0.32	20.67	0.23	0.34	14.28
LB	26.27	0.18	0.33	26.88	0.22	0.36	15.13
C	42.67	0.15	0.40	39.98	0.16	0.45	28.16
G/B	38.39	0.15	0.52	39.19	0.16	0.54	15.39
DG	34.82	0.15	0.53	39.70	0.16	0.55	15.73
LG	40.64	0.15	0.53	46.37	0.17	0.55	18.37
Y	77.23	0.23	0.54	91.35	0.21	0.55	44.31
O	51.72	0.36	0.51	64.84	0.34	0.53	35.48
R	47.82	0.40	0.49	56.10	0.42	0.52	47.62
W	100	0.20	0.47	100	0.20	0.46	0

From the results in table 4.6 the mean colourimetric error ΔE is calculated as 25.7 (j.n.d.). This value is perhaps still too high for practical applications and it is higher than commercial CCD TV colour cameras, considered to have a good colour reproduction quality while the mean colourimetric error is less than 4.3 [16]. However, when comparing to other amorphous silicon colour detectors, a value of 25.7 is within the range of those obtained by other researchers such as P. Rieve et al. [9], now that their mean colourimetric error varies from 6 to 49 (j.n.d.). In order to achieve the lower values of mean colourimetric error, such as 6, they apply colour correction methods. In our case we have not carried out any colour correction techniques and we still obtain a value which lies within the typical range for these amorphous silicon devices, even though our sensor is produced with a simple nip structure optimized to be most sensitive to red light. A nip structure similar to the one of a solar cell having a broader spectral response will be in principle more suitable to work as a PSD for colour detection.

In line with the colour theory, for the amorphous silicon sensor we have used the light power intensity measurements for red, green and green/blue light (not white) referred to in figure 4.35 in order to define the colour detection contribution of each R, G and B component. For this analysis we have assumed green/blue light to be blue since only a significantly small part of the green colour component seemed to be present. As expressed in equation 4.15, white is an arithmetic sum of all RGB components, however, here it is assumed that the colour detector has an equal sensitivity for red, green or blue. The amorphous silicon sensor is significantly more sensitive to red than to green or blue (see figure 4.14 or 4.35). For the red, green and blue colour components a maximum of 57.5%, 34.7% and 7.8% was detected respectively, and their sum equals 100% or white colour.

Besides being able to detect 3D object profiles, overall results obtained show that the 3D position sensitive detector made out of a single amorphous silicon nip junction can also detect primary colours of objects by a proper adjustment of the integration time of the sensor system and by combining white, red, green and blue (RGB) light sources. The variation of light intensity resulting from the loss caused by the colour filters used and the spectral response of the sensor at the green and blue wavelengths was compensated by adjusting the integration time of the system.

The system has been used to detect the different RGB colours by matching a light intensity value or range of values to a particular RGB hue. By using white light illumination we are able to identify a red colour surface from the ratio of the sensor signal obtained between a white surface and a red surface reflection. And of course we can also combine such a response together with the response obtained for red light illumination so as to verify red colour surface detection. When comparing such responses with the ones obtained for green, green/blue or blue light illumination we notice that primary green and blue colours can be distinguished as well as the derived and intermediate reddish colours. A typical mean colourimetric error of 25.7 has been obtained with this simple amorphous silicon nip sensor. Further improvements on colour detection can be made by proper optimization of the spectral response of the sensor.

4.10. Microscopy applications

Results obtained for the most relevant micropositioning and movement detection experiments performed are presented in this section. As already stated, the experimental setups described in section 3.5 (chapter 3) were used for most trials and only minor differences were introduced in order to acquire results regarding for example, the detection of the opening and closing of a microgripper.

4.10.1. Raw sensor micropositioning results

In line with the experimental trials described in section 3.5.1 (chapter 3), obtained results show a linear behavior of the photovoltage relating X and Y movement, a non-linearity of less than 2% and a spatial resolution of 600 μV/μm.

Results presented are related to the photovoltage signal measured on a multimeter with no bias applied to the sensor. The object was moving in the direction perpendicular to the sensor lines. The line numbering adopted is that one indicated in figure 3.13(a) (chapter 3) and the object movement starts at the highest number according to this numbering scheme (see figure 3.13(a)). First measurements were taken with the main purpose of determining the usefulness of the focusing lens placed before the sensor. These tests were done for the background reflected light and for other object positions.

The results for the background light with and without lens are shown in figure 4.40(a), while in figure 4.40(b) the photovoltage signal of several detectors is represented when the object is positioned at X = 0 and Y = -0.6 mm.

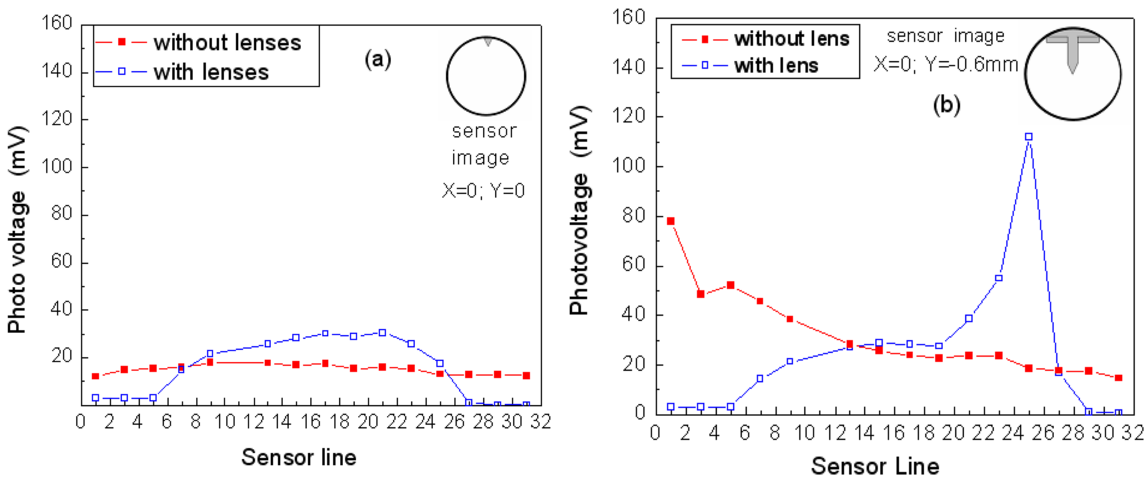

Figure 4.40 – Photovoltage measured at several 1D detectors of the 32 lines array sensor with and without focusing lens; (a) without image reflected (background) and (b) with image reflected.

From the results we observe that, by using the lens, the sensor lines from 1 to 5 and 27 to 32 were not detecting any light. That is due to the concentration of the beam in a smaller area when compared to when no lens was applied. On the other hand, also when using the lens, sensor line 25 shows the highest photovoltage. Lines 20–24 and 26 (figure 4.40(b)) also show a response. Without lens, lines from 1 to 14 have an enhanced signal compared to the background one, but when moving the object in the Y direction no significant change in the sensitivity was observed. Thus, the concentrated light by the lens is more adequate to signal selectivity and further results are all related to the measurements taken with lens.

The capability of the sensor was further evaluated by measuring the same detector lines as the position of the object was varied in Y and X direction. The object positions chosen are those shown in figure 4.41.

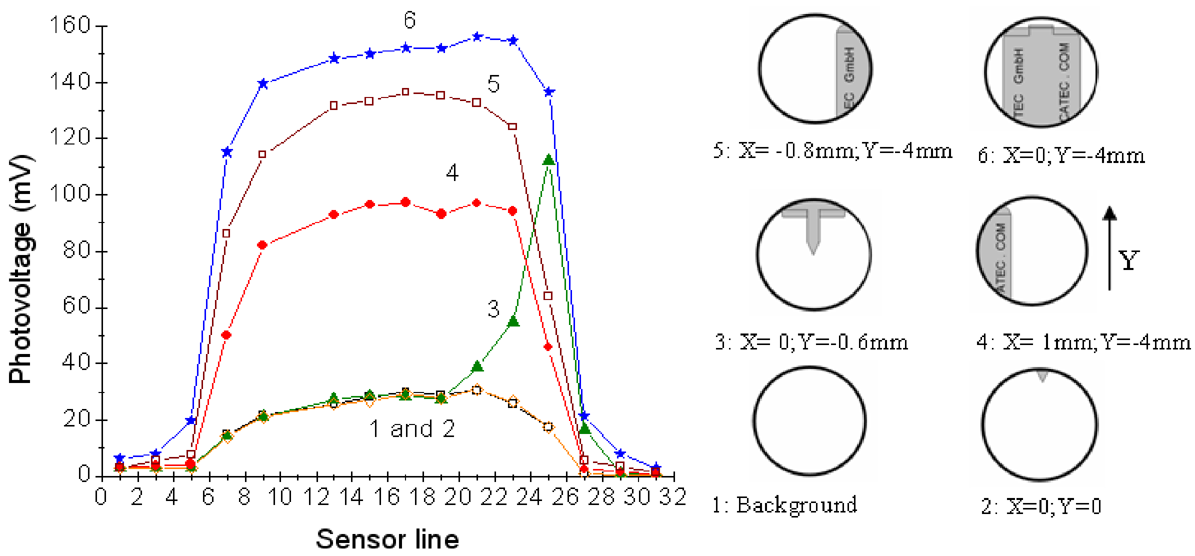

Figure 4.41 – Photovoltage signal measured at different lines of the 32 array PSD sensor and respective sketch of the object image for each corresponding position.

There we observe that for positions 1 and 2 the photovoltage signal measured at the 1D detectors clearly comes from background reflected light. In position 3 the cantilever starts to be detected by the sensors from 21 to 26, being the maximum signal obtained at line 25, which may correspond to some reflected light from the structure. When moving the object until the complete cantilever structure is observed (position 6), all sensor lines from 6 to 26 are detecting reflected light corresponding to a maximum signal of 140–160 mV. When keeping the Y position and moving the microcantilever structure in the X direction to positions 4 and 5 a decrease in the maximum detected signal is observed corresponding to less reflected light, however, every analyzed line detector is reading a photovoltage signal.

The results obtained for position 3 indicate that as the object is moving in the Y direction from position 1 (out of the field of vision of the microscope) to position 6 (whole cantilever holder inside the field of vision of the microscope) the sensor lines from 27 to 6 are detecting sequentially. To confirm that we have measured some of the active 1D detector lines for the Y position moving from 0 to -4 mm, the results are shown in figure 4.42(a).

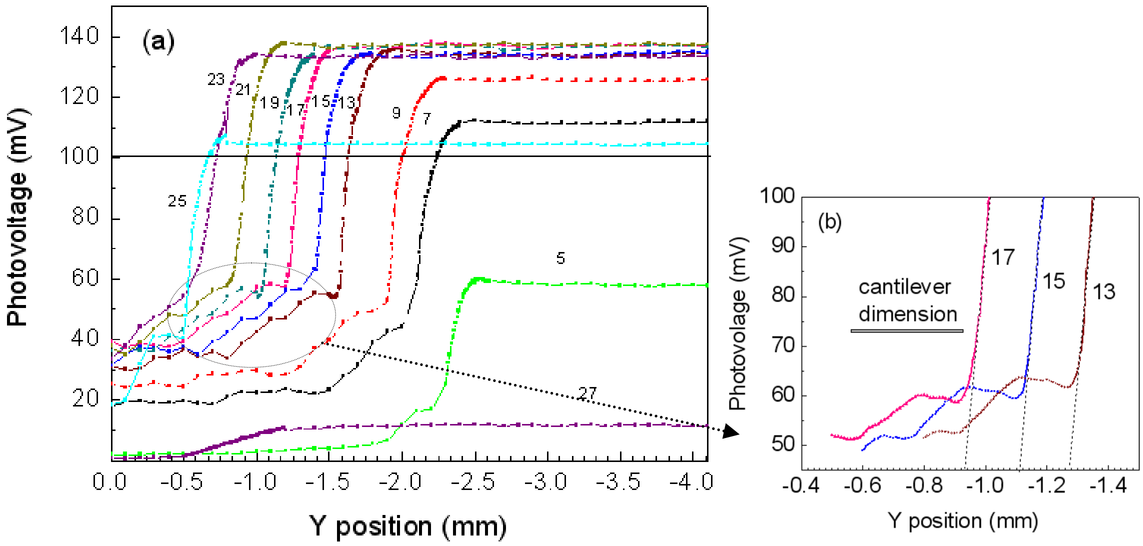

Figure 4.42 – (a) Photovoltage signal measured at different lines of the 32 array psd sensor and (b) enlargement of the region indicated in (a).

The variation of the photovoltage as the object is moving is similar for lines 23–7 being its shape shifted in the Y direction. We notice also that lines 5 and 27 are not detecting properly because they are in the limit of the microscope field image as already observed in figures 4.40 and 4.41. The spatial separation between the response of the lines is better analyzed in figure 4.42(b). Observing the response of lines 17, 15 and 13 in detail it can be seen that the spatial separation between them is constant and of about 170 μm. Within the width of the detector line, which is 270 μm wide, we have a linear variation of the photovoltage, from 60 mV to 130 mV, with a slope around 0.6 mV/μm for lines between 23 and 9. Therefore, we can say that the resolution of the sensor mainly depends on the moving step allowed by the mechanical system were the object is placed and on the electronic readout system.

The detection of the cantilever itself (not the holding structure) is also possible with this sensor. Looking in detail to the enlargement of figure 4.42(a), represented in figure 4.42(b), all lines have a bump corresponding to a 10 mV variation of the photovoltage just before the strong increase (60–130 mV). This variation happens for a spatial Y movement of around 400μm which corresponds to the dimension of the cantilever. Indeed, by analyzing the signal of the photovoltage of each line of a 32 sensor array it is possible to detect the position of a micrometer object, like this cantilever.

The linearity of the sensor is shown in figure 4.43.

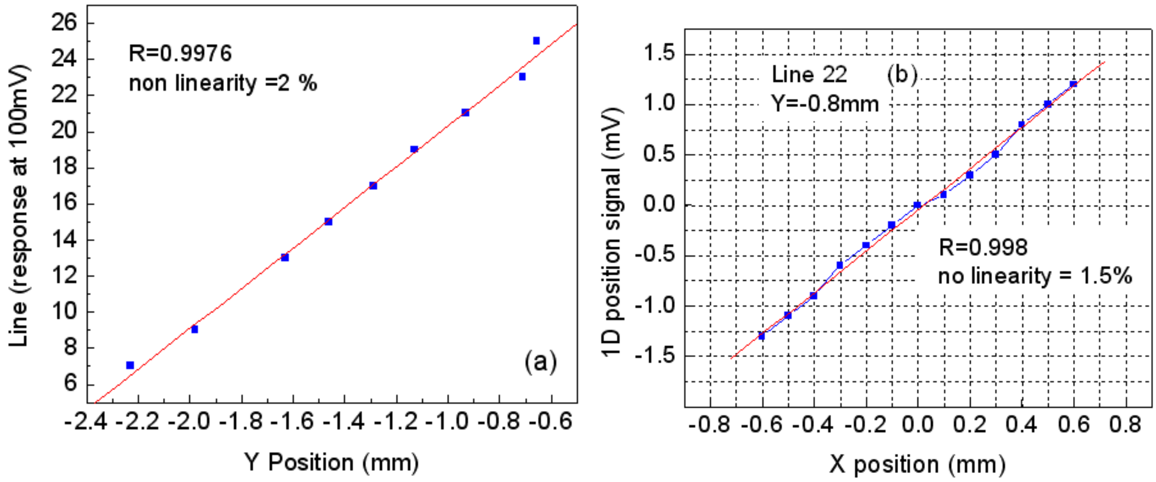

Figure 4.43 – (a) Response of the active sensor lines at a photovoltage of 100 mV as a function of Y position of the object (holding structure of cantilever). (b) Voltage signal of the top electrode of the sensor as a function of X position for a fixed Y position corresponding to the cantilever detection.

Figure 4.43(a) represents the behavior of each different detector for a photovoltage level of 100 mV as a function of the Y movement of the object. A linear response is obtained with a non-linearity of 2%. Besides the detection range of the sensor by moving the object in the Y direction, the 1D sensor also permits movement detection in the X direction keeping the Y position fixed. This can be observed by the graph of figure 4.43(b) where a linear and symmetric signal detection is observed. The results shown correspond to line detector 22, where the photovoltage signal relates to the cantilever light reflection (position 3). For this measurement the signal was taken using the two terminals of the TCO leaving the metal a floating terminal. That situation does not correspond to better sensitivity as it was demonstrated in previous works [17]. This explains the low voltage values measured, but still, a good uniformity and symmetry was observed. Anyhow, it is an evaluation of the functionality of the sensor in this mode.

The overall results obtained show the possibility of using a 32 linear array of 1D detectors based on the amorphous silicon technology to detect the movement of micrometer objects like a cantilever. X and Y movement can be detected with a resolution which will basically depend on the step movement of the table where the object is placed and on the precision of the electronic readout system. That is, it depends on the minimum voltage values that the electronic components can detect. Therefore further investigations are needed with an appropriate electronic controller in order to perform more measurements in order to find out the limitations (spatial resolution and linearity) and other possibilities of the sensor. The sensitivity of the sensor, in this particular application, with reverse biasing of the sensor as well as the application of calibrated resistances for improving the linearity of the 1D sensor measurement will be the focus of further and future work.

4.10.2. Sensor/System micropositioning results

In line with the experimental procedures described in section 3.5.1 (chapter 3), obtained results show a linear behavior of the photocurrent relating X and Y movement, with a non-linearity of about 3%, a spatial resolution of less than 2µm along the lateral dimension of the sensor as well as of less than 3µm along the perpendicular dimension of the sensor, when detecting just the micro-cantilever, and a spatial resolution of less than 1µm when detecting the holding structure.

Thereby, a good detection has been achieved with a linearity of about 97% along the lateral dimension of the sensor and the movement of the micro cantilever can also be properly detected with a resolution of better than 3µm (1µm corresponds to approx. 0.305 nA). The offset noise level present in reduced ambient light conditions, varies from a minimum value of 0.278 nA to approximately 0.417 nA, and never exceeds a maximum threshold value of 0.556 nA.

Results discussed in this section are related to the signal measured by a specially developed prototype system with 0 bias voltage applied to the sensor. That is, the sensor works in photovoltaic mode [18]. This mode is suitable for low light level and low frequency applications and it allows simplicity in system design and development. Response speed and linearity could improve via the application of a reverse bias, however, dark and noise currents as well as response variations due to temperature are likely to increase.

When the micro object is moving in the direction perpendicular to the sensor lines, the 1D/3D PSD detector line numbering adopted is that one depicted in figure 3.13(a) (chapter 3), where the micro object movement started at the highest number. However, when the micro object was moving in the direction parallel to the sensor lines, movement was taking place along a few sensor lines usually in the middle of the sensor (e.g., line number 17, 18).

All three different experimental results presented in figures 4.44(a–c) show the response of the sensor as the micro cantilever enters in parallel to the detectors. According to the numbering scheme in figure 3.13(a), the micro cantilever enters the sensor at line detector numbers 17, 18 for the case of figures 4.44(a) and (c) or at line detector number 7 for the case of figure 4.44(b). Movement detection happens as it moves in parallel to them. In figure 4.44(a), a focusing lens is used and channels 17 and 18 (C17, C18) detect, in figure 4.44(b), no lens is used and channel 7 (C7) detects and in figure 4.44(c), the micro cantilever is immersed in liquid and channels 17, 18 and 19 (C17, C18, C19) detect. The latter signal responses are a measurement of current (nA) versus position movement (µm). The instability presented on some signals is believed to be related to the flickering caused by the microscope lamp.

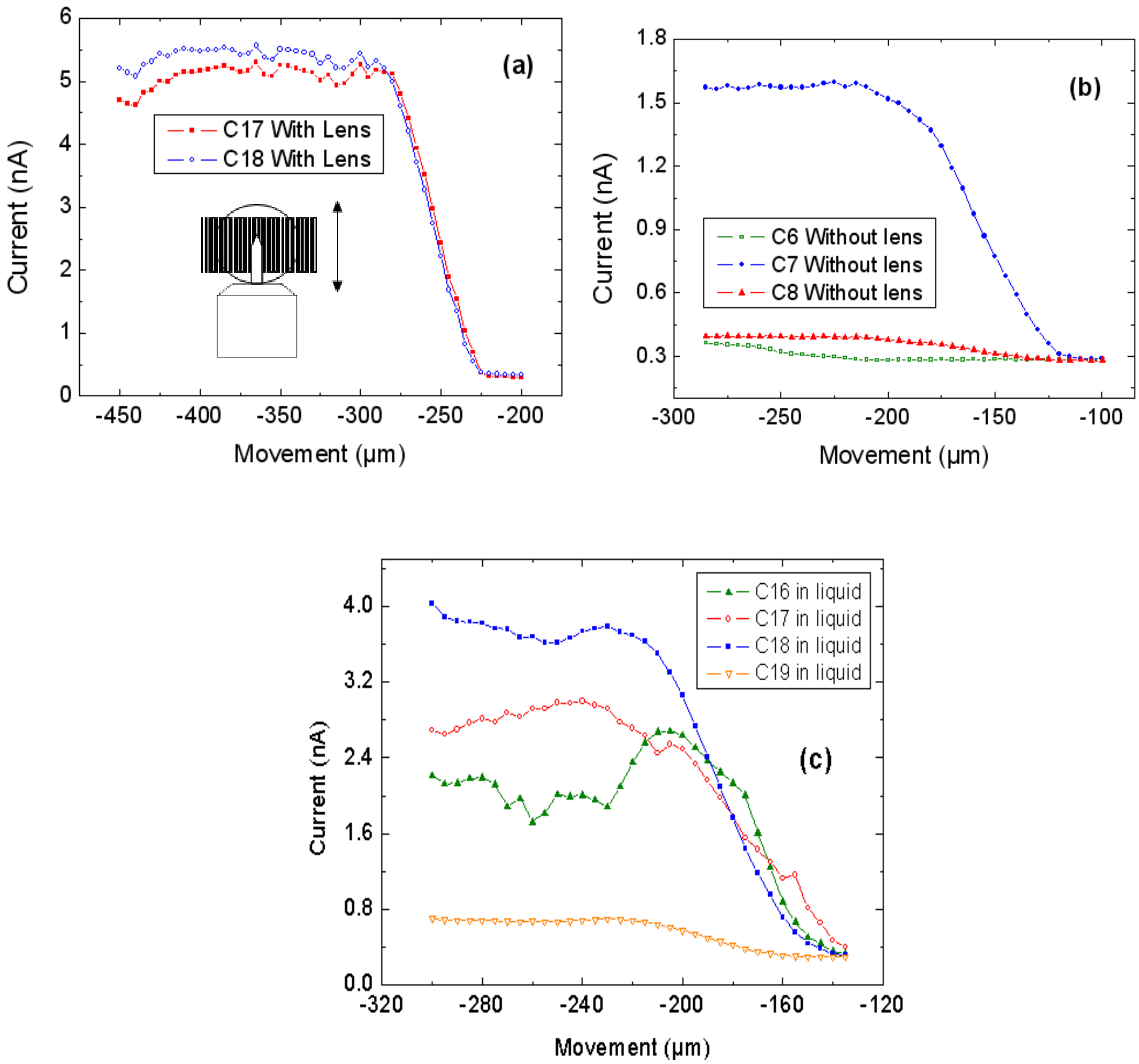

Figure 4.44 – (a) Sketch of the micro cantilever entering parallel to the sensor lines. It enters approximately at the centre of the sensor at detector 17 or 18 (b) Sketch of results according to when no focusing lens is used (c) Sketch of results for when the micro cantilever is immersed inside a liquid.

Liquid made it difficult to maintain the focus. In figure 4.44(c), the relevant three line detectors or channels (C17, C18, C19), obtain a signal response more than double that given by the noise level. The reason why there is instability coming from the response of at least one detector is because the slightest movement of the liquid was causing at some instances the loss of image focus on the sensor.

The set of results shown in figure 4.45 derive from the signal related to the movement detection coming from just the micro cantilever, which is being reflected on the viewing area of the microscope and do not derive from the signal linked to the movement detection coming from its holding structure. Now the micro cantilever was moved from side to side perpendicular to the detector lines. All channels except channel 7 (C7) show the response when the focusing lens is present and among these, channel 19 shows the response when the micro cantilever was moving inside a liquid. Channel 7 (C7) represents the behavior when no focusing lens is present. The viewing area of the microscope is projected around channel 7 when no focusing lens is present and around channels 17 or 18 when a focusing lens is present. An interesting observation from the results of figure 4.45 is that all channels are detecting for approximately 30 μm and this happens to be the same as the width of the micro cantilever.

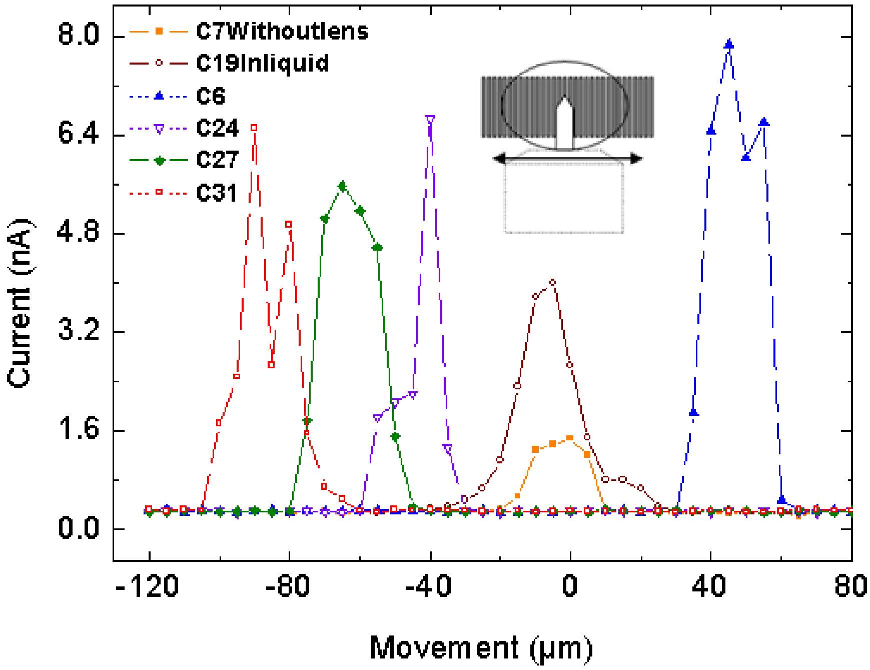

Figure 4.45 – Sketch of the micro cantilever moving sideways, after having entered parallel to the sensor lines as in figure 4.44.

The set of results in figure 4.46(a), show the response of the sensor as the micro cantilever enters perpendicular to it and therefore perpendicular to its channels too. These results also show the difference in terms of current (nA), between the signal linked to the movement detection coming from the micro cantilever and the signal related to the movement detection coming from its holding structure.

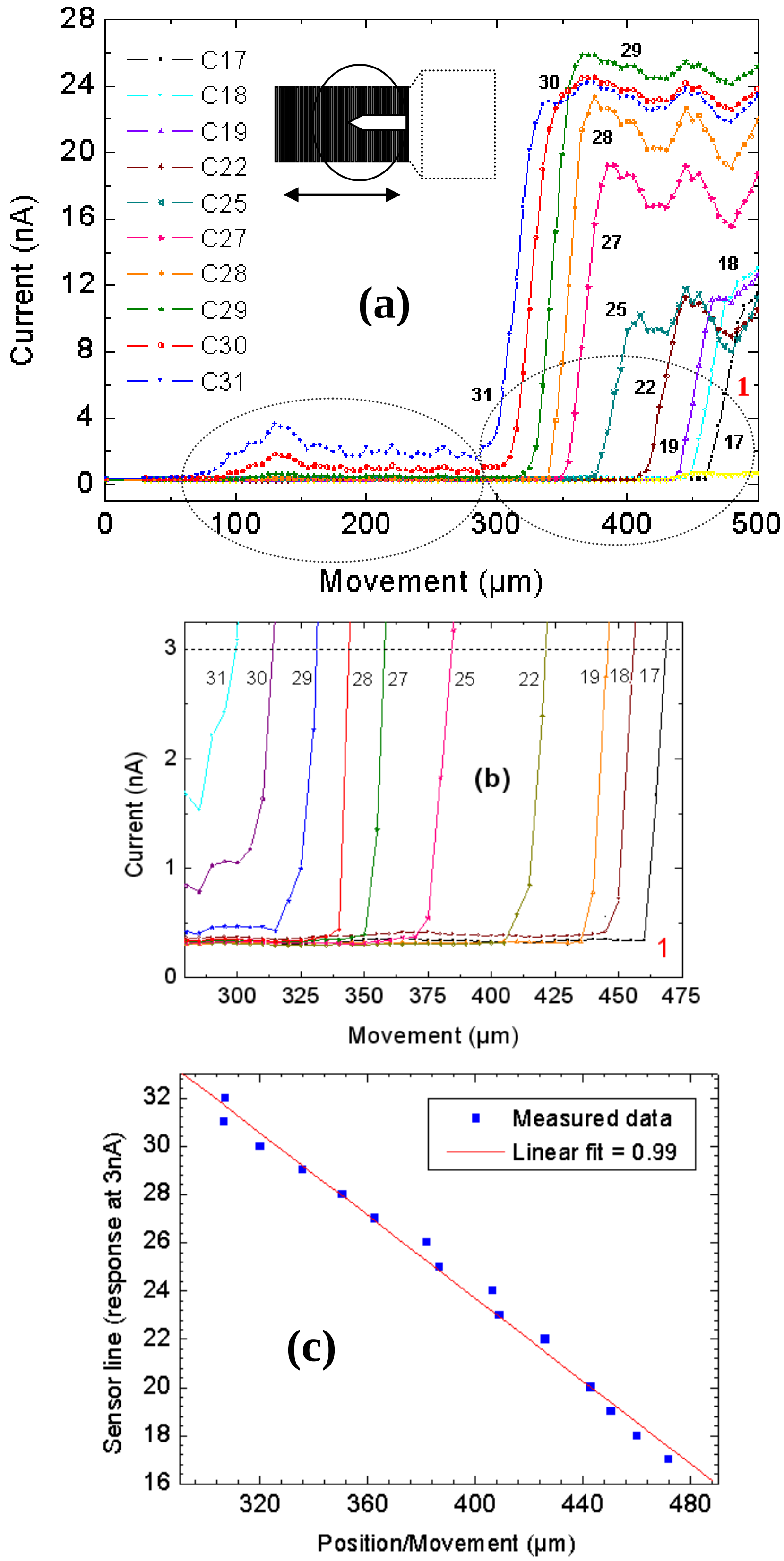

Figure 4.46 – (a) Sketch of the micro cantilever and its holding structure entering perpendicular to the sensor lines (b) Sketch of the response of each detector at the 3 nA threshold level, when just the holding structure of the cantilever is present (c) Sketch of the measured data at each detector for the 3 nA threshold level and its related linear fit.

As previously stated, the micro object was moving in the direction perpendicular to the sensor lines and the line numbering adopted is that one indicated in figure 3.13(a) (chapter 3), where movement started at the highest number. For these particular results, the movement of the micro cantilever and its holding structure were both scanned in steps of 5 µm.

In figure 4.46(a), the signal related to the movement detection coming from the micro cantilever extends from 100µm to about 300µm. This indicates that only the first 200 µm from the length of the micro cantilever are detected, as opposed to 400µm, which is the real length of the micro cantilever. The remaining 200µm of micro cantilever are believed to be included (and masked) in the signal detecting the holding structure which starts after 300 µm. It is at that point that the holding structure starts to enter the field of view and the signal response boosts rapidly stabilizing at that level. The difference between the light reflected by the micro cantilever and the holding structure is therefore clearly seen. As shown in figure 3.13(c) (chapter 3), the holding structure has a much bigger cross sectional area than the micro cantilever and therefore reflects much more light. Again, the instability present on some signals is believed to be related to the flickering caused by the microscope lamp.

Figure 4.46(b) shows the response (as a function of position/movement) obtained by all line sensors just for the signal related to the holding structure (not the signal related to the micro cantilever) at the 3 nA line, which cuts across in order to help determining linearity of the sensor in this particular situation, which is next sketched in figure 4.46(c).

Figure 4.46(c) presents the measured data by all sensor lines when they are detecting exactly at the 3 nA threshold. As the holding structure moves along (position in µm), the line sensors are detecting sequentially and in the right order as it should be. The linearity of the sensor is thus represented by the linear fit and the correlation coefficient is 0.99 (99%).

The set of measurements shown in figure 4.47(a) derive from the signal related to the movement detection coming from just the micro cantilever, and do not derive from the signal linked to the movement detection coming from its holding structure.

Once the micro cantilever is in the viewing area of the microscope, its movement is recorded as it is moved from one side to the other side of the sensor lines, in the indicated direction of movement. This time, the micro cantilever is moved along the lateral dimension of the detector lines and a focusing lens was used. The position signal response coming from several line detectors (C27, C28 and C29), clearly shows a difference between moving from left to right of the sensor. Each detector line measures 7mm and therefore the range extends from −3.5 mm to +3.5 mm. The reason why some channels perform better than others is because of minor differences in the internal material characteristics between each detector, resultant from the fabrication process.

Figure 4.47(b) shows only channel 28 (C28) from figure 4.47(a) because it is the sensor line that responds best to position detection. The sketched red line represents the linearity of this particular detector, in this particular situation, in which the linear correlation coefficient is 0.97 (97%).

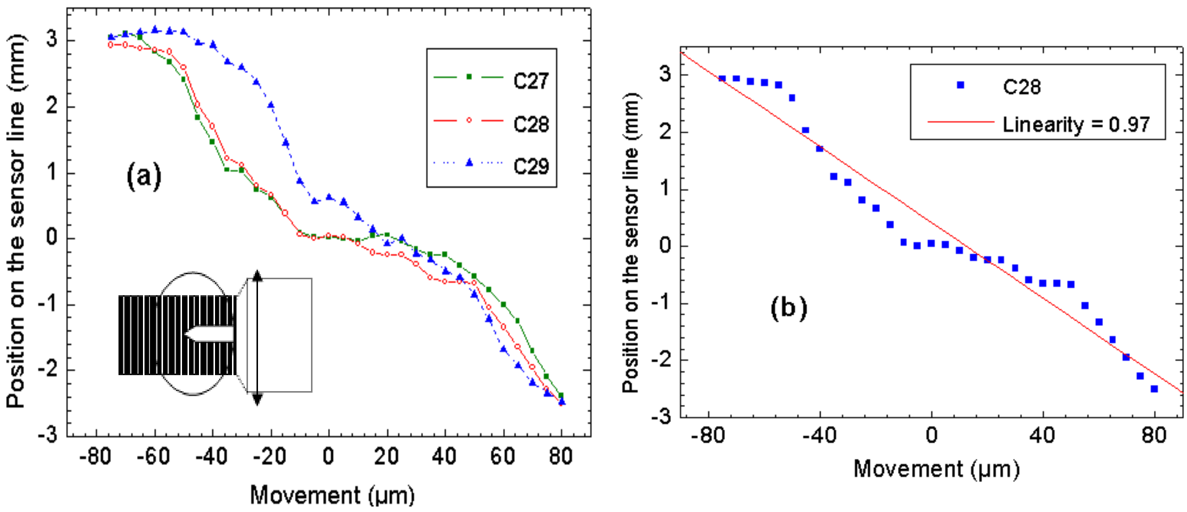

Figure 4.47 – (a) Sketch of the micro cantilever moving sideways, after having entered perpendicular to the sensor lines as in figure 4.46. (b) Sketch of the best channel response from figure 4.47(a) and its related calculated linearity.

The results obtained show the possibility of using a linear array of 32 1D line detectors based on the amorphous silicon technology and relevant system to detect the movement, dimensions and 2D position of micrometer objects like a cantilever. It can be concluded that placing a focusing lens before the sensor is preferred since a higher overall channel intensity signal is obtained. From the set of experimental results obtained in this work, it can also be concluded that the best way to detect the movement of the micro cantilever is when it enters the field of view parallel to the sensor lines. There is also a logical relationship between the cross sectional area of the object appearing in the field of view and the level of signal acquired. Of course, the greater the area of the object, the higher the light reflected.

As previously stated, in terms of dimensions, figure 4.45 shows all channels detecting for approximately 30 μm and this happens to be the same as the width of the micro cantilever.

Also as already mentioned, in figure 4.46(a) only the first 200 μm from the length of the micro cantilever are detected, as opposed to 400μm, which is the real length of the micro cantilever. The remaining 200μm of micro cantilever are believed to be included (and masked) in the signal detecting the holding structure (which starts after 300μm in figure 4.46(a)).

Concerning positioning, X and Y positions (2D) can be determined based on the information and/or the shape of the signal responses obtained. Also here X and Y movement can be detected with a resolution which will basically depend on the step movement of the table were the object is placed, the precision of the electronic readout system, and the optics used. That is, it depends on the minimum values of photocurrent that the electronic components can detect.

This kind of setup offers the possibility to detect if a micro object is moving, what are its dimensions and what is its position in two dimensions, even at high speeds. In microscopy applications, a micro object could be moving on the translation table of the microscope and reflecting the microscope light incident on it as an image onto the 32 linear array of 1D line detectors. Movement signals would be detected as it starts to appear perpendicular to the sensor and when it has already passed by and these will define one dimension (e.g., length) and will also determine the Y position of the reflected micro object on the sensor. The other dimension (width) and the X position would be detected when the object moves parallel to the sensor along the line detectors. On top of that it would be possible to detect those movement signals automatically if an object moves below the microscope by being able to trigger some kind of warning if movement occurred.

4.10.3. Sensor/System microgripper detection results

The following results were obtained in line with the experimental trials described in section 3.5.1 (chapter 3) when a microgripper was used.

The gripper was moved to different X and Y positions. The X and Y movement as well as the opening and closing of the microgripper were detected under microscope magnifications of 10X and 20X. Due to constraints in controlling the closing/opening of the micrograppers, in this case, measurements were only obtained when the gripper was fully opened or fully closed. Cables were connected to the microgripper as shown in figure 3.14 (chapter 3) so as to be able to apply a voltage (0 - 63V) through it in order to open or close the microgripper. Figure 4.48 shows a picture of the microgripper and its structure.

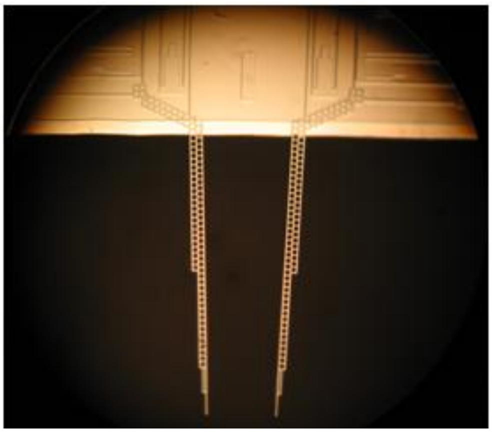

Figure 4.48 – Picture of the microgripper and its structure.

The dimensions of the microgripper were as listed in table 4.7:

Table 4.7 – Dimensions of microgripper

	Measured dimensions (μm)
Separation between tweezers at beginning of gripper	380
Separation between tweezers at middle part of gripper	336
Separation between tweezers at end part of gripper	285
Approximate length of each of the grippers	1000
Width of the tips at end of gripper	4
Approximate width of the tweezers at middle part	50
Approximate width of the tweezers at beginning of gripper	100

As already explained in the experimental trials described in section 3.5.1 (chapter 3), the 32 position sensitive detector array sensor was placed in parallel to the gripper within the field of vision of the microscope as shown below in figure 4.49.

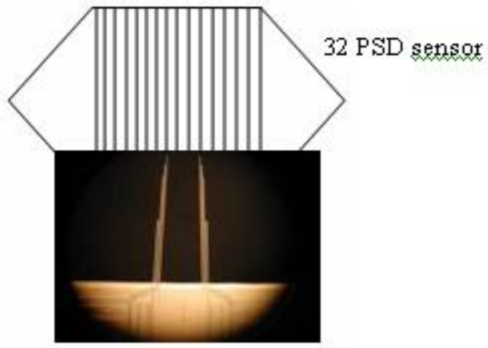

Figure 4.49 – Microgripper in parallel to the 32 PSD sensor active area.

In this configuration the image was focused only on the bottom part (lower half) of the sensor active area, therefore we were only using the lower half of the sensor for detection.

Figure 4.50(a) shows a picture of the microgripper as seen on the ocular of the microscope and figure 4.50(b) shows its detection or 2D representation by the PSD system when using a 3.5X microscope lens magnification and a maximum light intensity setting on the microscope. Here, the 15^{th} and 21^{st} channel of the sensor (seen from left to right) were detecting. All subsequent results in this section were also obtained at maximum microscope light intensity. Figure 4.50(c) shows the microgripper sensor system detection when a 13.5X magnification was used, and here, channels 12 and 24 were detecting the signal, since the image was now bigger due to an increase in magnification.

Figure 4.51(a) shows a picture of the tips or the end part of the tweezers and figure 4.51(b) shows the relevant PSD system 2D representation at 3.5X magnification. A maximum DC voltage of 63V was then applied to the microgripper which closed 15 degrees. Figure 4.51(c) shows the system response representation for the closed status of the microgripper tips also at 3.5X magnification. Here, 7 channels are sensing as opposed to the 4 channels detecting in figure 4.51(b), and this is why the area detected is bigger for each tip.

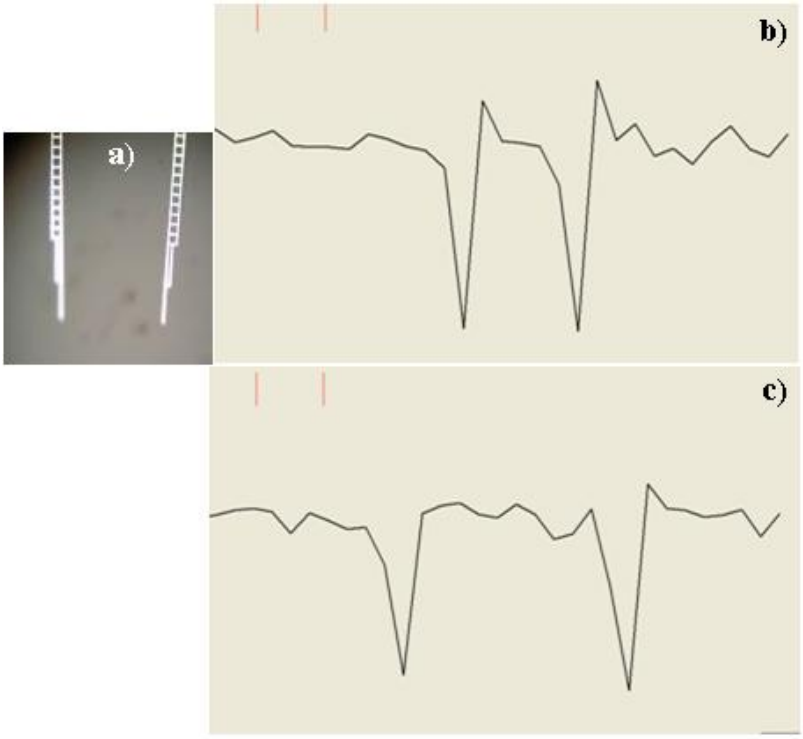

Figure 4.50 – (a) Picture of the microgripper as seen on the ocular of the microscope. (b) PSD system detection of gripper at 3.5X magnification. (c) PSD system detection of gripper at 13.5X magnification.

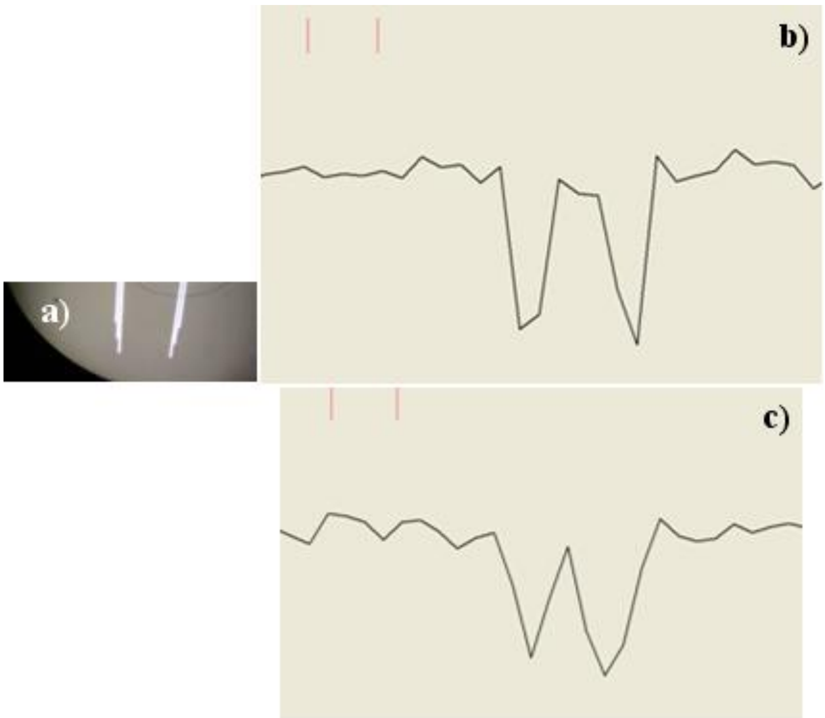

Figure 4.51 – (a) Picture of the microgripper tips. (b) PSD system detection of gripper tips at 3.5X magnification. (c) PSD system detection of gripper tips (3.5X) when closed 15º (63V).

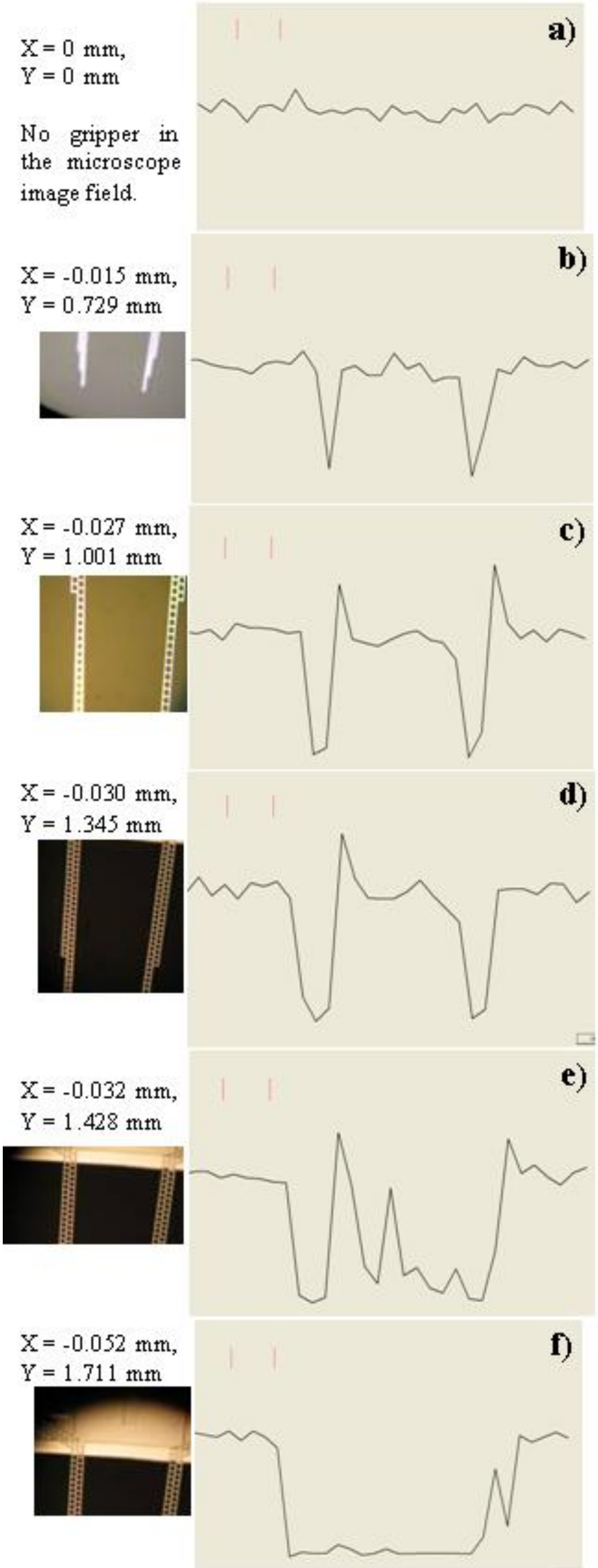

Figure 4.52 – Microgripper Y-axis movement PSD system detection (13.5X magnification).
(a) No gripper. (b) Gripper tips. (c) Middle part of tweezers. (d) Beginning of tweezers.
(e) Part of gripper structure and part of tweezers. (f) Gripper structure and small part of tweezers.

The microgripper was moved in the Y-axis and the PSD system sensed that movement as shown at several recorded positions, in figures 4.52(a-f).

Initially no gripper was present in the ocular of the microscope, however, gradually as the microgripper moved in the Y-axis, the tips, complete tweezers and its structure were all detected.

The microgripper was also moved in the X-axis and the PSD system also sensed that movement as shown at several recorded positions, in figures 4.53(a-d). The X movement started at the same position recorded in figure 4.52(c) and the microgripper moved in both directions (-X and +X) from that initial point. At first the middle part of the tweezers are present on the ocular of the microscope, however, gradually as the microgripper moved in the X-axis, only the left or right tweezer is detected for –X or +X displacement respectively.

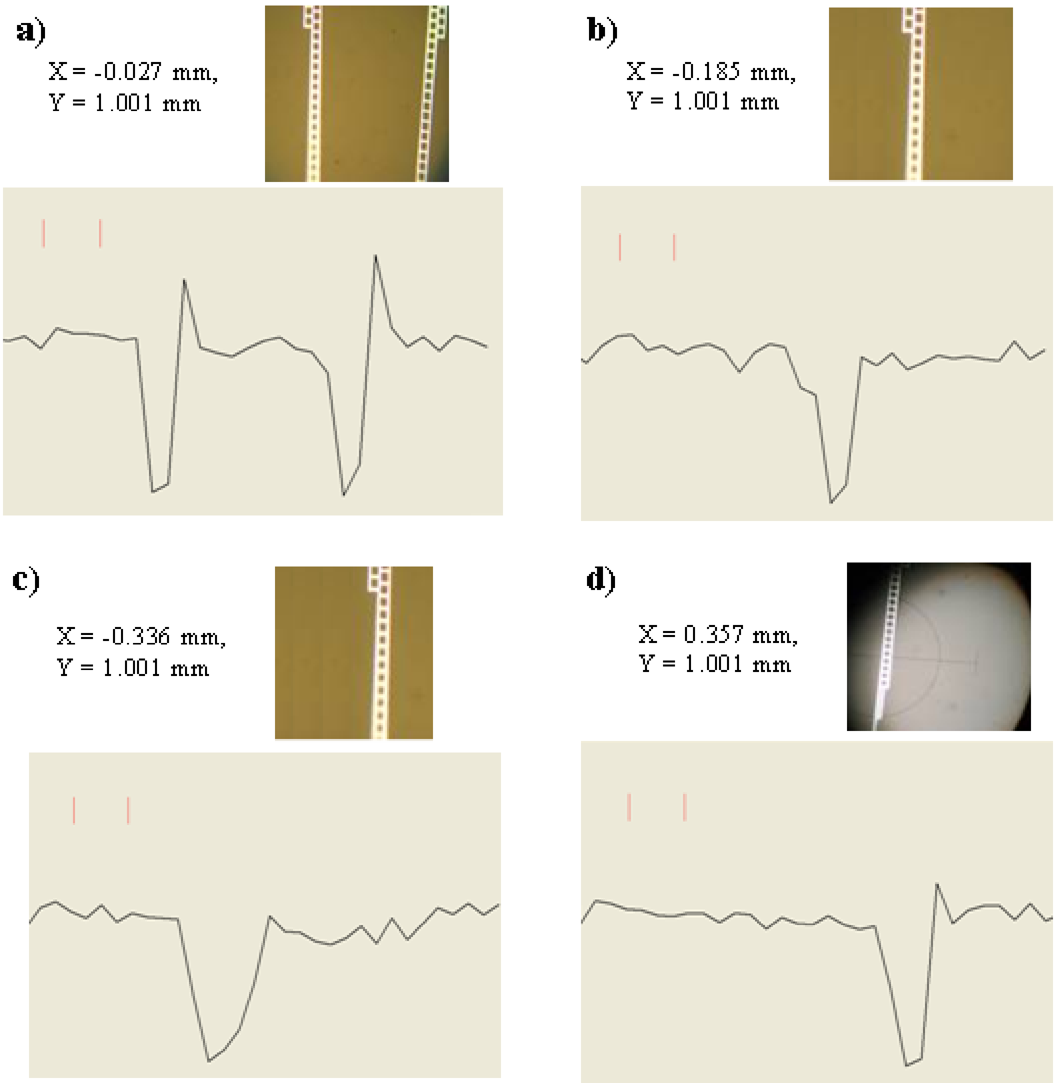

Figure 4.53 – Microgripper X-axis movement PSD system detection (13.5X magnification).
(a) Middle part of tweezers (figure 4.52(c)). (b) Left tweezer moved right (-0.185mm).
(c) Left tweezer moved further right (-0.336mm). (d) Right tweezer moved left (0.357mm).

From these results we conclude that the vertical and horizontal movement of a microgripper can be detected under the microscope using the sensor/system and at the same resolution as obtained when analyzing the microcantilever movement in section 4.10.2. Similarly, the opening and closing movement of the microgripper is also detected.

4.11. References

[1] A. Kawasaki and M. Goto, Sensors & Actuators A21-A23 534, 1990.

[2] A. Fantoni, M. Viera and R. Martins, “Influence of the intrinsic layer characteristics on a-Si : H p-i-n solar cell performance analysed by means of a computer simulation,” Sol. Energ. Mat. Sol. C. 73, 151-162, 2002.

[3] E. Fortunato, G. Lavareda, R. Martins, F. Soares and L. Fernandes, “High detection resolution presented by large-area thin film position-sensitive detectors,” SPIE Proc. 2397, 259-270, 1995.

[4] V. Raja and K. J. Fernandes, Reverse engineering - an industrial perspective (Springer, 2008).

[5] P. B. Petrović, “Rubberized cord thickness measurement based on laser triangulation, part I: technology,” FME Transactions 35, 77-84, 2007.

[6] S. Zhang, L. Raniero, E. Fortunato, X. Liao, Z. Hu, I. Ferreira, H. Águas, A.R. Ramos, E. Alves, and R. Martins, “Characterization of silicon carbide thin films and their use in colour sensor,” Sol. Energ. Mat. Sol. C. 87, 343-348, 2005.

[7] K. Eberhardt, T. Neidlinger, and M.B. Schubert, “Three-color sensor based on amorphous nipin layer sequence,” IEEE T. Electron Dev. 42, 1763-1768, 1995.

[8] J. Zimmer, D. Knipp, H. Stiebig, and H. Wagner, “Amorphous silicon based unipolar detector for color recognition,” IEEE T. Electron Dev. 46, 884-891, 1999.

[9] P. Rieve, M. Sommer, M. Wagner, K. Seibel, and M. Böhm, “A-Si:H color imagers and colorimetry,” J. Non Cryst. Solids 266, 1168-1172, 2000.

[10] H. Stiebig, J. Giehl, D. Knipp, P. Rieve, and M. Böhm, “Amorphous silicon three color detector,” Mat. Res. Soc. Symp. Proc. 377, 517-522, 1995.

[11] D. Knipp, H. Stiebig, J. Fölsch, F. Finger, and H. Wagner, “Amorphous silicon based nipin structure for color detection,” J. Appl. Phys. 83, 1463-1468, 1998.

[12] R. Martins, E. Fortunato, I. Ferreira, and A. Tagliaferro, “Process and method of adjustable color sensors operate able to achieve maximum accuracy in detecting color on light beams,” Portugal Patent PT103936, 2009.

[13] Sens-Tech Ltd, Langley, Berkshire, United Kingdom, SL3 8DS, www.sens-tech.com (accessed 02-09-2013).

[14] G. Wyszecki and W.S. Stiles, “Color science: concepts and methods, quantitative data and formulae,” (Wiley, 1982).

[15] J. Schwiegerling, “Field guide to visual and ophthalmic optics,” (SPIE Press, 2004).

[16] P. Seitz, D. Leipold, J. Kramer, and J.M. Raynor, “Smart optical and image sensors fabricated with industrial CMOS/CCD semiconductor processes,” Proc. SPIE 1900, 21-30, 1993.

[17] H. Águas, L. Pereira, D. Costa, E. Fortunato, and R. Martins, “Super linear position sensitive detectors using MIS structures,” Opt. Mater.27(5), 1088–1092, 2005.

[18] E. Fortunato, L. Pereira, H. Águas, I. Ferreira, and R. Martins, “Flexible a-Si:H position sensitive detectors,” Proc. IEEE 93(7), 1281–1286, 2005.

Chapter 5

Final conclusions and future work

Chapter 5. Final conclusions and future work

Summary

This chapter lays out the overall conclusions gathered during this thesis work and proposes new ideas for future work in this particular area.

To briefly summarize the work performed and support the conclusions drawn, one working system (32 PSD XDAS) was built for the 32 amorphous silicon PSD array sensor. Another two systems were also constructed for the 128 amorphous silicon PSD array sensors. The first of these systems (128 PSD XDAS) is functioning correctly in the same way as the system (32 PSD XDAS) for the 32 PSD sensor, since it is effectively an expansion of the latter in terms of size and capabilities. The remaining 128 PSD sensor system (128 PSD NIDAQ) suffered from excessive electronic noise and based on the acquired knowledge, a new system version is under development. All relevant hardware and software were integrated as detection systems. The 32 PSD array sensor was inserted into its relevant system whenever needed and their performance was evaluated for machine vision applications such as for example 3D object rendering as well as for microscopy applications such as for example micro object movement detection

The 32 PSD array sensor was fabricated as a nip structure without any intermediate buffer layers. The chosen n, i, and p layer thicknesses were 40, 600 and 10 nm respectively and none of these or other already addressed fabrication parameters were significantly varied since the position determination capability of the sensor array was working correctly via these settings. The spectral response peak of the nip structure is located at around 650 nm, corresponding to the highest sensitivity for red color and the overall response of the device extends from approximately 500 to 750 nm.

5.1. Conclusions regarding the use of the sensor/system for machine vision

Overall results demonstrate the possibility of using a linear array of 32/128 1D line sensors based on the amorphous silicon technology to render 3D profiles of objects. The system and setup developed enables 3D rendering at high speeds and at high frame rates. The system offers a wide dynamic range allowing it to adjust to the intensity levels produced by each sensor. In turn, this also means that a wide range of light source power levels is accepted by the system (even low ones). Sensor channel non-linearities of approximately 4 to 7% were achieved.

The speed analysis performed on the sensor system shows that the lower resolution of the fastest speed responses makes the objects look less detailed and thereby more rounded. This is because at the highest speeds the number of 3D scanned points is low such as for example, 40 points for 1 sensor channel 3D scan, as opposed to the 169 points scanned for the lowest speeds. Nevertheless, the sensor system is able to respond and detect at all speeds experimented.

A mean degradation percentage of about 42% was recorded for the 32 PSD array sensor, and a mean degradation percentage of 36% was obtained when the sensor was coated with SiO_2. Thereby, it can be concluded that coating the sensors with a SiO_2 layer can improve the degradation percentage (e.g. from results, by about 6%), even when a laser light is reflected for so many hours (1 week). This coating layer does not prevent degradation significantly, but it can somehow reduce the percentage of degradation of the sensor by some amount.

Based on results obtained, the minimum detail or gap that can be detected by the sensor system developed is approximately 350 μm. A value lower than 350 μm cannot be detected due to experimental setup limitations, such as the image frame optics reduction factor or a smaller sensor size than the real object. The possibility to render an object in 3D within a scanning angle range of 15º to 85º and identify its real height as a function of the scanning angle and the image displacement distance on the sensor, was demonstrated. It was also observed that small angles allow for a high detailed but slow 3D analysis of the object and inversely, large angles allow for a low detailed but rapid 3D analysis of the object. However, all the 3D detection experiments were performed keeping the incident beam at 45º relatively to the reflected one from the sensor.

Results show how simple and complex objects can be rendered in 3D properly and accurately also at high resolution, using this sensor and system platform. The accuracy of the method depends mainly on the sensor resolution as well as on the precision of the light source and the optical geometric dimensions used. The rate of acquisition and the translation table speed determine the gap between frames of the object. The higher the number of frames the higher the expected profile resolution. The sensor system is capable of acquiring data at a minimum of 8ms under the current configuration which is limited by Windows. At this rate of acquisition the lowest possible resolution obtained by the sensor system was 30μm. This means that during the 3D scanning process, one frame was acquired every 30μm. A sensor system repeatability of about 98.6% was achieved, thereby confirming its remarkable performance for scanning 3D profiles of objects.

Results reveal and conclude that it is possible to use the sensor and system to detect surfaces other than plastic and colours other than white. For example, a wood surface with light brown colour was detected and a sensor channel non-linearity of about 5% was achieved. It is also possible to use the sensor and system with various light color sources such as red and green lasers or any light color lamps corresponding to the spectral response of the sensor. The nip sensor system can detect primary and even derived colors of objects by a proper adjustment of the integration time of the system and by combining white, red, green and blue (RGB) light sources. The system was used to detect the different

RGB colors by matching a light intensity value or range of values to a particular RGB hue with a mean colorimetric error of 25.7.

It is important to note that all of the results reported in this work can be reproduced when using the 128 PSD array sensor system (128 PSD XDAS). The reason is that the underlying hardware, software and functioning of the 32 and 128 PSD systems is exactly the same but expanded.

5.2. Conclusions regarding the use of the sensor/system for microscopy

We have demonstrated the possibility of using the 32 linear array of 1D PSD detectors (32 PSD sensor) based on the amorphous silicon technology to detect the movement of micrometer objects like a cantilever. X and Y movement can be detected with a resolution which will basically depend on the step movement of the table where the sensor is placed and on the precision of the electronic readout system. That is, it depends on the minimum voltage values that the electronic components can detect. A linear behavior of the photovoltage relating X and Y movement was achieved with a non-linearity of less than 2% and a spatial resolution of about 600 µV/µm.

The 32 PSD array sensor and system was also used to detect the movement of micro objects such as a cantilever or a gripper. In this case results show a linear behavior of the photocurrent relating X and Y movement, as opposed to a photovoltage, and a non-linearity of about 3% was obtained as well as a spatial resolution of less than 2µm along the lateral dimension of the sensor as well as of less than 3µm along the perpendicular dimension of the sensor, when detecting just the micro-cantilever, and a spatial resolution of less than 1µm when detecting its holding structure. This kind of setup offers the possibility to detect if a micro object is moving, as well as its dimensions and position in two dimensions, even at high speeds. X and Y movement can be detected with a resolution which will basically depend on the step movement of the table were the object is placed, the precision of the electronic readout system, and the optics used. That is, it depends on the minimum values of photocurrent that the electronic components can detect. For the case of the microgripper, the opening and closing movement was also detected in addition to X or Y axis displacement. The X and Y positions (2D) can be determined based on the information and/or the shape of the signal responses obtained.

5.3. Future work

In order to obtain better 3D profile image quality an improvement on sensor channel position response, reproducibility and degradability is desirable for both the 32 and 128 PSD array sensors. To achieve that, an improvement on the encapsulation and SiO_2 protection layers could further reduce the degradation percentage of the sensor itself.

A new system is under development for the 128 PSD array sensor with new hardware/software implementations and modifications in order to remove the existing excessive electronic noise, as well as to enhance the capabilities of the present systems.

Further improvements on color detection can be made by proper optimization of the spectral response of the sensor.

For the integration of the 32 PSD sensor system in a microscopy application scenario, a micro object could be moving on the translation table of the microscope and reflecting the microscope light incident on it as an image onto the 32 linear array of 1D line sensors. Movement signals would be detected as it starts to appear perpendicular to the sensor and when it has already passed by, and these will define one dimension (e.g., length) and will also determine the Y position of the reflected micro object on the sensor. The other dimension (width) and the X position would be detected when the object moves parallel to the sensor along the line sensors. On top of that it would be possible to detect those movement signals automatically if an object moves below the microscope by being able to trigger some kind of warning if movement occurred.

APPENDIX A

Fabrication of the amorphous silicon position sensitive detector arrays (PSD arrays)

APPENDIX A - Fabrication of the amorphous silicon position sensitive detector arrays (PSD arrays)

A1 – Cleaning of the substrate

a) A glass measuring 10cm × 10cm × 0.1cm is taken. Using a special black pen, straight lines are drawn at 3.9cm from all edges of the 10cm × 10cm × 0.1cm glass. This leads to four smaller glass squares measuring 3.9cm × 3.9cm × 0.1cm which are cut via a glass cutting machine using the black lines as guides. These glass squares will be our four substrates.

b) In the next step a liquid detergent of the make Deconnex is used. Since it is concentrated detergent it needs to be mixed with ultra-pure water. Thereby, as indicated, a small container is filled with one fifth of detergent and the rest is filled with ultra-pure water. The four substrates are then washed using such a detergent mixture and handled with gloves and tweezers in order to avoid any particles of dirt to adhere onto the surface of the substrate. They are finally rinsed using ultra-pure and dried using a nitrogen gas gun.

c) During this step the substrates are placed inside a rack support. The rack support is immersed into a glass container filled with acetone which covers all samples. The glass container is placed inside an ultrasonic device for 15 minutes. Immediately after, the rack support is taken out of the glass container filled with acetone and is immersed another 15 minutes into a glass container filled with isopropanol (alcohol) which again covers all samples. Finally the rack support is taken out of the glass container and the bottom part of all samples is dried using a nitrogen gas gun. The samples are then ready for the next step, photolithography, which should be performed immediately after they are taken out of the glass container filled with isopropanol.

A2 - Photolitography

a) In line with the final part of step c) in the previous section A1, each of the four substrate samples is taken out of the rack support (which in turn has just been taken out of the glass container filled with isopropanol), is placed on a spinner and is rotated at high speed for drying purposes. The system vacuum ensures that the sample substrate is correctly fixed on the surface of the spinner.

b) In this step, each of the substrate samples is again placed on the surface of the spinner and photoresist is deposited evenly distributed on the substrate surface using a syringe preventing any air bubbles to be formed. A quantity of about 0.8ml of photoresist of type AZ6632 is inserted into the syringe also without any air bubbles. Of course, before placing each of the substrates on the spinner and applying photoresist, a nitrogen gas gun is applied onto each of them to remove any attached dirt particles. Finally, in this occasion, each substrate is also rotated at high speed making sure that the whole area of the substrate surface is covered by photoresist. Such a technique allows a firm adhesion of the photoresist and a uniform distribution over the surface of the substrate. Figure A.1 shows a photograph of the spinner and the centre part is where the samples are placed:

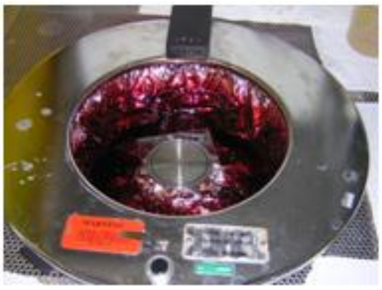

Figure A.1 – Photograph of the spinner

c) Once the spinning of every sample is finished, each of these is placed on top of a glass support. This glass support or supports, depending on the needs, are inserted inside an oven which has been preheated to 80º Celsius. The samples are cured for exactly 20 minutes inside the oven in order to dry the photoresist material and a timer is used to control the exact timing. Of course, all samples are handled with gloves and tweezers in order to maintain a clean environment and all procedures are realised inside a certified clean room.

A3 – Mask aligning and developing process

a) The first step is to load the specific mask onto the mask aligner. The system vacuum makes sure that the mask is properly held or fixed for aligning purposes. Each of the samples one at a time can then be loaded onto the mask aligner and so the first of the four substrates is inserted and aligned in relation to the specific mask used. Once the sample is properly aligned it is exposed to UV light for exactly fifteen seconds. The same task is then repeated for the other remaining three substrates.

Figure A.2 shows a photograph of the mask aligner used in the production of the PSD sensors:

Figure A.2 – Photograph of the mask aligner

b) The next step after UV light exposure is the developing process. One tray is filled with a developer solution and another tray is filled with ultra-pure water and they are placed next to each other. The first sample is immersed into the tray which contains the developer solution and it is moved for exactly 35 seconds inside the tray from side to side by tilting the tray until the existing photoresist traces seen inside the liquid disappear. The sample is then taken out from that tray straight away and it is quickly and briefly immersed in the other tray containing ultra-pure water. The sample is then taken out, rinsed again on the sink with ultra-pure water from the tap and dried using a nitrogen gas gun. The same tasks are then performed for the other three remaining substrates. The purpose of the developer solution is to dissolve the exposed areas of photoresist, without affecting the areas which were not exposed, as shown in figure A.3.

Figure A.3 – Photograph of the substrate after photolitography process using the metal mask.

This way, the substrate is imprinted with the relevant mask pattern. Again, all samples are handled with gloves and tweezers in order to maintain a clean environment and all procedures are realised inside a certified clean room.

A4 – Metallization

a) All four substrates are placed together facing downwards on a special support containing holes and the support is inserted inside the metallization equipment. Valves are closed and the samples are left in vacuum. Of course, the chromium metal sample is also inserted inside the electron gun or metallization equipment. Three vacuum stages are performed until a specific pressure is reached. The operating temperature is then set to 120º Celsius. Once this temperature is reached, the metallization procedure continues in order to set the thickness of the chromium metal layer to a required value of about 1500 Armstrong. Figure A.4 shows a photograph of the metallization or electron gun equipment used in the production of the PSD sensors:

Figure A.4 – Photograph of the electron gun or metallization equipment.

A5 – Lift-off

a) The first substrate sample is immersed into a glass container filled with acetone and this container is placed in ultrasounds until the metal areas not corresponding to the transferred metal mask pattern disappear and only the area of interest is left. The substrate is then taken out of that container filled with acetone and is immersed into another container filled with isopropanol (alcohol) and this container is also placed in ultrasounds for a few seconds. Then, the substrate is taken out of the container filled with isopropanol and is immersed into another container filled with ultra-pure water and this container is also placed in ultrasounds for a few seconds. Finally, the sample is then taken out of the container filled with ultra-pure water, is rinsed on the sink with ultra-pure water from the tap and is dried using a nitrogen gas gun. The same tasks are then repeated for the other three remaining substrates. Figures A.5a, b and c are photographs illustrating the steps of the lift-off process used in the production of the PSD sensors. Figure A.5a shows the initial step when acetone starts to remove the photoresist material. Figure A.5b shows how acetone also starts to remove the metal areas not corresponding to the transferred metal mask pattern and figure A.5c shows the final outcome being the substrate with the patterned metal layer imprinted on it.

Figure A.5 – a) Photoresist being removed. b) Photoresist and metal being removed. c) Substrate with patterned metal layer.

A6 – PECVD Plasma Enhanced Chemical Vapour Deposition

The films are deposited on 1mm thick glass substrates by radio frequency plasma enhanced chemical vapor deposition (RF-PECVD).

Figure A.6 shows a photograph of the multi chamber PECVD system used in the production of the PSD sensors:

Figure A.6 – Photograph of the PECVD system.

Before deposition, substrates are heated up to the substrate temperature, T_{sub}, while the base pressure in the chamber reaches 10^{-6} mbar. For the growth of intrinsic Si a mixture of H_2 and SiH_4 is used. For the growth of doped layers $B(CH_3)_3$ (trimethylboron or TMB) or PH_3 is added to the hydrogen-silane mixture to achieve p- or n- type doping, respectively. The deposition parameters of the individual thin films which are used in the n-i-p structure of the sensor are listed in the table A.1 below.

Table A.1 – Deposition conditions for a-Si:H thin films

Type of Si	F_{SiH4} sccm	F_{H2}, Sccm	F_{dopant}, sccm	D_H, %	R, %	T_{sub}, ºC	p_{base}, Torr	p_w, Torr	d_{I-E}, cm	P_{RF}, mW/cm^2	Thickness nm
n-	24	285	31	90.0	1.4	220	10^{-6}	2.0	2.5	50	~40
i-	100	300	-	75.0	-	225	10^{-6}	4.0	2.5	100	~600
p-	36	0	14	20.5	2.0	210	10^{-6}	0.6	2.5	30	~10

In table A.1, all parameters starting with F refer to the fluxes of the gases used, D_H is the hydrogen dilution, R or R_{dopant} is the dopant gas (TMB or PH_3) to silane flow ratio, T_{sub} is the substrate temperature, p_{base} and p_w are the base and working pressures, d_{I-E} is the inter-electrode distance, and P_{RF} is the power density.

The hydrogen dilution, D_H, is calculated as follows:

$$D_H = \frac{F_{H_2}}{F_{H_2} + F_{SiH_4} + F_{TMB}} \times 100\% \qquad \textbf{[1]}$$

and R_{dopant} is defined below:

$$R_{dopant} = \frac{F_{dopant}}{F_{SiH_4}} \times 100\% \qquad \textbf{[2]}$$

The flux of the dopant gas consists of a “TMB mixture” composed of 4.78% of TMB + 31.4% of SiH_4 + 63.83% of H_2 for the case of p-type doping, and of a “PH_3 mixture” composed of 1.51% of PH_3 + 30.2% of SiH_4 + 68.29% of H_2 for the case of n-type doping.

Figure A.7 shows a photograph of the substrates after deposition of the thin film layer n-i-p structures using the PECVD system:

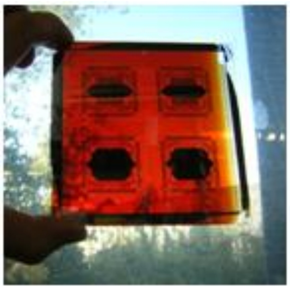

Figure A.7 – Photograph of the substrates after n-i-p
structure deposition using the PECVD system.

A7 – Dry etching

The substrates are initially placed in vacuum inside the dry etching equipment. A gas used for etching is inserted into a chamber and a secondary vacuum is performed. The gas is ionized between two electrodes inside the chamber by using radio frequency plasma. The etching gas used is SF_6, being fluorine the responsible element in the removal of silicon via the formation of SiF_4.

The parameters used for the dry-etching process are listed below:

- Material to remove: a-Si.
- Initial vacuum: 4 x 10^{-5} mbar.
- Discharge pressure: 6.5mTor.
- Applied power: 20W.
- Reflected power: 4W.
- Discharge time: 10 min.
- Gas: SF_6.
- Gas flux: 10 sccm.

Figure A.8 shows a photograph of the dry-etching equipment used in the production of the PSD sensors:

Figure A.8 – Photograph of the dry-etching equipment.

Once dry-etching is performed on all four substrates, each of them (one at a time) is taken out of the dry-etching system and is immersed into a glass container filled with acetone in order to remove the existing photoresist. If the photoresist is not removed, then the glass container is placed in ultra-sounds only for a few seconds, making sure that the photoresist will be removed. After this step, each substrate (again one at a time) is immersed into another glass container filled with ultra-pure water.

A8 – Wet etching

a) Out of the four substrate samples, the first substrate sample is immersed into a glass container filled with a solution to etch ZnO and remains there until the TCO is removed from the sensor. Such a solution can be re-used and it does not need to be disposed of, thereby all samples can be etched with the same solution. The sample is then taken out of the glass container, it is rinsed on the basin with ultra-pure water and it is dried using a nitrogen gas gun. A multi-meter is then used to check whether the TCO has really been completely removed. The same procedure is performed for the other three remaining substrates.

b) The next step is to immerse the first of the four substrates into a glass container filled with acetone for a few seconds until the photoresist (with a yellowish colour) disappears or is removed. The sample is then taken out of that glass container and it is immersed into another glass container filled with ultra-pure water for a few seconds. It is then taken out of the latter, it is rinsed on the basin with ultra-pure water and it is dried using a nitrogen gas gun. Here again, a multi-meter is used to check whether the photoresist has been completely removed. And again, the same procedure is performed for the other three remaining substrates.

APPENDIX B

Hardware and software developments for the amorphous silicon position sensitive detector array (PSD array) systems

APPENDIX B - Hardware and software developments for the amorphous silicon position sensitive detector array (PSD array) systems

B1 - NIDAQ 128 PSD hardware system

The hardware board (PCB) design comprised of 5 LAYERS is presented below:

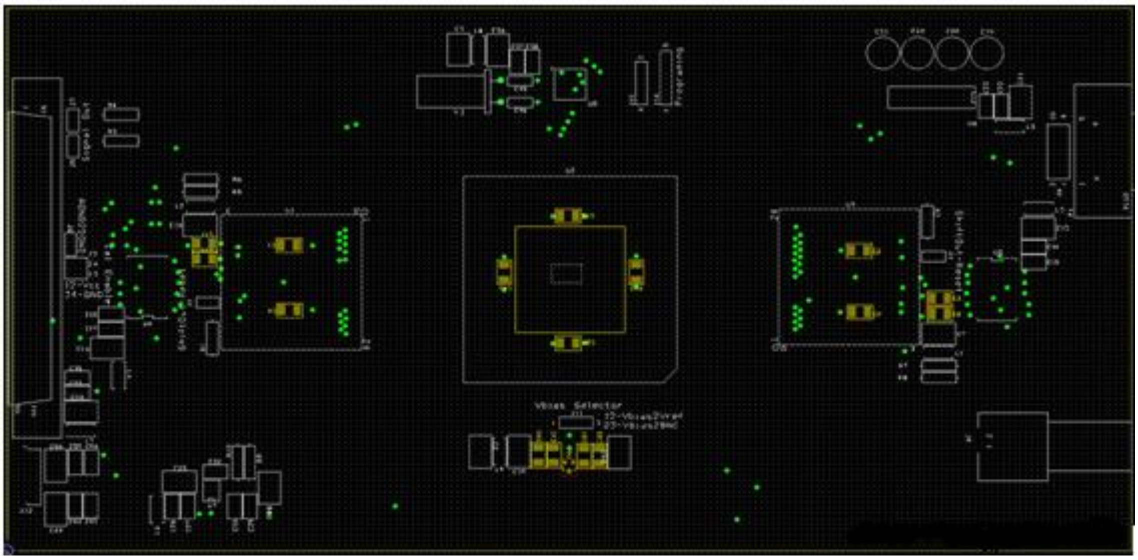

Figure B.1 – Serigraphy layer. Layer showing components to be soldered on the board.

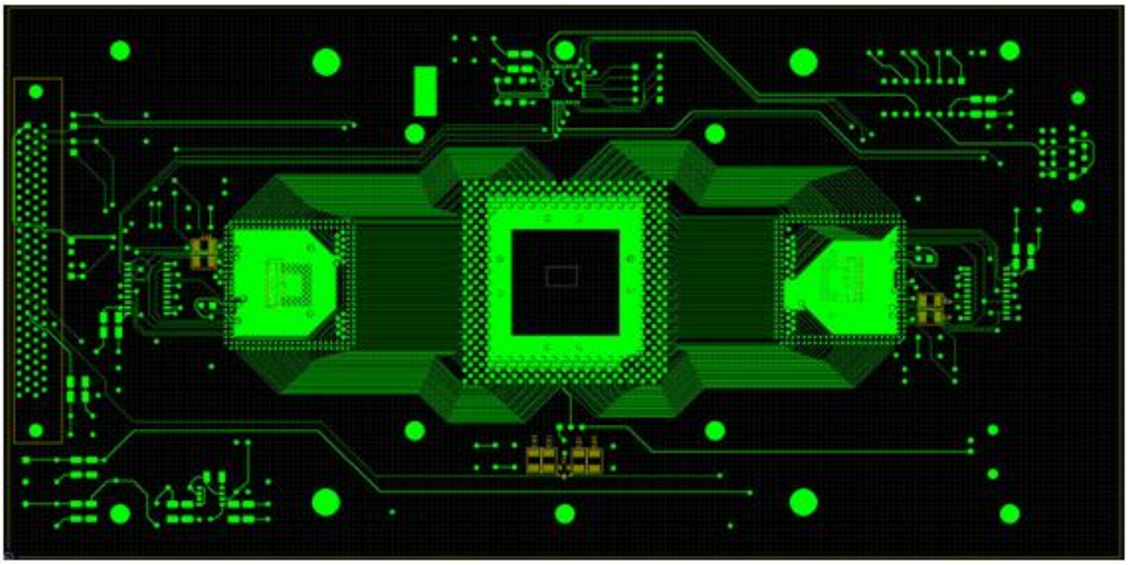

Figure B.2 – Top layer. Uppermost (TOP) layer showing board tracks routed.

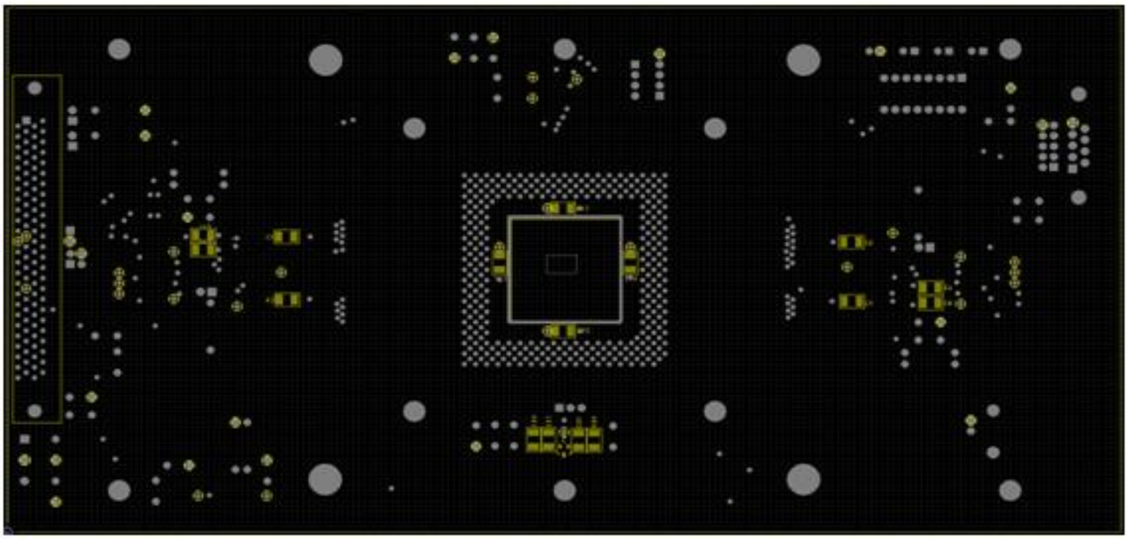

Figure B.3 – GND INV layer. Ground inverted layer showing, in grey colour, areas not connected to ground.

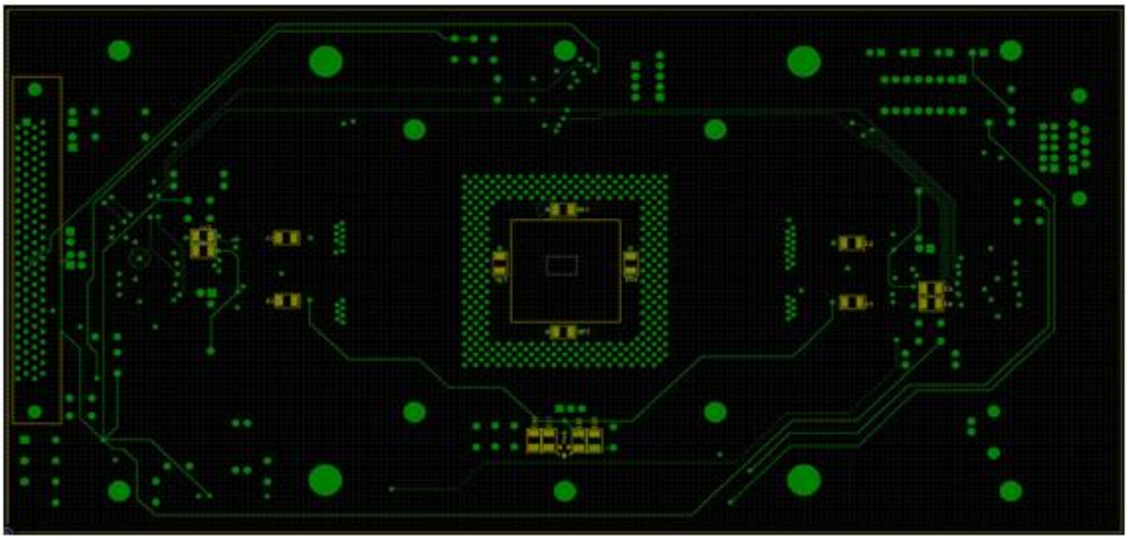

Figure B.4 – POWER layer. Green colour areas are connected to VDD (power supply) distributing 4 Volts.

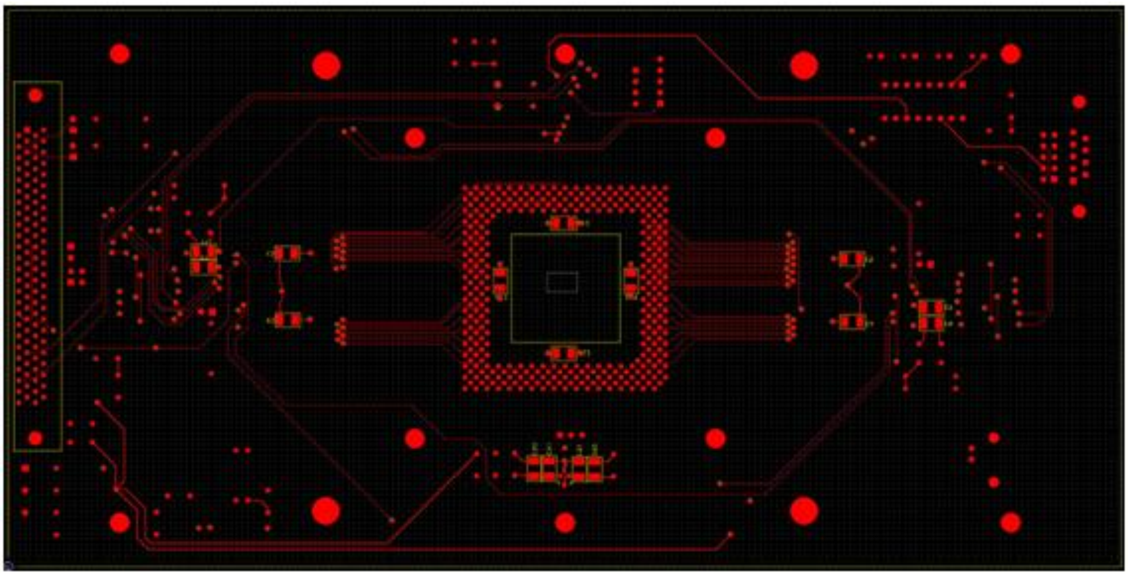

Figure B.5 – Bottom layer. Layer showing board tracks routed on the bottom part of the board.

B2 – 32 PSD sensor array software platform

Figure B.6 represents graphically the 32 sensor positions within a range of -3.5 to 3.5mm, which corresponds to the 7mm width of the active area of the sensor. Intensity is also represented in the Z-axis towards the viewer within a range of 0 to approx 55000 arbitrary units. Figure B.7 shows the rotation of the 2D plane in figure B.6 onto a 3D plane. Since the plane can be rotated in real time from 2D to 3D by just pressing the keyboard, figure B.6 and B.7 can be regarded as a graphical display 3D simulation software platform prepared for testing the 32 PSD sensor, as well as for tracking the movement of micro-macro objects within the detecting area of the 3D sensor itself. Figure B.8 shows the user interface developed where the values measured at that instant for position and intensity by the 64 acquisition channels that make up the 32 sensor channels are shown. No sensor was present in the system when this first system test was performed and therefore an analysis of the system noise present in these conditions was possible. The level of noise can be seen graphically in figure B.6 and it amounts to the deviation from the 0 position. Its value is indicated by the third number on the right, displayed in each channel in figure B.8.

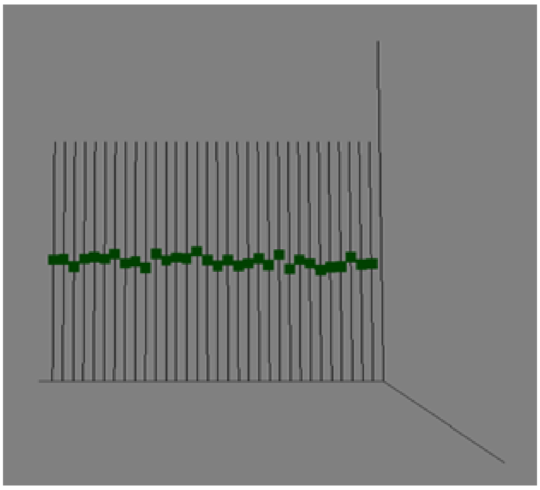

Figure B.6 – Software platform with graphical representation of the 32 PSD sensor positions and intensities.

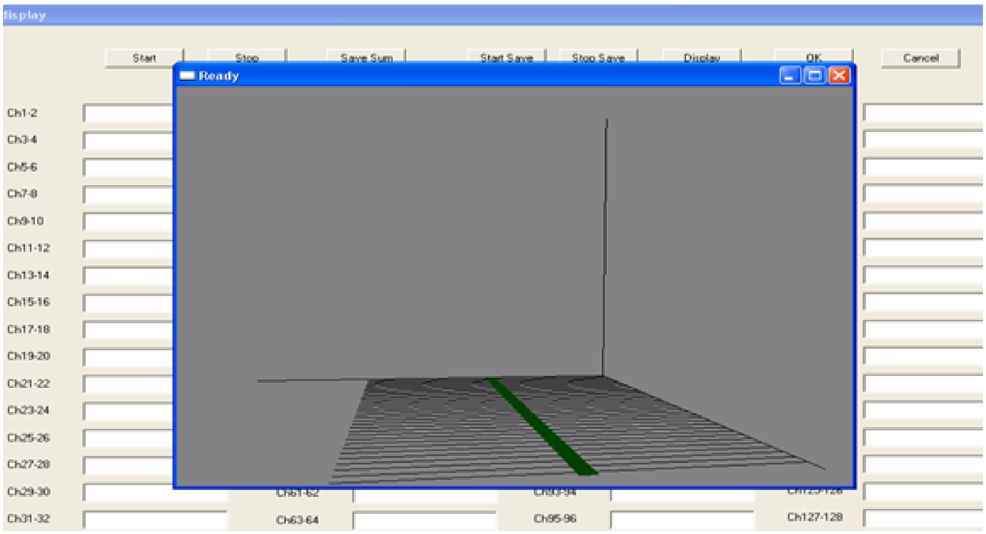

Figure B.7 – Rotation of the 2D plane in figure B.6 onto a 3D (x,y,z) plane.

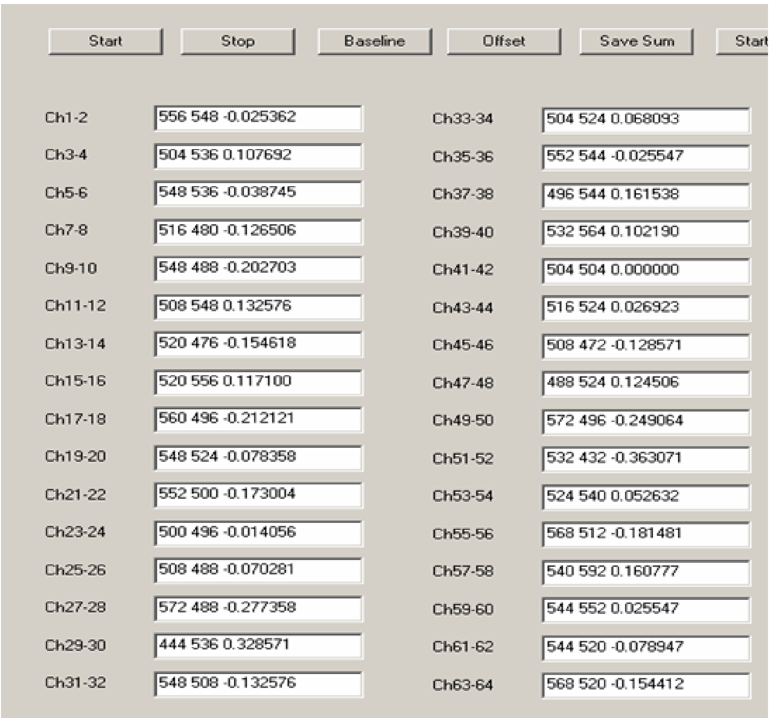

Figure B.8 – Software user interface where the 32 PSD sensor intensity and position values are displayed and recorded.

The sensor was tested with the software platform developed in order to certify the correct functioning of the software. An analysis was performed to view the position response of the sensor when shined with a red laser line on the left side of it. The outcome is shown in figures B.9 and B.10.

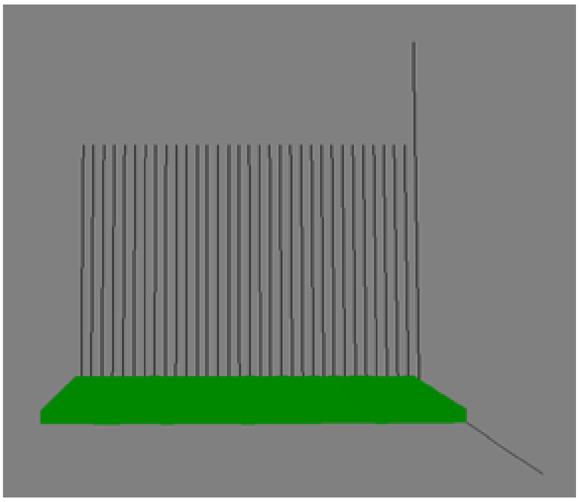

Figure B.9 – Red laser shined on the left side of the sensor. Position and intensity are displayed.

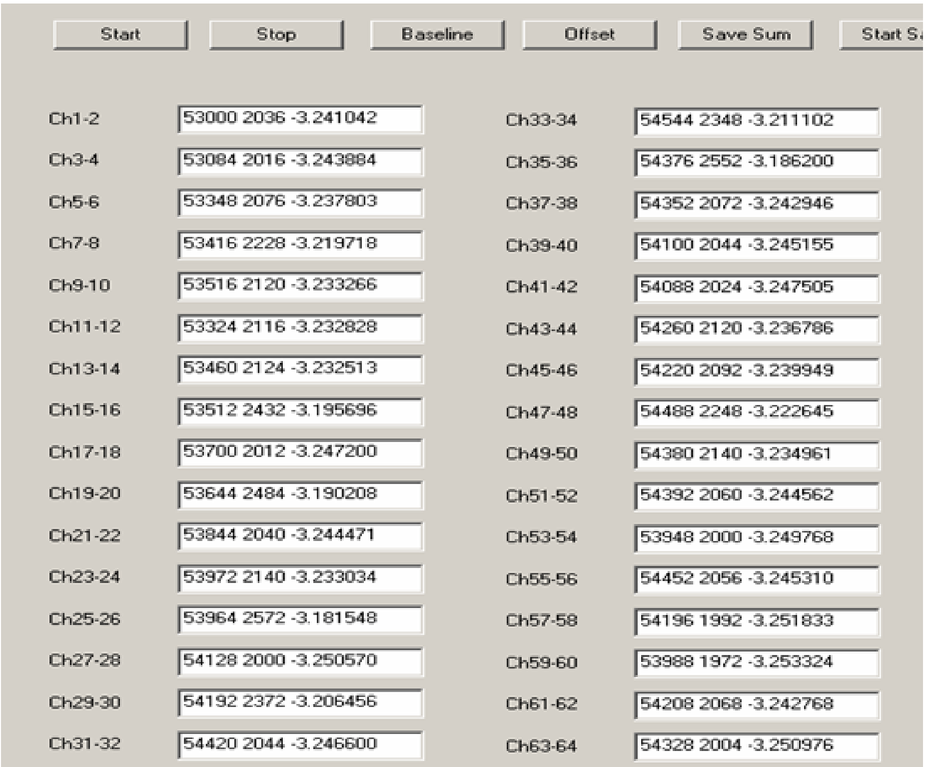

Figure B.10 – Red laser shined on the left side of the sensor. Intensity and position values are displayed and recorded.

As noticeable in figure B.9 and B.10, the 32 PSD sensor which was tested was working correctly since all 32 detectors were responding on the left side (approx. -3.2mm). This also certified that the software is working perfectly.

The same sensor was again tested with the secondary part of the software which, as already mentioned, is an OpenGL based 3D map in which the calculated sensor positions represent height information. Here, positions are displayed forming a 3D height map in real time. In order to certify the correct functioning of this secondary part of the software, again an analysis was performed to be able to view the position response of the sensor when shined with a red laser line on the left side of it. The outcome is shown in figure B.11.

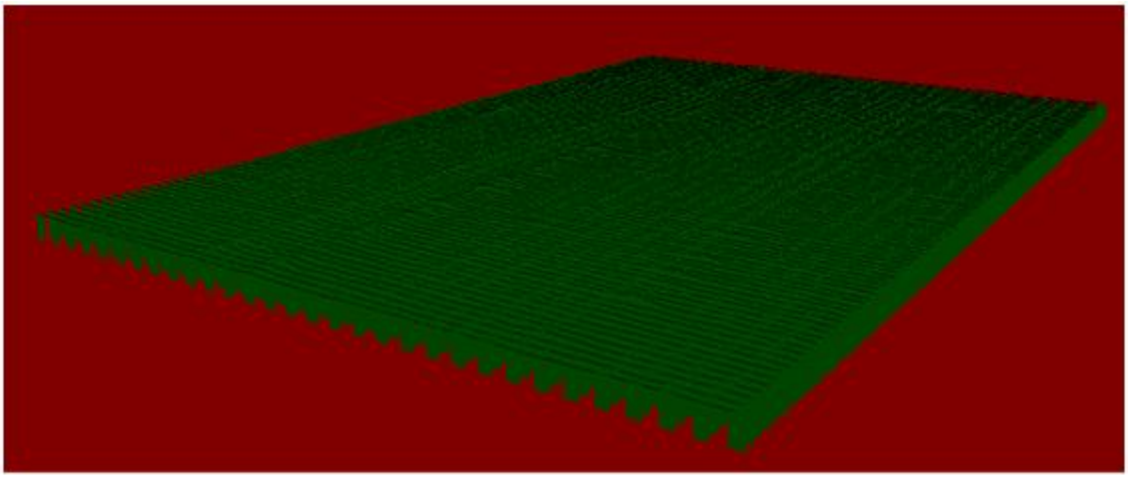

Figure B.11 – Red laser shined on the left side of the sensor for 3D rendering. Positions are displayed forming a real time 3D height map.

Figure B.11 only represents graphically the 32 sensor positions (not the intensities) within a range of -3.5 to 3.5mm on a 3D map representing 100 frames. The values measured at only one frame (out of 100) for position and intensity by the 64 acquisition channels that make up the 32 sensor channels are displayed in figure B.10. It is proven again that this sensor is working perfectly since all detectors are responding on the left side (-3.2mm) even when measured 100 times/frames on the rendered 3D map. Figure B.11 represents a smooth (no noise) 3D plane ready to start detecting the height of an object in 3D and in real time. It is smooth because as the laser line was projected on one side of the 128 sensor the existing BASELINE or "Zero line" option was selected from the user interface software. This is a calibration procedure which tells the system to set the position coming from every detector of the 128 sensor to one specific side meaning left or right depending on which side the laser is projected. Such a calibration method is only used when sensor channels are not working correctly so thereby the position of the sensor channels does not need to be forced to the correct one if a 100% working sensor has been fabricated. The 3D plane shows no noise at all and when an object is being rendered the 3D shape of the object can be seen in real time in the 3D plane of figure B.11 as it is being rendered. In this case, also the red laser is shined on the left side of the sensor for 3D rendering purposes. Positions are displayed forming a real time 3D height map of the object of interest.

B3 – 128 PSD sensor array software platform

The new (128) software platforms are based on the previous platform developed for the 32 sensor even though the hardware platform was larger or different. The major difference between the two software platforms developed for the systems including the commercial electronics module is the fact that the software platform prepared for the 128 PSD sensor is four times larger in relation to the number of channels and variables which need to be defined and used for the 32 PSD sensor. The user interface and 3D map is also four times larger in size and even the overall raw programming code is more extense.

Regarding the two existing and internally different software platforms for the 128 PSD sensor, their differences mainly lie on the fact that each has been developed to suit a distinct hardware architecture. However, externally (on the screen) or to the viewer's perspective their user interface is exactly the same. Of course, both software platform versions were prepared to perform 3D rendering with the "XDAS" and "NIDAQ" 128 PSD sensor systems.

There are two parts to the primary software code developed. One is the user interface part and the other is the 2D/3D virtual 128 PSD array sensor display. The latest version of the software user interface displaying both of these parts is shown in figure B.12.

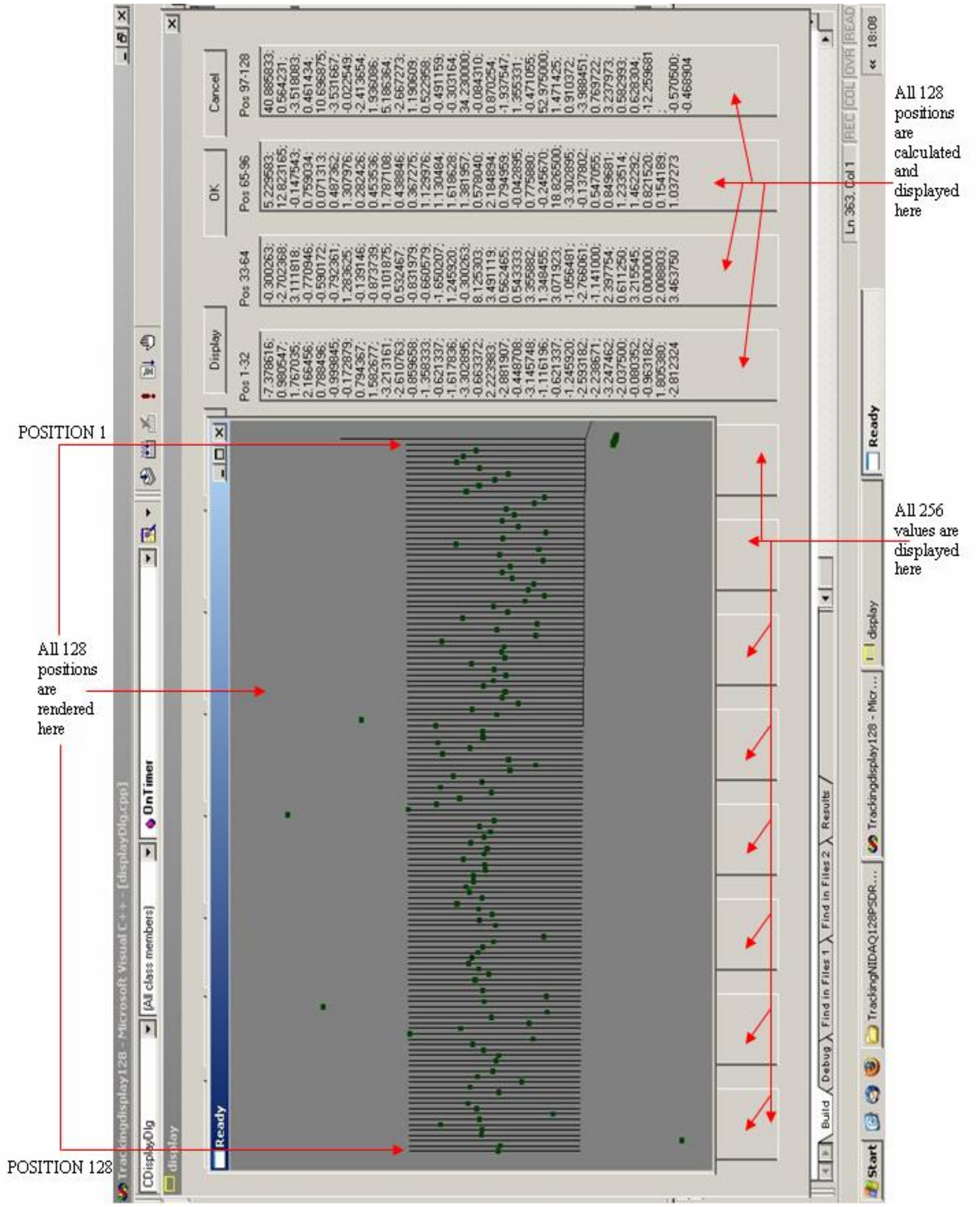

Figure B.12 – Latest version of the 128 PSD array sensor software user interface and 2D/3D virtual sensor display.

The secondary software code represents the 3D map where the 3D shape of the object is constructed as the object is scanned. If the object used is the white plastic fork shown in figure 3.9(b) of chapter 3, the outcome is the same as illustrated in figure 3.9(a) of chapter 3 but the final 3D image has four times greater resolution, since in this case a 128 PSD sensor is being used as opposed to a 32 PSD sensor and four times more information is actually acquired.